ISSUE – 1, VOLUME –5 , AUG 2020

# RESEARCH COMPENDIUM

(Faculty Research Publications)

Department of Mechanical Engineering

## (2019-20)

**BMS Institute of Technology & Management**

**Avalahalli, Yelahanka, Doddaballapura Main Road**

**Bangalore – 560064**

## Vision of the Department

To develop technically competent Mechanical Engineering professionals for the benefit of the society

## Mission of the Department

Impart quality education in Mechanical Engineering and allied areas by state- of- the- art- infrastructure and dedicated faculty.

Provide conducive environment for both students and faculty to pursue higher education & research and to work ethically for the benefit of society.

# CONTENTS

## International Journals

| Sl No | Name of Faculty | Title | Journal | Index |
|---|---|---|---|---|
| 1 | Dr. Nandini R | Energy-harvesting enhancement in composites of microwave-exfoliated KNN and multiwall carbon nanotubes | International Journal of Bull. Mater. Sci. (2019) 42:253 © Indian Academy of Sciences https://doi.org/10.1007/s12034-019-1938-6 | Scopus |
| 2 | Dr. K.M. Sathish Kumar | Influence of Process Parameters on Friction Stir Welded AA 6082-Cu Joints | International Journal of Mechanical and Production Engineering Research and Development (IJMPERD) ISSN (P): 2249–6890; ISSN (E): 2249–8001 Vol. 9, Special Issue, Dec 2019, 114–124 | Scopus |
| 3 | Dr. K.M. Sathish Kumar | Development of MATLAB Codes to Find the Natural Frequencies of a Composite Structure | Applied Mechanics and Materials ISSN: 1662-7482, Vol. 895, pp 319-323 doi: 10.4028/www.scientific.net/AMM.895.319 | Non-Scopus |
| 4 | G L Anantha Krishna<br>Dr. K.M. Sathish Kumar | Analytical and Finite Element Solution of Tractor Brake Link to achieve Weight and cost Reduction | Applied Mechanics and Materials ISSN: 1662-7482, Vol. 895, pp 307-312 doi:10.4028/www.scientific.net/AMM.895.319 | Non-Scopus |
| 5 | G L Anantha Krishna | Estimation and Comparison of Percentage Error of Theoretical and Experimental Natural Frequency of a Single Degree of Freedom System using Spring Mass System | International Journal of Engineering Science and Computing IJESC Volume 10 Issue No.2 | Non-Scopus |
| 6 | Dr Nandini R | Kinetic analysis of isothermal solid-state process for synthesized potassium sodium niobate piezoelectric ceramics | ScienceDirect Materials Today: Proceedings 5 (2018) 20939–20946 | Scopus |

| | | | | |
|---|---|---|---|---|
| 7 | Dr. Nandini R | Influence of Mwcnts/Zinc Oxide Nanoparticles/Epoxy Resin Composite Coating on Mild Steel to Enhance Anticorrosion and Mechanical Properties | International Journal of Innovative Technology and Exploring Engineering ISSN: 2278-3075, Volume-9 Issue-6, April 2020 | Scopus |
| 8 | Kiran M D<br>H. K Govindaraju | Evaluation of Mechanical and Fracture Properties of Nickel Coated Short carbon Fiber/ Epoxy Composites with Nanofillers | Jour of Adv Research in Dynamical & Control Systems, Vol. 12, Special Issue-02, 2020 | Scopus |
| 9 | S. Nithya Poornima | Multipurpose Agribot | International Journal of Latest Technology in Engineering, Management & Applied Science (IJLTEMAS) Volume VIII, Issue X, October 2019 \| ISSN 2278-2540 | Non-Scopus |
| 10 | Dr. Sangmesh B | Performance Evaluation of Cryogenic Treated and Untreated Carbide Inserts during Machining of AISI 304 Steel | International Journal of automotive and Mechanical Engineering, Vol 17, Issue 1, 2020 7709-7718. | Non-Scopus |
| 11 | G. L. Anantha Krishna | Analytical and Finite Element Analysis of a Typical Curved Beam | IJESC, Volume 10 Issue No.7, July 2020, ISSN 2321 3361. | Non-Scopus |
| 12 | H. K. Govindaraju, Kiran M D | Mechanical Behavior of Heat Treated Al6061-Tungsten Carbide and Graphite Reinforced Hybrid Composites | Journal of Critical Reviews ISSN- 2394-5125 Vol 7, Issue 17, 2020 | Scopus |
| 13 | Kiran M D | Dry sliding wear behaviour of short Carbon fibre reinforced aluminium matrix composites | Journal of Critical Reviews ISSN- 2394-5125 Vol 7, Issue 15, 2020 | Scopus |
| 14 | Sriganesh T G | Development of vertical axis wind turbine by Maglev suspension – An innovative approach | Journal of Physics: Conference Series, Vol 1473, 2020 https://iopscience.iop.org/article/10.1088/1742-6596/1473/1/012020 | Non-Scopus |
| 15 | Keerthi Kumar N | Impact of Nano additives on Performance and Emission Characteristics of C.I. Engine | Journal of Critical Reviews ISSN- 2394-5125 Vol 7, Issue 17, 2020 | Scopus |

| | | | | |
|---|---|---|---|---|
| | | Operated Using Blended Simarouba Oil Methyl Ester | | |
| 16 | Keerthi Kumar N | Experimental Study on Characteristics of Direct Injection Compressed Ignition Engine Using Waste Plastic Oil and Biodiesel Blends | International Journal of Mechanical and Production Engineering Research and Development (IJMPERD), ISSN (P): 2249–6890; ISSN (E): 2249–8001, Vol. 10, Issue 3, Jun 2020, 2085-2094 | Scopus |
| 17 | H. K. Govindaraju,<br>Kiran M D | Wear behavior of aluminum metal matrix composites: A Taguchi approach | AIP Conference Proceedings 2247, 040005 (2020); https://doi.org/10.1063/5.0003802 | Scopus,<br>Web of Science |
| 18 | Kiran M D<br>H. K. Govindaraju, | Fracture toughness of surface treated short fiber reinforced epoxy composites | AIP Conference Proceedings 2247, 020006 (2020); https://doi.org/10.1063/5.0003825 | Scopus,<br>Web of Science |

*Bull. Mater. Sci.* (2019) 42:253
https://doi.org/10.1007/s12034-019-1938-6


# Energy-harvesting enhancement in composites of microwave-exfoliated KNN and multiwall carbon nanotubes

**NANDINI R NADAR[1], M KRISHNA[2,*] and A V SURESH[1]**
[1]Department of Mechanical Engineering, BMS Institute of Technology and Management, Bangalore 560064, India
[2]Research and Development Centre, Department of Mechanical Engineering, R.V. College of Engineering, Bangalore 560059, India
*Author for correspondence (krishnam@rvce.edu.in)

MS received 25 May 2018; accepted 1 June 2019

**Abstract.** The objective of this research work is to investigate the effect of multiwall carbon nanotube (MWCNT) content (0.3–1.2 wt%) on a potassium sodium niobate (KNN)-based piezoelectric unimorph harvester for enhancing the energy generation capacity. KNN–MWCNT composites were fabricated by using a microwave solid state technique. The energy-harvesting performance of the KNN–MWCNT composite was determined by the base excitation method and sized to resonate between 20 and 100 Hz at 1 MΩ load resistance. The energy performance of the KNN composite at percolation threshold (0.6 wt% MWCNT) showed a maximum power generation of 2.94 μW, the power density of 7.15 μW $m^{-3}$ and overall efficiency of 83.75% at an input acceleration of 0.5 g and a load resistance of 1 MΩ. Improvements observed in the power generation by percolation phenomena and ionic flow over the nanotube surface of KNN composites prove to be a boon for low-power sensing devices.

**Keywords.** MWCNT; KNN; KNN–MWCNT harvesters; damping; energy conversion; power density.

## 1. Introduction

The limited operating life of batteries has made energy harvesting an essential requirement for powering remote sensors. Piezoelectric transducers have attracted the attention of researchers for energy harvesting due to their remarkable energy conversion efficiency and high-specific energy density [1]. They are slowly replacing conventional power sources in low-power applications like portable electronic devices, wireless sensors and health monitoring and control systems [2,3]. It also possesses market intrusion in remote operating devices, such as transducers [4,5], sensors [6,7], actuators [8,9], surface acoustic wave devices [10,11] and frequency control [2].

The piezoelectric energy harvester's capacity can be tailored by its functional properties, such as electromechanical coupling coefficients, piezoelectric strain coefficients, dielectric constant, density and electrical and mechanical quality factors. The major share of piezoelectric energy-harvesting market is captured by lead-based piezoelectric materials like lead zirconate titanate (PZT) due to their excellent performance [12–15]. The presence of 60% lead by weight in PZT is extremely toxic to the environment and human beings. In this regard, 'The restriction of hazardous substances directive' legislation was passed by the European Union in 2003 and exemption of its usage ends by 2016 [16]. Lead-free-based potassium sodium niobate (KNN) ceramics have revolutionized the piezoelectric industry for energy harvesting. It is mainly because of their high-Curie temperature and the presence of a morphotropic phase boundary between two-orthorhombic phases [17,18]. KNN finds numerous practical applications, such as electronic transducers [19], voltage transformers [20], multilayer actuators [21] and ultrasonic motors [22]. Alkaline ($Li^+$, $Ba^{2+}$, $La^{3+}$, $Bi^{3+}$) and transition ($Ti^{4+}$, $Sb^{5+}$, $Ta^{5+}$) element-doped KNN ceramics were developed to enhance the functional properties and thermal stability by shifting the polymorphic phase transition (PPT) [23–26]. Even though modified-KNN ceramics have captured the piezoelectric market for buzzers (lithium and Sb-doped KNN) [27] and actuators (K, Na, Li, Ba, Sr) (Nb, Ta, Zr) $O_3$ ceramic [28] applications, sensitive processing issues, temperature-dependent piezoelectric properties and poor stability of the poled domain state provide further scope for improvements [26,29,30] in KNN ceramics for electronics and energy-harvesting applications.

Carbon nanotube (CNT) reinforced polymer composite-based piezoelectric materials show remarkable enhancement in the stability of the poled domain state and improvement in processing sensitivity and thermal stability [31–34]. An increase of 61.3% in piezoelectric charge coefficient (19.8 pC/N), 67% increase in dielectric constant, 89% increase in dielectric loss factor, significant elastic moduli with a good frequency and energy conversion response were reported for CNT reinforced PZT–PVA 0–3 and CNT–PZT epoxy matrix composites [31–34]. Even though the CNT is a potential candidate for tailoring the functional properties of piezoelectric ceramics, no research studies have focussed on

Published online: 05 August 2019

developing CNT reinforced KNN-based piezoelectric energy harvesters (PEHs). The objective of the present research work was to develop and evaluate the energy conversion performance of a KNN–MWCNT (0.3–0.9 wt%)-based piezoelectric harvester. The developed piezoelectric harvesters were subjected to sinusoidal vibrations using a shaker in transverse mode by using the base excitation method at an input acceleration of $0.5g$, between 20 and 100 Hz for evaluating the energy performance of KNN composite-based harvesters.

## 2. Materials and methods

The stoichiometric computation of elemental powders, i.e., $Na_2CO_3$, $K_2CO_3$ and $Nb_2O_5$ of 35 g were preheated at 200°C for 2 h and were ball milled for 15 h at 300 rpm with a ball-to-powder ratio of 10:1 to obtain homogenously milled $(K_{0.5}Na_{0.5})$-$NbO_3$ nanopowder. The blended KNN powder was calcined at 900°C for 5 h and remilled for 2 h to obtain non-agglomerated KNN nanopowder. Functionalized, surface treated and ultrasonicated MWCNTs (0.3–1.2 wt%) were mixed with a known mass of KNN slurry in ethanol medium and sonicated for 2 h to obtain a uniform dispersion [35]. Then vacuum dried KNN–MWCNT composite powder was pressed uniaxially at 250 MPa for preparing discs with a diameter of 10 mm and a thickness of 1.5 mm. The green compacts of KNN composites were densified by microwave-assisted sintering at 1100°C for 30 min. The obtained KNN composite discs were polished by using silicon carbide powder and were coated with silver paste on both parallel surfaces for electrical measurements. For piezoelectric activation, all samples were polled in a silicon oil bath under a poling field of 2.5–4 kV $mm^{-1}$ dc for 30 min at an optimized temperature using the parallel plate contact polarization method and a Spellman SL Series high-voltage generator [35]. The strain induced in the KNN lattice due to the presence of MWCNTs was measured using a precision premier II ferroelectric tester (Radiant technologies.INC) to evaluate high-energy dissipating multiwall type failures and plastic buckling as reported in our previous research article [35]. It is simultaneously responsible for strengthening, toughening and softening of the matrix along strain induction in the KNN lattice.

The poled KNN–MWCNT (0.3–1.2 wt%) composites with a diameter of 10 mm and a thickness of 1.3 mm were attached to a steel cantilever beam of dimension 88 mm × 12 mm × 0.3 mm using silver epoxy and were cured for 12 h to obtain appropriate adhesion between the composite disc and the beam. The copper tape was applied to the edge surface of the disc and to the steel beam of the harvester to function as top and bottom electrodes. The fabricated harvesters and schematic of the test setup are shown in figures 1 and 2, respectively. KNN–MWCNT harvesters were characterized for their energy conversion performance by subjecting to sinusoidal vibrations using a shaker (LDS, V406/8-PA100E, Royston) (figure 1) at $0.5g$ acceleration

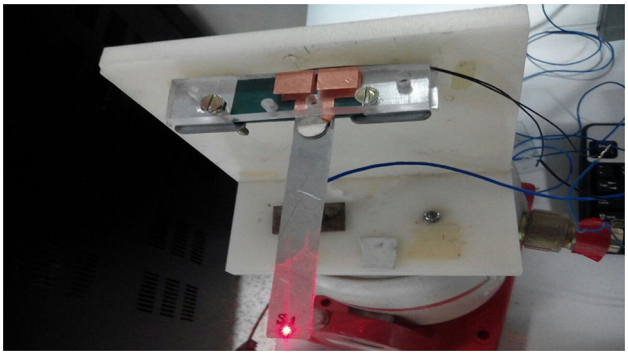

**Figure 1.** Fabricated KNN–MWCNT harvester subjected to a shaker tool.

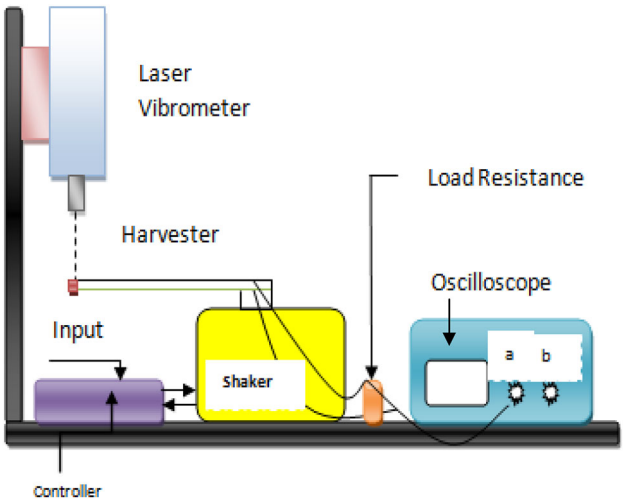


**Figure 2.** A schematic representation of the experimental setup to evaluate the performance of the KNN–MWCNT harvesters.

($g = 9.81$ m $s^{-2}$) between 25 and 100 Hz. The top and bottom electrodes of the harvester were linked to the load resistance and were coupled to the oscilloscope. The desired acceleration input of $0.5g$ was assigned to the shaker by using a controller and the relative displacement of the harvesters was monitored using a laser vibrometer (Polytec-GmbH, PDV-100, Germany). The potential voltage developed in the harvester due to vibrations was measured using a Tektronix TDS1002B oscilloscope (Oregon, USA) at an optimum load resistance of 1 MΩ (figure 2). The damping ratio ($\xi$) of the harvester samples was calculated through dynamic tip displacement [36]. The current flowing into the load resistance was derived from Ohm's law. The effective RMS value of the varying voltage (V) was computed from the peak value by assuming the source to be a sine wave. The power developed at load resistance was obtained from the product of effective values of voltage and current [37] and energy conversion efficiency was evaluated by using $k_p^2$ and $\zeta_m$ values $k_p^2/\zeta_m > 1$ [38]. The input power was calculated by the product of force applied (mass of the sample and input acceleration ($0.5g$)) and

displacement obtained from the harvester when subjected to base excitation. The power density was computed as the maximum output power divided by the volume of the cantilever to evaluate the power generation performance; the efficiency of the harvester was evaluated by using the output and input power parameters. Finally, the theoretical output power of the KNN–MWCNT-based piezoelectric energy-harvesting unimorph cantilever was calculated by the electric equivalent circuit model method [39,40].

## 3. Results

### 3.1 *Effect of temperature on the conductivity of KNN composites*

The behaviour of electrical conductivity of pure KNN and its composites as a function of temperature is shown in figure 3. The conductivity in KNN being 4.67 $E^{-5}$ S $m^{-1}$ at 22°C increased gradually, reached the peak at 60°C and decreased towards the PPT temperature at 198°C. The conductivity of KNN–MWCNT (0.3 wt%) composites as observed is 4.514 $E^{-5}$ S $m^{-1}$ at RT, was consistent up to 150°C and increased gradually towards PPT. The improved conductivity of 5.142 $E^{-5}$ S $m^{-1}$ observed for 0.6 wt% loading of MWCNTs at RT was consistent with slight variation (±0.66 $E^{-5}$) and increased gradually towards the PPT (198°C). Furthermore, the addition of 0.9 wt% of MWCNT resulted in an increased conductivity of 5.54 $E^{-5}$ S $m^{-1}$ at RT and obtained the maximum value of 1.16 $E^{-4}$ S $m^{-1}$ towards the phase transition temperature. Finally, the addition of 1.2 wt% of MWCNTs into the matrix resulted with the enhanced conductance of 6.22 $E^{-5}$ S $m^{-1}$ at RT but reduced drastically with an increase in temperature up to 150°C and increased gradually towards the phase transition temperature. Based on thermal stability, the percolation threshold for KNN composites is figured out to be 0.6 wt% addition of MWCNTs into the matrix.

### 3.2 *Displacement frequency response*

The tip displacement of the harvesters as a function of frequency for an input acceleration of 0.5*g* is shown in figure 4. The displacement values of all the samples measured between 10 and 50 Hz increased gradually with an increase in the frequency, reached maximum near its respective excitation frequency and reduced drastically thereafter as shown in figure 4. The KNN harvester measured displacement value was 1.23 mm at an excitation frequency of 31.22 Hz. The addition of MWCNTs (0.3–0.9 wt%) into the KNN matrix resulted in improvement of the displacement and excitation frequency of the KNN composite by 27.57% (1.25 mm), 30.35% (1.77 mm), 9.34% (1.34 mm), 0.70% (31.44 Hz), 0.80% (31.47 Hz) and 7.2% (33.47 Hz), respectively. Further loading of MWCNTs by 1.2 wt% into the KNN matrix above electrical percolation resulted in a reduced displacement value of 0.49 mm. The maximum displacement of 1.77 mm reported for KNN–MWCNT (0.6 wt%) composites indicates the completion of the electroconductive network within the matrix at percolation threshold.

### 3.3 *Voltage–current–power frequency response*

3.3a *Voltage frequency response*: The voltage frequency response of KNN composite harvesters for 0.5*g* input acceleration at a load resistance of 1 MΩ is shown in figure 5. The voltage potential developed by all the samples for the given input acceleration increased gradually and attained the maximum peak for their respective excitation frequency and reduced drastically thereafter as shown in figure 5. The

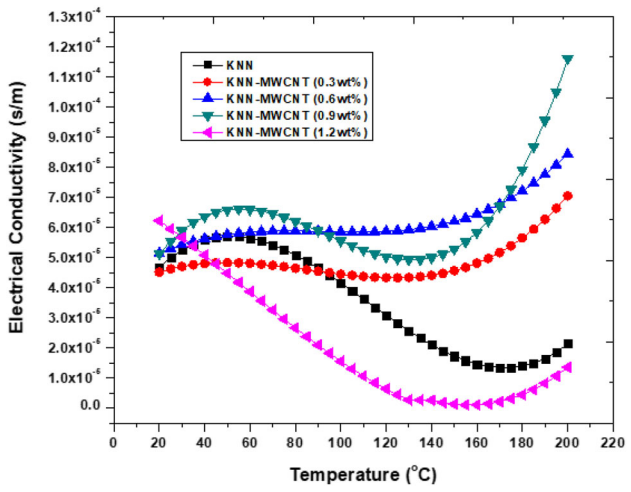


**Figure 3.** Temperature-dependent electrical conductivity of KNN and KNN–MWCNT composites.

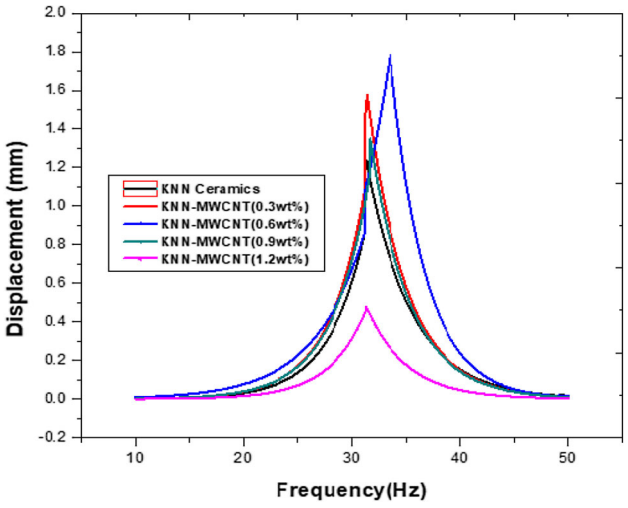


**Figure 4.** Displacement data of KNN harvesters extracted at a selected frequency range of 10–50 Hz.

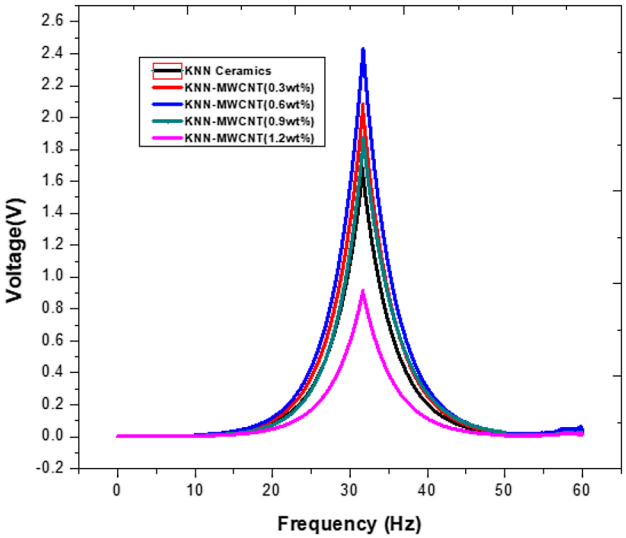


**Figure 5.** Voltage frequency response of KNN–MWCNT harvesters in comparison with KNN harvesters at an input acceleration of 0.5$g$.

voltage induced in the KNN harvesters due to vibrations was 1.66 V at an excitation frequency of 31.65 Hz. Furthermore, the addition of MWCNTs (0.3–0.9 wt%) into the KNN matrix resulted in the improvement of its voltage potential by 24.02% (2.06 V at 31.79 Hz), 48.53% (2.46 V at 31.95 Hz) and 12.24% (1.86 V at 31.79 Hz), respectively, with an increase in its corresponding excitation frequency. However, KNN–MWCNT composites with the concentration above the critical percolation (1.2 wt%) resulted in the development of a very low potential of 0.9153 V in the harvester. The maximum voltage of 2.46 V generated in the KNN–MWCNT (0.6 wt%) composite indicates the improved percolation path within the KNN matrix.

3.3b *Current frequency response*: The current frequency response of the harvesters for an input acceleration of 0.5$g$ is shown in figure 6. The current generated by all the harvester samples increased gradually and reached a maximum at their excitation frequency and decreased further as shown in figure 6a and b. It could be noticed that even the excitation frequency increased slightly with the addition of MWCNTs till 0.9 wt% and reduced thereafter as shown in figure 6b. The current generated by KNN harvesters was 1.6621 μA at an excitation frequency of 31.62 Hz. The addition of MWCNTs between 0.3 and 0.9 wt% into the KNN matrix enhanced the induced current by 25.30% (2.08 μA at 31.691 Hz), 46.33% (2.43 μA at 31.75 Hz) and 12.61% (1.87 μA at 31.79 Hz), respectively, with an increase in its corresponding excitation frequency. A further addition of MWCNTs by 1.2 wt% (above the electrical percolation) yielded only 0.9153 μA at the reduced excitation frequency of 31.69 Hz. The maximum current of 2.43 μA generated in the KNN–MWCNT (0.6 wt%)-based PEH can be attributed to the well dissipated electric energy within the composites.

3.3c *Power frequency response*: The power frequency response of the harvesters for an input acceleration of 0.5$g$ is shown in figure 7a and b, respectively. The output power of all the harvesters increased gradually and reached a maximum at their excitation frequency and further decreased subsequently as shown in figure 7b. The computed output power of KNN ceramics was 1.48 μW at 31.60 Hz. The addition of MWCNTs (0.3–0.9 wt%) into the matrix helped in the improvement of the output power by 52.20% (2.17 μW at 31.70 Hz), 89% (2.97 μW at 31.81 Hz) and 24.83% (1.78 μW at 31.91 Hz), respectively, with an increased excitation frequency due to enhanced percolation clusters and interfacial effects. However, the power generated by the addition of MWCNTs above the percolation threshold (1.2 wt%) resulted in least output power (0.4714 μW at 31.70 Hz) in comparison with pure KNN harvesters. This effect can be associated with reduced connectivity between the charge carriers within the matrix. It is due to the formation of agglomeration and high porosity for loading of MWCNTs above the threshold.

3.3d *Power density frequency response*: The harvested power density of KNN composites for loading of MWCNTs between 0.3 and 1.2 wt% as a function of frequency (14–45 Hz) is depicted in figure 8. It is observed from the graph that the amplitude of the power density for all PEHs increased gradually and reached a maximum near its respective excitation frequency and decreased sharply thereafter. The amplitude of the power density evaluated for KNN ceramics was 4.13 μW m$^{-3}$ at 31.66 Hz. The addition of MWCNTs (0.3–0.9 wt%) into the KNN matrix enhanced the power density by 26.63% (5.23 μW m$^{-3}$ at 31.70 Hz), 44.34% (5.97 μW m$^{-3}$ at 31.82 Hz) and 10.65% (4.57 μW m$^{-3}$ at 31.91 Hz), respectively, with an increase in its corresponding excitation frequency. However, the addition of MWCNTs above the percolation threshold (1.2 wt%) resulted in an reduction of the power density by 56.41% (2.33 μW m$^{-3}$ at 31.57 Hz). This effect can be attributed to the increased thermal resistivity for the flow of charge carriers within the matrix.

### 3.4 *Effect of MWCNTs on the performance of KNN composites*

3.4a *Damping ratio*: The effect of MWCNTs on the damping ratio, energy conversion and $K_p$ parameters of KNN composite harvesters is shown in figure 9a. $K_p$ values were taken from author's previous research work [35]. The damping ratio of 0.055 for KNN ceramics decreased gradually with the addition of MWCNTs up to 0.9 wt% (0.0213) and

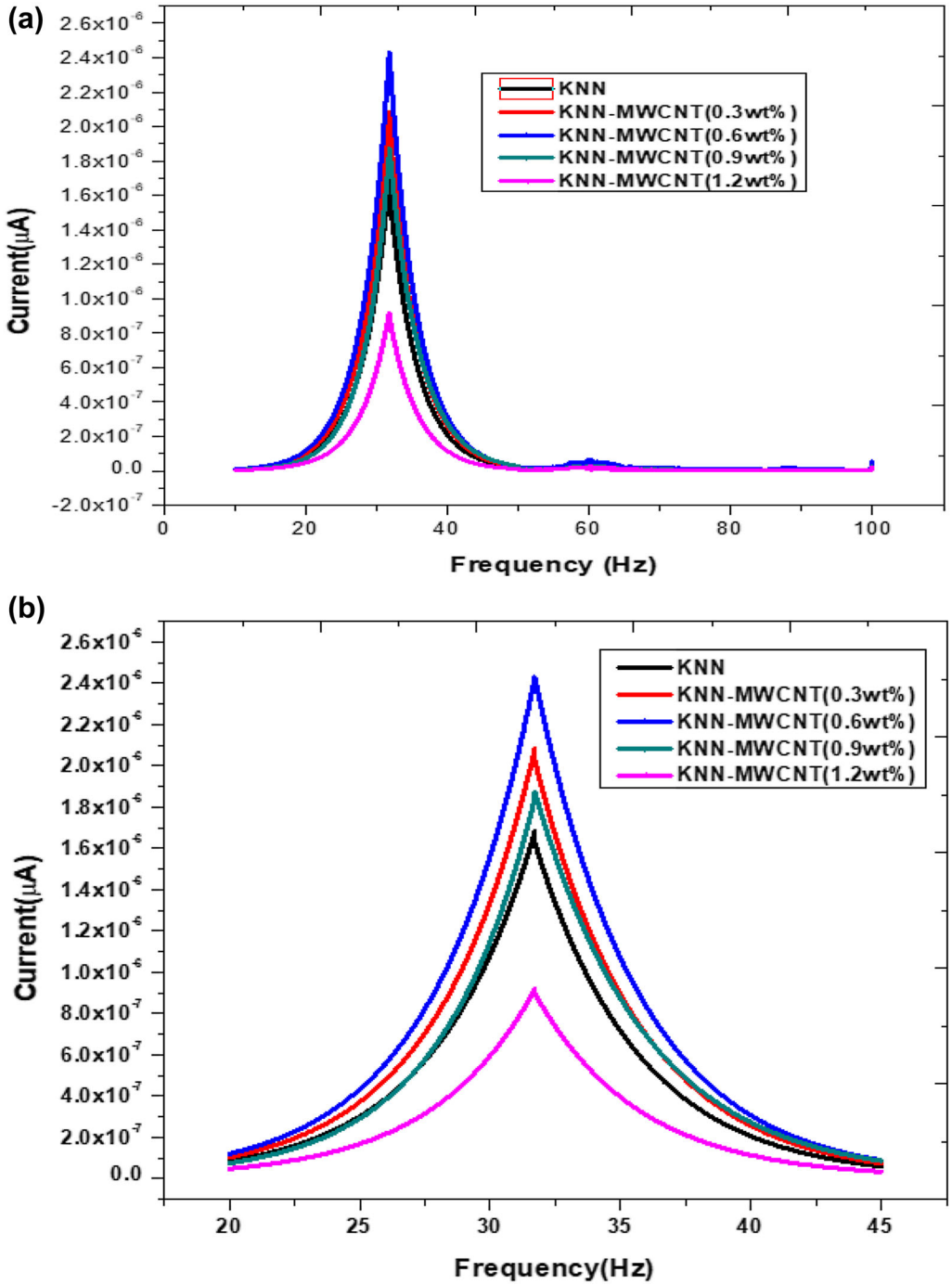


**Figure 6.** Current frequency responses of KNN and its composite-based harvesters (**a**) 0–100 Hz and (**b**) 20–45 Hz at an input acceleration of 0.5*g*.

increased for loading above the percolation threshold (0.0378 at 1.2 wt%) as shown in figure 9a. The reduction in the damping ratio of KNN–MWCNT-based PEH can be attributed to the effect of MWCNTs on slippages of atoms at the interface and an increase in the damping ratio can be associated with improper distribution of MWCNTs across bulk grains of KNN composites.

3.4b *Energy conversion*: The effect of MWCNTs on the energy conversion factor of KNN composites is shown in figure 9a. The energy conversion of KNN ceramics increased gradually with the addition of MWCNTs into the matrix, reached a maximum of 0.9 wt% and reduced for loading of MWCNTs above the percolation threshold. The conversion value of the KNN ceramics being 24.07%, increased to

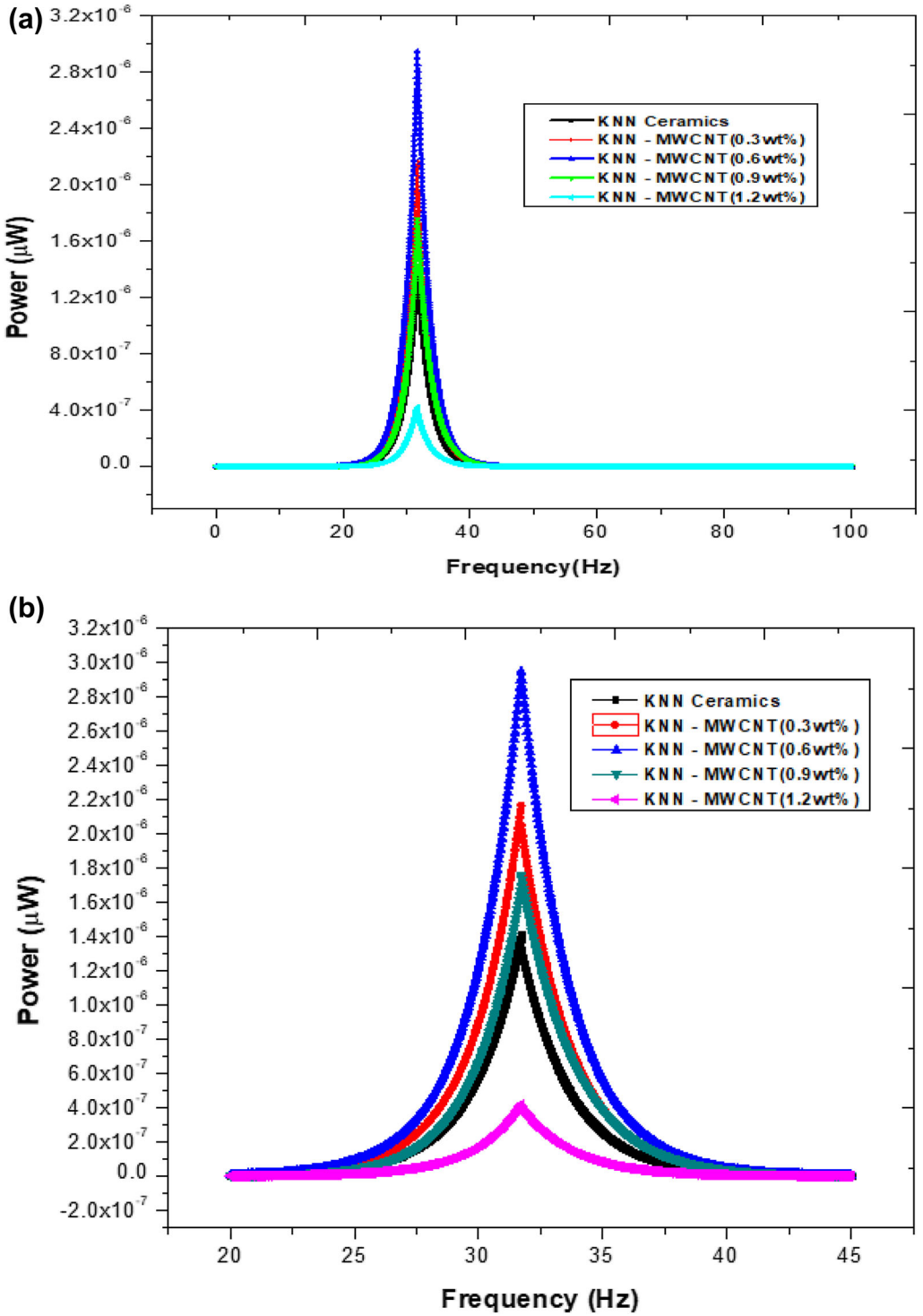


**Figure 7.** Power frequency response of KNN and its composite harvesters (**a**) 0–100 Hz and (**b**) 20–45 Hz at an input acceleration of 0.5$g$.

41.56% MWCNT (0.3 wt%), 63.39% MWCNT (0.6 wt%) and 100% MWCNT (0.9 wt%) and decreased to 28.34% for 1.2 wt% loading of MWCNTs. The obtained maximum energy conversion factor of 100% can be attributed to the least damping effect (0.0213($\xi$)) and high-coupling coefficient (0.46) achieved at 0.9 wt% as observed in figure 9a.

3.4c *Electromechanical coupling coefficients*: The effect of MWCNTs on the electromechanical coupling coefficient

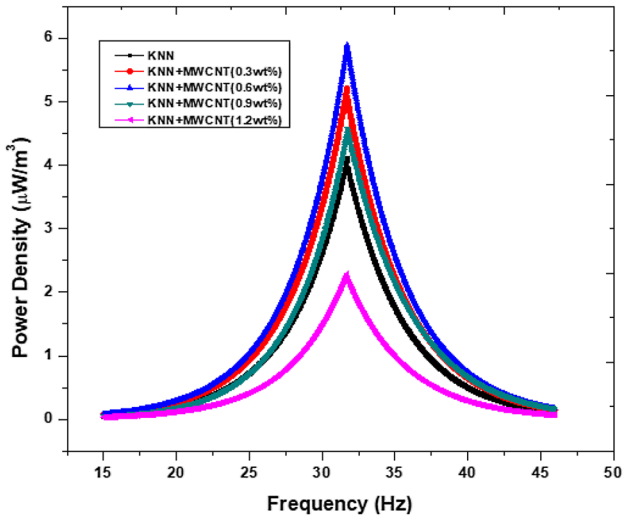


**Figure 8.** Harvested power density variation with frequency for different KNN composites.

of KNN composites is shown in figure 9a. The coupling coefficients of KNN ceramics increased with the addition of MWCNTs, reached a maximum at the threshold and reduced sharply for loading MWCNTs above the percolation threshold. KNN ceramics being 0.36 units increased by 8.79% (0.39 at 0.3 wt%), 17.74% (0.42 at 0.6 wt%) and 28.07% (0.46 at 0.9 wt%), respectively. A further addition of MWCNTs above the percolation threshold resulted in the reduction by 11.11% (0.32 at 1.2 wt%), which can be associated with the increased damping effect and improper distribution of MWCNTs within the KNN matrix. However, the maximum coupling coefficient (0.46) obtained for KNN–MWCNT (0.9 wt%) composites could be attributed to the strong electromechanical coupling coefficient achieved with the least damping effect.

3.4d *Output performance*: The variation of displacement, induced voltage and power output of KNN composites by addition of MWCNTs into the KNN matrix are shown in figure 9b. KNN ceramics are now observed with low-voltage potential (1.67 V), displacement (1.23 mm) and output power (1.42 μW). It increased gradually with the addition of MWCNTs, reached the maximum at percolation threshold (0.6 wt%) and reduced thereafter. A displacement of 1.23 mm, as reported for KNN ceramics, increased gradually and reached a maximum of 1.78 mm for 0.6 wt% addition of MWCNTs. However, the addition of MWCNTs above threshold resulted in reduced displacement (1.34 mm (0.9 wt%) and 0.47 mm (1.2 wt%)) values due to the increased stiffness of the matrix. The voltage of 1.67 V, being reported for KNN ceramics increased gradually and reached a maximum of 2.43 V at 0.6 wt% loading of MWCNTs due to the improved resistivity and strong electromechanical coupling system developed within the matrix as shown in figure 9b. However, there was a gradual reduction in the voltage potential developed (1.87 V (0.9 wt%), 0.92 V (1.2 wt%)) by the composites for loading of MWCNTs above the percolation threshold. This effect can be attributed to the enhanced resistivity within the composite. Power of KNN ceramics being 1.42 μW increased gradually with the addition of MWCNTs, reached a maximum of 2.95 μW at percolation threshold (0.6 wt%) and reduced drastically for loading MWCNTs above threshold (1.76 μW at 0.9 wt% and 0.419 μW at 1.2 wt%) as shown in figure 9b. This effect can be contributed to high-induced resistivity in the PEH of KNN–MWCNT composites.

3.4e *Work done, power density and efficiency parameters*: The effect of MWCNTs on work done, power density and efficiency parameters of KNN composites is shown in figure 10. The output parameters of KNN composites increased gradually with the addition of MWCNTs, reached maximum threshold (0.6 wt%) and decreased drastically beyond percolation threshold. KNN ceramics observed with a power density of 3.47 μW $m^{-3}$ increased with the addition of MWCNTs by 56.48% (5.43 μW $m^{-3}$ at 0.3 wt%), 88.15% (7.15 μW $m^{-3}$ at 0.6 wt%) and 31.41% (4.56 μW $m^{-3}$ at 0.9 wt%) and decreased by 14.40% (2.97 μW $m^{-3}$ at 1.2 wt%). This effect can be attributed to a reduction in the volume of the KNN–MWCNT-based cantilever for loading of MWCNTs within the percolation range. Furthermore, KNN ceramics observed with an input power (work done) of 2.44 J increased with the addition of MWCNTs by 29.50% (3.16 J at 0.3 wt%), 37.89% (3.52 J at 0.6 wt%) and 9.01% (2.66 J at 0.9 wt%) and decreased by 50.81% (1.20 J at 1.2 wt%) due to the reduced stiffness of the harvester. Finally, the efficiency of the KNN harvesters was found to be 58.15%, increased with the addition of MWCNTs by 10% (0.3 wt%), 25.16% (0.6 wt%) and 7.93% (0.9 wt%) and decreased by 23.7% (1.2 wt%) as shown in figure 10. This effect can be attributed to the structure, material, excitation and an electrical load resistance of KNN–MWCNT composites.

3.4f *Effect of MWCNTs on theoretical and measured output power*: A comparison between the theoretical and experimental power of KNN and its composites is depicted in figure 11. The measured and theoretical power of all the samples increased gradually, reached maximum at the threshold and reduced sharply. It can be attributed to the occurrence of percolation threshold for 0.6 wt% addition of MWCNTs into the matrix. The computed theoretical power was 1.43 μW for KNN ceramics and it increased with the addition of MWCNTs by 45% (2.20 μW at 0.3 wt%), 85% (3.08 μW at 0.6 wt%) and 32% (1.89 μW at 0.9 wt%) and decreased by 98% (0.45 μW at 1.2 wt%) with the addition of reinforcement above threshold. The trend of the measured output power was mapped with that of the theoretical output power for KNN and its composites. The deviation being least (1.04%) for KNN ceramics increased gradually with the addition of MWCNTs

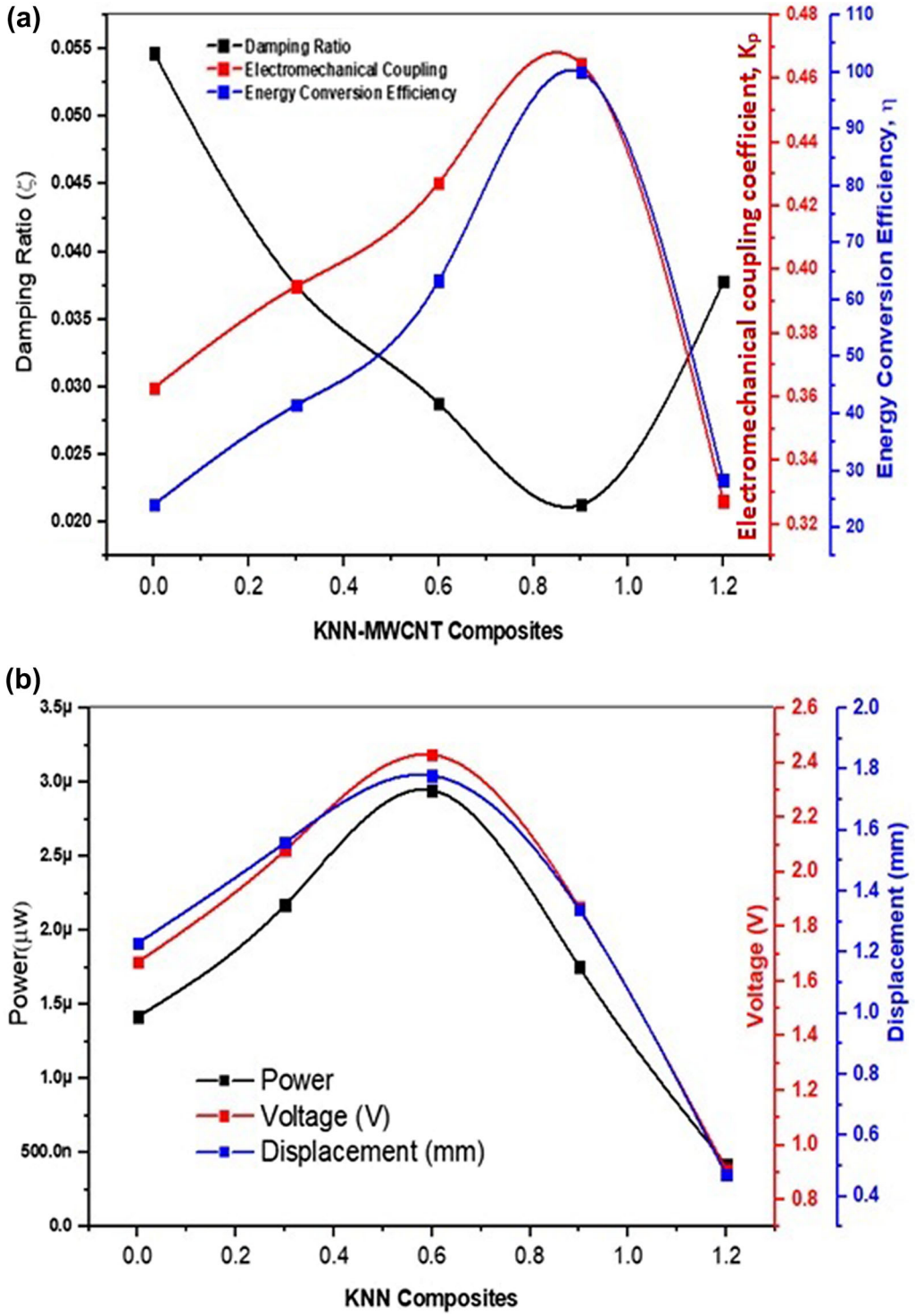


**Figure 9.** Effect of MWCNTs on (**a**) a damping ratio, electromechanical coupling coefficient, energy conversion and (**b**) voltage, displacement and power of KNN composites.

and was maximum (7.34%) for loading reinforcement beyond percolation threshold. The deviations observed may be due to various errors, which come across right from synthesizing, developing and characterizing KNN composite harvesters due to their functional specifications.

## 4. Discussion

The performance of KNN–MWCNT composite energy harvesters varies with the percolation of electrostatic charges, damping effect, electromechanical coupling coefficients and

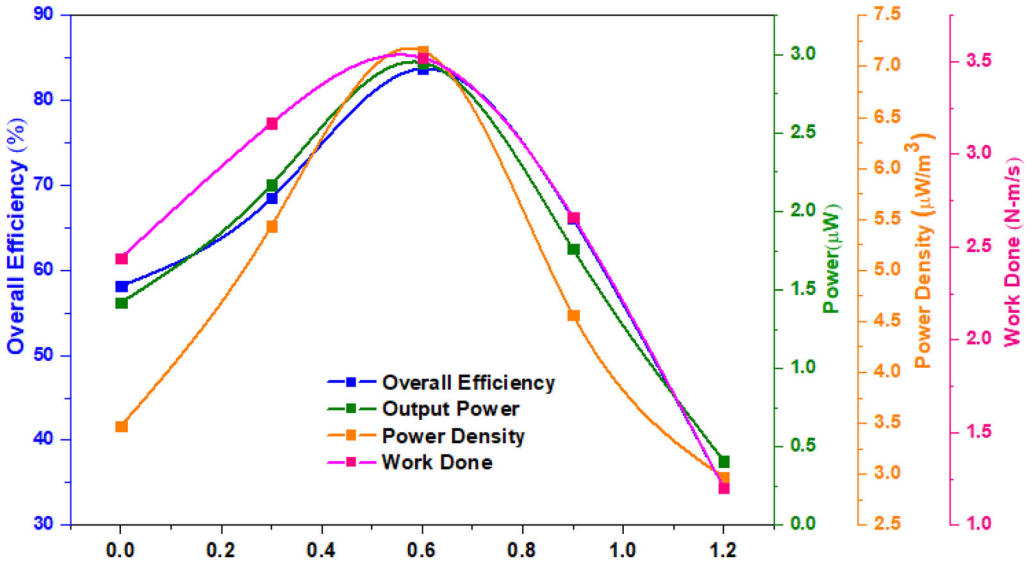


**Figure 10.** Effect of MWCNT on power, work done and efficiency of KNN composites.

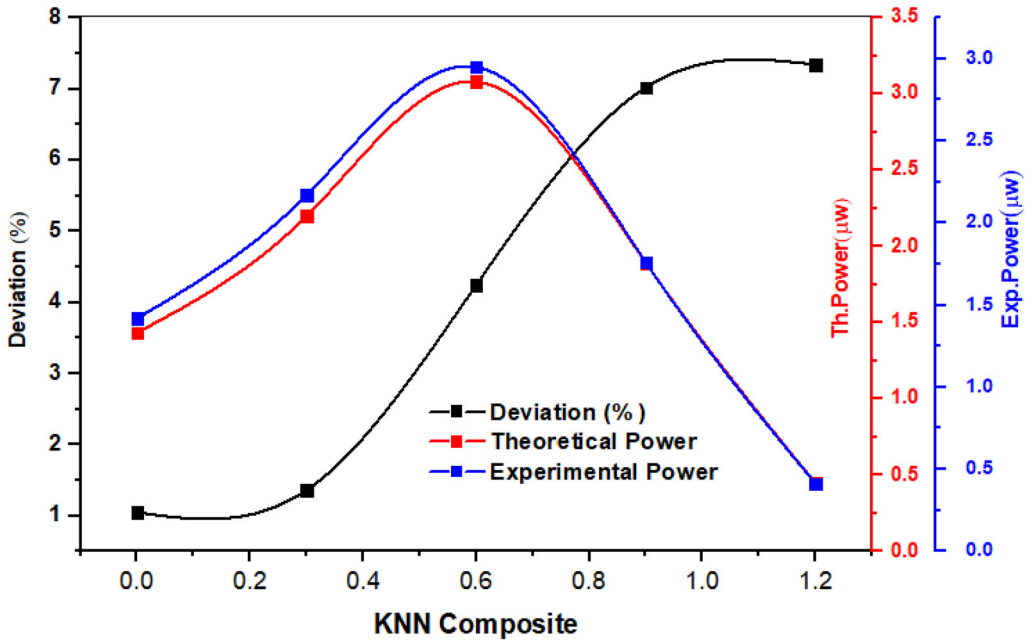


**Figure 11.** Effect of MWCNTs on theoretical/measured output parameters of KNN and its composites.

excitation frequency. The functional properties of KNN piezoelectric materials are satisfactory due to the existence of an energy band gap of 4.28 eV [41]. Although the valence (+10) electrons in KNN ceramics result in enhancing the electrical conductivity by the flow of electrons, the charges are accumulated only at the surface (figure 12a). It percolates through the ceramics by drift and diffusion currents during polarization. This results in low-energy conversion and functional properties ($d_{33}$, $K_P$, $\varepsilon_r$) [42]. From the sintered KNN ceramics, 2–3% porosity was observed from author's previous work [35]. The charges surrounding the pores were not percolated to the surface of the ceramics due to the lack of conductivity from the porous surface to outer surface during polarization. In the solid-state process, the solidification generally starts at the impurity or external particles or boundaries. The CNTs initiate the solidification at all stages, hence the CNTs sit in grain boundaries. It is because the solution of KNN and a known amount of MWCNTs were ultrasonicated, magnetically stirred separately and together for achieving uniform dispersion of MWCNTs into the KNN matrix. This

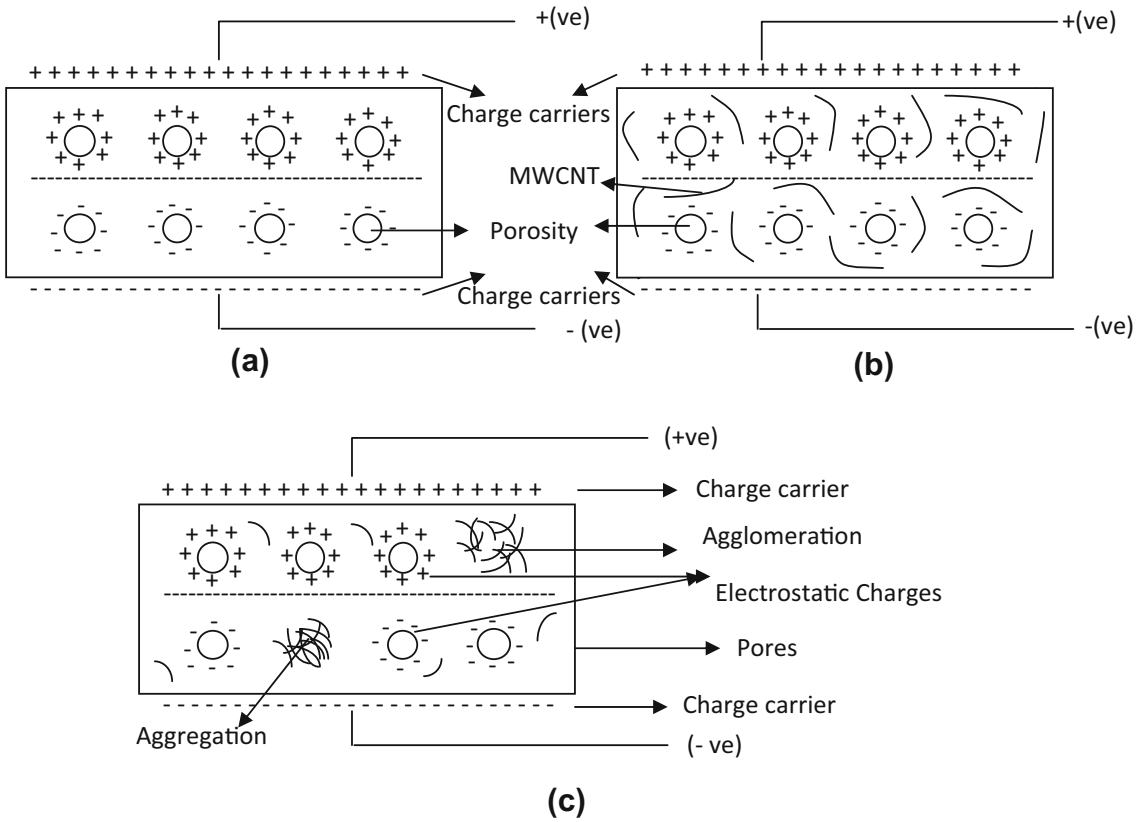


**Figure 12.** Schematic structure of poled (**a**) KNN ceramics, (**b**) KNN–MWCNT (0.3–0.9 wt%) composites within threshold and (**c**) KNN composite (1.2 wt%) above threshold.

was observed in the microstructure of densified KNN composites from our previous research work [35].

The addition of MWCNTs, which are isolated [43] near the grain boundary will interconnect effectively and form a conductive channel to transport the electrons to the surface, functioning like a ladder to cross the pores, cracks within the composite during polarization (figure 12b). It leads to an increased mobility of the charge carriers within the matrix, reduces the energy band gap due to structural modification [41], enhances the electrical properties and the voltage potential of KNN–MWCNT-based harvesters. The uniform dispersion of MWCNTs within the insulative KNN matrix results in fully dissipated electrical energy, strong piezo-damping effect [34,44] and high-electrical energy conversion coefficient. The reduced resistivity within the matrix due to the addition of MWCNTs results in an increased frequency of oscillation, empowers the electric output and average power generated [45] by the KNN–MWCNT-based PEHUC.

The addition of MWCNTs into the matrix above percolation threshold (1.2 wt%) resulted in agglomerations and aggregation of nanofillers [44], leading to the accumulation of charges in the form of clusters as shown in figure 12c. This change within the composite can be attributed to the sharp increase in conductivity due to the enhancement in the amount of localized-MWCNT percolation clusters, leading to drastic reduction in transportation of the charges to the surface due to the loss of connectivity between the porous and outer surface. This can be associated with the position of MWCNTs at bulk grain, which will not interconnect effectively to form the required conductive channel. As a result, energy does not get efficiently dissipated in the harvester and results in lower efficiency.

KNN ceramics possess lower interfacial bonding strength between the molecules. It leads to higher slippages at the interface, yields higher damping ratio and a lower mechanical quality factor. The lower mechanical $Q$ factor harvester experiences a smaller base motion amplitude and leads to lower energy conversion [44,45]. The addition of MWCNTs (0.3–0.9 wt%) into the composite enhanced the interfacial bonding strength between the matrix and reinforcement, leading to increased stiffness, reduced mobility of the interfacial atoms and lower slippages between the molecules. This results in a lower damping ratio [46] and a higher $Q$ factor, which can be attributed to high-energy conversion [47]. However, the KNN–MWCNT (1.2 wt%) composite shows lower stiffness and bonding strength of interfacial atoms due to uneven distribution (rare and dense) of nanofillers with lump mass aggregation. This resulted in an increased mobility of interfacial atoms, more slippages and higher damping ratio, leading to lower $Q$ factor and energy conversion.

The low-energy conversion rate of the KNN piezoelectric material leads to a weak electromechanical coupling

coefficient due to the accumulation and conversion of charges only at the 2-D surfaces. In contrast, KNN–MWCNT (0.3–0.9 wt%) composites show higher electrical energy conversion due to the accumulation and conversion of charges at 3-D spaces, as MWCNTs act like a ladder for carrying the charges from porous to the outer surface of the matrix. The high-conversion rate observed in KNN composites helps in improving the work done by the harvester due to the strong electromechanical system developed. However, in the case of KNN–MWCNT (1.2 wt%) composites, the presence of lump masses of the reinforcement fails to utilize 3-D spaces and results in low percolation and connectivity within the matrix. Hence, it results in a low-energy conversion rate and weak coupling coefficient.

The lower natural frequency ($\sqrt{k/m}$) and higher damping ratio ($c/c_c$) of the KNN harvester are due to its higher density [35] and lower stiffness observed in KNN ceramics. It leads to a conversion of higher mechanical energy to thermal energy instead of electrical energy. Hence, the KNN harvester vibrates at a slower speed and results in lower base motion amplitude, induced voltage potential, output power and energy conversion coefficient. In the case of KNN–MWCNT (0.3–0.9 wt%) composites, the addition of reinforcement resulted in reduced densities (4.34–4.30 g $cc^{-1}$) [35] and yielded in a high stiffness and low-damping ratio. So, KNN–MWCNT-based harvesters are getting excited at higher natural frequency and yields efficient conversion from mechanical energy to electrical energy with the minimum thermal loss. Hence, the KNN composite-based harvester results in higher base motion amplitude and enhances its output parameters. In addition, the KNN–MWCNT (1.2 wt%) composite exhibits a lower density (4.19 g $cc^{-1}$) [35] and lower stiffness due to the agglomeration of MWCNTs. Under highly induced porosity, the harvester above threshold gets excited at low frequency and results in dissipation of more thermal energy. Hence, it yields a low-voltage potential, output power and conversion rate.

## 5. Conclusion

The effect of MWCNTs on the energy performance of KNN–MWCNT composites was determined and the summary of the outcome of experimental results is given below:

1. The density of KNN composites decreases with increasing MWCNT reinforcement (up to 0.9 wt%), hence higher the specific stiffness and frequency with a lower damping ratio.
2. The thermal stability of KNN composites up to a temperature of 200°C for 0.6 wt% addition of MWCNTs is due to their good binding strength between the matrix and reinforcement.
3. The optimal result obtained for KNN–MWCNT (0.6 wt%) composite harvesters excelled with a least damping ratio (0.0288), high-electromechanical coupling factor (0.4273), energy conversion efficiency (63.90%), output power density (2.95 μW), power density (7.15 μW $m^{-3}$) and maximum overall efficiency (83.75%).
4. The experimentally obtained results are very close to the predicted theoretical output power of KNN–MWCNT composites.
5. The KNN–MWCNT (0.6 wt%)-based PEH is a potential candidate for energy harnessing and sensor applications.

## Acknowledgements

The authors would like to acknowledge the financial support of R.V.C.E., Bangalore under TEQIP-II, Subcomponent 1.2, Characterization facilities support at CENSE Department under INUP, Material Engineering Department at IISC, Bangalore and technical guidance from Dr Rammohan Sriramdas, CENSE Dept., IISC, Bangalore.

## References

[1] Shashank P 2007 *J. Electroceram.* **19** 167
[2] Kim H S, Kim J H and Kim J 2011 *Int. J. Precis. Eng. Manuf.* **12** 1129
[3] Beeby S P, Tudor M J and White N M 2006 *Meas. Sci. Technol.* **17** 175
[4] Park S E and Shrout T R 1997 *IEEE Trans. Ultrason. Ferroelectr. Freq. Control* **44** 1140
[5] Dubois M A and Muralt P 1999 *Appl. Phys. Lett.* **74** 3032
[6] Wang X, Zhou J, Song J, Liu J, Xu N and Wang Z L 2006 *Nano Lett.* **6** 2768
[7] Giurgiutiu V (ed) 2014 *Structural health monitoring with piezoelectric wafer active sensors* 2nd edn (Cambridge, USA: Elsevier Academic Press) p 1024
[8] Uchino K 1998 *Acta Mater.* **46** 3745
[9] Wang Q M, Zhang Q M, Xu B M, Liu R B and Cross L E 1999 *J. Appl. Phys.* **86** 3352
[10] Chu S Y, Chen T Y, Tsai I T and Water W 2004 *Sens. Actuators A Phys.* **113** 198
[11] Tang I T, Chen H J, Hwang W C, Wang Y C, Houng M P and Wang Y H 2004 *J. Cryst. Growth* **262** 461
[12] Koyama D and Nakamura K 2009 *Ultrason. Symp. (IUS): IEEE Int.* 1973
[13] Sodano H A, Inman D J and Park G 2004 *Shock Vib. Dig.* **36** 197
[14] Swee-Leong K, Mohamad N, Weng Y D F, Kien C S and Fu D C 2011 *Int. Conf. Electr. Control Comput. Eng. (INECCE)* **12** 420
[15] Ng T H and Liao W J 2005 *J. Intell. Mater. Syst. Struct.* **16** 785
[16] Egerton L and Bieling C A 1938 *Ceram. Bull.* **47** 1151
[17] Saito Y, Takao H, Tani T, Nonoyama T, Talkatori K, Homma T *et al* 2004 *Nature* **432** 84

[18] Panda P K 2009 *J. Mater. Sci.* **44** 5049
[19] Lam K H, Lin D M, Ni Y Q and Chan H L W 2009 *Struct. Health Monit.* **8** 283
[20] Guo M, Lam K H, Lin D M, Wang S, Kwok K W, Chan H L W *et al* 2007 *J. Mater. Sci.* **43** 709
[21] Kawada S, Kimura M, Higuchi Y and Takagi H 2009 *Appl. Phys. Express* **2** 111401
[22] Li E, Sasaki R, Hoshina T, Takeda H and Tsurumi T 2009 *Jpn. J. Appl. Phys.* **48** 09KD11
[23] Zuo R and Ye C 2007 *Appl. Phys. Lett.* **91** 062916
[24] Saito Y and Takao H 2006 *Ferroelectrics* **338** 17
[25] Ming B Q 2007 *J. Appl. Phys.* **101** 054103
[26] Zuo R and Fu J 2011 *J. Am. Ceram. Soc.* **94** 1467
[27] Xu W C, Lam K H, Choy S H and Chan H L W 2007 *Integr. Ferroelectr.* **89** 87
[28] Tanaka D, Tsukada T, Furukawa M, Wada S and Kuroiwa Y 2009 *Jpn. J. Appl. Phys.* **48** 09KD08
[29] Zhang Q 2010 *J. Alloys Compd.* **490** 260
[30] Wu J, Xiao D, Wang Y, Wu W, Zhang B and Zhu J 2008 *J. Phys. D.: Appl. Phys.* **41** 125405
[31] Prince V, Ram Pratap P, Manmeeta and Dhiraj S 2016 *AIP Conf. Proc.* **1728** 020341
[32] Cristina E C, Padurarju L, Lavinia P C, Lupu N, Lisiecki I, Deluca M *et al* 2014 *J. Appl. Phys.* **116** 164110
[33] Ray M C and Bart R C 2007 *Smart Mater. Struct.* **16** 1936
[34] Tian S, Cui F and Wang X 2008 *Mater. Lett.* **62** 3859
[35] Nadar R N, Munishamaiah K, Suresh A V and Murthy H N 2018 *Mater. Sci. Eng. B* **231** 40
[36] Huang H, Zheng C, Ruan X, Zeng J, Zheng L, Chen W *et al* 2014 *Ferroelectrics* **459** 1
[37] Sriramdas R, Ramya C M, Kumar J S, Jain A and Rudra P 2014 *J. ISSS* **3** 18
[38] Shu Y C and Lien I C 2006 *J. Micromech. Microeng.* **16** 2429
[39] Renaud M, Karakaya K, Sterken T, Fiorini P, Hoof C V and Puers R 2008 *Sens. Actuators A* **380** 145
[40] Kanno I, Ichida T, Kotera H, Shibata K, Horikiri F and Mishima T 2011 *Proc. Power MEMS* 110
[41] Jyothi R, Kumar P P, Nidhi A N, Singh H, Yadav K L and Prakash S 2014 *J. Mater. Sci. Technol.* **30** 459
[42] Hong C H, Kim H P, Choi B Y, Han H S, Son J S, Ahn C W *et al* 2016 *J. Materiomics* **2** 1
[43] Qing H and Gao L 2004 *J. Mater. Chem.* **16** 2475
[44] Banerjee S, Cook Chennault K A, Du W, Sundar U, Halim H and Tang A 2016 *Smart Mater. Struct.* **25** 115018
[45] Elvin N and Erturk A 2013 in *Advances in energy harvesting methods* N Elvin and A Erturk (eds) (New York, NY: Springer) p 3445
[46] Her S C and Lai C Y 2013 *Materials* **6** 2274
[47] Henry C, Fu K and Leang K 2012 *IEEE Control Syst. Mag.* **32** 95

International Journal of Mechanical and Production Engineering Research and Development (IJMPERD)
ISSN (P): 2249–6890; ISSN (E): 2249–8001
Vol. 9, Special Issue, Dec 2019, 114–124


# INFLUENCE OF PROCESS PARAMETERS ON FRICTION STIR WELDED AA 6082-Cu JOINTS

**CHETHAN. D[1] & K. M. SATHISH KUMAR[2]**

[1]*Assistant Professor, Department of Mechanical Engineering, M Visvesvaraya Institute of Technology, Bengaluru, Karnataka, India*

[2]*Professor & Head, Department of Mechanical Engineering, BMS Institute of Technology & Management, Bengaluru, Karnataka, India*

***ABSTRACT***

***The main purpose of this study is to evaluate the influence of process parameters on friction stir welded butt joints of 6082 aluminium alloy and pure copper plates of 4 mm thickness. With this purpose, welds were produced using HcHcr tool, with a cylindrical taperd pin having 5-mm major diameter and 3-mm minor diameter and 22-mm shoulder diameter, respectively. The main process parameters considered are tool rotational speed and travel speed. Copper plates were kept in advancing side of joint. Tensile and Bending tests (as per ASTM) were conducted to know the tensile and bending strength of weld joints. Vicker's microhardness test is done in transverse cross section of weld to know the hardness distribution in weld nugget. Experimental investigation reveals that at«tool rotational speed»of 1000 rpm and tool travel speed of 25 mm/min, the better Tensile Strength of 161 Mpa, Bending Strength of 26 Mpa and Hardness of 100 HV are obtained on the weld zone. Microstructure reveals that at the tool speed of 1000 rpm and travel speed of 25 mm/min more Cu particles were present in the Al side, higher tensile and bending strength is mainly due to the presence of Cu particles over the Al material in weld zone.***

***KEYWORDS: Friction Stir Welding, Aluminium Alloy, Pure Copper, Tensile Test, Hardness & Microstructure***

Original Article

## INTRODUCTION

Friction Stir Welding (FSW) is a type of solid state welding, the energy produced due to friction when two bodies slide on each other is transferred into heat, when the rate of movement is high and the heat is contained in narrow zone, welding occurs. It includes a non-consumable rotating tool with a probe, which is plunged inside the mating edges of the work pieces. The heat produced due to friction around the probe softens the material and tool rotation and translation combination leads to material movement from the front to the back of the pin. As a result, joint is produced [1].

Dissimilar welding is widely used in various industries such as electronics, electrical, nuclear, aerospace, etc., because of its practical and economical benefits [2]. The joining of Aluminium (Al) and Copper (Cu) is a difficult task because of wide changes in properties. These may lead to cracks, residual stresses and formation of intermetallic structures [3].

## LITERATURE REVIEW

The FSW of Al and Cu is generally restricted by fusion welding techniques. This is because of wide difference in properties [4]. However, both materials have a significant difference in melting points (nearly 500°C). Therefore,

it is very difficult to get the high quality welds with normal fusion welding techniques.

Kush P. Mehta *et al*. [5] studied the impact of tool profile and parameters on FSW of Copper to AA6061 welds. In this study, different FSW parameters such as travel speed, pin offset and plunge load. The results indicate that good quality joints were produced using a cylindrical tool pin profile.

Dhananjayulu Avula et al. [6] studied FSW of copper alloys to evaluate the microstructural and mechanical properties. This study mainly reveals the possibility of welding commercially available pure copper plates by FSW. Microstructure, microhardness and tensile strength and 94% of efficiency was found compared to the base material.

C. W. Tan et al. [7] conducted a work on Al–Cu joints to assess "microstructure and mechanical properties" produced by FSW. Study reveals that metallurgical relationship between Al and Cu principals to good tensile and bending strength.

Venkata Rao et al. [8] have studied the tool pin profile influence on corrosion and microstructural behavior of Al-2219 C u alloy by FSW. Study reveals that the large deformation produced in the weld zone and microstructure strongly affects the corrosion and hardness properties of the joints.

I. Galvao et al. [9] conducted experiments on morphological and structural properties of Al 5083/Cu joints. It was established that base materials positioning has strong influence on butt welds morphology and structure. The welds produced with keeping aluminium on advancing side of the tool were morphologically very irregular, due to the removal of the aluminium from the nugget zone. Increasing the "tool rotational "speed results in the formation of mixing regions with increased dimension, homogeneity and intermetallic content. Shoulder geometry has strong influence on the morphology and intermetallic content of the welds nugget.

## EXPERIMENTAL PROCEDURE

FSW of AA 6082 and pure Cu of dimensions 100 x 50 x 4 $mm^3$ are produced using the Vertical type Milling Machine. In this study, HcHcr tool with a cylindrical taper unthreaded pin having 5-mm major diameter and 3-mm minor diameter and shoulder diameter of 22 mm was used to produce FSW of Al-Cu by varying the tool rotational speed and feed rate, and other parameters are kept constant. A schematic of vertical milling machine and tool used are shown in figures 1 and 2. tables 1 to 4 gives the physical properties and chemical composition of Al 6082 and Pure Copper.


**Figure 1: Vertical Milling Machine.**

**Figure 2: Tool Used.**

**Table 1: Al 6082 Chemical Composition of Al 6082**

| Si | Cu | Mg | Cr | Fe | Mn | Zn | Al |
|---|---|---|---|---|---|---|---|
| 0.7–1.3 | 0–0.1 | 0.6–1.2 | 0.25 | 0–0.5 | 0.4–1 | 0–0.1 | Balance |

**Table 2: Physical Properties of Al 6082**

| | |
|---|---|
| Density | 2700kg/m$^3$ |
| Melting Point | 555°C |
| Modulus of Elasticity | 90 Gpa |
| Poisson's Ratio | 0.32 |

**Table 3: Chemical Composition of Copper**

| Element | Content (%) |
|---|---|
| Cu | 99.99 |

**Table 4: Physical Properties of Copper**

| | |
|---|---|
| Density | 8.96 gm/cm$^3$ |
| Melting Point | 1083°C |
| Modulus of Elasticity | 113 Gpa |
| Poisson's Ratio | 0.34 |

A butt weld preparation is used to produce the FSW joints. The welding edge of work piece is milled by end mill. The work piece dimensions are selected for convenience to suit the fixtures, which are attached to longitudinally traversing table of the FSW machine, and are representative of the heat sink inherently associated with larger or smaller work pieces. The FSW tool was loaded into the tool holder, brought up to set the rotation speed and then plunged into the butting joint. The work pieces were thoroughly cleaned before they were fixed on the fixture by different grade emery papers and acetone in order to remove the residues.

The welds are produced at a rotational speed of 1000 rpm and 1400 rpm, while the travel speed 16, 25 and 32 mm/min are used for both the speeds. The copper plates are kept on the advancing side and aluminium plates are kept on the retrieving side with zero mm offset. Figure 3 shows the welded joints.


**Figure 3: FSW Welded Joints.**

## RESULTS AND DISCUSSIONS

### Tensile Strength

The test specimens are prepared as per the ASTM standards shown in figure 4, then subjected to standard tensile testing and the results are tabulated in table 5. Figure 5 shows variation of tensile stress for conducted trials.

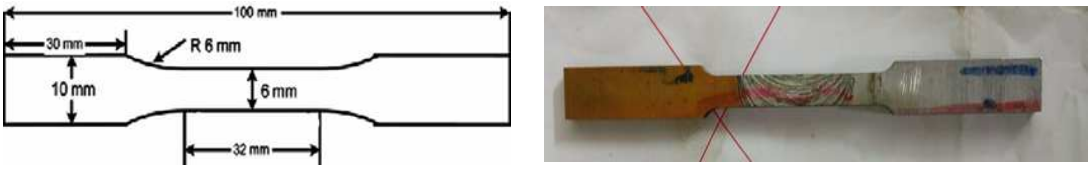


**Figure 4: Tensile Specimen as per ASTM Standard.**

**Table 5: Tensile Strength of Welded Joints**

| Trial No. | Tool Rotational Speed (rpm) | Tool Travel Speed(mm/min) | UTS(Mpa) | % of Elongation |
|---|---|---|---|---|
| 1 | 1000 | 16 | 98.5 | 1.7 |
| 2 | 1000 | 25 | 161.4 | 1.8 |
| 3 | 1000 | 32 | 121.5 | 1.5 |
| 4 | 1400 | 16 | 98.3 | 1.4 |
| 5 | 1400 | 25 | 90 | 1.5 |
| 6 | 1400 | 32 | 76.5 | 1.1 |

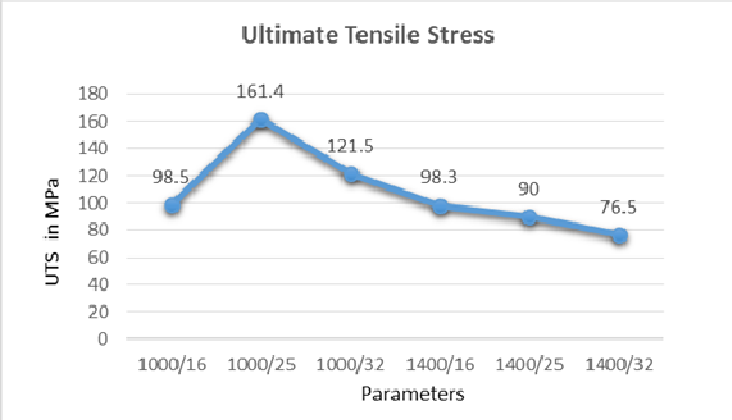


**Figure 5: Variation of Tensile Stress.**

**Bending Test**

Bend tests are used to understand the ductility and toughness properties of welds. The samples are cut as per the ASTM standard for 4-mm thickness plates using wire EDM, as shown in figure 6, and results are tabulated in table 6. Figure 7 shows the variation of bending stress.

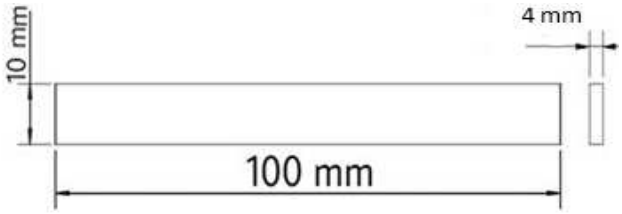


**Figure 6: Bending Specimen.**

**Table 6: Bending stress for Welded Joints**

| Trial No. | Tool Rotational Speed (rpm) | Tool Travel Speed(mm/min) | Bending Sress (Mpa) |
|---|---|---|---|
| 1 | 1000 | 16 | 1.7 |
| 2 | 1000 | 25 | 1.8 |
| 3 | 1000 | 32 | 1.5 |
| 4 | 1400 | 16 | 1.4 |
| 5 | 1400 | 25 | 1.5 |
| 6 | 1400 | 32 | 1.1 |

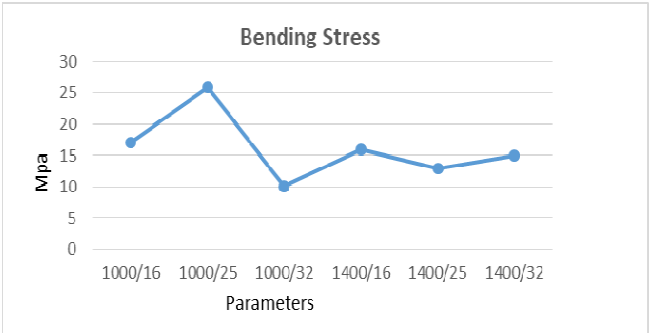


**Figure 7: Variation of Bending Stress.**

### Microhardness Test

In order to access the strength of FSW joints for selected parameters, the hardness test may be considered. The Vickers hardness test is conducted on various zones of the specimen. The results are presented in Table 7. Figure 8 shows variation of hardness on various zones.

**Table 7: Vickers Hardness Number on various zones for Welded Joints**

| Trial No. | Tool Rotational Speed (rpm) | Tool Travel Speed(mm/min) | Hardness(HV) (At nugget Zone) | TMAZ Al side | HAZ Al side | TMAZ Cu side | HAZ Cu side |
|---|---|---|---|---|---|---|---|
| 1 | 1000 | 16 | 95 | 87 | 107 | 80 | 81 |
| 2 | 1000 | 25 | 100 | 68 | 69 | 78 | 87 |
| 3 | 1000 | 32 | 92 | 90 | 115 | 83 | 85 |
| 4 | 1400 | 16 | 96 | 60 | 71 | 70 | 86 |
| 5 | 1400 | 25 | 98 | 68 | 73 | 90 | 96 |
| 6 | 1400 | 32 | 90 | 80 | 72 | 84 | 86 |

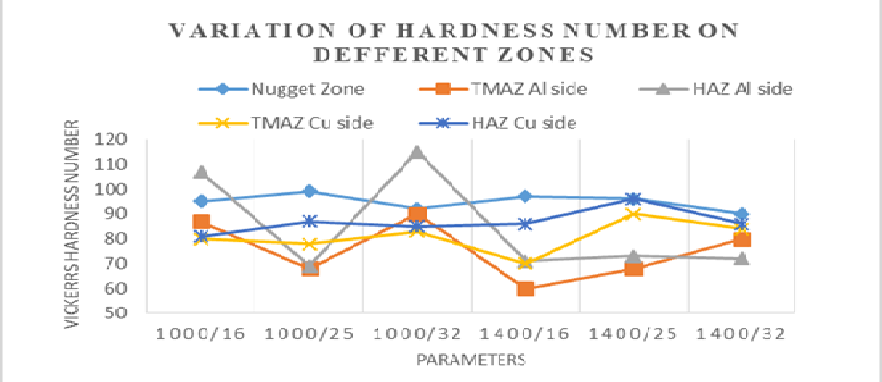


**Figure 8: Hardness on Various Zones.**

### Microstructure

To understand the amount of welded materials present at weld centerline, results of this test are considered. Microstructure Evaluation is studied using Scanning Electron Microscope (SEM) to know the quality of mixing of materials during FSW, since it is directly affecting the strength of welded joints. Figure 9 shows the prepared specimens for microstructure evaluation.

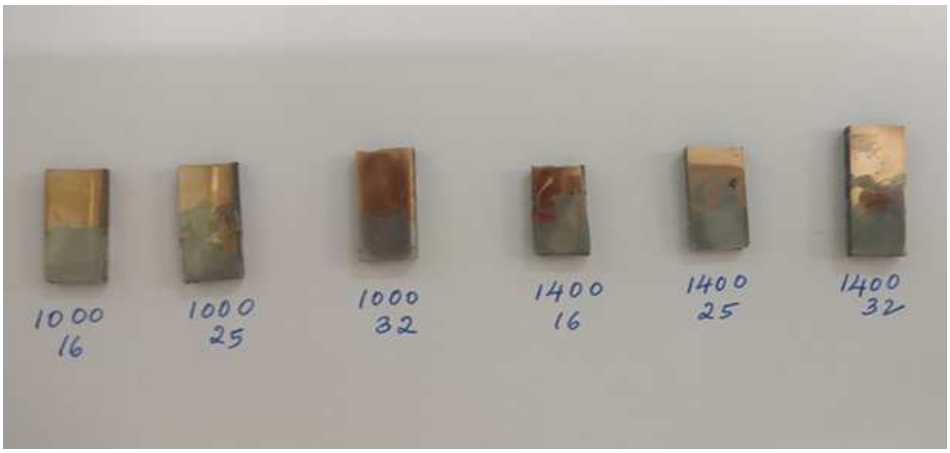


**Figure 9: Specimens for Microstructure Evaluation.**

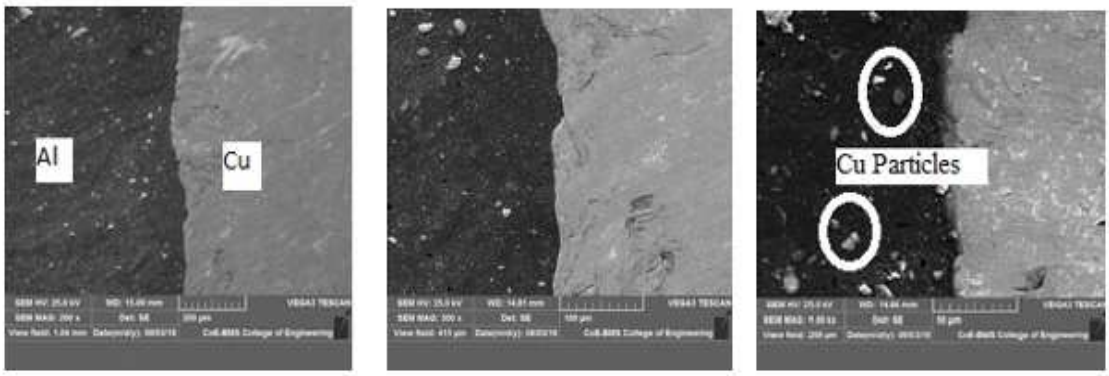


(a) 200x (b) 500x (c) 1000x

**Figure 10: SEM Images of Trail 1.**

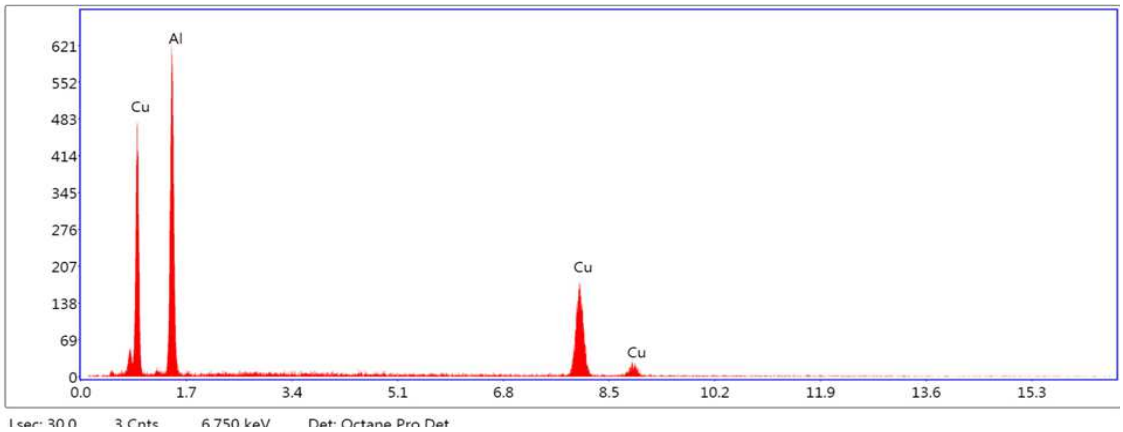


**Figure 11: EDS Analysis of Trail 1.**

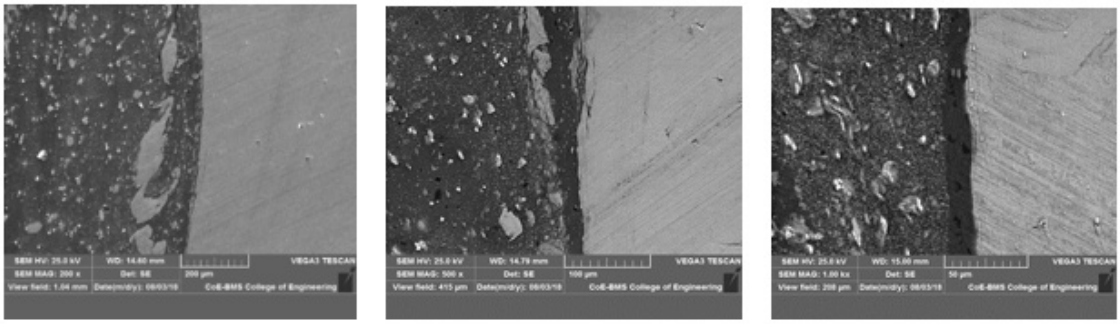

(a) 200x (b) 500x (c) 1000x

**Figure 12: SEM Images of Trail 2.**

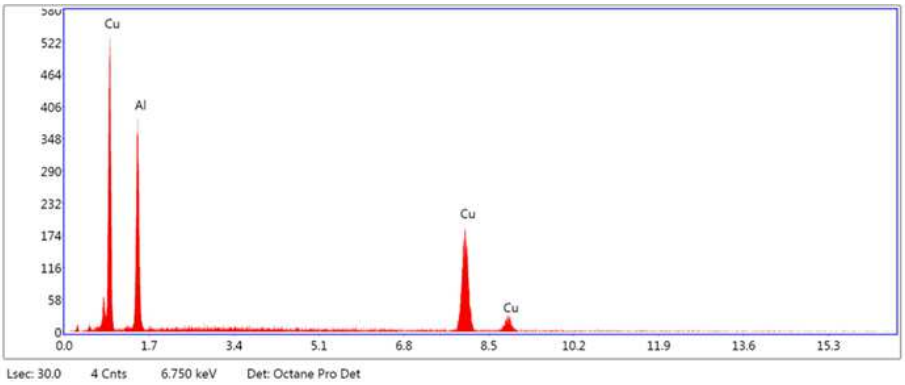


**Figure 13: EDS Analysis for Trail 2.**

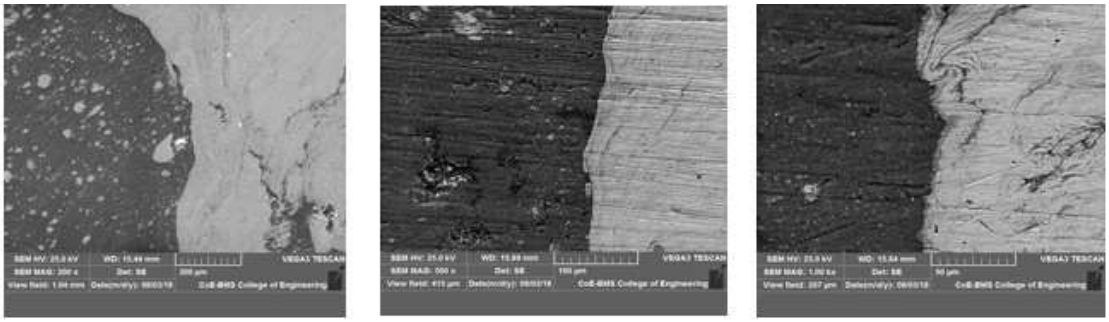

**(a) 200x** **(b) 500x** **(c) 1000x**

**Figure 14: SEM Images of Trail 3.**

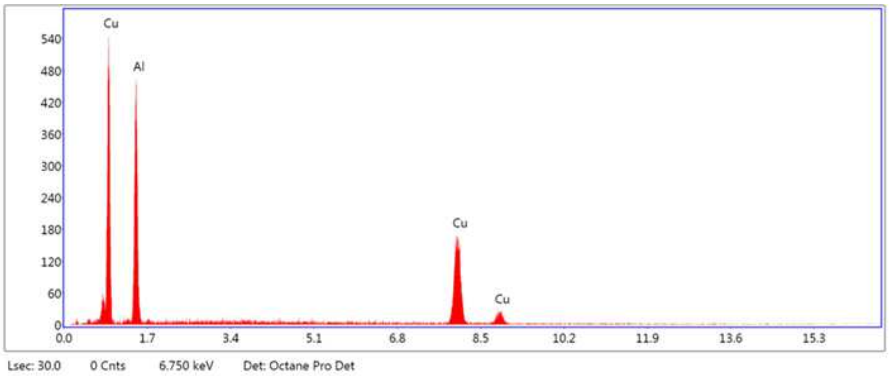


**Figure 15: EDS Analysis of Trail 3.**

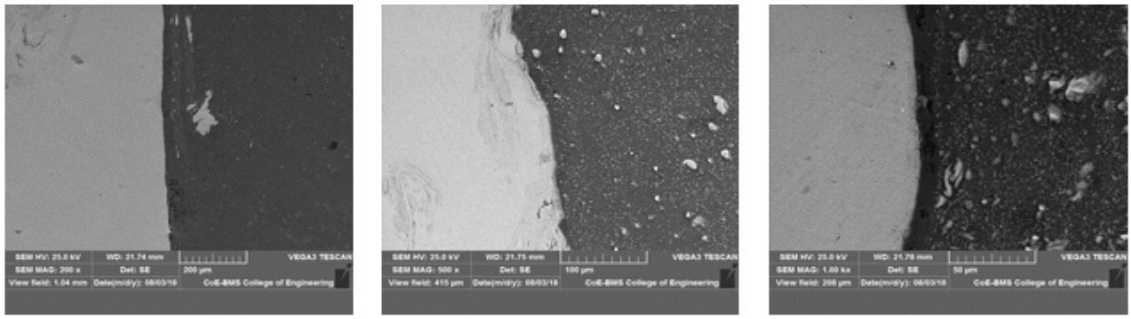

**(a) 200x** **(b) 500x** **(c) 1000x**

**Figure 16: SEM images of Trail 4.**

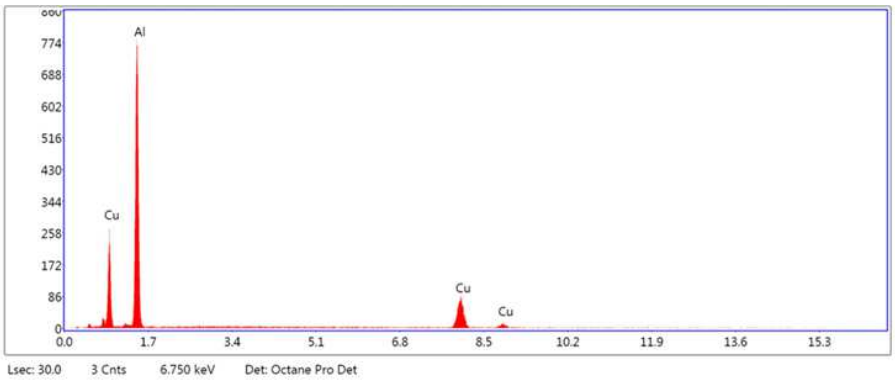


**Figure 17: EDS Analysis of Trail 4.**

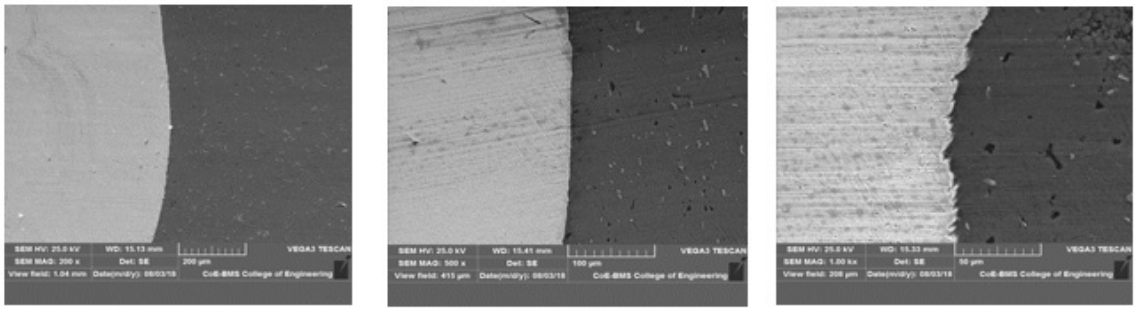

**(a) 200x** **(b) 500x** **(c) 1000x**

**Figure 18: SEM images of Trail 5.**

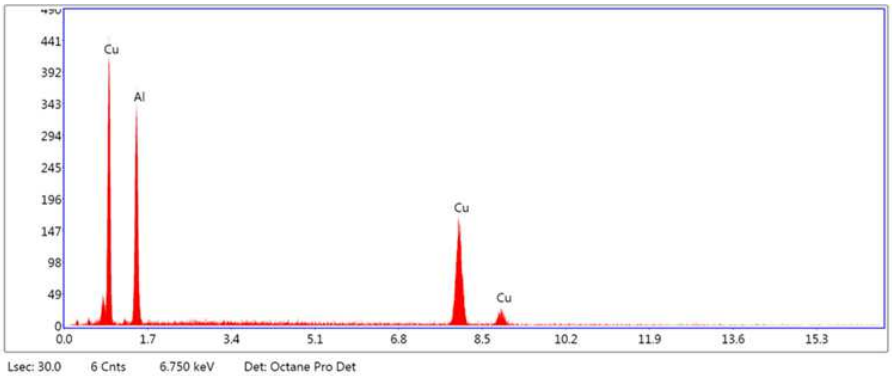


**Figure 19: EDS Analysis of Trail 5.**

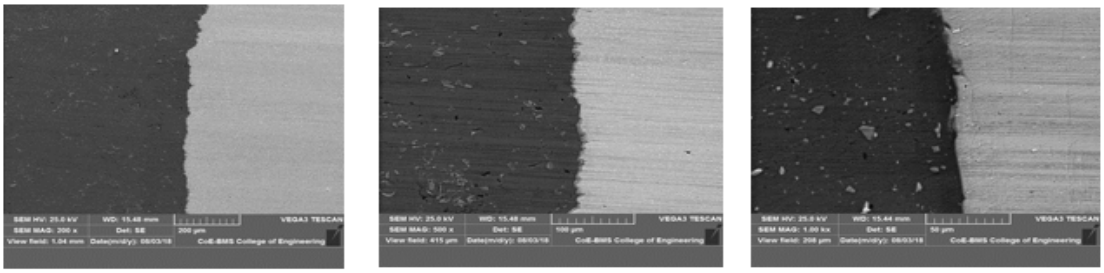

(a) 200x (b) 500x (c) 1000x

**Figure 20: SEM images of Trail 6.**

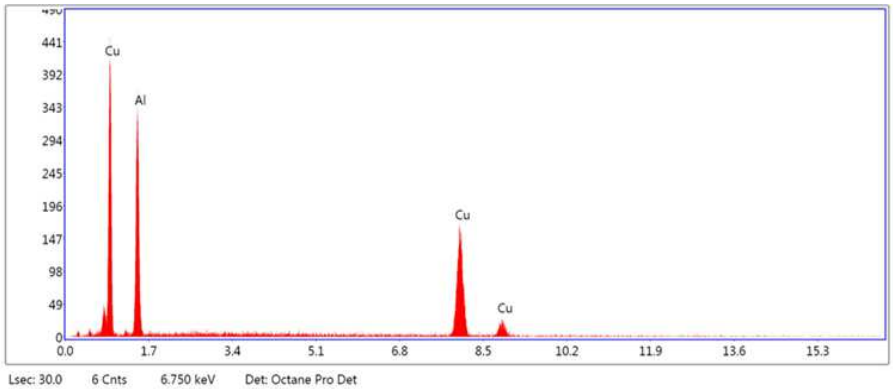


**Figure 21: EDS Analysis of Trail 6.**

## CONCLUSIONS

The influence of FSW parameters for Al-Cu joints is analyzed by conducting six trials. The main conclusions of the study are:

- Joints are successfully produced for the selected parameters.
- Selected tool material and pin can be employed for selected materials.
- From the experimental investigation, it is observed that the ultimate tensile and bending strength is maximum for parameter 1,000 rpm and 25 mm/min.
- Highest hardness of 100 HV reported for parameter 1000 rpm and 25 mm/min because intermetallic compounds' (IMCs) presence in the nugget zone increases the hardness.
- Microstructure and EDS Analysis reveals that at the rotational speed of 1000 rpm and travel speed of 25 mm/min, higher number of Cu elements are present in the Al section at the weld zone, that results in higher tensile, bending strength and hardness value.

***REFERENCES***

1. *Mukuna Patrick, Mubiayi & Akinlabi Esther "Friction Stir Welding of Dissimilar Materials between Aluminium Alloys and Copper- An Overview", Proceedings of the World Congress on Engineering, Vol.3, WCE 2013, July 3 - 5, London, U.K,2013.*
2. *M. Felix Xavier Muthu & V. Jayabalan, "Tool travel speed effects on the microstructure of friction stir welded aluminum–copper joints", Journal of Materials Processing Technology, Vol.217, pp.105–113, 2015.*
3. *Ahmed O. Al-Roubaiy, Saja M. Nabat &Andre D. L. Batako, "Experimental and theoretical analysis of friction stir welding of Al–Cu joints", International Journal of Advance Manufacturing Technology, Vol 71, pp.1631–1642, 2014.*

4. *Esther T. Akinlabi, and Stephen A Akinlabi, "Friction Stir Welding of Aluminium and Copper Fracture Surface Characterizations", Proceedings of the World Congress on Engineering, Vol.2, London, U.K, 2014.*
5. *Kush P. Mehta & Vishvesh J. Badheka, "Influence of tool design and process parameters on dissimilar friction stir welding of copper to AA6061-T651 joints", International Journal of Advance Manufacturing Technology, Vol.80, pp.2073–2082, 2015.*
6. *Dhananjayulu Avula, Ratnesh Kumar Raj Singh, D.K. Dwivedi, N.K. Mehta, "Effect of Friction Stir Welding on Microstructural and Mechanical Properties of Copper Alloy", World Academy of Science, Engineering and Technology, Vol. 5, pp.336–344, 2011.*
7. *C.W. Tan, Z.G. Jiang, L.Q. Li a, Y.B. Chen & X.Y. Chen, "Microstructural evolution and mechanical properties of dissimilar Al–Cu joints produced by friction stir welding, Materials and Design", Vol.51, pp.466–473, 2013.*
8. *Ch. Venkata rao, G. Madhusudhan reddy & K. Srinivasa rao, "Influence of tool pin profile on microstructure and corrosion behavior of AA2219 AleCu alloy friction stir weld nuggets", Defence Technology, Vol.11, pp.197–208, 2015.*
9. *Galvao, I., D. Verdera, D. Gesto, A. Loureiro, and D. M. Rodrigues, "Analysing the challenge of aluminum to copper FSW." Proceedings of 9th International Symposium on Friction Stir Welding, Huntsville, Alabama, US. 2012.*
10. *Kumar, P., Hussain, M., & Das, A. K. Effect of Process Parameters on the Surface Integrity of Micro-holes of ti6al4v Obtained by Micro-EDM.*
11. *Fayomi, O. S., Abdulwahab, M., Durodola, B. M., Joshua, T. O., Alao, A. O., Joseph, O. O., & Inegbenebor, A. O. (2013). Study of the electrochemical behavior and surface interaction Of AA6063 Type Al-Mg-Si alloy by sodium molybdate in simulated sea water environment. International Journal of Management, Information Technology and Engineering, 1(3), 159–166.*
12. *Elzanaty, H. (2014). Effect of different Si content on the mechanical properties in Al-based alloy. International Journal of Research in Engineering & Technology (IMPACT: IJRET), 2(7), 49–54.*
13. *Erfan, O. S. A. M. A., El-Nasr, A., BA, A., & Al-mufadi, F. (2014). Erosion-corrosion behavior of AA 6066 aluminum alloy. IJME, 3, 15–24.*

*Applied Mechanics and Materials*
*ISSN: 1662-7482, Vol. 895, pp 319-323*
*doi:10.4028/www.scientific.net/AMM.895.319*

*Submitted: 2019-01-13*
*Accepted: 2019-02-22*
*Online: 2019-11-01*

# Development of MATLAB Codes to Find the Natural Frequencies of a Composite Structure

Yashavantha Kumar G.A.[1,a*], K.M. Sathish Kumar[2,b]

[1-2]Department of Mechanical Engineering, BMS Institute of Technology & Management, India

[a]ygamech@bmsit.in, [b]sathishmech@bmsit.in

**Keywords:** Composite structure, MATLAB, natural frequency, Mode shape

**Abstract.** Modal analysis is a method to describe the dynamic properties of structure such as natural frequency, mode shape and damping ratio. These properties are important for design and analysis of structure in dynamic condition. MATLAB is a high-performance numerical computation and visualization software package. It provides an interactive environment with hundreds of built-in functions for technical computation, graphics, and animation. In present analysis, use of MATLAB is done for finding the free vibrational characteristics of a structure made of composite material. The study involves finding the natural frequencies of structure made of Glass-epoxy, Carbon-epoxy and Graphite fiber reinforced polyamide materials. In this case Euler's-Bernoulli beam theory is used for analytical solution and to construct MATLAB codes. The structure considered here is a beam with fixed-free condition. The results obtained from the MATLAB are accurate comparatively, the results obtained shows that the MATLAB can be further used to write programs which involve complicated iterations and cannot be done manually. The further work can be extended for writing the programs of much more complex equations in MATLAB and obtains exact solution.

## Introduction

Usage of composite materials is more because of its high strength, high stiffness and low density. The behavior of the structures is designed according to their usage and applications [1]. Hence the analysis of composite is very important from design point of view. Beams are the basic elements of structures and widely used in many applications. These structures undergoes a wide variety of static and dynamic loads, which leads to its failure [2]. Hence it has become a standard procedure to test for vibration in design of structures. The present work considers Euler-Bernoulli beam theory for construction of mathematical model. The Euler-Bernoulli beam theory is the most commonly used because it is simple and provides realistic engineering approximations for many problems [2]. MATLAB is commercial software which is used for science, engineering numerical computation and other fields [5]. MATLAB is a power full tool for technical problems like mechanical, electrical and biomedical problems. This software also used for modelling, simulation, visualization data and to develop the algorithms [4]. In industries, the MATLAB software is used for research, development and design [6]. Modal analysis is a process of describing a structure in terms of its free vibrational characteristics namely the frequency, mode shapes and damping. Based on changes in frequencies and mode shapes of vibration the modal characteristics provides an indication of structural condition directly.

## Methodology

The equation of motion can written without considering the damping is as follows.

$$m\ddot{x}+k(x) = 0 \quad (1)$$

Where 'm' is mass of system and 'k' is stiffness of system with respect to acceleration and displacement. Using Rayleigh's principle maximum kinetic energy at mean position is equal to maximum potential energy at extreme position. Consider motion of vibration is harmonic or simple harmonic motion. The expression for motion is given as.

$$x = A\sin\omega_n t \tag{2}$$

Differentiate the equation [2] with respect to t then above equation becomes

$$\ddot{x} = A\omega_n \cos\omega_n t \tag{3}$$

From Rayleigh's principle
Max velocity $\dot{x}_{max} = A\omega_n$ and Max amplitude $x = A$

Then KE becomes at mean position $= \frac{1}{2} m(A\omega_n)^2$ (4)

PE at extreme position $= \frac{1}{2} kA^2$ (5)

After solving above equation get

$$\omega_n = \sqrt{\frac{k}{m}} \tag{6}$$

The equation [6] is natural frequency of a SDF.
Euler beam theory is the most commonly used because it is simple and provides reasonable engineering problems.

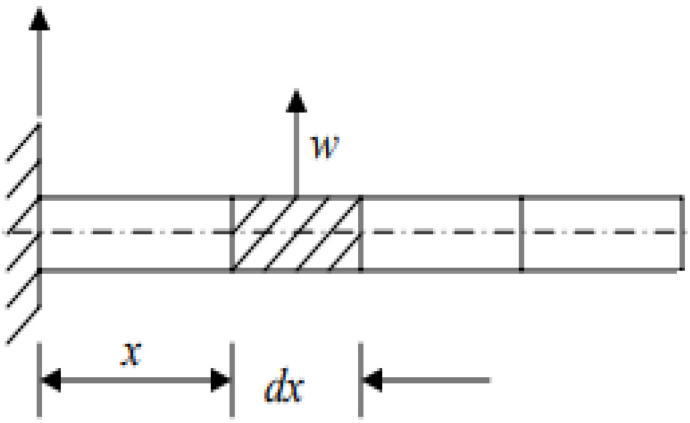


**Fig. 1: Cantilever beam under transverse vibration**

Consider a long thin beam as shown in Fig 1, it under go transverse vibration. And dx is a small elemental area of beam. At free end of beam x=L

Bending moment = EI $\frac{\partial^2 w}{\partial x^2} = 0$ (7)

Shear force = $\frac{\partial}{\partial t^2}[EI\frac{\partial^2 w}{\partial x^2}] = 0$ (8)

Equation of motion beam is given below in vibration

$$\frac{\partial^2 w(x,t)}{\partial t^2} + c^2 \frac{\partial^4 w(x,t)}{\partial x^4} = 0 \, , c = \sqrt{\frac{EI}{\rho A}} \tag{9}$$

Solve equation [9] by using variable separable method in partial differentiations. After variable separation method partial derivatives are replaced by total derivatives gives.

$$c^2 \frac{X^4(x)}{X(x)} = -\frac{T^2(t)}{T(t)} = \omega^2 \tag{10}$$

After solving the equation [10], the general solution expressed as

$$X(x) = a_1 \sin\beta x + a_2 \cos\beta x + a_3 \sinh\beta x + a_4 \cosh\beta x \quad (11)$$

Where

$$\beta^4 = \frac{\omega^2}{c^2} = \frac{\rho A \omega^2}{EI} \quad (12)$$

From equation [12]

$$\omega = \beta^2 \sqrt{\frac{EI}{\rho A}} = (\beta l)^2 \sqrt{\frac{EI}{\rho A l^4}} \quad (13)$$

The value of βl for the fixed free boundary condition is

$(\beta l)_{1,2,3}$ = 1.875104, 4.694091, 7.854757

$$\text{Mode shape} = W_n(x) = C_n[(\sin\beta_n x - \sin h\beta x_n) - \alpha_n(\cos\beta_n x - \cosh\beta_n x)] \quad (14)$$

$$\alpha_n = \frac{\sinh\beta_n l + \sin\beta_n l}{\cos\beta_n l + \cosh\beta l} \quad (15)$$

Using the equations a general MATLAB codes are developed.

**Results and Discussions**

The Fig 2 shows the geometry of the composite beam considered for the analysis. Here the beam is made of three different composite materials with same geometry. The properties of the materials are listed in Table 1.

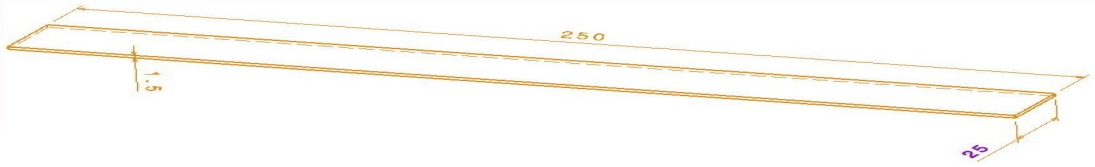


**Fig. 2: Physical model of beam**

Length (L) = 250mm
Width (b) = 25mm
Thickness (t) = 1.5mm

**Table 1: Material properties of composites**

| **Glass-Epoxy Composite** | **Carbon-Epoxy Composite** | **Graphite fiber Reinforced polyimide** |
|---|---|---|
| $E_x$ =40.59 Gpa | $E_x$ =144.8 Gpa | $E_x$ =129.207 Gpa |
| $\mu_{xy}$ = 0.22 | $\mu_{xy}$ = 0.3 | $\mu_{xy}$ = 0.3 |
| ρ =1830 Kg/m$^3$ | ρ =1389.2 Kg/m$^3$ | ρ =1550.0666 Kg/m$^3$ |
| $G_{xy}$ =3.1 Gpa | $G_{xy}$ =4.14 Gpa | $G_{xy}$ =5.15658 Gpa |

The MATLAB codes are written in a script file and made to run for it to get the natural frequencies and their corresponding mode shapes. Fig 2 to Fig 5 shows the first two mode shapes of the beam with all three different materials.

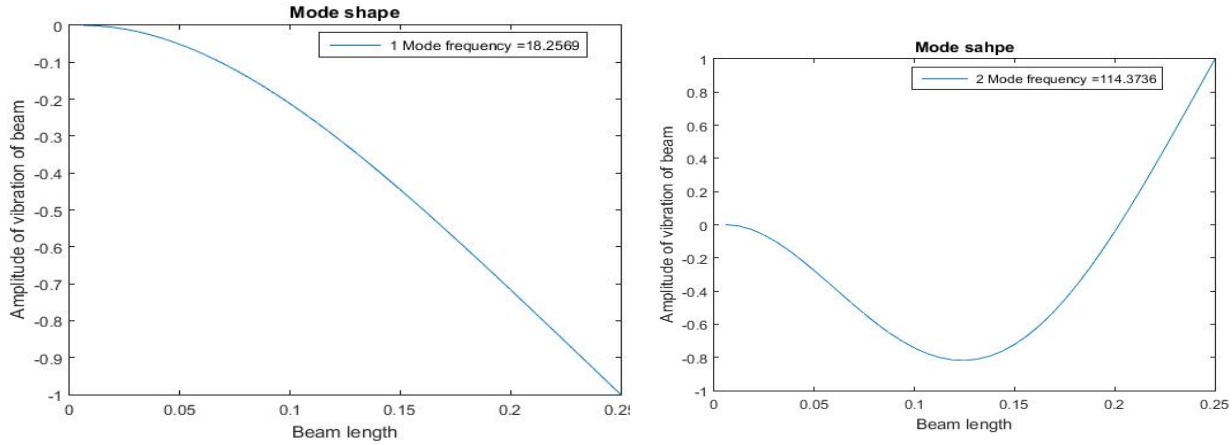


**Fig. 3: First two mode shapes of a Glass-Epoxy beam**

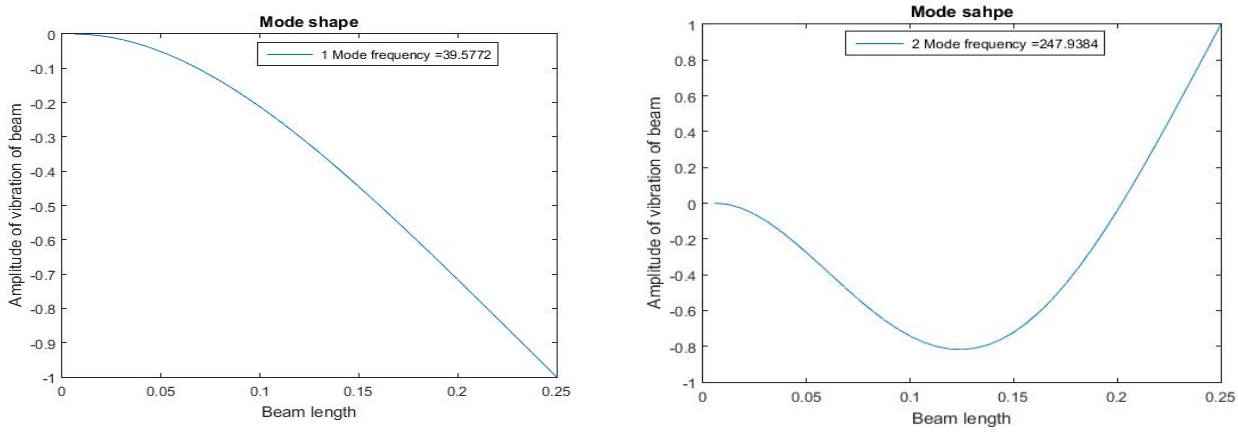


**Fig. 4: First two mode shapes of a Carbon - Epoxy beam**

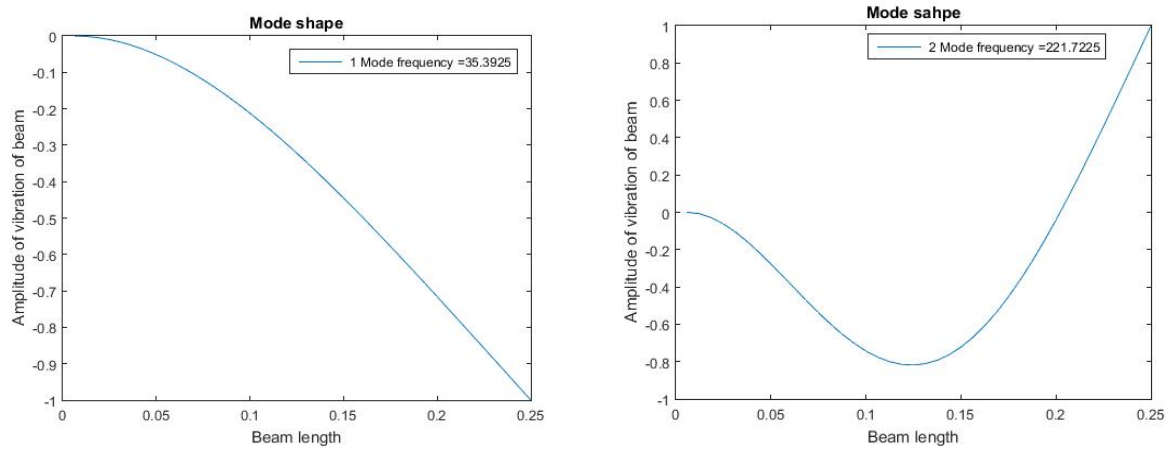


**Fig. 5: First two mode shapes of a Graphite fiber reinforced polymide beam**

The Table 2 gives the natural frequencies of the composite beam obtained from the MATLAB.

**Table 2: Results obtained from MATLAB**

| Composite materials | Boundary Conditions | First Natural frequency in [Hz] | Second Natural frequency In [Hz] | Third Natural frequency In [Hz] |
|---|---|---|---|---|
| **Glass Epoxy** | Fixed-Free | 18.256 | 114.373 | 320.336 |
| **Carbon Epoxy** | Fixed-Free | 39.577 | 247.938 | 694.423 |
| **Graphite Fiber reinforced polymide** | Fixed-Free | 35.392 | 221.722 | 620.998 |

## Conclusion

Modal analysis was performed on composite beam by considering three different composites materials with fixed free boundary conditions using analytical or MATLAB. By observing this program we can state that to evaluate much harder problems by considering the empirical formulas to obtain results MATLAB can be used as best numerical computation software. The further work can be extended for writing the programs of much more complex equations in MATLAB and obtains exact solution.

## References

[1] Krishan K. Chawla "Composite Materials Science and Engineering", springer. pp. 7-101

[2] Singiresu S. Rao "Mechanical vibrations", Pearson.pp. 639-643.

[3] Rudra Pratap,"Getting started with MATLAB", Department of Mechanical Engineering, Indian Institute of Science, Bangalore.

[4] Rishi Raj, Prabhat Kumar Sinha and Earnest Vinay Prakash. Modelling, simulation and analysis of cantilever beam of different material by FEM method, ANSYS & MATLAB. International journal of engineering research and general science. Volume 3, pp.89-100, 2015.

[5] M.Rastgaar Aagaah, M. Mahinfalah and G. Nakhaie Jazar. Natural frequencies of laminated composite plate using third order shear deformation theory. Composite structures, pp. 273-279, 2006.

[6] https://www.mathworks.com/help/vibration-analysis.

*Applied Mechanics and Materials*
*ISSN: 1662-7482, Vol. 895, pp 307-312*
*doi:10.4028/www.scientific.net/AMM.895.307*

*Submitted: 2019-01-14*
*Accepted: 2019-02-22*
*Online: 2019-11-01*

# Analytical and Finite Element Solution of Tractor Brake Link to Achieve Weight and Cost Reduction

G.L. Anantha Krishna[1,a], K.M. Sathish Kumar[2,b*]

[1]Assistant Professor, Department of Mechanical Engineering,BMS Institute of Technology&Management, Bengaluru, 560 064, India,

[2]Professor, Department of Mechanical Engineering, BMS Institute of Technology&Management, Bengaluru, 560 064, India,

[a]glamech@bmsit.in [b]sathishmech@bmsit.in

**Keywords:** Brake link, Stress, Weight reduction, Cost saving, Failure zone

**Abstract.** In tractor brakes, when the brake is applied, tension in the operating rod causes the links to turn the two actuating disc slightly, in opposite directions. The shape of the recesses in which the hardened steel balls locate is such that, as disc move relative to each other, the ball force them apart and apply pressure to the rotating discs. The automotive industry has for many years identified weight reduction as a way of improving product competitiveness and thus the ability to make profits. In present work, an attempt has been made to reduce the thickness of link and hence achieve weight reduction and cost savings. The actuator link has been analyzed for stresses. The existing link is of 6 mm thickness and is made of C – 40 steel. The existing link of 6 mm thickness along with links of 5 mm and 4 mm thickness were considered for analysis. It is found that the stresses in 5 mm thick link are well within limits with a factor of safety of 2.3. This reduction in thickness would yield a reduction in weight of link and hence would reduce the cost of link with a saving potential of Rs.14, 40000/= per year considering the fact that 6, 00,000 tractors are sold in India every year. Experimental investigation showed the zone of failure of link is in line with the high stress zone indicated by finite element analysis.

## Introduction

A brake is a machine element used to control the motion by absorbing kinetic energy of a moving body. The absorbed kinetic energy appears as heat energy which would get dissipated. Friction brakes are used as the means of slowing down or stopping. Friction is developed between rotating and non-rotating members of the vehicle itself. Drum and disc brakes are the two types of friction brakes used in practice

The tractor brake is essentially a disc brake where in when the brake is applied, tension in the operating rod causes the links to turn the two actuating disc slightly, in opposite directions. Schematic sketch of a tractor disc brake is as shown in Fig. 1. The shape of the recesses in which the hardened steel balls locate is such that, as disc move relative to each other, the ball force them apart and apply pressure to the rotating discs. The links in use currently are 6 mm thick and are subjected to tensile force. There are 4 such links per tractor. In the present work, an attempt has been made to investigate the suitability of 5 mm and 4 mm thick links leading to reduction in weight of links. This would reduce the cost of the link and benefits both the manufacturer and the customer. The failure zone is to be identified with finite element analysis and correlated with testing of link in tensile testing machine.

Fig. 1: Schematic sketch of a Tractor Disc Brake with links

At the conclusion of a brake application, the coil springs pull the actuating discs back into their original relative positions, the pressure is taken off the friction discs and the brake is released.

P. Vijayalakshmi and J. Lilly Mercy [1] obtained the fatigue life of the optimized model using Finite Element method along with optimization technique.

Peter O Jansson [2] investigated the stress distribution in link plates with varying amounts of material behind the link plate pins and developed them.

Swapnil R. Abhang and D.P.Bhaskar [3] found that friction force on the disc brake with carbon ceramic matrix works more efficiently.

V.M.M.Thilak et.al [4] made an attempt to investigate the suitability of hybrid composite material for extended service life and long term stability.

S. Sarip [5] tried to reduce weight by vehicle with regenerative braking system based on the relationship obtained between rotor weight, thickness, undercut affect and offset between hat and friction ring.

Amandeep [6] worked on brake pedal linkage of a tractor. Modeling is carried out using CATIA software and finite element analysis is carried out using ANSYS software. The maximum stress is found to be 173.51 MPa which is well below the yield stress of material which is 250MPa. Maximum deformation was 21.053 mm which according to the author is within safe limits.

From the literature survey, it can be seen that there exist a lot of potential for exploration in reducing the weight of components in tractors. One such component is brake link which the author intends to investigate for weight reduction and thereby reducing the cost.

**Methodology**

The actuating link currently in use is of 6 mm thickness. It is intended to check the suitability of 5 mm thick and 4 mm thick link by adopting both analytical and finite element method. Finite Element Analysis is to be carried out using ANSYS software to find out maximum stress. The link is to be analyzed as plate with a hole concept and theoretical calculations are to be based on this concept. For the purpose of analysis, a pedal effort of 30 Kg is considered. Pedal ratio and linkage ratio are considered as 15. The link material is C-40 steel whose yield stress is 324 MPa.

The load is applied as pressure on the surface. The pressure to be applied depends on the cross section of the links. The areas of cross sections over which pressures are applied for 6 mm, 5 mm and 4 mm links are 88.2 $mm^2$, 73.5 $mm^2$ and 58.8 $mm^2$ respectively. A new thickness of link is to be proposed based on results from analytical and finite element analysis. Based on the above observations cost reduction per year is to be calculated and tabulated. Tensile test is to be carried out to ascertain the location of failure zone.

**Analytical Calculation of Stresses in 6 mm Thick Link**

The pedal effort of 30 Kg and pedal and linkage ratio of 15 are considered for calculations and analysis. Hence, the load applied is 4415 N. However, load of 4500 N is considered for calculations.

Fig. 2 indicates the dimensions of existing link. Following are the Specification of the link in use currently

- Material = Mild Steel (C-40, Density = 7850 kg/m$^3$)
- Thickness t = 6 mm
- Width of plate, w = 25 mm
- Hole Diameter d = 11.18 mm

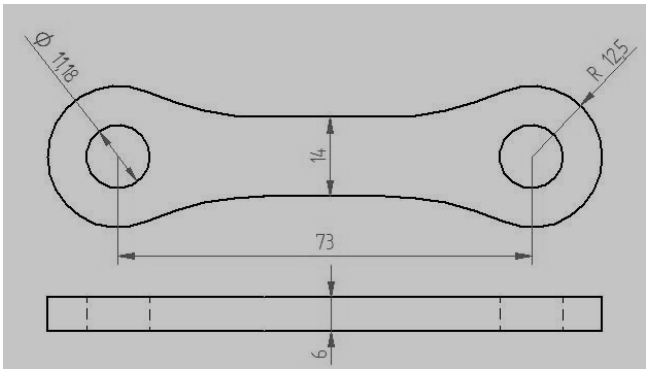


Fig. 2: Geometry of existing link

For plate with a hole concept, ratio of hole diameter to width of plate is to be found out ie.

d/w (1)

11.18/25 = 0.4472

For d/w =0.4472, the stress concentration factor from design data hand book is $K_\sigma$= 2.2 [6] where $K_\sigma$ is stress concentration factor

A = (w-d) x t (2)

A = (25-11.18) x 6 = 82.92 mm$^2$

$\sigma_{nominal}$ = F / A where $\sigma_{nominal}$ is the nominal stress in MPa (3)

$\sigma_{nominal}$ = 4500 / 82.92 = 54.27 MPa

$\sigma_{maximum}$ = $K_\sigma$ x $\sigma_{nominal}$ where $\sigma_{maximum}$ is the maximum stress in MPa (4)

$\sigma_{maximum}$ = 2.2 x 54.27 = 119.4 MPa

Factor of safety (FOS) = $\sigma_{yield}$ / $\sigma_{maximum}$ (5)

FOS = 324 / 119.4 = 2.7

Similarly stresses and FOS for 5 mm and 4 mm thick links are calculated and tabulated in Table 1

Table 1: Maximum stresses induced

| Sl no. | Link Thickness[mm] | Maximum stress, [MPa] | FOS |
|---|---|---|---|
| 1 | 6 | 119.4 | 2.7 |
| 2 | 5 | 143.3 | 2.3 |
| 3 | 4 | 179.1 | 1.8 |

**Finite Element Analysis of 6 mm, 5mm and 4 mm thick links**

For Finite Element Analysis (FEA) the load is applied as pressure. The pressure values are as discussed earlier. Tractor brake link is analysed for stresses using ANSYS. The element used is SOLID BRICK 8node45

As the load is applied on brake pedal, the force is transmitted to the link through the pin. One side of the link hole is constrained whereas the other hole has tensile pull acting on it. As in Fig. 3, 180˚of the hole is constrained for all the degrees of freedom, since the movement of the hole is controlled by the pin at that area.

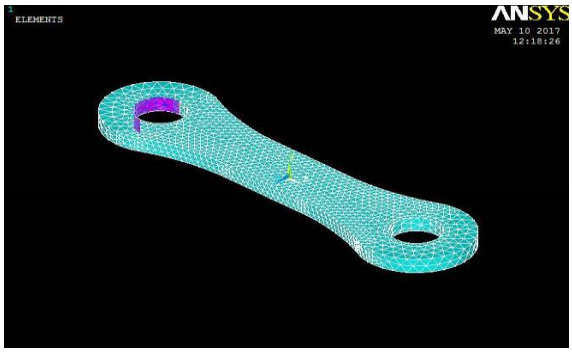


Fig. 3: F E model with boundary conditions

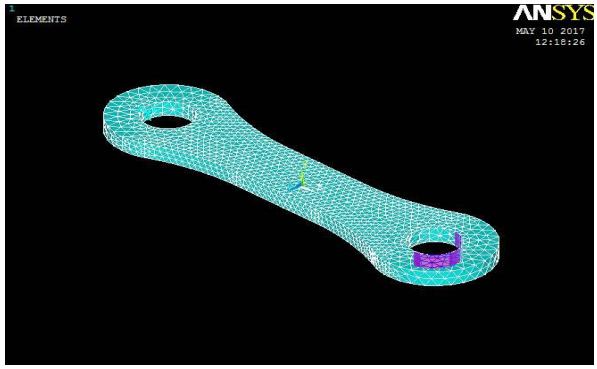


Fig. 4: F E model with loading

Axial tensile pressure acting on 180˚ of the hole is applied as shown in the Fig. 4, since the operating rod pulls the link axially at this area. The pressure of 51.02 MPa, 61.22 MPa and 76.53 MPa are on 6 mm, 5 mm and 4 mm thick links respectively is applied on one of the hole and the other side of the hole is constrained. Fig. 5, Fig. 6 and Fig. 7 indicates the stresses and deformation in the links.

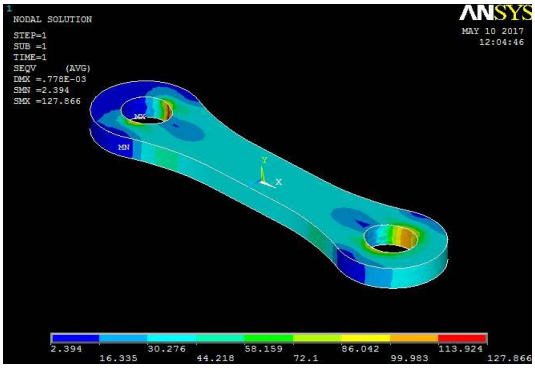


Fig. 5: Stress and deformation in 6 mm thick link

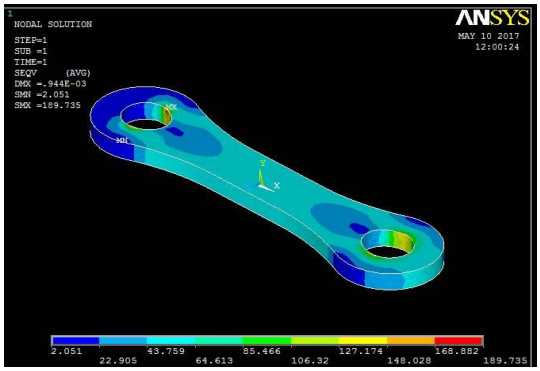


Fig. 6: Stress and deformation in 5 mm thick link

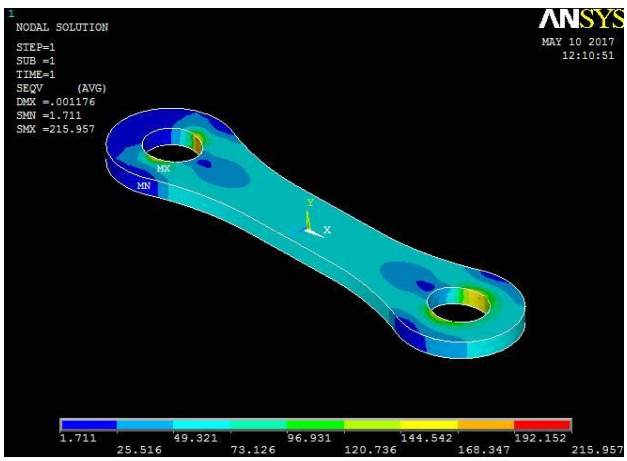


Fig. 7: Stresses and deformation in 4 mm thick link

Stresses obtained by both analytical and finite element methods are compared. Comparison of stresses and FOS obtained analytically and from FEA are tabulated in Table 2.

Table 2: Stresses through analytical calculations and FEA

| Sl no. | Link thickness, [mm] | Stress from analytical method [MPa] | Stress from FEA [MPa] | FOS from Analytical method | FOS from FEA |
|---|---|---|---|---|---|
| 1 | 6 | 119.4 | 127.8 | 2.7 | 2.5 |
| 2 | 5 | 143.3 | 189.7 | 2.3 | 1.7 |
| 3 | 4 | 179.1 | 215.9 | 1.8 | 1.5 |

Based on the analytical and FE analysis, for 4500 N load, the stress induced in 6 mm, 5 mm and 4 mm thick specimens are well within the 324 Mpa yield stress of the material C - 40. Hence, based on strength criteria the component is safe. From analytical and FEA, both in 5 mm and 4 mm thick links, the stress induced are well within the limits and FOS obtained is safe. But, safety of human being is paramount while designing brakes. Hence, a higher value of FOS is desirable. Hence, 5 mm thick link may be considered for use in practice.

Tensile test for existing link of 6 mm thickness was conducted in a Universal Testing Machine to identify the location of failure zone and correlate with that of FEA. During the tensile test, the fracture occurred at the area of lowest radius of curvature where stress concentration is maximum. This is as shown in Fig. 8. This is in agreement with the high stress zone indicated in FEA.

Fig. 8: Fractured 6 mm thick link

Weight reduction is of high importance since reduction in weight of link reduces total weight of the tractor which improves the efficient working of the tractor. The weight of both 6 mm and 5 mm thick link is calculated by considering the density of steel to be 7850 Kg/m$^3$ and surface area of 1457.4 mm$^2$. The weight of 6 mm thick link is 69 grams where as that of 5 mm thick link is 57 grams. The weight saved by using 5 mm thick link is 12 grams. The cost of 1 Kg of steel is considered as Rs.50 for calculations. According to the survey conducted by Tractor Manufacturers Association in 2013 [7], a total of 6, 00,000 number of tractor units were sold in India. There are totally two disc brakes in a tractor. Each disc brake consists of two links. So a tractor consists of 4 actuating links. Hence total number of links manufactured is 24, 00,000. Hence, total cost saved is Rs.14, 40000/=.

From the above analysis and calculations, it can be concluded that by using 5 mm thick link, the cost saved is quite substantial.

## Conclusions

The main focus of this project was to find the stress induced analytically and by finite element methods for link of various thickness and estimate the weight reduction and in turn cost saving. Through analytical and finite element analysis of actuating link, it was found that the stress induced in 6 mm thick link as well as 5 mm thick link was well within safe limit under the loading condition of 4500 N. By using 5 mm thick link, the material saved is 12 grams per link. The cost analysis is performed for 5 mm link and it was found that Rs.14,40000/= per annum can be saved for

24,00,000 links which are manufactured per year considering that 6,00,000 tractors are produced every year. Hence, 6 mm thick link may be replaced by 5 mm thick link.

## References

[1] P. Vijayalakshmi and J. Lilly Mercy, Failure Analysis and Re-Design of Tractor Brake Actuating Link**,** Indian Journal of Science and Technology, Volume 8, 59138, (2015).

[2] Peter O. Jansson, Analysis of Stress Distribution in Link Plates Used for Suspending Bridge Beams, P.E., Structural Research Unit Construction and Technology Division Research Project TI-2097 Research Report No. R-1517.

[3] Swapnil R.Abhang, D.P Bhaskar, Design and analysis of disc brake, International journal of Engineering Trends and Technology –Volume 8, (2014), Number 4-.

[4] V.M.M.Thilak, R.Krishnaraj, Dr.M.Sakthivel, K.Kanthavel, Deepan Marudachalam M.G, R.Palani,Transient Thermal and Structural Analysis of the Rotor Disc of Disc Brake, International Journal of Scientific & Engineering Research Volume 2, (2011) 1 ISSN 2229-5518.

[5] S. Sarip, Design Development of Lightweight Disc Brake for Regenerative Braking – Finite Element Analysis, Member, International Journal of Applied Physics and Mathematics, Volume 3, (2013), No. 1.

[6] Amandeep, Atul Kumar Kaushik, Amit Goyal, Punit Kumar Rohilla, Finite Element Simulation of Brake Pedal Linkage of Tractor, International Journal of Mechanics and Solids, Volume 12,Number 1 (2017), 41 – 51.

[7] Machine Design data hand book by K Lingaiah.

[8] Information on http://www.tmaindia.in/tractor-industry.php

ISSN 2321 3361 © 2020 IJESC

Research Article Volume 10 Issue No.2

# Estimation and Comparison of Percentage Error of Theoretical and Experimental Natural Frequency of a Single Degree of Freedom System using Spring Mass System

G. L. Anantha Krishna
Assistant Professor
B M S Institute of Technology and Management, Bengaluru, India

**Abstract:**
Vibration is the motion of a particle or a body or system of connected bodies displaced from the position of equilibrium. The system tends to return to equilibrium position due to restoring forces. Presence of unwanted vibrations in a system is undesirable and hence it is required to find the natural frequency of a system. The natural frequency can be calculated using stiffness and mass of the system. In the present work, an attempt is made to compare theoretical and experimentally obtained natural frequencies and ascertain the percentage error. From the experimental investigations, it is found that the percentage error in natural frequency is greatly reduced with the increase in mass attached to the set up. It is found that percentage error is 13.12% for the maximum mass attached to the set up. This comparison would help in finding out accurate values of natural frequency of a system which in turn would help in enhancing the ride and comfort levels for passengers in automobiles.

**Keywords:** Vibration, Spring mass system, Natural frequency, Static deflection.

## I. INTRODUCTION

All objects in the universe are made up of matter which can exist in solids, liquids or gaseous form. Any of these forms can exist in microscopic forms such as ions, atoms, molecules or as huge sizes like planets and their satellites. They are all composed of matter which essentially possesses mass. Masses without the action of forces on them can be stationary and only force acting on them is gravitational force which leads to weight. Masses under the action external forces are subjected to translations and rotations. The time rate of change of translations will lead to linear velocity. If it is rotation, it will lead to angular velocity. The time rate of change of linear and angular velocities will lead to linear and angular accelerations. Masses under the influence of accelerations develop inertia forces. All the bodies which possess mass and elasticity are capable of vibrations. Any motion which repeats itself after an interval of time is called vibration or oscillation or periodic motion.

**Everything is related to vibration**

| | |
|---|---|
| Biology | : Pulse rate, breathing rate |
| Physics | : waves, sound |
| Chemistry | : Atomic vibration, Spectroscopy |
| Astronomy | : Planetary orbits |
| Geology | :Earthquakes, Volcanic eruptions, Seismic tremors |
| Economics | : Financial cycles, Business cycles |

To & fro motion of a body in a particular time interval is said to be subjected vibrations

**Causes of vibration are**
- Unbalance forces in the machines
- External excitations by Impact loads
- Earthquakes leads to failure of buildings & structures
- Winds cause vibration of transmission lines

**Harmful effects of vibrations:**
- Excessive stresses
- Undesirable noise
- Loosening of parts
- Partial or complete failure of parts

**Useful effects of vibration:**
- Musical instruments
- Shakers
- Stress relieving

**Following are the ways to eliminate vibrations**
- Removing cause of vibration
- Putting screens if noise is an objection
- Placing machinery on proper isolators
- Shock absorbers

Amplitude is the maximum distance travelled by the vibrating particle from its mean position. Period of vibration or time period is the time interval after which the motion is repeated itself. The period of vibration is usually expressed in seconds. Cycle is the motion completed during one time period Frequency is the number of cycles described in one second. Its unit is Hertz (Hz) or cycles per second (CPS)

**Types of vibrations are**
- Free or natural vibrations
- Forced vibrations
- Damped vibrations

In the present work a single degree of freedom system is considered using a spring mass system to understand the variations in frequencies in theoretical and experimental analysis. Also, the percentage error is to be estimated and analyze the influencing factors for higher errors occurring between theoretical and experimental values. This would help researchers and practicing engineers to find the natural frequencies of a system close to the theoretical values.

## II. LITERATURE REVIEW

Pratik Muliya [1] et.al have compared the methods to calculate natural frequency of a simple vibrating system. They have compared analytical methods such as equilibrium method, maximum energy method and Rayleigh's method with the experimental results. They have found that the results of experiments are in line with those of analytical methods Nandan Rajeev [2] et al have identified comfortable ride frequencies for various vehicles such as passenger cars, rally cars etc. They infer that the ride frequency of the suspension system plays a major role in the design of the vehicle. They provide an insight into natural frequency, ride frequency and how they are valuable in the design of springs for suspension system. T. Ravi teja[3] have made an attempt to analyze multi degree freedom system for natural frequencies and mode shapes. These mode shapes can be superimposed to get actual displacement pattern of a given system. The author has developed a multi degree freedom system in Mat Lab platform. The Mat Lab program could plot the amplitudes of the vibrating bodies. Using this designer can work out various parameters and arrive at an optimum specification of the system

## OBJECTIVES

To find natural frequency of a spring for various masses theoretically
To find natural frequency of a spring for various masses experimentally.
To find the percentage error between

## III. METHODOLOGY

In the present work a simple set up consisting of a spring mass system as shown in Fig. 1 is chosen for carrying out the experimentation. Various masses are considered for experiments. The theoretical values of natural frequency for various masses are calculated using the equation $f_{th}= 1/2\pi \sqrt{g / \delta}$ where 'g' is acceleration due to gravity in mm/s$^2$ and 'δ' is static deflection. The chosen masses are mounted on the setup and allowed to oscillate for 10 oscillations. Then time per oscillation is calculated and in turn frequencies are calculated.

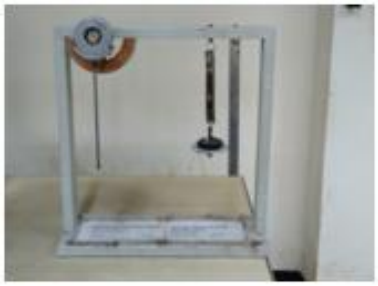

**Figure.1. Spring Mass System Set Up**

## IV. RESULTS AND DISCUSSIONS

Theoretical natural frequency (Specimen calculation)
Initial length of spring =105mm
Mass attached, m =0.43Kg
Final length of spring =175mm
Static deflection of spring, δ = Final length of spring - Initial length of spring
= 175 – 105 = 70mm
Acceleration due to gravity, g =9810mm/s$^2$

$f_{th} = 1/2\pi \sqrt{g / \delta}$
$= 1/2\pi \sqrt{9810 / 70}$
$= 1.884$ Hz

Similarly, for various masses static deflections are noted and theoretical frequencies are calculated. They are tabulated as shown in Table 1

**Table.1. Theoretical Frequencies for Various Masses**

| Sl. no | Mass, m Kg | Initial length of spring, mm | Final length of spring, mm | Static deflection, δ, mm | Theoretical frequency, Hz |
|---|---|---|---|---|---|
| **1** | 0.43 | 105 | 175 | 70 | 1.884 |
| **2** | 0.63 | 105 | 225 | 120 | 1.439 |
| **3** | 0.73 | 105 | 260 | 155 | 1.266 |
| **4** | 0.93 | 105 | 320 | 215 | 1.075 |

Experiments were conducted using the set up as shown in Fig 1 for various masses considered. The time for 10 oscillations was recorded and time per oscillation is calculated. Table 2 indicates the experimentally obtained frequencies for the corresponding masses.

**Table.2. Experimentally Obtained Frequencies**

| Sl. no | Mass, m Kg | Initial length of spring, mm | Final length of spring, mm | Time for 10 oscillations, seconds | Time per oscillation, seconds | Experimental frequency, Hz |
|---|---|---|---|---|---|---|
| **1** | 0.43 | 105 | 175 | 7.1 | 0.71 | 1.408 |
| **2** | 0.63 | 105 | 225 | 8.9 | 0.89 | 1.123 |
| **3** | 0.73 | 105 | 260 | 9.6 | 0.96 | 1.042 |
| **4** | 0.93 | 105 | 320 | 10.7 | 1.07 | 0.934 |

Percentage error between theoretical and experimental frequencies are tabulated as shown in table 3

**Table.3. Comparison of Theoretical and Experimental Frequencies and % Error**

| Sl. no | Theoretical frequency, Hz | Experimental frequency, Hz | % error |
|---|---|---|---|
| **1** | 1.884 | 1.408 | 25.26 |
| **2** | 1.439 | 1.123 | 21.95 |
| **3** | 1.266 | 1.042 | 17.69 |
| **4** | 1.075 | 0.934 | 13.12 |

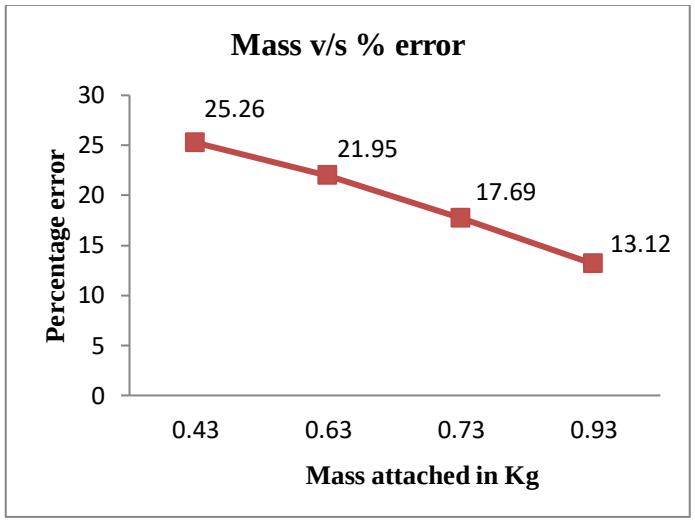


**Figure.2. Percentage Error Decreases with Increase in Mass Attached**

## V. CONCLUSIONS

In the present work, natural frequency of a given spring is calculated theoreticallyand compared with that of experimentally obtained natural frequency the natural frequencies are calculated with different masses. The percentage error is estimated. From experimental investigations it is found that the percentage error is reducing with the increase in mass attached. This may be due to the fact that as the mass increases, the recording of time becomes more and more accurate and hence the percentage error gets reduced. It can be concluded that the recording of time need tobe more accurate during experimentation. Also, the researchers and practicing engineers can note that the experimentally obtained natural frequency will be more in concurrence with theoretical natural frequency if the mass attached is increased.

## VI. REFERENCES

[1]. Pratik Muliya, Anil Kachhadiya, Jaydev Haranesha, Ghana shyam Tejani, “An experimental investigation on the natural frequency of free undamped, damped and forced damped vibrations” RK Universities First International Conference on Research & Entrepreneurship (ICRE 2016), Pg 1584 – 1595.

[2]. Nandan Rajeev, Pratheek Sudi, “Natural Frequency, Ride Frequency and their Influence in Suspension System Design, International Journal of Engineering Research and Applications (IJERA), Vol. 09, No. 3, 2019, pp 60 – 64.

[3]. T. Ravi teja, Computation of Natural Frequency of Multi Degree of Freedom System, International Journal of Engineering Research & technology, Vol. 1, Issue 10, December 2012, pp 1-5.

[4]. Mahesh Chandra Luintel, Tri Ratna Bajracharya, “Dynamic Response of a Timoshenko Shaft With a Rigid Disk”, Journal of Engineering and Applied Sciences, 14(4):, 2019, ISSN:1816 – 949X, pp 1239 – 1246.

[5]. Levitan, Edwin S, Forced Oscillation of a Spring Mass System having Combined Coulomb and Viscous Damping”, Journal of Acoustical Society of America 32.10: 1265 – 1269.

Available online at www.sciencedirect.com

ScienceDirect

Materials Today: Proceedings 5 (2018) 20939–20946

materialstoday: PROCEEDINGS

www.materialstoday.com/proceedings

ICSEM 2016

# Kinetic analysis of isothermal solid state process for synthesized potassium sodium niobate piezoelectric ceramics

Nandini R Nadar [a]*, Krishna M [b]

[a*b] *R. V. College of Engineering, R& D centre, Department of Mechanical Engineering,Bangalore-560059,INDIA.*

Solid state kinetic models were developed for predicting conversion fraction (α), reaction rate (dα/dt), kinetic triplet (model f(α), frequency factor (A) and activation energy ($E_a$)) of $(K_{0.5}Na_{0.5})NbO_3$ceramics using thermos-gravimetric analysis data obtained at constant temperature of 900°C .The integral reaction model g(α), were evaluated for experimental data and theoretical reaction models. Kinetics of solid state reaction of KNN ceramics was a homogenous nucleation process with one dimensional nuclei growth per particle at constant rate, 2D diffusion controlled reaction mechanism, particles with spherical/cubical shape based on Mapel, JMAEK nucleation, Jander Model and contracting volume model respectively.


Selection and Peer-review under responsibility of INTERNATIONAL CONFERENCE ON SMART ENGINEERING MATERIALS (ICSEM 2016).

*Keywords:*KNN; solid state reaction; Kinetics analysis; Kinetic Triplet; Reaction model; Diffusion model;Nucleation model; Crystal imperfections.

## 1. Introduction

Presently, potassium sodium niobate (KNN) based lead free piezoelectric ceramic materials have high potential applications in emerging areas of micro-motors[1], energy harvesting devices[2], magneto-electrical sensor [3] etc., due to their high curie temperature ($T_C$ )[4], piezoelectric and ferroelectric properties[5]. Solid state method is a convenient way to decompose the presence of carbonates and oxides in KNN piezoelectric materials with good control on particle morphology [6-7]. The KNN is a heterogeneous material with melting point of two alkali

* Corresponding author. Tel.:+91-958-892-2999; fax: +91-806-717-8011
*E-mail address:* nandini.nadar@gmail.com, krishnam@rvce.edu.in


Selection and Peer-review under responsibility of INTERNATIONAL CONFERENCE ON SMART ENGINEERING MATERIALS (ICSEM 2016).

elements close to normal calcination temperature in solid state route. Hence establishment of the calcination temperature may result in the formation of non-stoichiometric phases due to volatile nature of the alkaline elements, which hinders the densification and piezoelectric properties [8-10]. In this direction many researchers have investigated the influence of calcination parameters and alkali carbonates on phase transformation of KNN from orthorhombic to tetragonal crystal structure [11-13].

Many researchers have worked on kinetic (isothermal or non-isothermal) analysis of model-fitting and model-free (iso-conversional) methods [14-19] for amorphous, polymeric and pharmaceutical materials in the solid state route. Avrami models were used to achieve required reaction mechanism and to determine kinetics of $(GeS_2)_{0.3}(Sb_2S_3)_{0.7}$ glass, zirconia gel $ZrO_2$[15]crystalline material, crystallographic transition[16], decomposition kinetics of the $AlH_3$ polymorphs, thiourea and thiourea oxides[17-18], hydrogen adsorption or desorption of $MgH_2$ with single walled carbon nano tubes (SWNT) and metallic catalyst[19], hydration of tricalcium and dicalcium silicate mixtures [20]and de-solvation of sulfa meter solvates [21] respectively. Thermal decomposition of $AgMnO_4$ crystals for polymorphic transformation was analyzed by kinetics models based on Maxwell-Boltzmann distribution of energy [22]. Acid -base type solid chemicals such as sulfonamide and ammonia adducts [23] showed that diffusion model plays a vital role when the crystal lattices of the reactants are separate. The dehydration process of calcium oxalate monohydrate followed geometrical contraction models [24].Thermal oxidation of porous silicon [25]followed Mapel (First-order) Model. But as per authors knowledge no or few research is focused on solid state kinetic analysis to optimize the synthesis route of KNN piezoelectric materials to achieve $(K_{0.5}Na_{0.5})NbO_3$ system without non-stoichiometric phases for better piezoelectric properties.

The purpose of the work was to investigate solid state kinetics of KNN ceramic particles for the system $(K_{0.5}Na_{0.5})NbO_3$ isothermally by thermal gravimetric analysis. The isothermal reaction rate ($d\alpha/dt$), the kinetic triplet (A, Ea, $f(\alpha)$) and integral reaction model $g(\alpha)$ was determined by conversion fraction($\alpha$). The nucleation, geometrical contraction, diffusion, reaction-order models were studied to achieve completion of the isothermal reaction of KNN piezoelectric materials, without non-stoichiometric phases by model fitting method for better piezoelectric properties.

## 2. Experimentation

The potassium sodium niobate piezoelectric ceramics was synthesized by conventional solid state method [26].The synthesized homogeneous KNN nano powders were subjected for thermo-gravimetric analysis to study isothermal solid state kinetics ,behind solid state route of KNN ceramics. Thermo-gravimetric measurements was done by using simultaneous thermos-gravimetry / differential thermal analyser, (DTG-60/60) Shimadzu, with an analytical measuring instrument to work in inert atmosphere (50ml $min^{-1}$ $N_2$). Small sample (2.724mg) was placed in a platinum cell to reduce the phenomena of heat and mass transfer. A constant rate controlled thermal degradation curve was obtained to study the solid state kinetics of KNN ceramic powders. The measured parameters were transformed into a conversion fraction ($\alpha$) to analyse the reaction mechanism of KNN piezoelectric ceramic powders.

## 3.Results and Discussions

### 3.1 Isothermal curves of KNN powder

The measured isothermal gravimetric data of KNN powder at 900°C for dwell time between 1-1000 min was transformed into conversion fraction ($\alpha$) by using equation 1. $m_0$, $m_t$, $m_\infty$ is the initial mass , mass at time t, and final mass of KNN powder at 1000min. The obtained $\alpha$ values were plotted against the dwell time, from 1-1000 min. Isothermal curve ($\alpha$ vs. t) of synthesized KNN powder is depicted by Fig. 1(a). The parabolic nature of the graph indicates gradual increase in the mass fraction of the KNN powder as the reaction mechanism progress till 500min. Enhancement in the mass fraction during isothermal reaction is due to removal of moisture, decomposition of KNN powder from carbonates into bi-carbonates with the release of $CO_2$ gas. Further the mass fraction of the isothermal reaction from 500-1000 min was constant. This ensured that isothermal reaction mechanism of KNN powder at 900°C is completed. The reaction rate of the KNN powder at 900°C was evaluated by determining change in mass fraction to change in dwell time ($d\alpha/dt$) and was plotted against the conversion fraction as shown in

Fig 1(b). Here the reaction rate reduced gradually as the reaction progressed and almost zero towards the mass fraction value of 1 ensuring that, kinetic model of KNN ceramic powders can be grouped under deceleratory models.

$$\propto = \frac{m_0 - m_t}{m_0 - m_\infty} \quad (1)$$

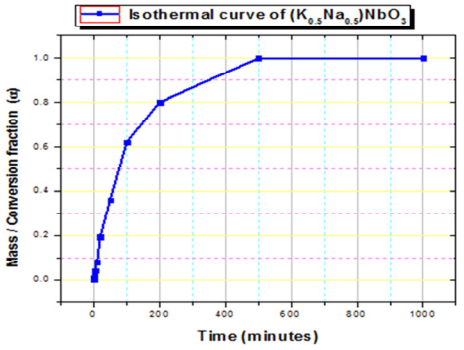


Fig. 1(a). Mass fraction(α) vs. time of synthesized($K_{0.5}Na_{0.5}$)$NbO_3$ceramic

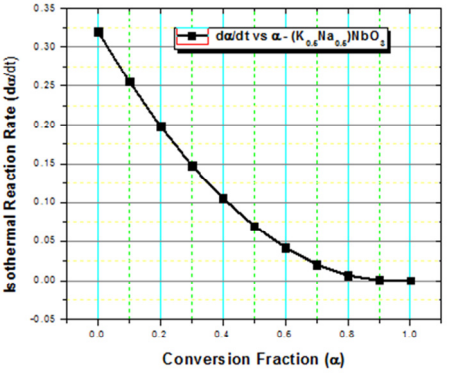


Fig. 1(b). Reaction rate vs. Mass fraction(α) of synthesized ($K_{0.5}Na_{0.5}$)$NbO_3$ ceramic powder.

### 3.2 Order based models of KNN

The conversion fraction (α) and reaction rate (dα/dt) computed from the measured parameter of isothermal gravimetric analysis was used to determine reaction model f(α) and integral reaction model g(α) of KNN particles. The experimental f(α) value was determined by equations 2,3 and g(α) by Eqs. 4,5 respectively. The frequency factor, activation energy, absolute temperature, gas constant, heating rate, reaction and integral reaction model is denoted by A, $E_a$ ,T, R, β ,f(α) and g(α) respectively. The heating rate [β] is given by the equation dT/dt.

$$\frac{d\propto}{dt} = A\, e^{-(E_a|RT)}\, f\,(\propto) \quad (2)$$

$$\frac{d\propto}{dt} = \frac{A}{\beta}\, e^{-(E_a|RT)} f(\alpha) \quad (3)$$

$$g(\propto) = A\, e^{-(E_a|RT)} f(\propto) \quad (4)$$

$$g(\propto) = \frac{A}{\beta} \int_O^T e^{-(E_a|RT)}\, f(\propto) \quad (5)$$

The theoretical first, second and third order reaction models where determined by the Eqs. 6- 8 using conversion fraction (α) values of KNN particles. The order of integral reaction models was evaluated by Eqs. 9-11.The reaction and integral models of KNN powder computed from measured parameters where mapped with derived order based models by model fitting method.

$$f(\propto) = (1-\propto), \quad 1st\ order \quad (6)$$

$$f(\propto) = (1-\propto)^2,\ 2nd\ order \quad (7)$$

$$f(\propto) = (1-\propto)^3, 3rd\ order \quad (8)$$

$$g(\propto) = (ln|(1-\propto)), \quad 1st\ order \quad (9)$$

$$g(\propto) = (1/(1-\propto)) - 1, \quad 2nd\ order \quad (10)$$

$$g(\propto) = (1|2)\big((1-\propto)^{-2} - 1\big), \quad 3rd\ order \quad (11)$$

In this regard, the plot of order based models of synthesized KNN nano-powders is indicated by Fig. 2a and 2b. In Fig. 2a, The f(α) vs. (α) for different order of the reaction was almost similar to homogenous kinetics. The nature of the graph ensured reaction rate (dα/dt) and the mass fraction (α) were proportional to each other, raised to a particular power, called to be the reaction order. The evaluated reaction model f(α) of KNN experimentally was compared with derived models for different orders (1, 2 and 3). The nature of the experimental reaction model was similar to second order reaction at initial and final α values. The other consecutive α values of the experimental reaction model was fitting towards first order model. To confirm the reaction order of the synthesized KNN nano-powders, the graph of integral reaction models g(α) vs. mass fraction (α) for different order was plotted as shown in

Fig.2b. The experimental integral reaction model g(α) fitted exactly with the derived second order reaction model, ensuring that synthesized KNN powders in the system $(K_{0.5}Na_{0.5})NbO_3$ is the second order solid state reaction.

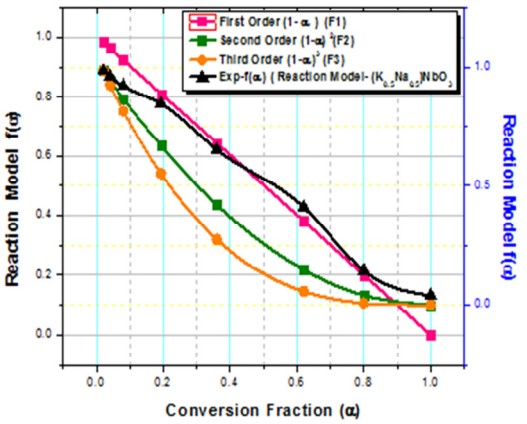


Fig. 2(a) Order based reaction models of synthesized $(K_{0.5}Na_{0.5})NbO_3$

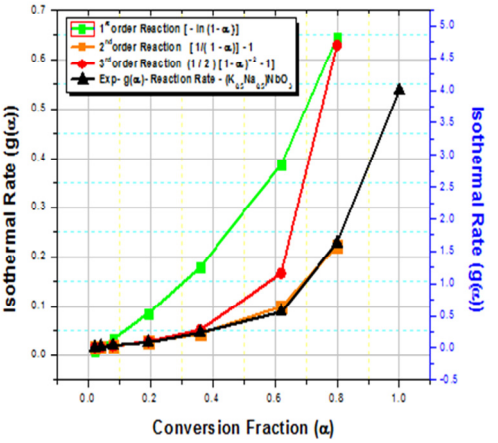


Fig.2(b) Integral reaction model of synthesized $(K_{0.5}Na_{0.5})NbO_3(K_{0.5}Na_{0.5})NbO_3$

### 3.3 Activation Energy [$E_a$] of KNN.

The activation energy [$E_a$] of the synthesized KNN powders can be evaluated by the rate law as shown in Eq. 2 or 4 ,after evaluating dα/dt, f(α) and g(α) values of KNN particles. Here A is the frequency factor, T is the absolute temperature, R is the gas constant, f(α) is the reaction model. The variation in activation energy for synthesized KNN nano-powders by solid state reaction is indicated by Fig. 3. The uniqueness and variance in activation energy ensured that it is a complex reaction mechanism with two or more elementary steps in the mechanism. In such a case, change in activation energy will be observed as the reaction progress [29]. This indicates that during a reaction, reactivity changes due to formation of the required system $(K_{0.5}Na_{0.5})NbO_3$, and presence of crystal defect and intra crystalline strain. The reactivity of KNN solid state reaction is also affected by experimental variables, which changes the kinetics of reaction mechanism. The dependence of E on α in decreasing mode confirms that it is an endothermic reversible reaction which follows an irreversible reaction [30].

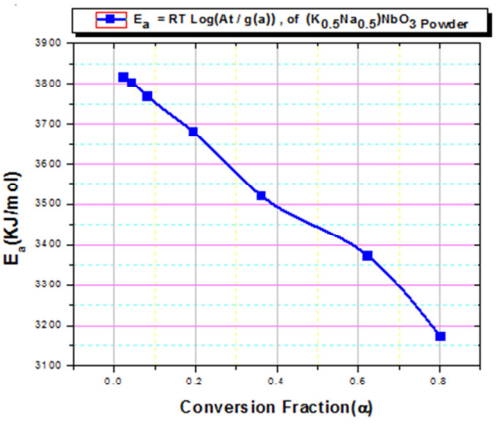


Fig. 3. Dependence of E on α for synthesized KNN powders

### 3.4 Kinetics of solid state reaction of KNN piezoelectric powders

#### 3.4.1 Nucleation Model.

The kinetics behind solid state reaction of KNN particles can be divided into nucleation models, geometric contraction, and diffusion and reaction order based on its reaction mechanism. The nucleation based integral reaction expression were derived by Power law, Avrami , Mapel and JMAEK models from Eqs. 12 to 20 as shown below.

$P2 = \propto^{1/2}$ (12) $A2 = [-(1-\propto)]^{1/2}$ (15) $B1 = ln[\propto/(1-\propto)] + c^a$ (18)

$P3 = \propto^{1/3}$ (13) $A3 = [-ln(1-\propto)]^{1/2}$ (16) $-ln(1-\propto) = kt$ (19)

$P4 = \propto^{1/4}$ (14) $A4 = [-ln(1-\propto)]^{1/4}$ (17) $[-ln(1-\propto)]^{1/n}$ (20)

The formation of the required system i.e.$(K_{0.5}Na_{0.5})NbO_3$ was achieved by decomposition [27] of the reactant with the release of $CO_2$ in the lattice of reactant ($K_2CO_3$, $Na_2CO_3$ and $Nb_2O_5$).The nucleation rate of the experimental value was comparatively higher than that of Avrami (Fig.4b)and power model (Fig.4a) which indicates problem of ingestion and overlap of nuclei [26].Prout-Tompkins (B1) model was not relevant to experimental g(α) values of KNN. The integral reaction rate of KNN powder mapped with the derived value of Mapel Nucleation model, ensured single nucleus per particle in the synthesized system of $(K_{0.5}Na_{0.5})NbO_3$ ceramic materials as shown in Fig4b. The nature of the diffusion controlled nucleation models (JMAEK) for n=1.5 was in agreement with reaction rate of KNN particles as indicating Fig. 4c. This JMAEK model ensured that it is a homogeneous nucleation with one dimensional nuclei growth at constant rate, considered under bulk mechanism [29].

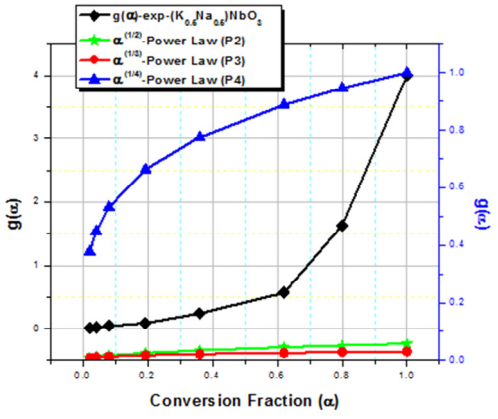


Fig. 4a. Power law models of synthesized $(K_{0.5}Na_{0.5})NbO_3$

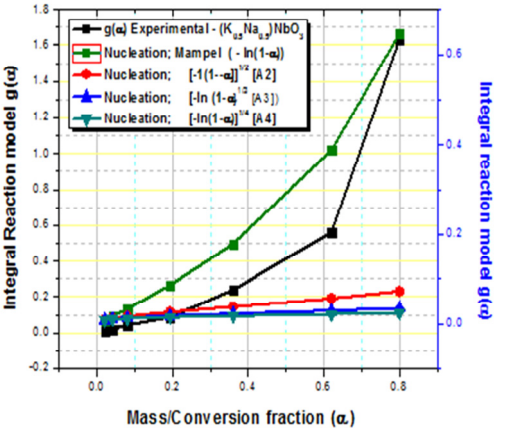


Fig. 4b. Avrami and Mapel models of synthesised $(K_{0.5}Na_{0.5})NbO_3$powders

### 3.4.2 Diffusion model of KNN powder

The experimental rate controlling process for the reaction mechanism of the KNN powder was analysed by diffusion models. In this regard 1-D,2-D,3-D and Brounshtein models were derived from α values of KNN particles, using below mentioned equations 21-24.

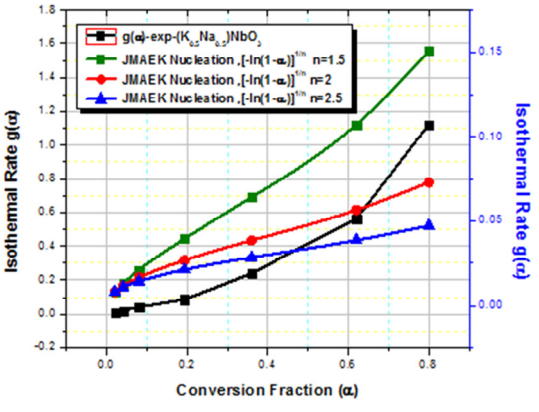


Fig. 4.(c)JMAEK nucleation models of $(K_{0.5}Na_{0.5})NbO_3$powders

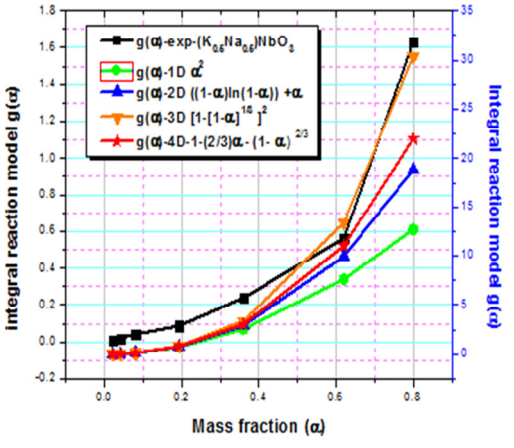


Fig. 5. Diffusion Models (a) 1D, 2D, 3D, D4- of $(K_{0.5}Na_{0.5})NbO_3$powders.

$$D1 = \propto^2 \quad (21)$$

$$D2 = \big((1-\propto)ln(1-\propto)\big) + \alpha \quad (22)$$

$$D3 = \left[1-(1-\propto)^{1/3}\right]^2 \quad (23)$$

$$D4 = 1 - (2/3) \propto -(1-\propto)^{2/3} \quad (24)$$

The rate controlling process (Diffusion) for the solid state reaction of KNN powders is indicated by Fig.5.The experimental integral reaction expression g(α) of the KNN powders was mapped with the derived diffusion models for 1, 2 , 3 and 4 dimensions models. The reaction model was not proportional to mass fraction values (α) conforming that, it is not 1D model. The Jander model(D3) which assumes spherical shape of the solid particle and Ginstling and Bounstein(D4 ) for low conversion values ,didn't hold good for integral reaction rate models of KNN powders. The graphical shape of the experimental diffusion model maps with the 2D-Diffusion model. 2D-Diffusion model which was in agreement with the integral reaction rate of KNN ensured, that the synthesized KNN solid particles are in cylindrical shape with increased reaction zone at radial diffusion through a cylindrical shell. The product formation rate decreased proportionally as shown in Fig.1b, in diffusion controlled reactions with a barrier to the product layer [31]. Hence we can conclude that, solid state kinetics of KNN powder is a 2D-diffusion controlled reaction mechanism.

### 3.4.3 Geometrical contraction model of KNN powders

Contraction (Phase Boundary) models of synthesized KNN powders which assumes nucleation to occur quickly across the surface of the KNN crystal is indicated by Fig.6a and 6b. The reaction rate and integral reaction rate of the model was derived from Eqs. 25 - 26, using mass fraction (α) value, obtained from measured gravimetric data. The experimental integral reaction value g(α) of KNN particles was mapped with derived models of contracting area and volume as shown in Fig. 6. Since the reaction interface of KNN powder progress towards the centre in contraction models ,the rate of degradation can be controlled. The graphical shape of reaction and integral reaction rate model at almost all α values, excluding few of KNN particles as shown in Fig.6a and 6b, was in match with contraction volume model [27]. This confirmed that, the KNN solid particles where spherical/cubical in shape.

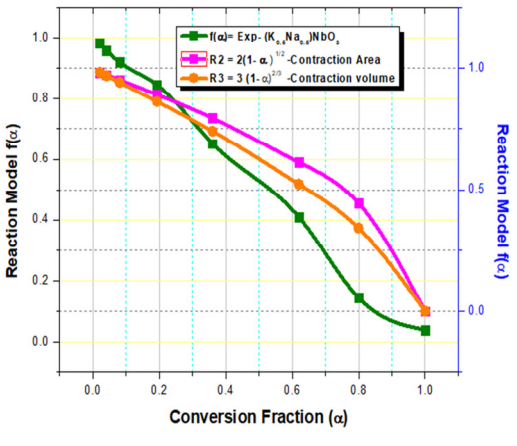


Fig. 6a. Geometrical contraction (R) reaction models f(α).

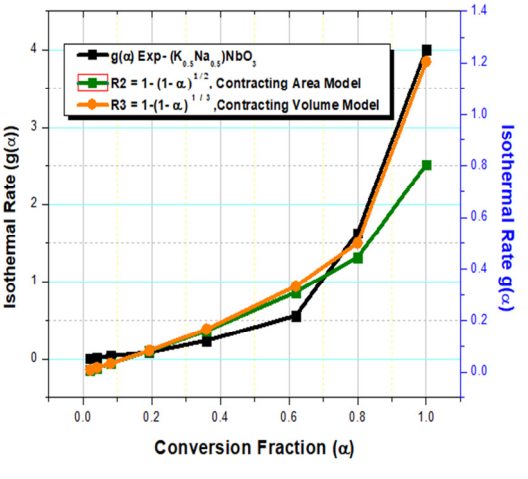


Fig. 6b. Geometrical contraction (R) Integral reaction models g(α).

$$R\,2 = 2(1-\propto)^{1/2} \quad (25)$$

$$R3 = 3(1-\propto)^{2/3} \quad (26)$$

$$R2 = 1-(1-\propto)^{1/2} \quad (27)$$

$$R3 = 1-(1-\propto)^{1/3} \quad (28)$$

## 4. Conclusion

The current work was focussed on isothermal kinetic analysis, to study the kinetics behind solid state reaction of potassium sodium niobate piezoelectric ceramics. Mass fraction (α) and reaction rate of KNN powder achieved completion of the solid state reaction at 900°C,500min with a deceleratory reaction rate. The $E_a$ values revealed that synthesized KNN powders were of complex endothermic reversible reaction followed with irreversible reaction. Order based model concluded that reaction mechanism of KNN is the second order solid state reaction. The Mapel and JMAEK nucleation model revealed that $(K_{0.5}Na_{0.5})NbO_3$ ceramic materials is an constant rate homogenous nucleation with one dimensional growth of single nucleus per particle. Jander Model conclude that, solid state kinetics of KNN powder is a 2D-diffusion controlled reaction mechanism. Geometrically contacting volume model ensured that the synthesized KNN solid particles where spherical/cubical in shape.

In summary, the theoretical based experimental approach helped to analyze the kinetics behind reaction mechanism of calcined KNN nanopowders through various derived solid state models. Solid state kinetics tool helped in achieving completion of the reaction mechanism successfully without non-stoichiometric phases, there by leading for betterment of piezoelectric properties.

## References


[1]. Kim H, Tadesse Y, Priya S, In: Priya S, Inman DJ (eds).Piezoelectric energy harvesting, energy harvesting technologies. Springer, New York, 2009, p. 3–39.

[2]. Priya S, Advances in energy harvesting using low profile piezoelectric transducers, J Electroceram, 2007,19,pp167–184.

[3]. Hollenstein E, Damjanovic D, Setter N. Temperaturestability of thepiezoelectricproperties of Li-modified KNNceramics. J. Eur Ceram Soc 27,2007,13(15),p.4093–4097.

[4]. Park S-E, Shrout TR .Ultrahigh strain and piezoelectric behaviour in relaxor based ferroelectric single crystals. J Appl Phys 1997, 82(4),p1804–1811.

[5]. Herklotz Aet al. Electrical characterization of PMN–28%PT(001) crystals used as thin film substrates. J Appl Phys 2010,108(9).p.094-101.

[6]. Ahn C Wet.al. Effect of elemental diffusion on temperature coefficient of piezoelectric properties in KNN-based lead-free composites. J Mater Sci Lett,(2010), 45(14).p.3961–3965.

[7]. Bomlai P et al. Effect of calcination conditions and excess alkali carbonate on the phase formation and particle morphology of $(Na_{0.5}K_{0.5})NbO_3$ powders. J Am Ceram Soc 2007, 90(5),p.1650–1655.

[8]. J. L. Zhang, X. J. Zong , y. Gao , y. L. Qing , M. L. Zhao , C. L. Wang. Recent study progresses of (K, Na)NbO3-based lead-free piezoelectric ceramics., J. of Optoelectronics and advanced mate 2010, 12( 9), p. 1921 - 1925.

[9]. E.K.Akdogan, K.Kerman, M.Abazari, A.Safari Origin of high piezoelectric activity in ferroelectric $(K_{0.44}Na_{0.52}Li_{0.04})$-$(Nb_{0.84}Ta_{0.1}Sb_{0.06})O_3$ceramics. Applied Physics Letters 2008,92(11 ),p.2908.

[10]. J. Fu, R. Z. Zuo, X.H.Wang, L.T.Li, Phase transition and domain variation contributions to piezoelectric properties of alkaline niobate based lead-free systems. J.Mater. Sci. 21 ,2010 ,p.519-522.

[11]. Bomlai P et al. Effect of calcination conditions and excess alkali carbonate on the phase formation and particle morphology of Na0.5K0.5NbO3 powders. J Am Ceram Soc .2007,90(5),p.1650–1655

[12]. Skidmore TA,Milne SJ.Phasedevelopment during mixed-oxide processing of $a[(Na_{0.5}K_{0.5})NbO_3]_{1-x}[LiTaO_3]_x$ powder. J Mater Res 2007, 22(08):2265–2272 .

[13]. Wang Y et al. Compositional Inhomogeneity in Li- and Ta-Modified (K, Na)$NbO_3$Ceramics.J.Am Ceram. Soc., 2007,90(11),p.3485–3489.

[14]. L.A.Perez-Maqueds, J.M.Criado, P, E, Sanchez-Jimenez, Combined kinetic analysis of solid state reactions: A powerful tool for the simultaneous determination of Kinetic parameters and the kinetic model without previous assumptions on the reaction mechanism., J.Phys.Chem.A, 2006, 110,p.12456-12462.

[15]. Jeri Malek. Kinetic analysis of crystallization process in amorphous materials, thermo chima acta.,2000, 335,p 239-253.

[16]. Burnhnam, A.K.,Weese, R.K.,Weeks.A distributed activation energy model of thermodynamically inhibited nucleation and growth reactions and its application to the β-δ phase transition of HMX. B.L.J. Phys. Chem. B. 2004,108,p.19432-19441.

[17]. Jason Graetz, J. J. Reilly, Decomposition Kinetics of the AlH 3 Polymorphs,The Journal of Physical Chemistry B, 2006,109(47),p.22181-5.
[18]. Wang,S. Gao, Q.Y, Wang. Thermodynamic analysis of decomposition of thiourea and thiourea oxides. J.C. J.Phys.Chem.B,2005,109,p.17281.
[19]. Wu C, Wang P, Yao X, Liu C, Chen D, Lu GQ, Cheng H, Effects of SWNT and metallic catalyst on hydrogen absorption/desorption performance of MgH2. J Phys Chem. B. 2005 ,109(47),p.22217-21.
[20]. Peterson,V.K., Neumann,D.A, Livingston,R.A. Hydration of tricalcium and dicalcium silicate mixtures studied using quasielastic neutron scattering. J. Phys. Chem. B .,2005,109, p.14449.
[21]. Khawam, A, Flanagan, D.R. Complementary use of model-free and modelistic methods in the analysis of solid-state kinetics. J.Phys.Chem.B.2005, 109, p.10073
[22]. Peter J. Skrdla , Rebecca T. Robertson., Semi-empirical Equations for Modelling Solid-State Kinetics Based on a Maxwell−Boltzmann Distribution of Activation Energies: Applications to a Polymorphic Transformation under Crystallization Slurry Conditions and to the Thermal Decomposition of $AgMnO_4$ Crystals. *J. Phys. Chem. B*2005, *109* (21), p.10611–10619.
[23]. Wyandt, C.M, Flanagan, D.R. Solid-state non-isothermal kinetics of sulfonamide-ammonia adduct desolvation. Thermochim. Acta 1992, 109, p. 379.
[24]. J.E. House Jr., Randal W. Eveland. Kinetic Studies on the Dehydration of Calcium Oxalate Monohydrate. J. Solid state Chem,1993,105(1) p.136-142.
[25]. Joakim Riikonen, Mikko Salomaki, Jessica van Wonderen, Marianna Kemell, Wujun Xu, Ossi Korhonen, Mikko Ritala, Fraser MacMillan, Jarno Salonen, Vesa-Pekka Lehto. Surface Chemistry, Reactivity, and Pore Structure of Porous Silicon Oxidized by Various Methods.J.ACS.pub.2012, *28* (28), p.10573–10583.
[26]. Carniti, P, Gervasini, A, Bennici, S. Experimental and modelization approach in the study of acid-site energy distribution by base desorption. Part I: modified silica surfaces. J. Phys. Chem. B 2005,109,p15-28.
[27]. Sestak,J.Berggren, G.study of the kinetics of the mechanism of solid state reactions at increasing temperatures., Thermochim. Acta 1971, 3, 1.
[28]. Haibo Yang, Ying Lin, Jianfeng Zhu, Fen Wang, An efficient approach for direct synthesis of $(K_{0.5}Na_{0.5})NbO_3$ powders. Powder Technology ,2009,196,p.233-236.
[29]. L.A.Perez-Maqueda,J.M.Criado,J.Malek, Combined kinetic analysis for crystallization kinetics of non-crystalline solids. J.Non-Crystalline Solids ,2003,320,p.84-91.
[30]. Sergey vyazovkin ,Wolfgang linert, Kinetic analysis of reversible thermal decomposition of solids. Int.J.Chem.Kinetics 1995,27(1),p73-84.
[31]. Chirsty M.Wyandt, Douglas R. Flanagan, Solid -state non isothermal kinetics of sulphonamide-ammonia adduct desolvation. Thermochimica Acta, 1992, 196(2),p379-389.

# Influence of Mwcnt's/Zinc Oxide Nano Particles/Epoxy Resin Composite Coating on Mild Steel to Enhance Anticorrosion and Mechanical Properties

**Sandeep.V.Gujjar, Nandini R Nadar, Kanaram Choudhary, Anand. M. Hunashyal**

***Abstract:*** ***The motive of this research is to develop a new hybrid Nano composite on the surface of mild steel to eradicate the rate of corrosion that takes place on the surface of the mild steel and to enhance mechanical properties. For this, a hybrid Nano composite of Multi-Walled Carbon Nano Tube's (MWCNT's), Zinc Oxide (ZnO) Nano particles and Epoxy resin has been used to overcome the major disadvantage of mild steel which is corrosion. The mechanical property of mild steel is also increased. Ultra-sonication method is adopted for better dispersion of ZnO Nano particles and MWCNT's. In this study, Ethanol is used for better dispersion. After applying the coating on the surface of newly developed Nano composite by using pneumatic gun spray method is used. FESEM was conducted to study the surface morphology of corroded surface of mild steel. The rate of anticorrosion and mechanical properties get improved by the application MWCNT's/ZO Nano particles/Epoxy resin.***

***Keywords: MWCNT's, Zinc Oxide Nano particles, Epoxy Resin, Anticorrosion, Mechanical Properties.***

## I. INTRODUCTION

The Coating industry is growing rapidly around the globe. Today, coating not only helps for beautification of structure but also protects the valuable metals and buildings from corrosion. Application of nanotechnology in the field of coating can improve upon the coating industry. Properties like corrosion resistance, flame resistance, UV stability, gloss retention, chemical and mechanical properties are enhanced by making use of nanoparticles. The main merits of using Nano-coating are: (1) Provides better surface appearance, (2) Offers good resistance to chemicals, (3) Increases thermal stability, (4) Surface is easy to clean, (5) Has anti-fogging, anti-graffiti, anti-skid, and anti-fouling properties, (6) Improves electrical and thermal conductivity, (7) It is anti-reflective in nature, (8) It is Lead and chromate free, and (9) Has good adherence.

**Revised Manuscript Received on March 30, 2020.**

**Sandeep.V.Gujjar,** Assistant Professor, Department of Civil Engineering, Pillai HOC College of Engineering and Technology, Rasayani, Dist. Raigad - 410207, Maharashtra, India.

**Dr. Nandini R Nada**r, Assistant Professor, Department of Mechanical Engineering, B.M.S.Institute of Technology and management, Bangalore-64, Karnataka, India.

**Kanaram Chaudhary**, Civil and infrastructure engineering from Rustomjee Academy for Global Careers, Dahanu road (E) - 401602, Maharashtra, India

**Dr. Anand. M. Hunashya**l, Associate Professor, Department of Civil Engineering, Visvesvaraya Technological University, KLE Institute of Technology, Hubballi-580021, Karnataka, India.

The anti-corrosion hybrid coatings provide a very effective method to protect the element against corrosion. There are various types of corrosion resistant coatings available such as urethanes, latexes, epoxies, and silicone alkyd. Two major mechanisms are accountable for the breakdown of coating protection, namely, diffusion of water through the coating and dis-bond propagation between the coating and the substrate (Aglan, Allie, et al. 2007). Corrosion is degradation of materials' properties due to chemical reaction with the environment, and corrosion of most metals is unavoidable. While primarily associated with metallic materials, all types of materials are susceptible to degradation. Approaches convenient for controlling corrosion include: Application of protective coatings to metal surfaces to act as a barrier and perhaps provide votive protection, the addition of chemical species to the environment to inhibit corrosion, alteration of alloy chemistry to enhance the resistance to corrosion, and the treatment of the surface of a metal to increase its resistance to corrosion (Shaw and Kelly 2006).

Multi-Walled Carbon Nanotubes, invented by Iijima and Ichihashi, have attracted considerable interest due to their application in fabricating a new classes of advanced materials owing to their distinctive structural, mechanical and electronic properties. MWCNTs possess good mechanical properties. The tensile strength of carbon nanotubes is about 100 times greater than that of steel of the same diameter. Two factors account for this strength. The first is the strength dispensed by the interlocking carbon-to-carbon covalent bonds. The second is the fact that each carbon nanotubes is one large molecule (Yeole, Mahajan et al. 2015).

Zinc oxide (ZnO) forms colour-less hexagonal crystals or a white dusty powder. When heated, the colour changes into lemon yellow. It reverts into white again when cooled down. Zinc oxide has a density of 5.61 g/cm³. It evaporates at 1300 °C and above and sublimates as it reaches a temperature of 1800 °C. Hence, there is no (liquid) melt but a direct transition from the solid into the gaseous aggregate state. ZnO nanoparticles have attracted great attention because of their unique catalytic, electrical, electronic and optical properties as well as their low cost and vast applications in different areas (He 2004).

Epoxy resin is the most popular material in the world for anti-corrosive coating of materials. This type of materials has high resistance to chemicals and possesses attrition resistance. Epoxy resin has good mechanical properties and electrical properties, and also offers resistance against chemical and atmospheric attacks (Dunn 1959).

## II. EXPERIMENTAL PROGRAM

### 1.1 Materials:

Materials required are Multi-walled carbon nanotube's (MWCNT's), Zinc Oxide Nano particles (ZO), Epoxy resin (E) (Fine coat EP 200/A) and hardener (Fine coat EP 200/B), Mild steel, Thinner (Thinner-643), Ethanol, etc.

Multi-Walled Carbon Nano Tubes were prepared by CVD method. Epoxy resin (FINECOAT- EP 200A & EP 200B) is a two- component epoxy clear lacquer, cured with polyamide hardener. It cures at room temperature (above 10$^{o}$C). Multi- Walled Carbon Nano Tube's (MWCNT's) and Zinc Oxide Nano particle's (ZO) as shown in Figure.1 and 2 were purchased from "Platonic Nanotech private limited," Jharkhand, India.

Epoxy resin was purchased from the "Fine Finesh Organics Pvt.Ltd" (ISO 9001- 2008 certified company) Taloja, Navi Mumbai, India. Pneumatic spray gun was purchased from, "Burhani hardware", Dahanu road, Palghar dist., India. Mild steel was brought from "Shubh M. L. Shah and Sons Steel Pvt. Ltd." Dahanu road, Mumbai, India.

The technical specifications of Multi -Walled Carbon Nano Tubes (MWCNT's), Zinc Oxide Nano particles (ZO) and Epoxy resin are mentioned below in Table. No.1, 2, and 3 respectively.


**Figure.1. Multi-Walled Carbon Nano-Tube's (MWCNT's)**


**Figure.2. Zinc Oxide Nano Particles (ZO)**

**Table.1.Technical specification of Multi-Walled Carbon Nano-Tube's (MWCNT's)**

| Sl. No. | Specifications | Value |
|---|---|---|
| 1. | Tensile Strength | 30 ~ 180GPa (100 times of metal) |
| 2. | Thermal Conductivity | 6,000W/m·k (2 times of that of diamond) |
| 3. | Electric Conductivity | 6,000S/cm (1,000 times of that of copper wire) |
| 4. | Modulus | 1 ~ 2TPa (7 times of that of metal) |
| 5. | Diameter | 10 ~ 15 nm |
| 6. | Length | 2-10 microns |

| | | |
|---|---|---|
| 7. | Purity | >99 % |
| 8. | Ash content | ＜.01 % |
| 9. | Fe | <4000 mg/kg |
| 10. | Al | <3500 mg/kg |
| 11. | Mo | <800 mg/kg |
| 12. | Specific Surface Area | 250 ~ 270 $m^2/g$ |
| 13. | Bulk Density | 0.06 ~ 0.09 $g/cm^3$ |
| 14. | Physical Form | Fluffy, Very Light Powder |
| 15. | Color | Black |
| 16. | Chemical Formula | C |

**Table.2.Technical specification of Zinc Oxide Nano Particles (ZO)**

| Sl. No. | Specifications | Value |
|---|---|---|
| 1. | Purity | 99.90% |
| 2. | Average Particle Size | 30-50 nm |
| 3. | Specific Surface Area | 20-60 $m^2/g$ |
| 4. | Molecular Weight | 81.408g/mol |
| 5. | Bulk Density | 0.28-0.48 $g/cm^3$ |
| 6. | True Density | 6 $g/cm^3$ |
| 7. | Morphology | Spherical |
| 8. | Molecular Formula | ZnO |
| 9. | Physical form | Powder |
| 10 | Color | Milky White |
| 11. | ZnO | >99.9% |
| 12. | Pb | <0.01% |
| 13. | Si | <0.02% |
| 14. | Mn | <0.02% |
| 15. | Cu | <0.01% |

**Table.3.Technical specifications of epoxy resin**

| Sl. No. | Characteristic | Specifications |
|---|---|---|
| 1. | Colour | Clear. Can be dyed as per the requirement |
| 2. | Finish | Glossy |
| 3. | Mixing Ratio | Base : Hardener = 2 : 1 (by volume) |
| 4. | Pot life | 14 - 16 Hours @30°C |
| 5. | Theoretical covering capacity | 12 sq.m. /lit @25 microns dft. |
| 6. | Application method | Air-assisted / airless spray / brush |

### 1.2 Preparation of Multi-Walled Carbon Nano Tube's/Zinc Oxide Nano Particles:

The composite materials i.e. MWCNTs / ZO are prepared by blending various proportions of MWCNT's (0.25%, 0.5%, 0.75% and 1% by weight of resin) and ZO (2%, 4%, 6% and 8% by weight of resin). For dispersion, both the Nano materials are Ultra-sonicated individually in ethyle alcohol (40% weight of resin) for 30 minutes as shown in Figure.5. Then, the materials are combined together for additional ultrasonication for another 30 min. After the ultra-sanitation is completed, the composite was mixed for 30 minutes at 50ºC temperature by means of the magnetic stirrer to generate MWCNTs / ZO hybrid Nano composite.

**Figure.5. Ultra sonication process of MWCNT's and SiO**

### 1.3 Preparation of MWCNT's/ZO/E Composite coating:

For development of Nano composite coating, primarily, Epoxy resin (E) (Fine coat EP 200/A) of 10 g is added and mixed for an hour and then it is degassed for 20 min under the process of Ultra-sonicator. The detail regarding MWCNTs/ZO/E composite materials with various ratios is specified in Table.4. Then, hardener (Fine coat EP 200/B) is further added in MWCNTs / ZO/ E, and the composite is mixed by magnetic stirrer for 5 minutes along with the thinner. The prepared MWCNTs / ZO / E Nano composite coating was then sprayed by using pneumatic spray gun on the surface of the mild steel. The distance between the sample and spraying gun is kept at about 100 mm to 150 mm and the thickness of coating is about 120 micron to150 µm. After the coating was applied to the surface of mild steel, the samples were dried for 48 hours at room temperature, and then the sample were kept in the oven at 150 ºC for one hour. The samples of mild steel coated with Nano composite were kept underwater containing 3.5% NaCl for 14 days (336 Hours).Corrosion rate is determined and then it is again subjected to Salt Spray Method (ASTM B-117:2016) at 34.8 to 35.1 degree centigrade, 5% NaCl, salt type. AR grade was conducted for 3 days (72 Hours) to find out the corrosion rate by the percentage of weight loss.

Samples with the same combinations were also made for testing the tensile strength Test. The specimens were tested by using fully computerized Servo Hydraulic Universal Testing Machine facility – AGIS 250kN in which Yield stress, Gauge length, Final length, Initial area, Gauge diameter, Elongation percentage, Ultimate load, initial and final thickness, yield load, Ultimate tensile Strength, and Fracture are evaluated. The scratch hardness test was also conducted to evaluate the surface hardness of the specimens.

**Table.4. Detail of MWCNT's/ZO/E coating specimens**

| Sl. No. | Specimen Reference | Constituents | % of MWCNT's by Weight of Resins | % of Silicon oxide Nano Particles by Weight of Resins | Epoxy Resin(E) (gm.) |
|---|---|---|---|---|---|
| 1 | PMS | Plain Mild Steel | Nil | Nil | Nil |
| 2 | E | Epoxy | Nil | Nil | 10 g |
| 3 | MZE 1 | MWCNT's+ZO+E | 0.25% | 2% | 10 g |
| 4 | MZE 2 | MWCNT's+ZO+E | 0.50% | 4% | 10 g |
| 5 | MZE 3 | MWCNT's+ZO+E | 0.75% | 6% | 10 g |
| 6 | MZE 4 | MWCNT's+ZO+E | 1.00% | 8% | 10 g |

### 1.4 Preparation of mild steel surface

The Mild Steel specimen with 12mm diameter bar is cut to a span of 300mm (Figure.4) for Tensile test and flat specimen having (125 x 60 x 6) mm (Figure.4) for Scratch hardness test was sand blasted with Sanding paper P80 on the surface of Mild Steel and washed by acetone to clean and remove oxides present on surface of mild steel. Then, the specimen is allowed for drying by exposing to room temperature for more than an hour before application of resin coating. After the coating on mild steel specimen was dried for 48 hours at the room temperature, the specimens were kept in the oven at $150^0$ C for one hour.

The prepared MWCNT's/ZO/E Nano composites of different ratios were sprayed by pneumatic spray gun on surface of mild steel. The distance between the spraying gun and the specimen is kept at about 100-150 mm and the thickness of coating was 160-180µm.

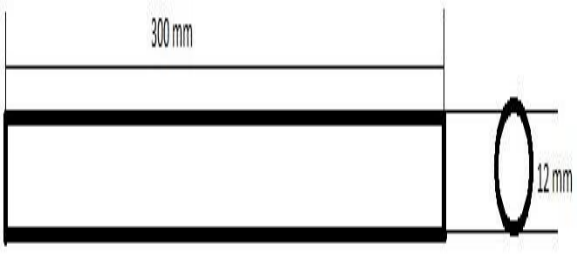


**Figure.3. Tensile and Salt Spray test specimen**

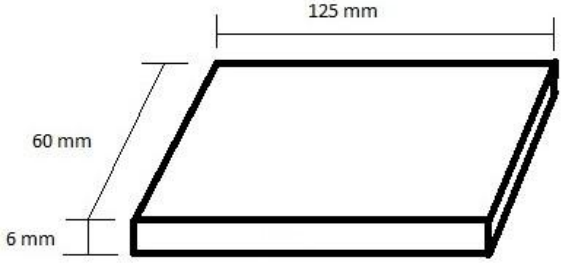


**Figure.4. Specimen sample after hardness test**

**2.4 FESEM studies** were done to study the corrosion external morphology of mild steel covered with MWCNT's/Silicon Oxide Nano Particles/Epoxy Resin coating with different combinations by field emission scanning electron microscope (FESEM). The corrosion surface is studied by gold coating to evade any charging and then images were captured at dissimilar magnification. The corroded surface using FESEM operated at an accelerating voltage of 20 kV.

### 1.5 Corrosion Analysis

### 1.6 Immersion Test:

The corrosion resistance properties of MWCNTs/Zinc Oxide Nano Particles/Epoxy Resin coated on the mild steel was were analyzed by immersion of samples. The samples were immersed in the distilled water containing 3.5% NaCl for 336 hours and corrosion rate was determined by weighing technique. The weight of the sample with resins coated is measured before and after immersion in the above

mentioned solution to determine the rate of corrosion.

### 1.7 Salt Spray Test (ASTM B117):

In addition Corrosion resistance of mild steel coated with the MWCNTs/Zinc Oxide Nano Particles/Epoxy Resin was evaluated by means of the standard Salt Spray (Fog) test method as per ASTM B117:2016. In this examination, the mild steel specimens coated by the resins were kept at constant temperature where the specimens were open to the fine spray of salt solution having 5 percent for a definite period, and washed in water and dried. The extent of corrosion of test parts can be expressed as percent of red rust.

### 1.8 Mechanical Properties

### 1.9 Tensile Strength Test (A370:2017)

The effect of MWCNTs/Zinc Oxide Nano Particles/Epoxy Resin coated on the external surface of mild steel was studied by tensile test method on Universal Testing Machine (A370:2017). The Ultimate Tensile Strength, Yield load, Ultimate Load, Yield stress were evaluated in this experiment.

### 1.10 Scratch Hardness Test:

Scratch Hardness test was conducted on the flat plain mild steel sample having 120 mm length, 60 mm breadth and 6 mm thickness. Scratch Hardness testing method is conducted according to IS 101(Part-5, Sec.2):1988. The minimum load to cause failure is noted as the Hardness of the hybrid Nano coating.

## III. RESULTS AND DISCUSSIONS

### 1.11 Corrosion properties of MWCNT's/ZO Nano Particles/Epoxy Resin coating:

The corrosion resistance properties of MWCNTs/Zinc Oxide Nano Particles/Epoxy Resin coated mild steel samples were studied by immersion method. The samples were immersed in the distilled water containing 3.5% NaCl for 336 hours by weighing method. This method was carried out to determine the percentage of loss of weight and then corrosion analysis was continued by using salt spray method for 72 hours in which the percentage of weight loss was yet again calculated. The total percentage of weight loss was considered by collective addition of both the methods mentioned above. The Comparison of corrosion protection by MWCNTs/ZO /E composite with neat Epoxy coated sample and plain mild steel in %, is shown in Figure.6 for only immersion test and Figure.7 for both immersion and salt spray test.

The samples having Epoxy resin before and after the corrosion indicates the highest percentage of protection of mild steel samples from corrosion with 65.29 %. Whereas MZE-1 indicates the second highest value about 32.57% as shown in Figure.13 and 14 before and after the corrosion respectively. The MZE-3, MZE-2 and MZE-4 show 16.28%, 12.63%, and 8.06% of anti corrosion respectively compared to plain mild steel sample without coating shown in Figure.16 and 17 (before and after corrosion). The percentage of protection by Nano composite against corrosion is mentioned in Table.5. (Immersion test) and Table.6. (Immersion and salt spray test).

**Table.5. % of protection by coating against corrosion by immersion test**

| Sl. No. | Specimen | % of protection by resin against corrosion after 336 hours (Immersion test) |
|---|---|---|
| 1 | PMS | 0 |
| 2 | E | 96.95 |
| 3 | MZE 1 | 61.79 |
| 4 | MZE 2 | 45.96 |
| 5 | MZE 3 | 49.77 |
| 6 | MZE 4 | 44.14 |

**Table.6. % of protection by coating against corrosion by immersion test and Salt Spray Test**

| Sl. No. | Specimen | % of protection by resin against corrosion after 408 hours (Immersion and Salt Spray Test) |
|---|---|---|
| 1 | PMS | 0 |
| 2 | E | 65.29 |
| 3 | MZE 1 | 32.57 |
| 4 | MZE 2 | 12.63 |
| 5 | MZE 3 | 16.28 |
| 6 | MZE 4 | 8.06 |

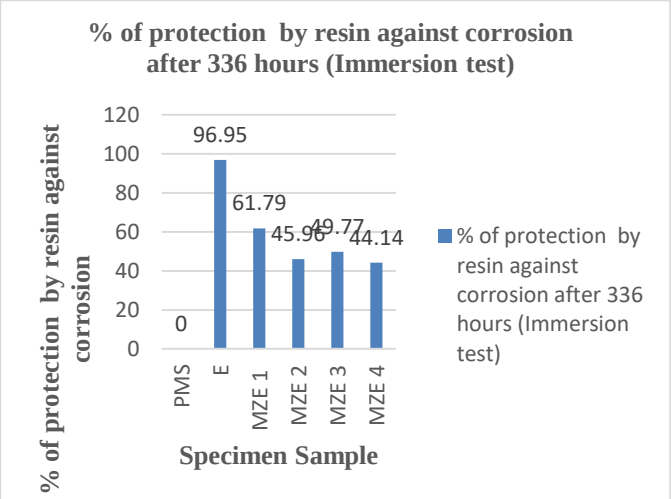


**Figure. 6. Comparison of corrosion protection by MWCNT's/ZO/E in % by immersion test.**

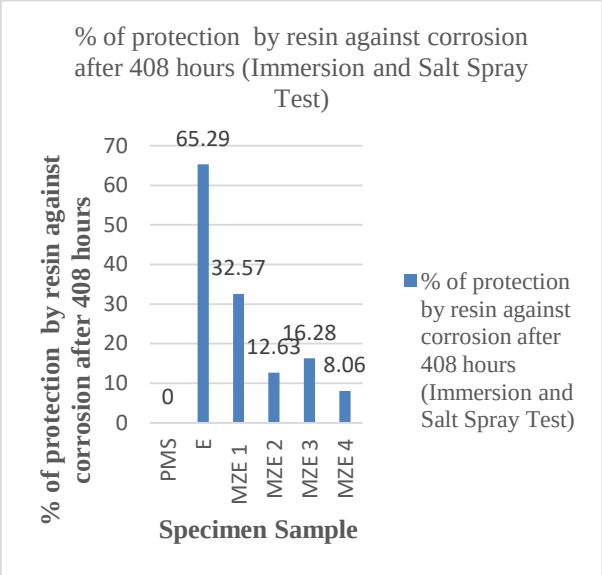


**Figure. 7. Comparison of corrosion protection by MWCNT's/ZO/E in % by immersion and salt spray test.**

### 1.12Mechanical Properties

#### 1.12.1 Tensile Strength Test (A370:2017):

The effect of Nano composite coated on surface of mild steel was studied by tensile test method on Universal Testing Machine. The Ultimate Tensile Strength test results and percentage increase in Ultimate Tensile Strength of plain mild steel, neat Epoxy resin, MZE-1, MZE-2, MZE-3 and MZE-4 coated samples are given in table no.7 and no.8. The standard deviation of Ultimate Tensile Strength and Percentage increase in Ultimate Tensile Strength are shown in Fig.8 and Fig.9.

The samples having MZE-1 coated samples show the maximum Ultimate Tensile Strength with 585.08 N/mm$^2$, Whereas neat Epoxy resin coated samples have 505.82 N/mm$^2$, MZE-4 have 491.11 N/mm$^2$, MZE-3 with 485.21 N/mm$^2$, MZE-2 with 479.58N/mm$^2$ and Plain mild steel have the least Ultimate Tensile Strength value of 456.23 N/mm$^2$ as shown in Figure.8.

The samples having MZE-1 shows the maximum percentage of increase in Ultimate Tensile Strength compared to mild steel samples with 22.02 %. Whereas neat Epoxy coated sample with 9.8 %, MZE-4 have 7.1 %, MZE-3 have 5.97% and the MZE-2 with least 4.86% increase in Ultimate Tensile Strength compared to mild steel samples without coating as shown in Fig.8.

**Table.7.Ultimate Tensile Strength (N/mm$^2$)**

| Sl. No. | Specimen Reference | Ultimate Tensile strength (KN/mm$^2$) |
|---|---|---|
| 1 | PMS | 456.23 |
| 2 | E | 505.82 |
| 3 | MZE 1 | 585.08 |
| 4 | MZE 2 | 479.58 |
| 5 | MZE 3 | 485.21 |
| 6 | MZE 4 | 491.11 |

**Table.8. % increase in Ultimate Tensile Strength**

| Sl. No. | Specimen Reference | % increase in Ultimate Tensile Strength |
|---|---|---|
| 1 | PMS | 0 |
| 2 | E | 9.8 |
| 3 | MZE 1 | 22.02 |
| 4 | MZE 2 | 4.86 |
| 5 | MZE 3 | 5.97 |
| 6 | MZE 4 | 7.1 |

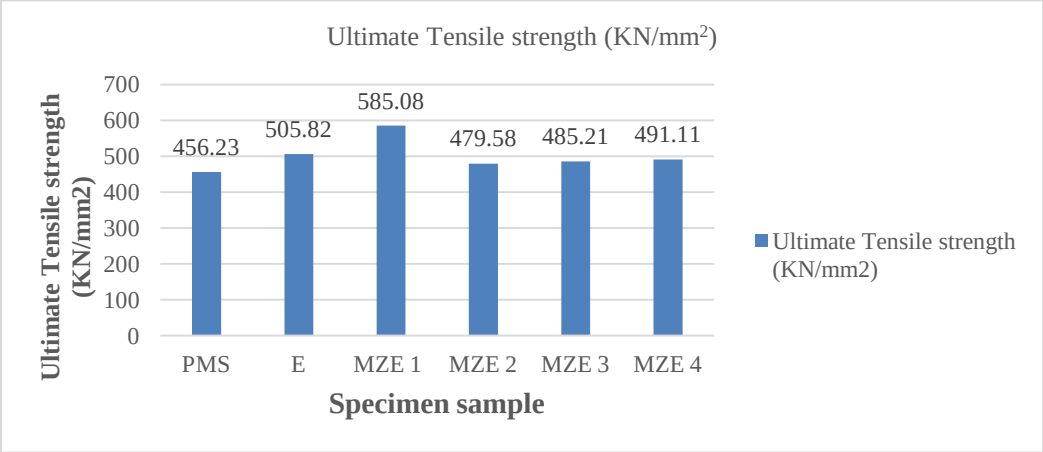


**Figure.8. Ultimate Tensile Strength (N/mm$^2$)**

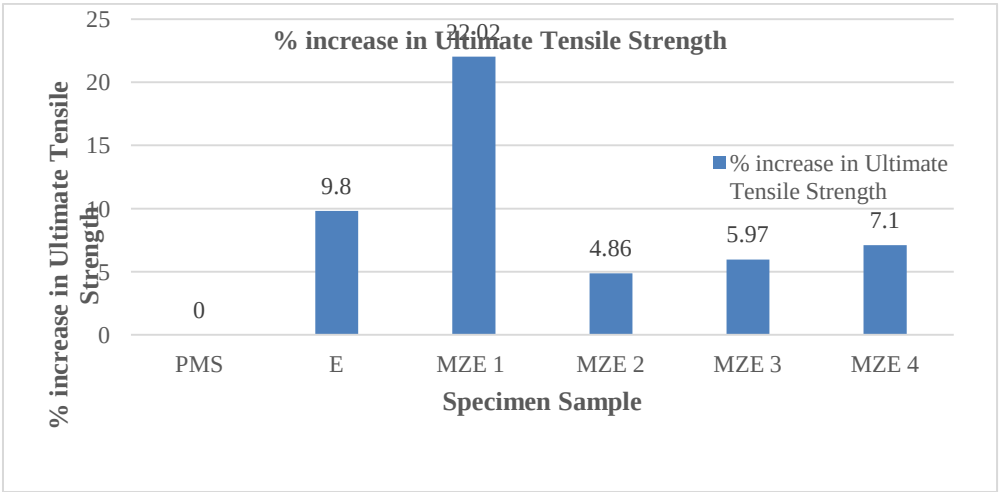


**Figure.9. % increase in Ultimate Tensile Strength**

### 1.12.2 Scratch Hardness Test:

The least load to cause failure is distinguished as the Scratch Hardness of the hybrid Nano composite coating. Scratch Hardness with standard deviation with Epoxy resin and MZE-1 coated mild steel samples are as shown in Fig.10. Neat Epoxy coated sample shows the maximum hardness with 700 mg, and MZE-1 coated sample with 500 mg. The scratch hardness values of the neat Epoxy and MZE-1 Nano composite coated surface values are as given in Table.No.9.

**Table.9. Scratch Hardness (in mg)**

| Sl. No. | Specimen | Scratch Hardness (in mg) |
|---|---|---|
| 1 | EPOXY | 700.00 |
| 2 | MZE1 | 500.00 |

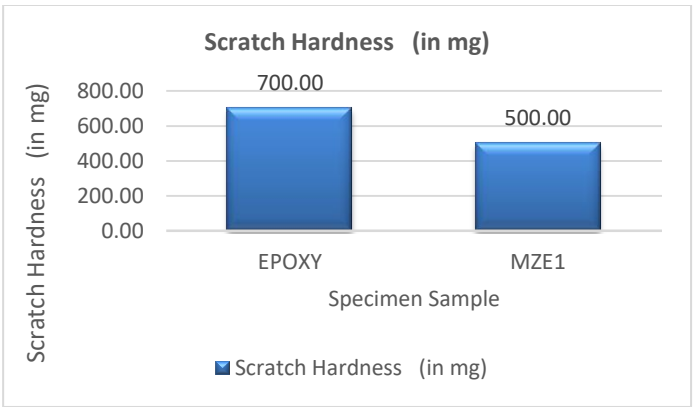


**Figure.10. Scratch Hardness with standard deviation with Epoxy resin and MZE-1 coated mild steel samples.**

### 1.13Morphology

Figure.11 and 12 display the images of FESEM of Neat Epoxy resin coated samples before and after subjecting to corrosion. Figure.12 displays the corrosion products formed on the mild steel surface. Figure.13 and 14 are the images of MZE-1 coated samples. Figure.14 shows MZE-1 coated samples with protection of the mild steel surface with least rust with 32.57 % corrosion protection on its surface when compared to other ratios of Nano composite coating.

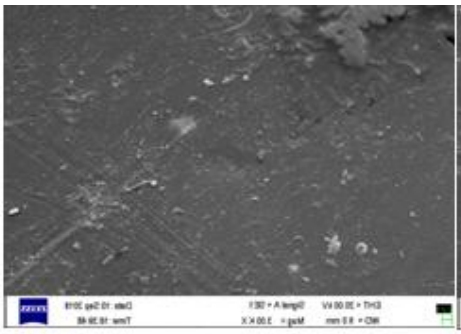

Figure.11.FESEM image of sample coated with Epoxy Resin before corrosion

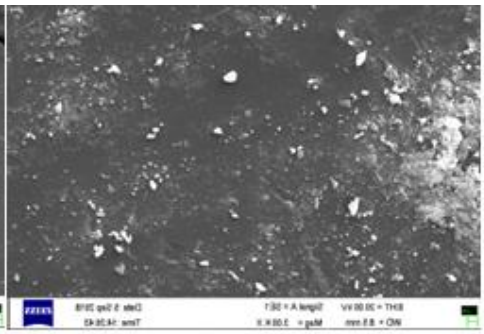

Figure.12.FESEM image of sample coated with Epoxy Resin after corrosion

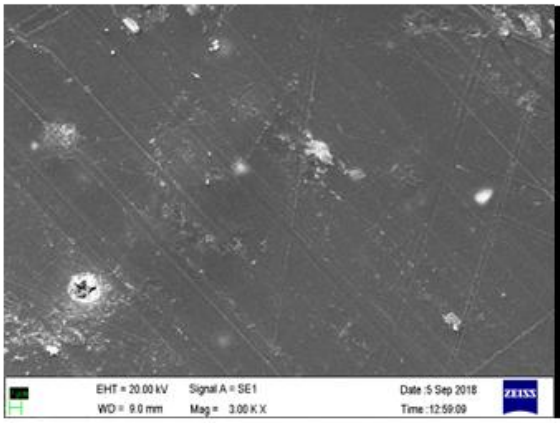


Figure.13.FESEM image of sample coated with MWCNT's/ZO/E (MZE1) Nano composite before corrosion

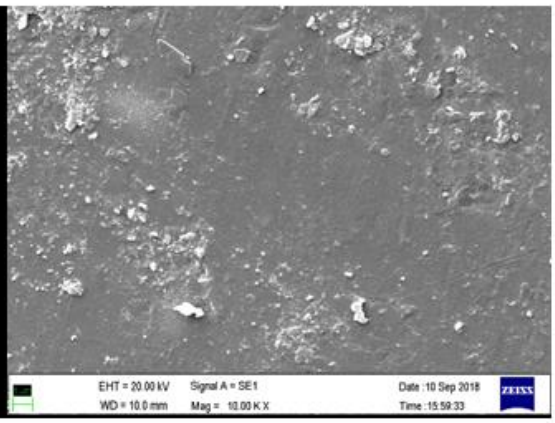


Figure.14.FESEM image of sample coated with MWCNT's/ZO/E (MZE1) Nano composite after corrosion

It is clearly seen that the mild steel samples coated with the Neat Epoxy resin (Figure.12) show the lowest corrosion products compared to MZE-1 Nano composite coated samples as per Figure.14.

## IV. CONCLUSIONS:

The MWCNTs / ZO/ E (MSE1) Nano composites having 2% of ZO and 0.25% of MWCNT's indicate the upgraded properties as compared the plain mild steel , neat Epoxy and different proportions of MWCNT's and ZO. The superior properties include anticorrosion, Ultimate Tensile Strength and scratch hardness. The results from the test of MZE-1show 32.57% of anti-corrosiveness property, which is noted to be second maximum value. Scratch hardness property noted was 500 mg which is also the second highest value when compared to the neat Epoxy samples, the Ultimate Tensile Strength recorded was 585.08 $N/mm^2$ which is the highest value and the existence of Epoxy resin, Nano ZO and MWCNT's particles specifies that the increased mechanical properties as well as anti-corrosion properties when compared to the samples with Neat Epoxy and plain mild steel. Hence, it was concluded that the combination of 0.25% of MWCNT's, 2% of ZO with respect to weight of Epoxy resin used is an ideal combination for both anticorrosion and mechanical property. There is a wide scope for the study of mechanical and anticorrosion properties of mild steel with the combination of MWCNT's / ZO/ E with new practices of dispersion, deviation in percentages used, with upgraded properties of MWCNT's, ZO and Epoxy Resin.

## ACKNOWLEDGEMENT:

The authors are highly thankful to "Rustomjee Academy for Global Careers", Dahanu, Mumbai for providing financial support to carry out this experimental study. This work forms a part of Ph.D. Thesis work of Mr.Sandeep. V. Gujjar.

## REFERENCES:

1. Aglan, A., Allie, A., Ludwick, A. and Koons, L., (2007). Formulation and evaluation of nano-structured polymeric coatings for corrosion protection. *Surface and Coatings Technology*, ***202***(2), pp.370-378.
2. Yeole.K.V, Mahajan, L.H. and Mhaske, S.T., (2015). Poly(o-anisidine)-MWCNT nanocomposite: Synthesis, characterization and anticorrosion properties. *Polymer Composites*, ***36***(8), pp.1477-1485.
3. He, Y., (2004). Preparation of polyaniline/nano-ZnO composites via a novel Pickering emulsion route. *Powder Technology*, ***147***(1-3), pp.59-63.
4. Veleva, L., Chin, J. and Del Amo, B., (1999). Corrosion electrochemical behavior of epoxy anticorrosive paints based on zinc molybdenum phosphate and zinc oxide. *Progress in Organic Coatings*, ***36***(4), pp.211-216.
5. Ramezanzadeh, B., Attar, M.M. and Farzam, M., (2010). Effect of ZnO nanoparticles on the thermal and mechanical properties of epoxy-based nanocomposite. *Journal of thermal analysis and calorimetry*, ***103***(2), pp.731-739.
6. Ramezanzadeh, B. and Attar, M.M., (2011). Studying the effects of micro and nano sized ZnO particles on the corrosion resistance and deterioration behavior of an epoxy-polyamide coating on hot-dip

galvanized steel. *Progress in Organic Coatings*, ***71***(3), pp.314-328.
7. Valença, D.P., Alves, K.G.B., Melo, C.P.D. and Bouchonneau, N., (2015). Study of the efficiency of polypyrrole/ZnOnanocomposites as additives in anticorrosion coatings. *Materials Research*, ***18***, pp.273-278.
8. Yeole, K.V., Agarwal, I.P. and Mhaske, S.T., (2016). The effect of carbon nanotubes loaded with 2-mercaptobenzothiazole in epoxy-based coatings. *Journal of Coatings Technology and Research*, ***13***(1), pp.31-40.
9. Ramezanzadeh, B, Ahmadi, A & Mahdavian, M (2016) Enhancement of the corrosion protection performance and cathodic delamination resistance of epoxy coating through treatment of steel substrate by a novel nanometric sol-gel based silane composite film filled with functionalized graphene oxide nanosheets. *Corrosion Science*, **109** pp. 182-205.
10. Kumar, A., Ghosh, P.K., Yadav, K.L. and Kumar, K., (2017). Thermo-mechanical and anti-corrosiveproperties of MWCNT/epoxynanocomposite fabricated by innovative dispersion technique. *Composites Part B: Engineering*, ***113***, pp.291-299.
11. More, A.P. and Mhaske, S.T., (2016). Anticorrosive coating of polyesteramide resin by functionalized ZnO-Al2O3-Fly ash composite and functionalized multiwalled carbon nanotubes. *Progress in Organic Coatings*, ***99***, pp.240-250.
12. Guo, Y., Bao, C., Song, L., Yuan, B. and Hu, Y., (2011). In situ polymerization of graphene, graphite oxide, and functionalized graphite oxide into epoxy resin and comparison study of on-the-flame behavior. *Industrial & Engineering Chemistry Research*, ***50***(13), pp.7772-7783.
13. Park, S. and Shon, M., (2015). Effects of multi-walled carbon nano tubes on corrosion protection of zinc rich epoxy resin coating. *Journal of Industrial and Engineering Chemistry*, ***21***, pp.1258-1264.
14. He, Y., Fan, Y., Chen, C., Zhong, F. and Qing, D., (2015). Synthesis of mica-multiwalled carbon nanotube (MWCNT) hybrid material and properties of mica-MWCNT/epoxy composites coating research. *High Performance Polymers*, ***27***(2), pp.191-199.
15. Kumar, A.M. and Gasem, Z.M., (2015). In situ electrochemical synthesis of polyaniline/f-MWCNT nanocomposite coatings on mild steel for corrosion protection in 3.5% NaCl solution. *Progress in Organic Coatings*, ***78***, pp.387-394.
16. Sonawane, S.H., Bhanvase, B.A., Jamali, A.A., Dubey, S.K., Kale, S.S., Pinjari, D.V., Kulkarni, R.D., Gogate, P.R. and Pandit, A.B., (2012). Improved active anticorrosion coatings using layer-by-layer assembled ZnOnanocontainers with benzotriazole. *Chemical engineering journal*, ***189***, pp.464-472.
17. Ammar, S., Ramesh, K., Vengadaesvaran, B., Ramesh, S. and Arof, A.K., (2016). Amelioration of anticorrosion and hydrophobic properties of epoxy/PDMS composite coatings containing nanoZnO particles. *Progress in Organic Coatings*, ***92***, pp.54-65.
18. Yu, D., Wang, J., Tian, J., Xu, X., Dai, J. and Wang, X., (2013). Preparation and characterization of TiO2/ZnO composite coating on carbon steel surface and its anticorrosive behavior in seawater. *Composites Part B: Engineering*, ***46***, pp.135-144.
19. Lu, W.K., Elsenbaumer, R.L. and Wessling, B., (1995). Corrosion protection of mild steel by coatings containing polyaniline. *Synthetic Metals*, ***71***(1-3), pp.2163-2166.
20. Zheludkevich, M.L., Shchukin, D.G., Yasakau, K.A., Möhwald, H. and Ferreira, M.G., (2007). Anticorrosion coatings with self-healing effect based on nanocontainers impregnated with corrosion inhibitor. *Chemistry of Materials*, ***19***(3), pp.402-411.
21. Rahman, M. M., R. Suleiman and H. Do Kim (2017). "Effect of functionalized multiwalled carbon nanotubes on weather degradation and corrosion of waterborne polyurethane coatings." Korean Journal of Chemical Engineering 34(9): 2480-2487.

## AUTHOR'S PROFILE:

**Sandeep.V.Gujjar** is currently pursuing PhD from Visvesvaraya Technological University, Karnataka and working as an Assistant Professor in Department of Civil Engineering, Pillai HOC College of Engineering and Technology, Rasayani, Dist. Raigad - 410207, Maharashtra, India. He has published books related to civil engineering, research papers, filed patents related to nano composite coating which enhances mechanical and anticorrosive properties of mild steel. He has guided several students pursuing post graduate and under graduate students for research work in civil engineering. He has more than 11 years of teaching, industry and research experience in Indian and international organization. Ph: 8793169868, E-mail: sandeep.gujjar@rediffmail.com

**Dr. Nandini R Nadar** is currently working as an assistant Professor, Department of Mechanical Engineering, B.M.S.Institute of Technology and management, Bangalore-64, Karnataka, India. She has completed her P.hD in "Development of lead free piezo-electric materials for energy harvesting applications" from Visvesvaraya Technological University, Karnataka, India. She has published various research papers in mechanical engineering, filed patents related to nano composite. He is guiding several students pursuing post graduate and under graduate students for research work in material science and mechanical engineering. She has more than 12 years of teaching experience, 1year industrial and 1 year research experience. Ph: +91-9588922999, E-mail: nandini.nadar@bmsit.in

**Kanaram Chaudhary** is a graduate in Civil and infrastructure engineering from Rustomjee Academy for Global Careers, Dahanu road (E) - 401602, Maharashtra, India affiliated to University of Wolverhampton, UK. Ph: 7387165610, E-mail: kanaramchoudhary3@gmail.com

**Dr. Anand. M. Hunashyal** is presently working as an Associate Professor in the Department of Civil Engineering, Visvesvaraya Technological University, KLE Institute of Technology, Hubballi-580021, Karnataka, India. He has completed his P.hD from Visvesvaraya Technological University, Karnataka, India. He has published various research papers civil and mechanical engineering, filed and awarded patents related to nano composite coatings which enhance mechanical and anticorrosive properties of mild steel and many more. He is guiding several students pursuing doctorate, post graduate and under graduate students for research work in civil engineering. He has more than 20 years of teaching and research experience. Ph:9739192399, E-mail:amhunashyal@kletech.ac.in

# Evaluation Of Mechanical And Fracture Properties Of Nickel Coated Short Carbon Fiber/Epoxy Composites With Nanofillers

[1]Kiran M D, [1]H K Govindaraju, [2]Lokesh Yadhav B R
[1] BMS Institute of Technology and Management, Bengaluru 560064, India.
[2]R.L.Jalappa Institute of Technology, Doddaballapur, India.

**Abstract:**The objective of the present research article is to study the mechanical and fracture properties of epoxy polymer composites reinforced with nickel coated short carbon fiber with Aluminium oxide ($Al_2O_3$), Titanium dioxide ($TiO_2$) and Silica($SiO_2$) nano powder with different loading. The samples were prepared using open mould technique using a matrix and fiber weight ratio of 98:02. The nano fillers were mixed with epoxy using mechanical stirrer with particle loading of 2%, 4% and 6% of weight. Results of hybrid composites were evaluated with the tensile and impact strengths and fracture toughness andwhose results are mainly dependent on type of filler and filler loading. The addition of nano fillers enhances the cross-linking in the matrix and it leads to increase the mechanical properties and fracture toughness.Addition of 6% $Al_2O_3$with epoxy matrix enhanced the tensile strength by 25% and impact strength and fracture toughness by 77% and 103% respectively.
**Key words:** Titanium dioxide ($TiO_2$), Silica($SiO_2$), fracture toughness

## Introduction

Polymers and Polymers matrix composites have gained attention for various applications which include structural, automotive and aerospace [1-2]. Epoxy based polymer composites have significant importance in various engineering applications due to better mechanical electrical and thermalproperties[3].Due to ease processing and better mechanical properties, polymer composites reinforced with Short fibergained significant importance in engineering and structural applications [4-8]. Epoxy matrix composites shows the improvement in fracture toughness with addition of short fibers than the neat epoxy. Short carbon fiber reinforcement to epoxy matrix composites exhibits better fracture toughness than short glass fiber reinforcement [9-11]. Mechanical properties of fiber reinforced polymer composites will be contingent on adhesion between fiber and matrix since load carried by composites will be transferred through interface between matrix and fiber [12-14]. Both cryogenic and oxidative surface treatments significantly reduces the chemical inherent, upsurges the surface roughness and leads to enhancement in adhesion between fiber and matrix due to improvement in mechanical interlocking and it shows better mechanical properties [15]. Fibers are coated with copper, borax, nickel etc. using both electroless and electroplating coating processes with single or dual layer on carbon fiber surface. Carbon fibers coated with nickel using electroplating technique exhibits improved mechanical properties and resists the oxidization at high temperature applications [16-17].
The current research trend is to improve the mechanical properties by the addition of filler to the polymer matrix composites. The desired mechanical and fracture properties of polymer matrix composites have been achieved by the incorporation of various particulate fillers like aluminium oxide, silica, titanium dioxide, silicon carbidesince fillers have larger modulus and stiffness as related to matrix [18-23].Subsequently the mechanical and fracture properties of particulate filled polymer matrix composites mainly depends on particle size, distribution and particle loading with composite since it iscontingent with load transfer between matrix and filler [24].The Stiffness of composite is significantly better at size of particle is in nanoscale and below and is due to nano-effect which causes the more surface area of contact [25].
In the present research work, nano-sized aluminium oxide ($Al_2O_3$), titanium dioxide ($TiO_2$) and silica ($SiO_2$) particles have been mixedwith epoxy matrix. Nickel coated short carbon fiber(NC) used as reinforcement for modified resin. The mechanical properties and fracture toughness were evaluated for different composition under static loading condition. The details of fabrication procedure and evaluation of test results are described in the subsequent sections.



DOI: 10.5373/JARDCS/V12SP2/SP20201090
*Corresponding Author: Kiran M D, Email: kiranmdg@gmail.com
Article History: Received: Dec 08, 2020, Accepted: Mar 03, 2020

## Experimental Details

### 1. Materials and sample preparation:

The composite materials used in present research includes nickel coated short carbon fiber about 7µm diameter and 6mm length as reinforcement with matrix material epoxy Lapox L-12 with Triethylene Tetro amine (TETA) K6 curing hardener. Aluminum oxide, Titanium dioxide and silica particles are used as filler materials with size about 30 to 50µm which are supplied by Ultrananotech Pvt. Ltd, Bengaluru. The organo-reactive silane couplingagent was used to treat these fillers.Pre-calculated quantity of epoxy resin and nano filler were mixed using ultra-sonicator and after sonication 2 wt%of nickel coated carbon fiber were mixed with matrix using mechanical stirrer. The mixture was poured to mould and it was cured at room temperature for 24hours and after removing from mould, composite was post cured for 1hour at $110^0$ C and 2 hours at $140^0$ C using auto clave facility. Table 1 illustrates the designation and composition of epoxy and nano fillers in 2wt% nickel coated short carbon fiber used in the present research.

**Table 1** Composites fabricated for present work

| Composites (designation) | Epoxy (wt.%) | Al2O3 (wt.%) | $TiO_2$ (wt.%) | $SiO_2$ (wt.%) |
|---|---|---|---|---|
| NCE (NCE) | 98 | - | - | - |
| $Al_2O_3$ + NCE (NCE-2A) | 96 | 2 | - | - |
| $Al_2O_3$ + NCE (NCE-4A) | 94 | 4 | - | - |
| $Al_2O_3$ + NCE (NCE-6A) | 92 | 6 | - | - |
| $TiO_2$ + NCE (NCE-2T) | 96 | - | 2 | - |
| $TiO_2$ + NCE (NCE-4T) | 94 | - | 4 | - |
| $TiO_2$ + NCE (NCE-6T) | 92 | - | 6 | - |
| $SiO_2$ + NCE (NCE-2S) | 96 | - | - | 2 |
| $SiO_2$ + NCE (NCE-4S) | 94 | - | - | 4 |
| $SiO_2$ + NCE (NCE-6S) | 92 | - | - | 6 |

### 2. Determination of voids

Void fraction is a measurement of the void in a material and is a fraction of the volume of voids over the total volume. There are different ways to find the voids in the composites. In the present investigation for polymer composites the volume fraction of voids was found using theoretical and actual density of the composites.

*2.3Testing Procedure*

The tensile strength and tensile modulus of the NCE composites with and without nano fillers were found as per ASTM D-638 under displacement control of 5mm/min cross head speed. Impact strength of the composites were determined usingizord test methodaccording to ASTM D-256 using conventional V-notched specimen.And fracture toughness of the composites was tested using single edge notched beam method by determining critical-stress intensity factor $K_{IC}$ as per ASTM D5045-99. It involves three-point bending test of a notched specimenwith pre-crack as per standard.Water jet cutting method was used to cut the specimen as per ASTM standards.

## Results And Discussion

### 1. Density and volume fraction

Density of polymer matrix composites be contingent to the proportion of the matrix material and reinforcement materials. Theoretical density of the fabricated composite was determined using rule of mixture by considering weight fraction. Due to the presence voids in the fabricated composite density measured experimentally was slightly lesser than the theoretical density. The theoretical and experimentally measured densities and volume fraction of voids of NCE composites with and without nano fillers are listed in Table 2. The result shows very less volume fractions of voids which may due to the process used to fabricate these composites and $Al_2O_3$filled NCE composites are shows slightly higher volume fraction of voids compared to other composites.

**Table 2**Theoretical experimentally measured densities and volumefractionof voids of fabricated composites

| *Composites* | *Theoretical density ($g/cm^3$)* | *Theoretical density ($g/cm^3$)* | *Volume fraction of voids (%)* |
|---|---|---|---|
| NCE | 1.108 | 1.084 | 2.166 |
| NCE-2A | 1.126 | 1.092 | 3.019 |
| NCE-4A | 1.142 | 1.107 | 3.064 |
| NCE-6A | 1.159 | 1.128 | 2.674 |
| NCE-2T | 1.124 | 1.096 | 2.491 |
| NCE-4T | 1.141 | 1.106 | 3.067 |
| NCE-6T | 1.158 | 1.131 | 2.331 |
| NCE-2S | 1.120 | 1.096 | 2.142 |
| NCE-4S | 1.131 | 1.112 | 1.679 |
| NCE-6S | 1.143 | 1.127 | 1.399 |

**2. Tensile properties**

The experimental results of tensile strength and young's modulus of nickel coated short carbon fiber reinforced epoxy composites with and without nano fillers noted and shown in Figures 1 and 2 respectively. The tensile strength of composites with different nano fillers is shown in Figure 1. It is observed from figure 1 that addition of nano fillers to the composites shows increase in tensile strength with increase in filler loading.Among the three nano fillers used in the study,tensile strength of $Al_2O_3$filled composite shows maximum increment as compared to other two nano fillers. The tensile strength of NCE composite with addition of nano fillers enhanced compared to unfilled NCE composites due to interface bonding between silane treated fillers and matrix which leads to effective load transfer to fillers. The tensile modulus of composites with different nano fillers is shown in Figure 2. The tensile modulus of the composites enhanced with the increase in loading of nano fillers to the composites since the particulate fillers have greater stiffness than the matrix. The tensile modulus of $Al_2O_3$filled composite is higher than the $TiO_2$ and $SiO_2$ filled composites and it may due to improved interfacial bonding between filler and matrix.

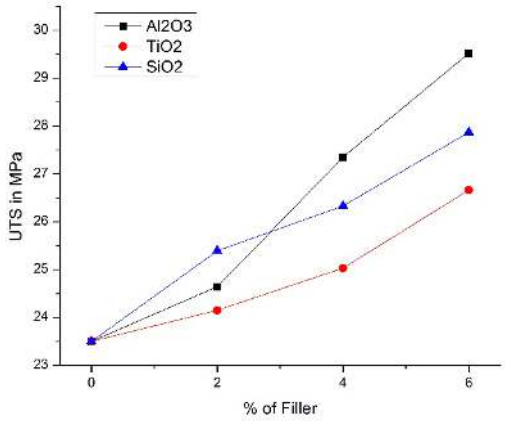


**Figure 1.** Variation of Ultimate tensile strength with the addition of nano fillers.



DOI: 10.5373/JARDCS/V12SP2/SP20201090
*Corresponding Author: Kiran M D, Email: kiranmdg@gmail.com
Article History: Received: Dec 08, 2020, Accepted: Mar 03, 2020

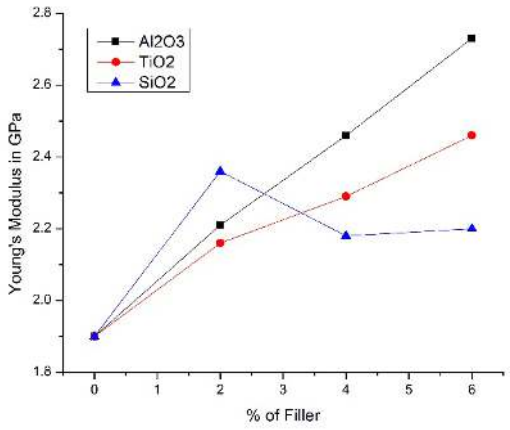


**Figure 2.** Variation of tensile modulus with the addition of nano fillers.

**3. Impact strength**

The experimental results of impact strength of NCE composites with and without nano fillers noted and shown in Figures 3. From the experimentation, it has been observed that $TiO_2$ and $SiO_2$ filled composites exhibits better impact strength than the unfilled and $Al_2O_3$filled composites. due the better adhesive strengthand stiffness, the $SiO_2$ filled composite shows highest impact strength [26].

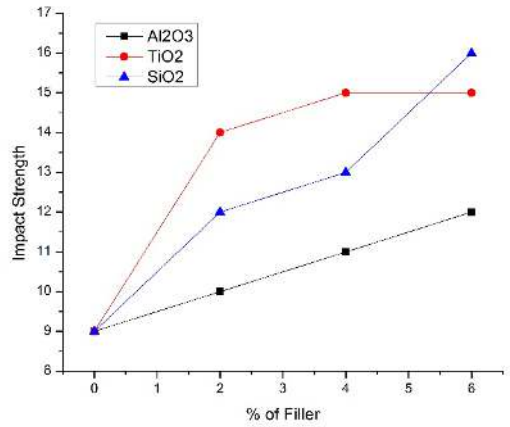


**Figure 3.** Variation of impact strength with the addition of nano fillers.

**4. Fracture Toughness**

Fracture toughness of composites was studied and shown in figure 4. The result indicates loading of nano fillers significantly enhances the fracture toughness of the nickel coated short carbon fiber reinforced epoxy composites.

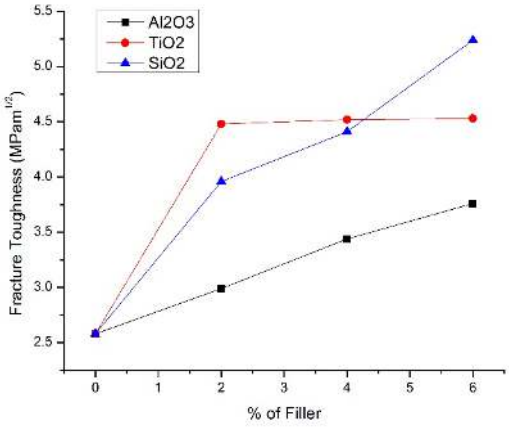


**Figure 4.** Variation of fracture toughness with the addition of nano fillers.

Addition of $Al_2O_3$changed the fracture toughness of NCE composite by 45% compared to unfilled NCE composites. However, the effect of addition of $TiO_2$ and $SiO_2$is more significant and enhanced respectively by 75% and 103% compared to unfilled NCE composites. The enhancement in the fracture toughness of particulate filledNCE composites was due to the improvement in the interfacial bond strength between theNano-phased matrix and the Nickel coated carbon fibre. The fracture toughness of $SiO_2$ is significantly high compared to other fillers due its toughness and high-volume occupancy.

## Conclusions

In the present work, nickel coated short carbon fiber-based epoxycomposites filled with different weight percentages ofaluminium oxide ($Al_2O_3$), titanium dioxide ($TiO_2$) and silica ($SiO_2$) nano fillers are fabricated and mechanical and fracture properties were evaluated.Addition of nano fillers to NCE composites shows significant enhancement of tensile strength and tensile modulus, and it was found that the tensilestrength and tensile modulus of the present NCE composites significantly highwith$Al_2O_3$ fillers compared to other fillers. The impact strength of the NCE composites filled with $TiO_2$and $SiO_2$was significantly high when compared to $Al_2O_3$filled composites. Impact strength of the NCE composites is high at 6% loading of $SiO_2$ than the $TiO_2$ and $Al_2O_3$ filled NCE composites.The fracture toughness of the NCE composites increases with the addition of nano fillers. The NCE composites filled with $SiO_2$showed significantly high fracture toughness when compared to $TiO_2$and $Al_2O_3$filled composites.

## References

[1] Osswald T and Menges G. Failure and damage of polymers. In: Osswald T and Menges G (eds) Mater Sci PolymEng 2003; 22: 447–519.
[2] Kaundal, R., Patnaik, A., &Satapathy, A.Mechanical characterizations and development of erosive wear model for Al2O3-filled short glass fiber-reinforced polymer composites. Proceedings of the Institution of Mechanical Engineers, Part L: Journal of Materials: Design and Applications (2016)., 146442071665430. doi:10.1177/1464420716654307.
[3] Broughton WR, Koukoulas T, Woolliams P, et al.Assessment of nanoparticle loading and dispersion inpolymeric materials using optical coherence tomography.Polym Test 2013; 32: 1290–1298.
[4] Derringer, G. C. Short Fiber-Elastomer Composites. Journal of Elastoplastics, 3(4), 230–248. doi:10.1177/009524437100300403.
[5] Jafari, B., Mohsenin, V.Endothelial dysfunction and hypertension in obstructive sleep apnea - Is it due to intermittent hypoxia?(2013) Journal of Cardiovascular Disease Research, 4 (2), pp. 87-91. DOI: 10.1016/j.jcdr.2013.04.001
[6] Kuni Zu'aimah Barikah. "Traditional and Novel Methods for Cocrystal Formation: A Mini Review." Systematic Reviews in Pharmacy 9.1 (2018), 79-82. Print. doi:10.5530/srp.2018.1.15
[7] K, m. S. K., alias, . M. & r., . S. K. (2018) a review on novel uses of vitamin e. Journal of Critical Reviews, 5 (2), 10-14. doi:10.22159/jcr.2018v5i2.24282



DOI: 10.5373/JARDCS/V12SP2/SP20201090
*Corresponding Author: Kiran M D, Email: kiranmdg@gmail.com
Article History: Received: Dec 08, 2020, Accepted: Mar 03, 2020

[8] F.-X. Perrin, T. M. H. Nguyen, and J.-L. Vernet, "Modeling the Cure of an Epoxy-Amine Resin with Bisphenol A as an External Catalyst," Macromol. Chem. Phys., vol. 208, no. 1, pp. 55–67, 2007.
[9] G. Agarwal, A. Patnaik, and R. K. Sharma, Mechanical and Thermo–Mechanical Properties of Bi-directional and Short Carbon Fiber Reinforced Epoxy Composites, vol. 9, p. 15, 2014.
[10] W. Dong, H.-C. Liu, S.-J. Park, and F.-L. Jin, Fracture toughness improvement of epoxy resins with short carbon fibers, J. Ind. Eng. Chem., vol. 20, no. 4, pp. 1220–1222, Jul. 2014.
[11] J. M. L. Reis and A. J. M. Ferreira,Assessment of fracture properties of epoxy polymer concrete reinforced with short carbon and glass fibers," Constr. Build. Mater., vol. 18, no. 7, pp. 523–528, Sep. 2004.
[12] X. Fu, W. Lu, and D. D. L. Chung, "Improving the bond strength between carbon fiber and cement by fiber surface treatment and polymer addition to cement mix, Cem. Concr. Res., vol. 26, no. 7, pp. 1007–1012, Jul. 1996.
[13] D. M. Blackketter, D. Upadhyaya, T. R. King, and J. A. King, "Evaluation of fiber surfaces treatment and sizing on the shear and transverse tensile strengths of carbon fiber-reinforced thermoset and thermoplastic matrix composites," Polym. Compos., vol. 14, no. 5, pp. 430–436, 1993.
[14] J. D. H. Hughes, "The carbon fiber/epoxy interface—A review," Compos. Sci. Technol., vol. 41, no. 1, pp. 13–45, Jan. 1991.
[15] S.-J. Park and M.-H. Kim, "Effect of acidic anode treatment on carbon fibers for increasing fiber-matrix adhesion and its relationship to interlaminar shear strength of composites," J. Mater. Sci., vol. 35, no. 8, pp. 1901–1905, Apr. 2000.
[16] . Hua, Y. Liu, G. Yao, L. Wang, J. Ma, and L. Liang, "Preparation and Characterization of Nickel-Coated Carbon Fibers by Electroplating," J. Mater. Eng. Perform., vol. 21, no. 3, pp. 324–330, Mar. 2012.
[17] N. Kumar, H. C. Chittappa, A. Allen D. Mello, and K. M D, Fatigue Behavior of Carbon Fiber Reinforced Aluminum Metal Matrix Composites, *Adv. Sci. Eng. Med.*, vol. 10, pp. 463–466, Mar. 2018.
[18] R. N. Rothon, Mineral Fillers in Thermoplastics: Filler Manufacture and Characterization,*Advances in Polymer Science*, Vol. 139, 1999, pp. 67-107.
[19] Marino, Xanthos. Functional fillers for plastics. Weinheim: Wiley-VCH; 2005.
[20] M. D. Kiran, H. K. Govindaraju, and T. Jayaraju, "Evaluation of fracture toughness of epoxy-nickel coated carbon fiber composites with Al2O3 nano filler," *AIP Conf. Proc.*, vol. 2057, no. 1, p. 020002, Jan. 2019.
[21] Jiao W, Liu Y, Qi G. Studies on Mechanical Properties of Epoxy Composites Filled with Grafted Particles PGMA/Alumina. Composites Science Technology 2009; 69: 391-5.
[22] Zhu ZK, Yang Y, Yin J, Qi ZN. Preparation and Properties of Organosoluble Polyimide/Silica Hybrid Materials by Sol-gel Process. Applied Polymer Science 1999; 73: 2977-84.
[23] M D Kiran, H K Govindaraju, T Jayaraju, Review-Effect of Fillers on Mechanical Properties of Polymer Matrix Composites, ScienceDirect, Materials Today: Proceedings 5 (2018) 22355–22361, Volume 5, Issue 10 and Part 3.
[24] Hsueh, C.H. Effects of Aspect Ratios of Ellipsoidal Inclusions on Elastic Stress Transfer of Ceramic Composites. Journal of American Ceramic Society, 72, 344-347.
[25] Shao-Yun Fu, Xi-Qiao Feng, Bernd Lauke, Yiu-WingMai,Effectsofparticlesize,particle/matrixinterfaceadhesion andparticleloading on mechanical propertiesofparticulatepolymer composites, www.elsevier.com,Composites: Part B 39(2008) 933–961.
[26] Ramesh K. Nayak, Alina Dash and B.C.Ray, "Effect of epoxy modifiers (Al2O3/SiO2/TiO2) on mechanical performance of epoxy/glass fiber hybrid composites", Procedia Materials Science, 2014, pp.1359 – 1364.

# Multipurpose Agribot

S. Nithya Poornima

*Assistant Professor, Dept. of Mechanical Engineering, BMS Institute of Technology and Management, Doddaballapur Main Road, Avalahalli, Yelahanka, Bengaluru, Karnataka, India*

***Abstract:*** **- Agriculture being one of the major occupations in India, it is very essential to discover and implement new idea in this field, though lot of work has been done in this area. It is unfortunate that, these ideas are not been implemented properly in actual field. This is due to high cost and is complicated for rural people. Multipurpose Farming Machine is basic and major equipment involved in agriculture for maximum yielding. Conventional method of planting and cultivating crops is a laborious process and hence for that reason there is a scarcity of labors, this result in delayed agriculture to overcome these difficulties, multipurpose agriculture equipment is designed. This Agricultural vehicle is an agricultural machine of a considerable power and great soil clearing capacity. This multipurpose system gives an advance method to sow, plow, water and cut the crops with minimum man power and labour making it an efficient vehicle. The machine will cultivate the farm by considering particular rows and specific column at fixed distance depending on crop. Moreover the vehicle can be controlled manually by driving the vehicle using seating arrangement. This agricultural vehicle will be running with batteries. Batteries will be charged using Solar Energy. So ultimate aim is to develop a agricultural vehicle which uses renewable sources for operation.**

***Keywords:*** **agriculture, automated farming, multipurpose farming machine, solar energy**

## I. METHODOLOGY

First, we surveyed thoroughly about all the types of existing forms of Agribots. We then designed the chassis taking into account crops, seed spacing, soil parameters and costs. We also designed the tools for all the intended operations. Then we fabricated the chassis and tools according to the design.

The chassis structure was fabricated as per the design. The mild steel metal strips is welded together as a lap joint using arc welding. Then Motor clamps were mounted on the chassis through welding to attach the wheels. Wheels and motor was attached to the clamps. Roller has been fabricated using hollow cylinder, screw rod, fasteners and arm attachments and welded to the chassis. Seed sowing equipment was also fabricated and attached on chassis. Harvesting tool was also fabricated and mounted. A solar panel is connected to the battery for it to be charged thus fulfilling our objective of making the Agribots eco-friendly. All the operations were connected by the 8 channel relay as intended.

## II. WORKING PRINCIPLE

This agribot was constructed using 8 channel relay system to select various operations using infrared remote ,solar panel to charge the battery ,DC motors to actuate the various operations and drive the vehicle Agribot can be used for other horticultural tasks such as pruning, weeding, spraying and monitoring. Agribot - can also be used in livestock applications (livestock robotics) such as automatic milking, washing and castrating. Agricultural vehicles like these have many benefits for the agricultural industry, including a higher quality of fresh produce, lower production costs, and a smaller need for manual labor.

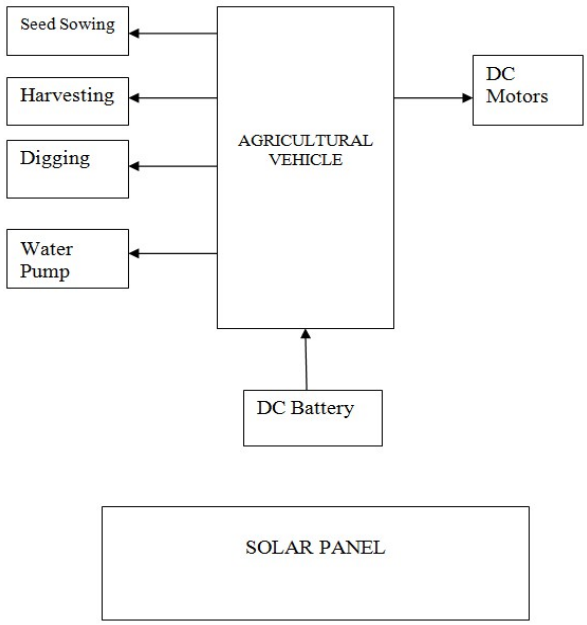


## III. COMPONENTS AND EQUIPMENT'S

*Material Used:*

1. Mild steel frame
2. Fasteners
3. Battery (12v)
4. Dc motors (60 rpm)
5. Dc motor (10 rpm)
6. Wheels
7. Motor clamps
8. Flex board
9. Wheel grip belt
10. Cutting wheel
11. Mild steel cylinders
12. Welding rods
13. Solar panel
14. Relay board and remote

Equipment's

1. Tool Kit and Measuring Equipment
2. Arc Welding Plant
2. Cutting Machine
4. Saws

## IV. BASIC DESIGN

The basic design has a chassis to which ploughing tool and roller is mounted. 4 motor clamps are mounted for the wheels with 2 motors. A wheel belt drive will come around the wheels to provide strength as well as to avoid the soil getting stuck on the wheels. A seed sowing equipment is also be mounted on the ploughing tool side. Two motors to drive the vehicle will be mounted with the wheels. 1 motor will be driving the up and down movement of the ploughing tool, 1 will actuate the seed sowing, 1 will be for the harvesting tool and 1 more to pump the water for irrigation.Chassis and all the tools are designed according to the crop requirements and cost.

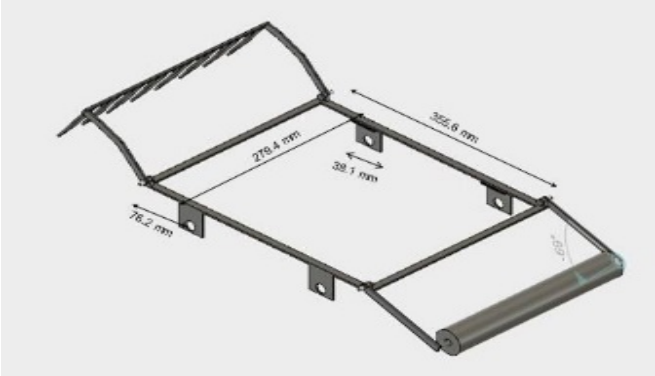


## V. DESIGN CALCULATIONS

Maximum Speed
Diameter of wheel – 65mm
Speed of motor driving the wheels – 60rpm
Circumference of wheel (c) – 204.2035 mm [πd]
Speed of the vehicle – 12.252 m/min

*Roller*

Volume of hollow cylinder:28.128cc
2washers:9.899cc
Screw Rod:21.944cc
Two roller attachment arms:7.2cc
Total Volume:67.171
Density:7.87g/cc
Weight:600g

*Ploughing Tool*

Blade support: 7.62 cc
8 Blades: 15.24 cc
Attachment Arm : 7.2 cc TOTAL VOLUME : 30.0
Density : 7.87g/cc
Weight:236.572g
Rake angle:67.79$^{o}$
{tan-1(2.54/1)

*Chassis*

2 strips 14 in 21.336cc
2 strips 11 in 16.764cc
Total volume:38.1cc
Density :7.87g/cc
Weight:236.572g

*Total weight on chassis*

| | |
|---|---|
| Roller | : 600g |
| Ploughing Tool | : 240g |
| Seed Sowing Equipment | : 200g |
| Harvesting Tool | : 150g |
| Battery | : 700g |
| Miscellaneous | : 3kg |

(Motors, circuit board, pump, solar panel etc.)

TOTAL WEIGHT : 5-6 kg

*Design Analysis*

Based on the total weight acting on the chassis, analysis was done on Solid Works.
Total load applied on the chassis: 10 kg
Chassis material: Mild Steel
Type of stress analysed: Von Misses Stress
A uniformly distributed load of 10 kg was applied as shown.

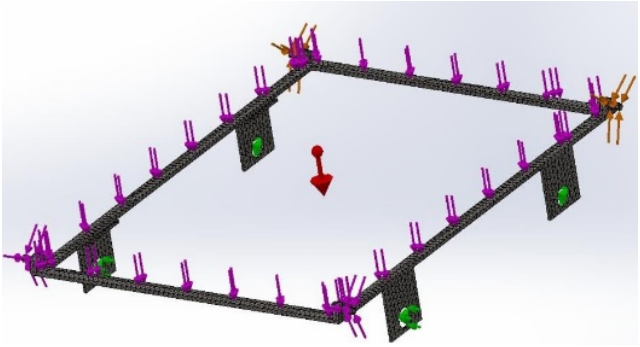

**The maximum deformation was found out to be 1.407**

*Displacement*

*Stress*

Analysis of Von Mises stress is as shown

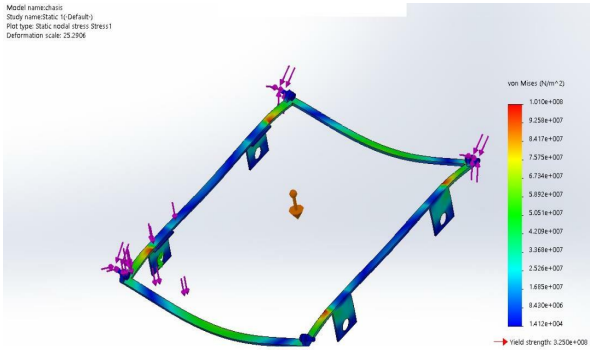

*Strain*

It was found that the proposed chassis structure was able to withstand a load upto 10 kg with 1.4 mm deformation only . Since the agribot requirement was only 6 kgs the design fabrication was justified

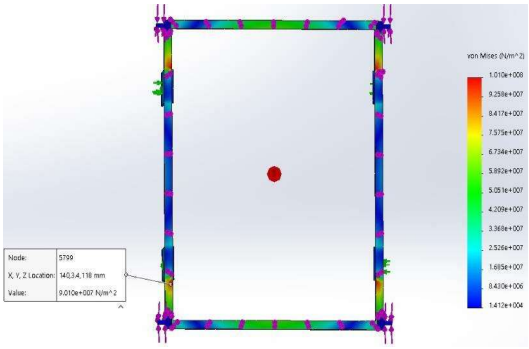

## VI. RESULTS AND DISCUSSIONS

After fabrication, we tested the agribot to ensure that the vehicle is operating as intended. The results of all the operations are as follows. Vehicle was able to move smoothly on flat ground. The vehicle also moved freely on soil. It was even able to move on grassy land. All the 5 operations were working properly by using remote control. Ploughing tool was able to dig the soil and vehicle was able to overcome the torque resistance of the soil. Rolling operation was also smoothly performed by the vehicle. Seed sowing and harvesting equipment is also working. Battery is also charging perfectly from the solar pan

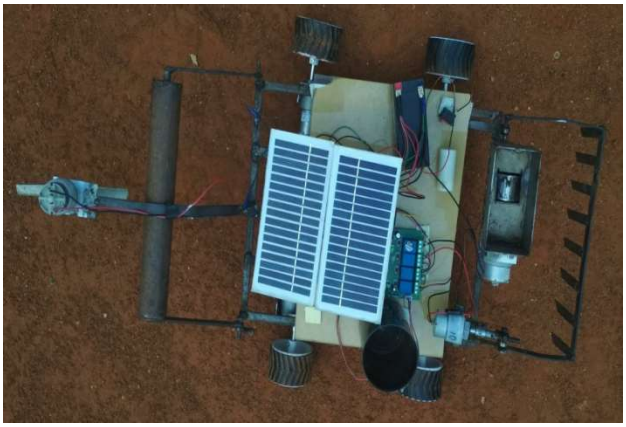

## VII. CONCLUSION

The agribot developed can perform 5 operations ploughing, seed sowing, harvesting, rolling and irrigation. All these operations can be performed by a single machine without any need of driver. This would reduce the cost and make it simple to be used which would be helpful for the farmers. If this model is adopted in real applications it would really improve the agriculture sector drastically.

## ACKNOWLEDGEMENT

We express our thanks to all my students and friends for all the help and co-ordination extended in bringing out this paper successfully in time. We will be failing in duty if we do not acknowledge our gratitude to the authors of the references and other literatures referred to in this project. I feel great to express our humble feeling of thanks to all who have supported my work in the institution.

## REFERENCES

[1]. Amrita Sneha.A, Abirami. E, Ankita. A, Mrs. R.Praveena, Mrs.R.Srimeena - Agricultural Robot for Automatic Ploughing and Seeding
[2]. Timo Blender, Thiemo Buchnery, Benjamin Fernandezy, Benno Pichlmaiery and Christian Schlegel - Managing a Mobile Agricultural Robot Swarm for a Seeding Task
[3]. Lars Grimstad, Cong D. Pham, Huynh T. Phan, P˚al J. - On the design of a low-cost, light-weight, and highly versatile agricultural robot
[4]. Mostafa Sharifi, Prof. XiaoQi Chen - A Novel Vision Based Row Guidance Approach for Navigation of Agricultural Mobile Robots in Orchards
[5]. Akhila Gollakota, M.B. Srinivas - Agribot - A Multipurpose Agricultural Robot
[6]. D.A. Mada, Sunday Mahai, [2013]
[7]. V.K. Tewari, A. Ashok Kumar, Satya Prakash Kumar, Brajesh Nare[2012]
[8]. F.A. Adamu, B. G. Jahun and B. Babangida [2014]
[9]. P. Šařec, O. Šařec [2015]

INTERNATIONAL JOURNAL OF AUTOMOTIVE AND MECHANICAL ENGINEERING (IJAME)
ISSN: 2229-8649 e-ISSN: 2180-1606
VOL. 17, ISSUE 1, 7709 – 7718
DOI: https://doi.org/10.15282/ijame.17.1.2020.18.0573

ORIGINAL ARTICLE

# Performance Evaluation of Cryogenic Treated and Untreated Carbide Inserts during Machining of AISI 304 Steel

Nagraj Patil[1,2*], K. Gopalakrishna[3] and B. Sangmesh[4]

[1]Department of Mechanical Engineering, School of Engineering and Technology, Jain Deemed-to-be University, Bangalore - 562112,Karnataka, India
[2]Visvesvaraya Technology University, Belagavi - 590018, Karnataka, India
[3]Centre for Incubation Innovation Research and Consultancy, Jyothy Institute of Technology, Bangalore – 560082, Karnataka, India
[4]Department of Mechanical Engineering, BMS institute of Technology and Management, Avalahalli, Yelahanka, Bangalore-560064, Karnataka, India, Mobile: +91 9590785153; Fax: +9180-27577199

**ABSTRACT** – The cutting tool in the machining process plays an important role as it acts on the working material. There are a few methodologies have been persued to improve tool life, for example traditional cooling, single layer coating, multilayer coating, heat treatment process, nitrogen cooling and latest being the cryogenic treatment which reported a significant improvement in cutting tool life, chip morphology, reduction in heat generation. Hence, the cryogenic treatment is emerged as the sustainable machining process. This paper presents machining of AISI 304 steel using both cryogenic treated (CT) and untreated (UT) cutting tool insert. The commercially available uncoated carbide insert has been cryogenically treated at -196°C for 24 hours soaking period. The machining test has been conducted under four different cutting speeds. The material characterization of cutting insert is studied by using scanning electron microscopy (SEM), hardness test, and microscopic image analysis has been carried out before and after cryogenic treatment. The cutting tool performance is assessed in terms of of wear, cutting temperature, chip morphology, surface roughness under the influence of cryogenic machining and the results are contrast with UT one. The exploratory findings reveals that the deep cryogenic treatment (DCT) with 24 hours soaking period, performed better wear resistance and improved surface roughness of the cutting tool. Also considerable reduction in the flank wear, crater wear, cutting temperature is obtained and found improved chip morphology.

**ARTICLE HISTORY**
Revised: 17th Dec 2019
Accepted: 20th Jan 2020

**KEYWORDS**
*Cryogenic treatment, Tool wear, Cutting temperature, Chip morphology.*

## INTRODUCTION

The machining study aims to increase tool life and better surface quality. Over few years, a tremendous research took place on the tool material to overcome the heat generation in order to enhance tool life. The flow of chip on the tool rake face causes an excessive heat generation. The raise in temperature during machining influences on tool life, quality of machining, tool wear, cutting force and formation of serrated chips etc. [1]. Consequently the machining industries are consistently making an endeavor to discover new material that is lighter and more grounded to withstand high temperature. In this regards selection of good cutting tool material before machining operation is very essential. Different types of tool inserts are available commercially, namely uncoated, coated, multilayer coated inserts. However; tungsten carbide (WC) insert is the majority suitable cutting insert for machining with stainless steel [2,3]. A continues effort has been made to enhance properties of the tool material. There are a few methodologies have been persued to improve tool life, for example traditional cooling, single layer coating, multilayer coating, heat treatment process, nitrogen cooling and latest being the CT, which reported a significant enhancement in cutting tool life and reduction in heat generation due to formation of carbide particles over the surface roughness.

In an cryogenic turning of AISI & MDN 250 steel, found a reduction in wear and improved surface finish, are other considerable findings which enhanced machinability [4,5]. Similarly, Varghese et al. [6] in his inveatigation, also claimed significant reduction in tool wear in CT machining in contrat with non CT machining, respectively. In this regard, Chetan et al. [7] reported that CT insert significantly improved in wear resistance, reduced cutting force and chip tool contact length. In another study, da silva et al. [8] studied the performanc of cryogenically high speed tools in contrast with tool of a similar material however, conventional heat treated, during machining and during sliding abrasion tests. It was observed that the CT tools compared to the UT one. Likewise, Padmakumar et al. [9] investigated the tool performance for crystal structure and magnetic properties between DCT and sintered with cobalt (Co) on WC cutting insert. The authors claimed that the presence of cobalt in the cutting insert experience transformation of phase when subjected to DCT. In another work by Deshpande et al.[10] revealed an improvement in hardness due to the presence of cobalt after CT to carbide insert. Gill et al. [11] also claimed CT performed better in continuous and interrupted machining operation. In another study Gill et al. [12] analysed the effect of CT on metallurgical and mechanical characterization of cryogenically treated (CT) tungsten carbide. The insert were exposed to two different treatment, namely (a) shallow

*CORRESPONDING AUTHOR | Nagraj Patil | ✉ nagrajpatil81@gmail.com

cryogenic (-110°C) (b) deep cryogenic (-196°C). It was found that the DCT insert exhibited formation of precipitation of multiple carbide particles that has the indication of η-phase. The results also revealed a phase transformation from retained austenite to martensite which leads to enhance wear resistance and hardness. Likewise, Seah and Zang et al. [13,14] claimed CT process shows significant improvement in wear resiatnce in comparision with UT insert. Similarly, Gill et al. [15] analysed the effect of adhesion strength of coating deposit of carbide substrate. The experimental results revealed a positive result for deep cryogenic insert followed by shallow cryogenic treatment.

In another work, Dhananchezian et al. [16] studied the cause of CT machining on stainless steel and modified physical vapor diposition coated carbide insert. The results indicated a lower cutting temperature by 45%, cutting force by 16%, and surface roughness was reduced by 25% when the insert was exposed to cryogenic cooling.Whereas, Venugopal et al. [17] concluded that cryogenic cooling method during machining has shown remarkable improvement in the wear resistance and decrease in the cutting temperature. Whereas, Rahman et al. [18] studied the performance of CT and UT carbide insert for moderated carbon (C) steel. The experimental results rendered a positive result for intermittent machining operation. Likewise, Ozbek et al. [19] found that DCT-24 sample showed highest hardness rate due to precipitation and homogeneous distribution of η phase particles. He et al. [20] performed a numerical study on stainless steel AISI 304 with coated and carbide insert. The results found the coated tool showed lower cutting temperature in comparision with uncoated tool. Dhar et al. [21] analysed the effect of cryogenic cooling by liquid nitrogen and performance of the cryogenic cooling insert found to be better compared to conventional cooling.

In another study, Dhar et al. [22] claimed a significant decrease in the temperature during machining, chip tool interface temperature and reduced wear rate after CT. kaynak et al. [23] investigated on NiTi alloys and results revealed a lower value of the tool-chip contact length, chip thickness, cutting force in comparison with dry condition. Nayak et al. [24] studied the improvement in tool life of Nitrile Rubber after lower-temperature machining as compared with dry machining. They found that the reduction in cutting force and radial force after lower-temperature machining. Singh et al. [25] studied the effects of minimum quantity lubrication machining over dry and flooded machining on tool wear and surface roughness. They observed that tool lives were increased by 9.68% and 32.26% after a dry and minimum quantity lubrication machining respectively. The literature on extensive experimental study on cutting temperature, flank wear rand surface roughness and chip morphology of the carbide insert on stainless steel is lacking and this spells the need of comprehensive experimental study. Hence, in the present investigation, focused to carry out the performance evaluation of CT on cutting temperature, wear rate and surface roughness and chip morphology is considered in the present work. The machining test has been carried out under different machining parameters. In addition, the investigation has been carried out with microscopic images analysis to support the experimental results.

## METHODS AND MATERIAL

An AISI304 austenitic stainless steel workpiece having a dimension of 40 mm diameter and 300 mm length in size was machined under dry machining condition and has been used a workpiece material in the current study. The composition of the workpiece, consists of 0.085% C, 18% Cr, 66.34% Fe, 2% Mn, 8% Ni, 0.045% P, 0.035S, 1% Si. The cryogenic process involved mainly cooling, soaking, raise in temperature. CT of the insert has been performed in a cryogenic chamber. Initially, the inserts were cooled from room temperature to -196°C at a controlled condition and kept it for 24 hours maintaining the same temperature once it attained -196°C followed by increase in temperature till it attains ambient conditions. The temperature has been raised further up to 200ºC for 2 hours. The machining trails are executed on CNC Machine (ace jobber xl) and uncoated carbide insert (Seco CNMG 120408 Grade MF3 029) supplied by Seco Tools India Pvt. Ltd and the cutting tool were rigidly mounted on tool holder designated by DCLNR 2525 M12.

To investigate the effect of CT on tool wear, surface roughness, cutting temperature and chip morphology were performed at different cutting parameters on both CT and UT carbide insert. The wear test was performed on CNC Machine, at different cutting speed (100.52m/min, 125.66m/min, 150.79m/min and 175.92m/min), constant feed rate 0.14mm/rev and depth of cut 0.5mm. In the course of experimentation, different types of wear tests were formed on the cutting tool at different speeds. To investigate the performance of wear mechanism, microscopic study of the tungsten carbide inserts has been carried out in terms of maximum tool wear for every 2 minutes of machining operation. The machining process was stopped at every 2 minutes and the amount of flank wear and crater wear formed on the inserts has been measured before and after machining using digital microscope (Model: AM3113T: Range: 20 to 250x). The maximum flank width of the flank wear when it reaches 0.6 mm during machining is considered as tool life of the cutting tool as ISO standard.

The micro-hardness test was performed for both insert using Vickers hardness test with a load of 0.5N for a dwell time of 15sec. To investigate the performance of wear mechanism, microscopic study has been carried out before and after machining by using digital microscope and the energy dispersive spectroscopy (EDX) test was carried out to identify the weight percentage of foreign particles on the tool surface area. Formation of built-up edges during high speed machining is evaluated using Mitutoyo SJ210 surface roughness tester. The experiment has been repeated for three trails and the average of the three readings has been considered for the analysis to overcome the experimental error. During machining operation the chip was flowing over the rake face of the tool due to rubbing action that leads to heat generation, was measured in terms of increased temperature using infrared thermometer (Make: Equinox ED-DT530A:range: -32°C to 530°C), Accuracy: ± 2 ºC or 2%: Resolution 0.1 ºC / 0.1ºF: Emissivity: 0.95 (fixed).

## RESULT AND DISCUSSION

### Cutting Tool Characterisation by using SEM and EDX

Figure 1(a) and 1(b), represents the microstructure of CT and UT inserts. Following phases present in the microstructure; alpha (α) phase which indicates WC particles, beta (β) phase indicates cobalt binder, gamma (γ) phase consists of (tantalum carbide) TaC, (titanium carbide) TiC and Eta (η) that contains multiple carbide. It is clearly observed from SEM images in Figure 1. The angular pattern with light grey in the microscopic image represents the WC particles while dark grey in between the lighter grey are the cobalt binders as shown in Figure 1(a), the α phase of CT insert is seen in a triangular shape which is the most balanced state, whereas the α phase in UT insert is unstable. The most balanced α phase helps to improve the wear resistance and hardness of CT insert due to stress-free appearance of the microstructure which leads to precipitation of fine η phase carbide on the top surface of the carbide insert. This enhanced the wear resistance in comparison with UT insert. A similar finding was also claimed by previous researchers [26, 27].

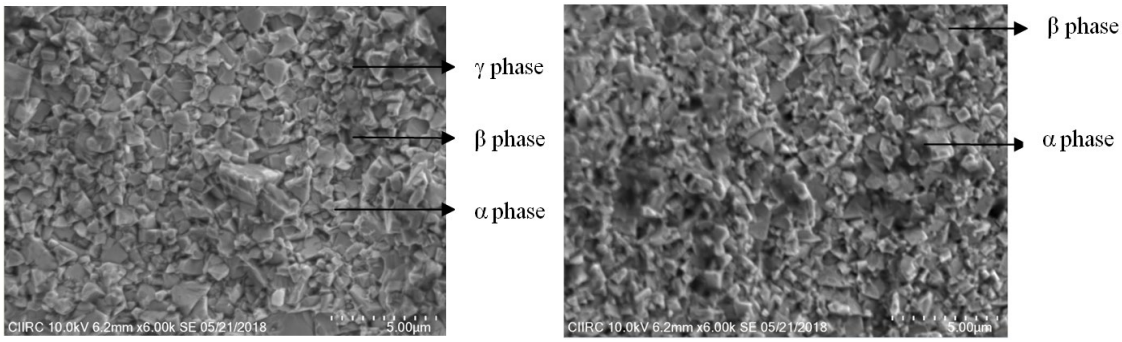


(a) CT (b) UT

**Figure 1.** Microstructure of carbide inserts.

EDX analysis was carried out to examine the weight percentage of CT and UT carbide insert. EDX spectra along with the chemical composition of both the carbide insert shown in Figure 2(a) and 2(b). From the Figure, observed a change in the chemical composition in cryogenic inserts. The growth in the Co and carbon (C) percentage are seen over the top surface of the cryogenic insert, after the CT. The weight percentage of C and Co of CT insert (C: 9.47% and Co: 11.79%) was found to be higher in comparison with UT (C: 8.80% and Co: 8.19%). This indicated the densification of Co binder for CT inserts. The growth in carbon percentage leads to precipitation of η phase carbide, which is hard in nature, leads to an increase in the wear resistance in comparison with UT insert. Similar finding were also claimed by the previous researchers [28, 29].

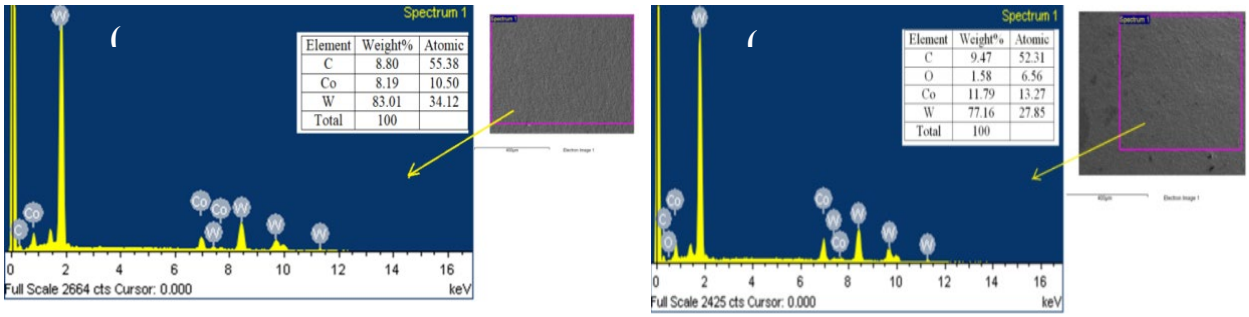


(a) UT (b) CT

**Figure 2.** EDX analysis of carbide inserts.

### Hardness Analysis

In the present experimental study, hardness rate is evaluated for both CT and UT insert. The average value of the micro-hardness along with standard deviation of both carbide inserts are shown in Figure 3. The hardness value of the CT insert having higher value approximately 4% had obtained in comparison with UT. The increase in hardness rate is due to densification of cobalt binder and precipitation of η carbide, which seems to be the harder phase and this, was confirmed in the EDX test. From the EDX it is confirmed that the cobalt binder decreased. Since, due CT of carbide inserts, the α phase is exposed to compressive stresses β phase exposed tensile stress. The quantity of the stresses in the α phase increases with reduction in β phase content due to rapid cooling. The sudden cooling leads to increase in compressive stresses would lead to an increase in the formation of η phase carbide. This leads to increase in the micro-hardness [30]. The DCT in the cutting insert enhanced mechanical properties, especially hardness has improved by 20% in comparison with UT insert, which enhance strength of the material [31].

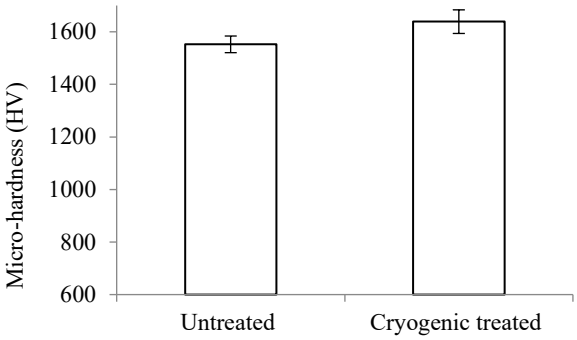


**Figure 3.** Micro-hardness of carbide inserts.

## Effect of Cryogenic Treatment on Tool Wear

### *Flank wear*

A rapid wear rate is observed initially, in this region; cutting is quickly broken down, established a wear land and uniform wear is noticed in which the wear rate gradually increases with increase in machining time followed by uncontrolled wear region [32]. Figure 4 and 5 show the maximum width of the flank wear (VBmax) for both CT and UT insert respectively. The tool life criteria (VBmax=0.6mm) is applied for all four cutting speeds by keeping feed rate and depth of cut constant. In this experiment the work piece has been machined at different cutting speed up to it reaches the maximum tool wear (VBmax=0.6mm). In the result it is found that the flank wear appeared after 4 minutes of machining operation for both the types of cutting inserts. The CT insert performed better in all the cutting speed in comparison with UT insert and improved by 40% at 100.52 m/min, 13% at 125.66 m/min, 23% at 150.79 m/min and 21% at 175.92 m/min. Due to the CT, the microstructure of the carbide insert has been improved mainly because of precipitation of η phase carbide particles. This clearly depicts that the CT establishes a prolonged tool life than the UT cutting insert. The DCT improves mechanical properties of the cutting insert, due to homogenous distribution of carbide particles over the surface leads to outstanding enhancement in wear resistance which in turn improves tool life and this was also reported in the literature [33, 34]. The Table 1 represents the tool life (VBmax=0.6mm) of CT insert and UT insert under different cutting speed.

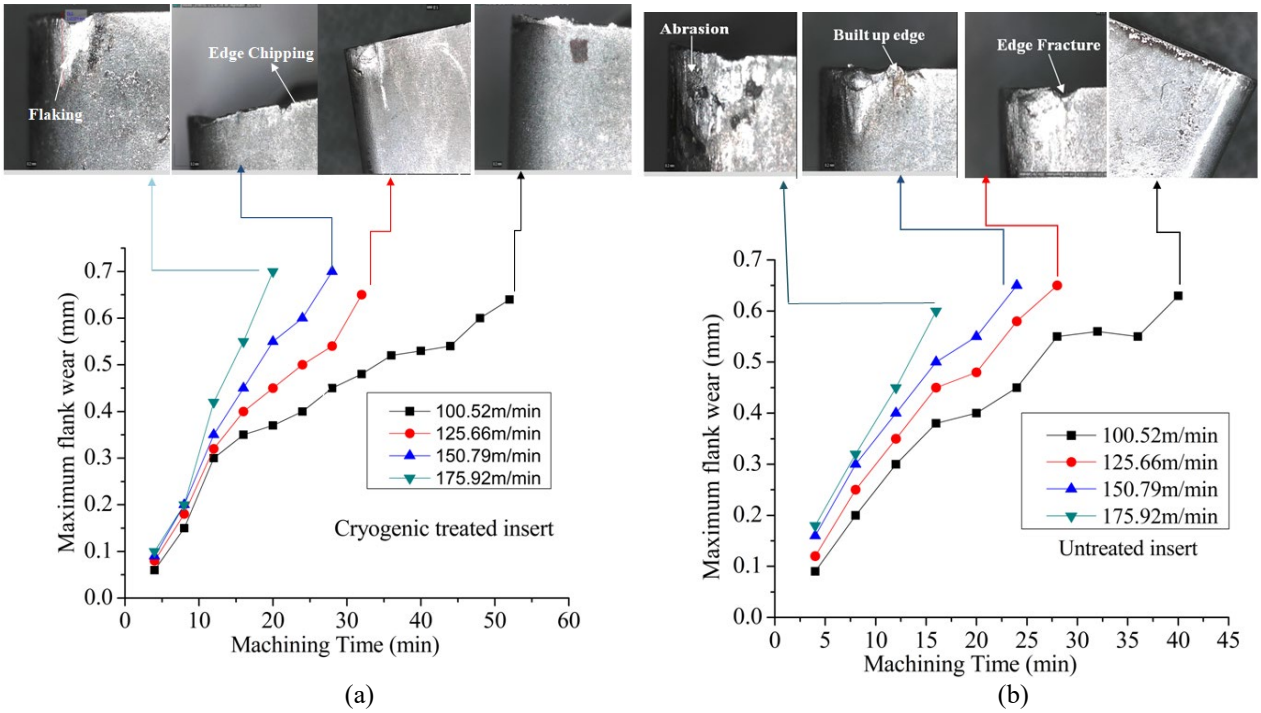


**Figure 4.** Variations of flank wear according to machining time of (a) CT and (b) UT insert

To evaluate the diffusion at the tool-workpiece interface, EDX analysis has been carried out at tool rake face of the both the cutting inserts. Figure 6(a) and 6(b) shows the EDX spectra along with chemical composition of both the insert. The uninterrupted embossment of chip over the rake face for prolonged time duration has resulted in adhesion over the rake face. The reactive nature of iron (Fe), chromium (Cr) and nickel (Ni) is the cause of such behavior. The amount of Fe as per the table indicated in EDX analysis found to be considerably lower in case of CT (9.48%) compared with UT one (45.12%). In addition, lower amount of Cr (3.70%) and Ni (1.06%) is being detected in case of CT inserts. The EDX analysis clearly depicted that the adhesive wear is more intensive in UT inserts. The substantial amount of chemical

composition of the workpiece material is found over the rake face which clearly shows the presence of built up edge formation in UT inserts whereas negligible amount of work piece material is seen in case of cryogenically treated (CT) inserts. Hence the adhesive wear and uncontrolled chip removal caused maximum wear in UT inserts whereas less wear has been detected in case of CT insert due to lower rate of built up formation of edges over the rake face.

**Table 1.** Shows tool life (VBmax=0.6mm) of CT insert and UT insert under different cutting speed.

| Cutting speed (m/min) | Cutting insert | Machining time (min) |
|---|---|---|
| 100.52 | CT insert | 48 |
| | UT insert | 39 |
| 125.66 | CT inset | 30 |
| | UT insert | 25 |
| 150.79 | CT insert | 24 |
| | UT insert | 22 |
| 175.92 | CT insert | 17 |
| | UT insert | 16 |

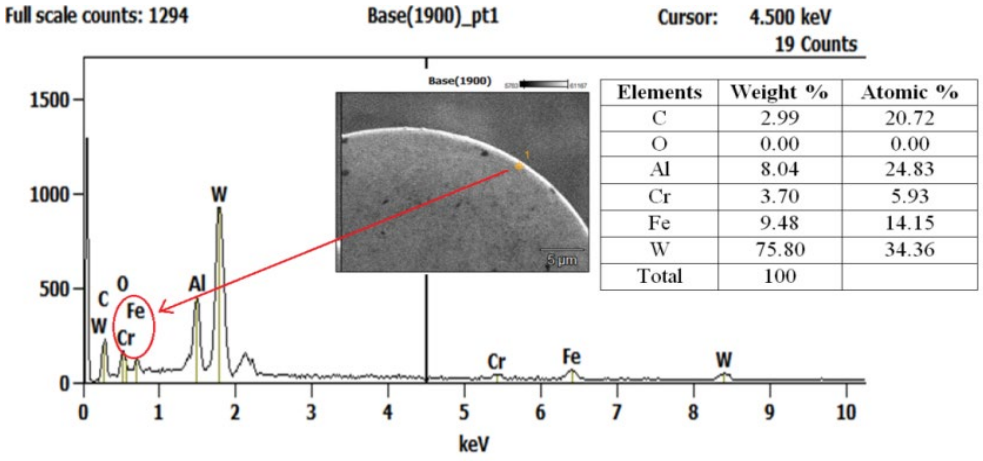


(a)

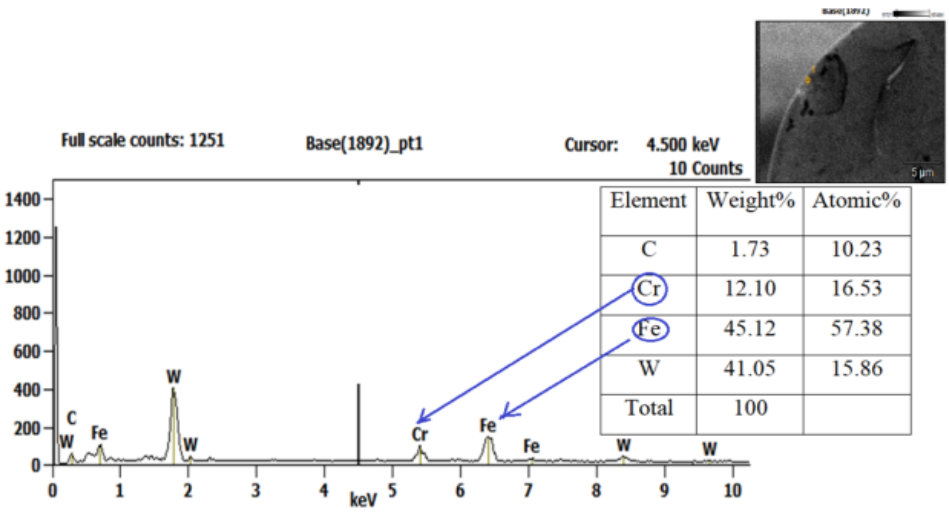


(b)

**Figure 6.** EDX results after machining for (a) CT (b) UT inserts.

### *Crater wear*

The microscopic images of the rake surface have been carried out at four cutting speeds to study the crater wear. An exhaustive literature along with experimental analysis has been performed on the cutting inserts, observed three different wear mechanisms for all the parameters and this also has been confirmed by various authors [1, 26]. The tip of the cutting insert is normally prone to fracture, adhesion, chip formation due to the excessive generation of built-up edges. In addition, abrasion peeling also being observed at the rake surface region. Figure 7 to Figure 10 shows the crater wear for both the cutting inserts for different cutting speeds. However, as per the microscopic images, the lowest rate of crater wear is being observed for CT as indicated in Figure 7(a). From the Figure 7, it is indicated that the width of crater wear has observed less for CT insert (0.084 mm) and 0.296 mm is obtained for UT one.

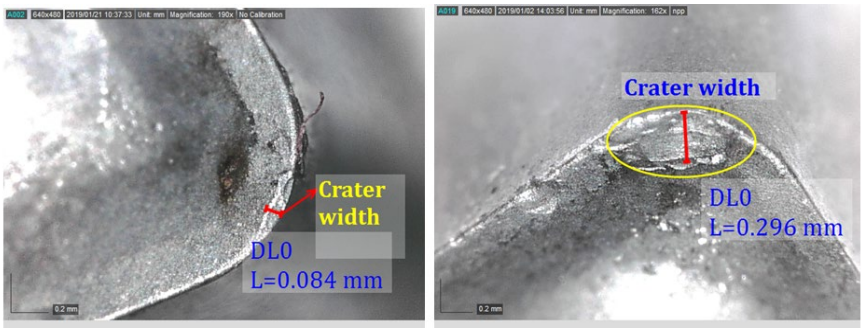


(a) (b)

**Figure 7.** Microscopic image of crater wear observed at cutting speed of 100.52 m/min on (a) CT (b) UT insert.

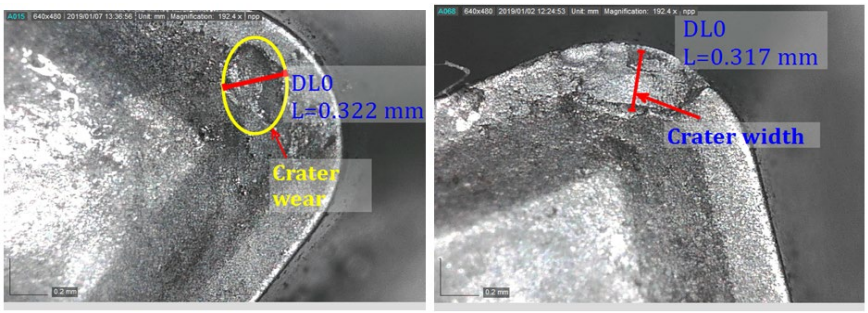


(a) (b)

**Figure 8.** Microscopic image of crater wear observed at cutting speed of 125.66 m/min on (a) CT (b) UT insert.

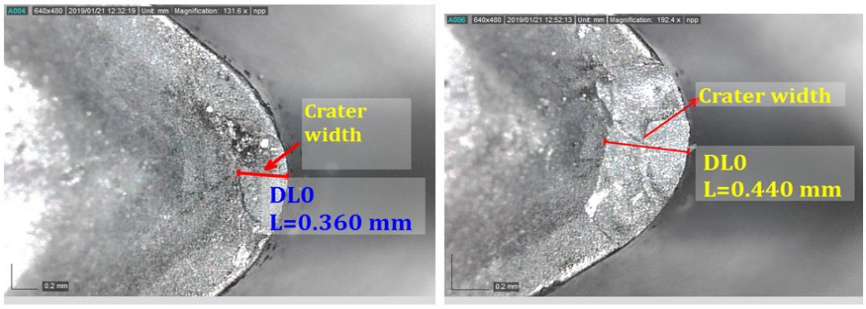


(a) (b)

**Figure 9.** Microscopic image of crater wear observed at cutting speed of 150.79 m/min on (a) CT (b) UT insert.

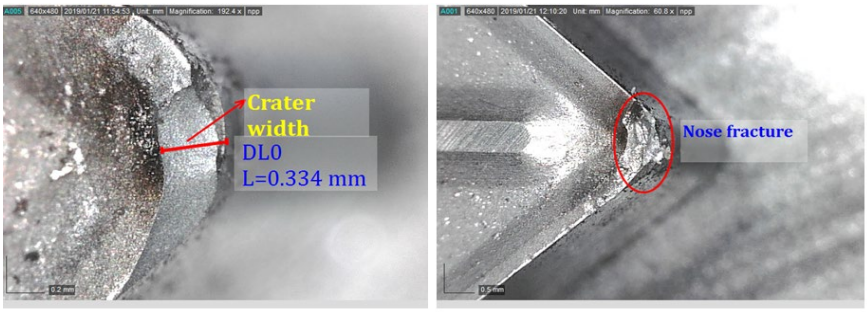


(a) (b)

**Figure 10.** Microscopic image of crater wear observed at cutting speed of 175.92 m/min on (a) CT (b) UT insert.

On the other hand for a cutting speed of 125.66 m/min, very less crater wear had found on the tool rake of the tool CT insert in comparison with UT insert as shown in Figure 8. The crater width of the CT found to be less for different cutting speeds in all the cases. Further increase in the cutting speed, the UT insert under goes nose fracture while the CT insert significantly performed better than UT insert. The higher wear resistance due to precipitation of η phase carbide as the reason for the advancement. The increase in cutting speed, advanced into faster removal of material which further triggered to attain higher temperature at the rake face. CT insert has prohibited the built-up edge damage and fracture failure of insert. Along with this, it has curbed the propagation of plastic deformation of the cutting edge. This is happened for the reason that the deployment of CT diminishes the residual stresses developed during sintering of the cutting insert. The improved micro-hardness and toughness as a result of CT followed by tempering treatment assisted to decrease the

tool wear, cutting temperature, increased thermal conductivity, heat dissipation capacity are some of the reason which decreases the tool wear under cryogenic machining [35].

### Chip Morphology Study

In the present investigation chip morphology study helps to understand the mechanism accountable for emergence of different types of chips formed at different machining conditions, also useful to assess better surface quality of machined work piece and tool life. Figure 11 portrays the SEM images of the crest of the chips formed without treatment and with CT. By observing the Figure it is clear that, both the cutting inserts generates chips in the form zigzag shape while more saw edged chips were seen in case of UT cutting insert compared to CT insert. At 100.52m/min speed no segmented chips are found for both the type of cutting inserts whereas increase in the cutting speed the width of the chip increased, showing more serration chips.

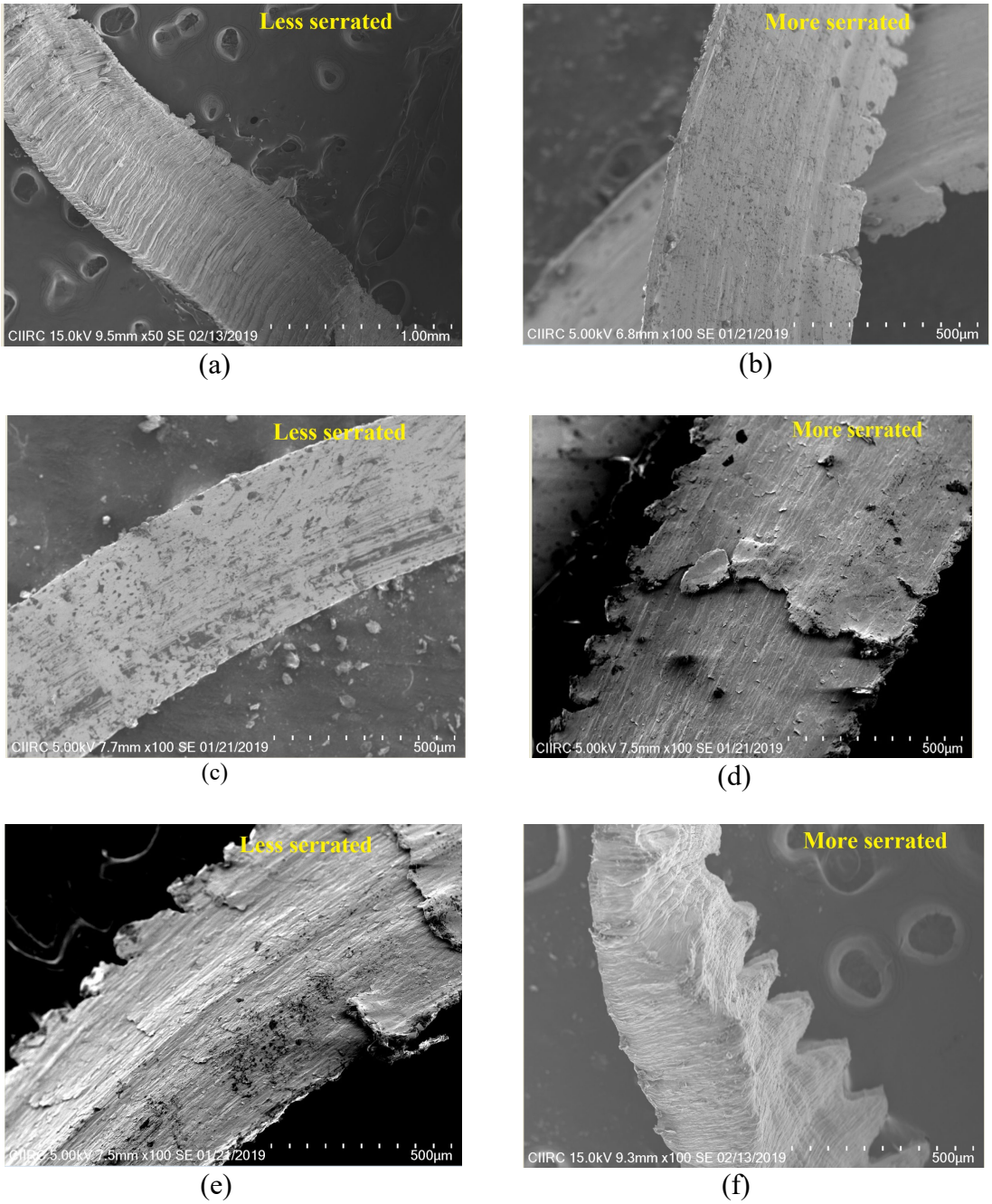


**Figure 11.** SEM chip morphology at different cutting speed: (a), (c), (e) are CT at100.52m/min, 125.66m/min, 150.79m/min, (b), (d), (f) are UT insert at 100.52m/min, 125.66m/min, 150.79m/min.

The serrated chips size has been expanded with increase in speed. The serrations are more advanced in case of UT than CT one. It has been observed from the Figure 10(b), 10(d) and 10(f) that the UT insert have high degree of serration in comparison with CT insert presented in Figure 10(a), 10(c) and 10(e). The increase in the mechanical properties due to CT would results in enhanced wear resistance, high hardness and increase in toughness leads to less serrated chip in

comparison with UT insert. Khan A et [29] reported more serrated chips were found on UT insert at higher cutting speed in contrast with CT insert.

### Effect of Cutting Speed on Cutting Temperature under Cryogenic Machining Condition

It was observed from the Figure 11 the temperature increased with increase in cutting speed. The results revealed that the reduction in cutting temperature in case of CT insert found 36% in contrast with UT cutting insert. The difference between CT and UT insert is 27% when the cutting speed increases from 100.52m/min to 125.66m/min followed by 20% for further increase in speed from 125.66m/min to 150.79m/min. At 175.92m/min speed, the difference is found to be 10%. This attributed to the fact that the CT cutting inserts account for the reduction in temperature with increase in speed. A lower value of temperature is found in case of CT insert is mainly due to increase in thermal conductivity and heat dissipation over the rake surface. The increase in temperature is seen in UT insert would increase in wear rate. The performance of UT insert is not satisfactory. The results indicated that with a raise in cutting speed the cutting temperature raises for both the cases. However, the entire CT cutting inserts performed better in contrast with UT insert due to improvement in the mechanical properties and similar results are observed in [23]. Other researches also claimed that the increase cryogenic effect reduces the cutting temperature [16, 17].

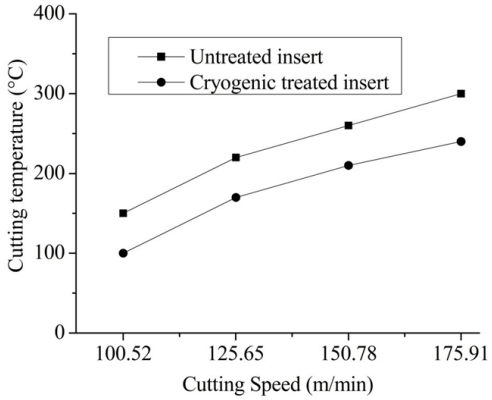


**Figure 12.** Development of cutting temperature at different cutting speed.

### Effects of Cutting Speed on Surface Roughness

The enhancement of surface quality of the working material is also equally important in addition to increase the machinability of the working piece. There are many factors that cause the surface quality of the specimen such as feed, speed, vibration, environmental factor and cutting temperature. The surface roughness has been carried out for both inserts. The typical average value of the surface roughness is shown in Figure 13. It is clear that, CT insert exhibited a better surface finish and more stable reading is obtained than UT insert. The unstable reading has been reported for UT insert due to the excessive generation of chips on the tool rake surface. This may cause to increase in the level of friction and produce residual stresses over the surface which leads to poor surface finish. Whereas surface quality has been shown good in case of CT and found to be around 18% over UT insert. It is revealed that the surface quality improves for all the cutting speed tested in the current study. This is due to higher wear resistance, minimized cutting temperature and lesser distortion of cutting edge. Also the lower cutting temperature due to CT improves thermal conductivity which leads to better heat dissipation and in turn helps to obtain good surface roughness. It is found that the surface roughness is being reduced with raise in cutting speed and for both the inserts. The built-up edge formation and vibration further worsen the surface roughness. Previous researcher also claimed that CT insert improves the surface roughness [36].

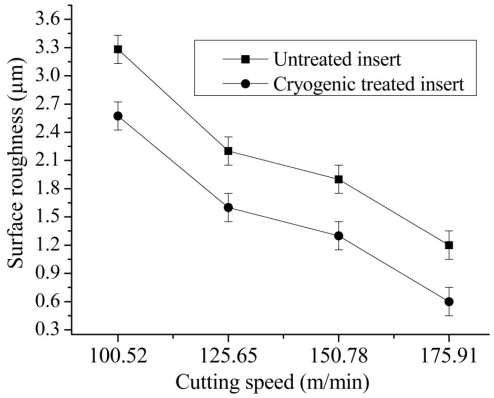


**Figure 13.** Development of surface roughness at different cutting speed.

## CONCLUSION

In the present experimental investigation, machining of AISI304 austenite stainless steel is carried out with cryogenic treated (CT) cutting insert and the results are compared with untreated (UT) insert one. Different types of wear mechanism, cutting temperature, chip morphology and surface roughness has been assessed and compared.

i. The CT cutting insert resists wear more effectively than untreated cutting tool. The enhanced in the micro-hardness due to CT enabled to withstand wear resistance at high speed up to certain extent, but it decreases with further increase in speed. However, the cryogenic treated cutting insert reported least flank wear in comparison with untreated cutting insert.

ii. The CT inserts account for the reduction in temperature with increase in speed compared to UT insert. This attributed to the fact that the CT cutting insert improved mechanical properties and heat dissipation over the rake surface. The rise in temperature is seen in untreated insert would adversely affects the hardness and wear rate.

iii. After CT, the fine η carbides improved the hardness without significantly affecting the toughness. While the α phase of the CT cutting tool is seen in more stable condition The stable form of α phase might have supported to enhance wear resistance of CT cutting tool.

iv. The reduction in tool temperature due to increase in the thermal conductivity, which reduced the tool wear under CT condition in contrast with UT.

v. The highest percentage of reduction in surface roughness during cryogenic machining is 82% in contrast with UT insert.

vi. The results clearly depicts that, both the cutting tools produce ser-rated chips while lower serrations with CT cutting inserts were seen. The high stress, shear force and excess amount of heat generation in the UT cutting insert would have produced large serrated chips.

vii. The results revealed that the reduction in cutting temperature in case of cryogenic treated insert found 36% in comparison with untreated cutting insert. The difference between CT and UT insert is 27% when the cutting speed increase from 100.52m/min to 125.66m/min followed by 20% for further increase in speed from 125.66m/min to 150.79m/min. At 175.92m/min speed, the difference is found to be 10%.

## REFERENCES

[1] Gill SS, Singh H, Singh R, Singh J. Flank wear and machining performance of cryogenically treated tungsten carbide inserts. Material and Manufacturing Processes. 2011;26(11):1430-1441.

[2] Fernández-Abia, AI, García JB, López de Lacalle LN. High-performance machining of austenitic stainless steels. Machining and Machine-Tools. 2013;29–90.

[3] Shokrani A, Dhokia V, Newman ST. Cryogenic high speed machining of cobalt chromium alloy. 7th HPC 2016–CIRP Conference on High Performance Cutting. 2016;46:404-407.

[4] Patil N, Gopalakrishna K, Sangmesh B, Sudhakar K, Vijaykumar GC. Performance studies on cryogenic treated carbide cutting tool for turning of AISI304 steel. Journal of Mechanical Engineering and Sciences. 2018;12(3):3927-3941.

[5] Varghese V, Ramesh MR, Chakradhar D. Experimental investigation of cryogenic end milling on maraging steel using cryogenically treated tungsten carbide-cobalt inserts. 2019;105:2001-2009.

[6] Varghese V, Ramesh MR, Chakradhar D. Experimental investigation and optimization of machining parameters for sustainable machining. Material and Manufacturing Processes. 2018; 33(16):1-10.

[7] Chetan, Ghosh S, Rao PV. Performance evaluation of deep cryogenic processed carbide inserts during dry turning of Nimonic 90 aerospace grade alloy. Tribology International. 2017;115:397-408.

[8] Da Silva FJ, Franco SD, Machado ÁR, Ezugwu EO, Souza AM. Performance of cryogenically treated HSS tools. Wear. 2006;261(5-6):674-685.

[9] Padmakumar M, Guruprasath J, Achuthan P, Dinakaran D. Investigation of phase structure of cobalt and its effect in WC–Co cemented carbides before and after deep cryogenic treatment. International Journal of Refractory Metals and Hard Materials. 2018;74:87-92.

[10] Deshpande RG, Venugopal KA. Machining with cryogenically treated carbide cutting tool inserts. Materials Today: Proceedings. 2018;5(1):1872-1878.

[11] Gill SS, Singh R, Singh H, Singh J. Wear behaviour of cryogenically treated tungsten carbide inserts under dry and wet turning conditions. Interational Journal of Machine Tools Manufacture. 2009;49(3-4):256-260.

[12] Gill SS, Singh J, Singh H, Singh R. Metallurgical and mechanical characteristics of cryogenically treated tungsten carbide (WC-Co). International Journal of Advanced Manufacturing. 2012;58(1-4):119-131.

[13] Seah KHW, Rahman, Yong KH. Performance evaluation of cryogenically treated tungsten carbide cutting tool inserts. Proceedings of the Institution of Mechanical Engineers, Part B: Journal of Engineering Manufacture. 2003;217(1):29-44.

[14] Zhang H, Chen L, Sun J, Wang W, Wang Q. An investigation of cobalt phase structure in WC-Co cemented carbides before and after deep cryogenic treatment. International Journal of Refractory Metals and Hard Materials. 2015;51:201-206.

[15] Gill SS, Singh J, Singh H, Singh R. Investigation on wear behaviour of cryogenically treated TiAlN coated tungsten carbide inserts in turning. Interational Journal of Machine Tools Manufacture. 2011;51(1):25-33.

[16] Dhananchezian M, Kumar MP, Sornakumar T. Cryogenic Turning of AISI 304 Stainless Steel with Modified Tungsten Carbide Tool Inserts. Material and Manufacturing Processes. 2011;26(5):781-785.

[17] Venugopal KA, Paul S, Chattopadhyay AB. Tool wear in cryogenic turning of Ti-6Al-4V alloy. Cryogenics. 2007;47(1):12-18.

[18] Yong AYL, Seah KHW, Rahman M. Performance of cryogenically treated tungsten carbide tools in milling operations. International Journal of Advanced Manufacturing Technology. 2007:638-643.

[19] Özbek NA, Çiçek A, Gülesin M, Özbek O. Investigation of the effects of cryogenic treatment applied at different holding times to cemented carbide inserts on tool wear. Interational Journal of Machine Tools Manufacture. 2014;86:34-43.

[20] He H-B, Li H-Y, Yang J, Zhang X-Y, Yue Q-B, Jiang X, Lyu S. A study on major factors influencing dry cutting temperature of AISI 304 stainless steel. International Journal of Precision Engineering and Manufacturing. 2017;18(10):1387-1392.

[21] Dhar NR, Kamruzzaman M. Cutting temperature, tool wear, surface roughness and dimensional deviation in turning AISI-4037 steel under cryogenic condition. Interational Journal of Machine Tools Manufacture. 2007;47:754-759.

[22] Dhar NR, Islam MW, Islam S, Mithu MAH. The influence of minimum quantity of lubrication (MQL) on cutting temperature, chip and dimensional accuracy in turning AISI-1040 steel. Journal of Materials Processing Technology. 2006;171(1):93-99.

[23] Kaynak Y, Karaca HE, Noebe RD, Jawahir IS. The effect of active phase of the work material on machining performance of a NiTi shape memory alloy. Metallurgical and Materials Transactions A. 2015;46(6):2625-2636.

[24] Rajesh N, Akshay N, Raviraj S. Low Temperature machining of nitrile rubber. International Journal of Automotive and Mechanical Engineering. 2018;15(3):5500-5510.

[25] Singh T, Dureja JS, Dorga M, Bhatti MS. Machining performance investigation of AISI 304 austenitic stainless steel under different turning environments. International Journal of Automotive and Mechanical Engineering. 2018;15(4):5837-5862.

[26] Chetan, Behera BC, Ghosh S, Rao PV. Wear behavior of PVD TiN coated carbide inserts during machining of Nimonic 90 and Ti6Al4V superalloys under dry and MQL conditions. Ceramics International 2016;42(13):14873-14885.

[27] Özbek NA, ÇİÇek A, GülesİN M, Özbek O. Application of deep cryogenic treatment to uncoated tungsten carbide inserts in the turning of AISI 304 stainless steel. Metallurgical and Materials Transactions A. 2016;47(12):6270-6280.

[28] Thakur D, Ramamoorthy B, Vijayaraghavan L. Influence of different post treatments on tungsten carbide-cobalt inserts. Materials Letters. 2008;62(28):4403-4406.

[29] Khan A, Maity K. Comparative study of some machinability aspects in turning of pure titanium with untreated and cryogenically treated carbide inserts. Journal of Manufacturing Processes. 2017;28:272-284.

[30] Varghese V, Ramesh MR, Chakradhar D. Influence of deep cryogenic treatment on the performance of cemented carbide (WC-Co) inserts during dry end milling of maraging steel. Journal of Manufacturing Processes. 2019;37:242-250.

[31] Gao Y, Luo BH, Bai ZH, Zhu B, Ouyang S. Effects of deep cryogenic treatment on the microstructure and properties of WC-Fe-Ni cemented carbides. International Journal of Refractory Metals and Hard Materials. 2016;58:42-50.

[32] Che Haron CH, Ginting A, Goh JH. Wear of coated and uncoated carbides in turning tool steel. Journal of Materials Processing and Technology. 2001;116(1):49-54.

[33] Bordin A, Bruschi S, Ghiotti A, Bariani PF. Analysis of tool wear in cryogenic machining of additive manufactured Ti6Al4V alloy. Wear. 2015;328-329:89-99.

[34] Vimal AJ, Bensely A, Lal DM, Srinivasan K. Deep cryogenic treatment improves wear resistance of EN 31 steel. Material Manufacturing Processes. 2008;23(4):369-376.

[35] Kara F, Karabatak M, Ayyıldız M, Nasc E. Effect of machinability microstructure and hardness of deep cryogenic treatment in hard turning of AISI D2 steel with ceramic cutting. Journal of Materials Research and Technology. 2019;1-15.

[36] SreeramaReddy TV, Sornakumar T, VenkataramaReddy M, Venkatram R. Machinability of C45 steel with deep cryogenic treated tungsten carbide cutting tool inserts. International Journal of Refractory Metals and Hard Materials. 2009;27(1):181-185.

ISSN 2321 3361 © 2020 IJESC

Research Article Volume 10 Issue No.7

# Analytical and Finite Element Analysis of a Typical Curved Beam Under loading

G. L. Anantha Krishna
Assistant Professor
B M S Institute of Technology and Management, Bengaluru, India

**Abstract:**
Beam is a structural member subjected to a transverse load. The two types of beams are straight beams and curved beams. In straight beams the centroidal axis and neutral axis are coincident. In curved beams the centroidal axis and neutral axis are not coincident. Straight beams when subjected to moment the neutral axis is bent whereas in curved beams the neutral axis is already bent even before the application of moment. In the present work, an attempt is made to understand the application of finite element technique through an application on a curved beam. A typical curved with proper dimensions was chosen and deformation was found using analytical technique through equating the moment equation and strain energy. The deformation was found to be 6.82mm The same curved beam was analyzed using a finite element software. The deformation from finite element analysis was found to be 7.03mm. The variation between analytical finite element technique was found to be well within the limits.

**Keywords:** Curved beam, Deformation, Finite elements, Moment of inertia.

## I. INTRODUCTION

Many members that are subjected to bending however are curved before a bending moment is applied to them. Such members are called curved beams. Examples of curved beam are crane hooks, chain links, closed rings and frames of punching presses. Curved beam is defined as a beam in which the neutral axis in the unfolded condition is curved instead of straight. The following assumptions are made in the stress analysis of curved beams.

- Plane sections perpendicular to the axis of the beam remain plane after bending
- The moduli of elasticity in tension and compression are equal
- The material is homogeneous and obeys Hooke's law

**The factors that distinguish the stress distribution in straight and curved beams are**

- The neutral and centroidal axes of the curved beam are not coincident
- The neutral axis is shifted towards the centre of curvature
- The stress distribution is hyperbolic in curved beams

In the present work, a typical curved beam with rectangular cross section of dimension 25mm * 4mm is chosen for analysis.

## II. LITERATURE REVIEW

Souvik Das et.al[1] identified accounts of repeated failure of crane hooks at the coil yard of a Hot Strip Mill which pose a serious threat to safety in the area. More than 4 hooks failed in less than 5 years. The crane hook (rated for 36000 kg) failed from the threaded shank while lifting a load of 18143 kg. The metal in the hook was revealed by chemical analysis to be IS: 4367 20C15 steel. The hook rod failed from a step where there was a cross sectional change and the locations were associated with machining and chatter marks. Such cross-sectional changes are the potential sites of stress concentrations leading to crack initiations. Fracture surfaces of broken pieces of hook reveal initiation of beach marks from both sides with granular rough surface at the middle of fracture zone. Beach marks initiated from both sides indicate origin of reverse bending fatigue. Distinct granular rough zone at the middle is due to final brittle fracture. Microstructure of the polished sample revealed numerous inclusions which indicate that the steel was not clean .Such a huge number of inclusions are not desirable as they can act as stress concentration sites and lead to fatigue crack initiation. Etched microstructure of failed hook reveals coarse cast structure having inhomogeneous microstructure with a mixture of ferrite and pearlite. This inhomogeneous coarser cast structure is outcome of lower reduction ratio during rolling followed by improper heat treatment process. The fracture was concluded to have occurred due to stress concentration from the step region due to inferior material. Preventive maintenance and condition monitoring procedures should be applied to identify and minimize the risk.

Kijun Kang et. al [2] applied exact closed-form solution and a numerical solution by the differential quadrature method (D.Q.M.) to predict the out-of-plane static behavior of a curved beam subjected to torque, based on the curved-beam version of the classical (Bernoulli-Euler) and shear deformable (Bresse-Timoshenko) beam theories. Deflections, twist angles, angles of rotation, bending moments and twisting moments are calculated for the case of a circular are of circular cross section with clamped and simply supported boundary conditions, and the results obtained by both methods (exact and D.Q.M.) are compared. It is found that the D.Q.M. gives good accuracy for only a limited number of grid points.

Amitkumar Premdas Chavan et al [3] identified that the existing formulas of stress and deflection calculations on beams are

commonly for straight beams that undergo small linear deflections. They are not applicable to curved beams. The depth of the cross section of a slender curved beam is small compared with its radius of curvature. It usually has large deformation. The load-deflection relationship of a slender curved beam is often nonlinear. It is much more challenging to analyze the deformation of a nonlinear slender curved beam than a linear straight beam. In this paper, the authors have presented a stress calculation formula for slender curved beams. The nonlinear deformations of slender curved beams are analyzed. The deformations and stresses of slender curved beams are simulated.

Yeong-Bin Yang et al [4] intended to derive the nonlinear differential equations of equilibrium for a horizontally curved I-beam. Based on the principle of virtual displacements, the equilibrium of a bar is established for its deformed or buckled configuration using a Lagrangian approach. Central to the consideration of the effect of curvature is the expression of various quantities in cylindrical coordinates and the incorporation of radial stresses in the virtual work statement. The governing differential equations are obtained for the curved beam as the Euler-Lagrange equations of the functional using a variational procedure. Rationality of the present theory is demonstrated for some typical examples, where the sources of errors in existing theories are traced. Also illustrated is the inconsistency involved in a conventional finite element analysis in which a curved beam is represented by several straight beam elements.

G. Mathiyazhagan et al [5] are of the opinion that the curved beams are more efficient in transfer of loads than straight beams. The transfer in the curved beam is affected by means of bending, shear and membrane action. This is particularly important in studying initially curved beams. The aim of this project is to improve the use and flexibility of curved beams in various mechanical components and structures. In this project the finite element formulation is used to analyze static and dynamic analysis of a curved cantilever beam with various cross sections, various types of curvature under various types of load and its directions, for linear elastic isotropic materials. The numerical analysis for the beam is solved by means of ANSYS and the deflection values are tabulated

**OBJECTIVES**

To find out deformation in a curved beam analyticaly and compare the same using the finite element technique.

**III. METHODOLOGY**

The deformation of the curved beam is found by using the moment and strain energy methods. Finite element analysis is carried out using ANSYS software. The results of both the methods are compared.

**IV. RESULTS AND DISCUSSIONS**

**ANALYTICAL SOLUTION**

In the present work a typical curved beam of rectangular cross section of 25 mm wide and 4 mm thick is chosen for analysis as shown in fig 1

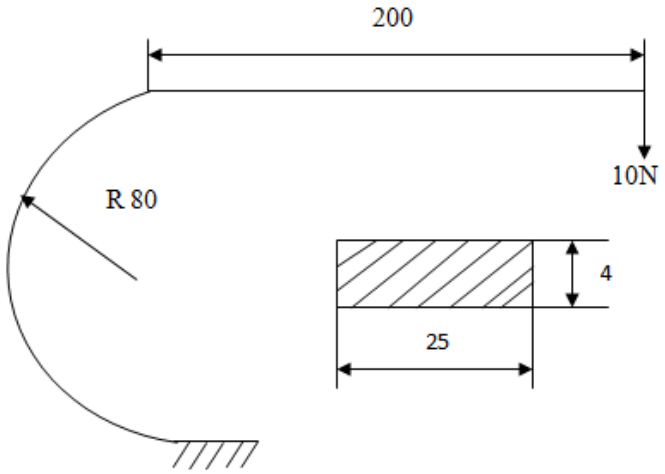


**Figure.1. A curved beam with rectangular cross section**

The chosen curved beam is subjected to a load of 10N. The material of chosen curved beam is having modulus of elasticity of 205GPa.

Considering an element of length ds on the beam, the moment $M=W(200+80\sin\theta)$

At a distance 'x' from load, moment $M=Wx$

The strain energy

$U=\int M^2 ds/2EI=1/2EI\ [\int_0^{\pi}\ [W(200+80\sin\theta)]^2\ R\ d\theta + \int_0^{200}\ (Wx)^2\ dx]$ and

$\delta=\Delta U/\Delta W =1/2EI\ [\int_0^{\pi}\ [2W(200+80\sin\theta)]^2\ R\ d\theta + \int_0^{200}\ 2Wx^2\ dx]$

$\delta=W/EI\ [8000\{432\pi - 0 -320(-1-1)\}+200^3/3]$

$\delta= 10*18.644*10^6 / 205000*(24 * 4^3/12)$

$\delta= 6.82mm$

**FINITE ELEMENT SOLUTION**

The finite element method provides a systematic procedure for the derivation of the approximation functions over sub regions of the domain. The method has three features. First one is geometrically simple sub domains called finite elements. Second, over each finite element, interpolating functions are derived using the idea that any continuous function can be represented by a linear combination of algebraic polynomials. Then the algebraic relations among the nodal values are obtained by satisfying the governing equations over each element. In the present work, the geometric model of the chosen curved beam is created using ANSYS 11 software. It is as shown in Fig

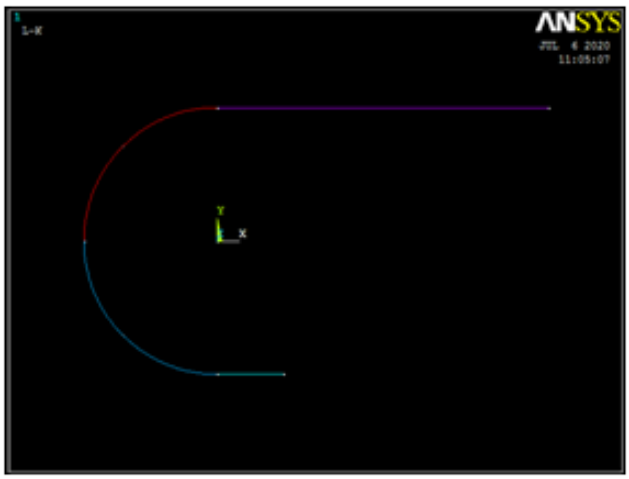


**Figure.2. Geometric model of curved beam**

The geometric model is then descretized using beam elements namely Beam 2D elastic. It is as shown in Fig 3.

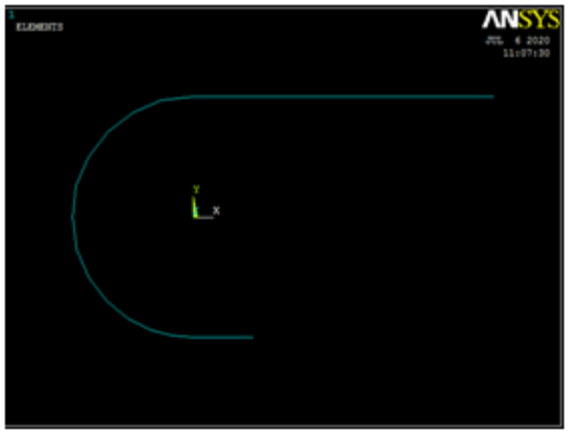


**Figure.3. Finite element model of curved beam**

The real constants for the rectangular cross section such as area of cross section and moment of inertia are calculated
Area of cross section, A = 25mm x 4mm = 100mm$^2$
Moment of inertia, I = bh$^3$ / 12 where 'b' is width of cross section, ie b=25mm. 'h' is the thickness of cross section, ie h = 4mm
I = 25 * 4$^3$ / 12 = 133.33mm$^4$
The constraints and load are applied as shown in Fig4

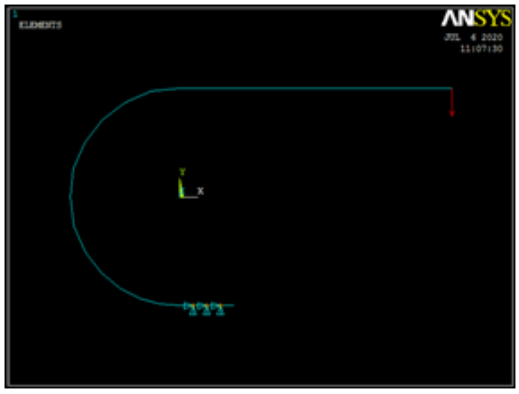


**Figure.4. Constraints and load applied**

Analysis is carried after applying the constraints. The values of deformation at various locations of curved beam are indicated. The deformation values are shown in fig 5

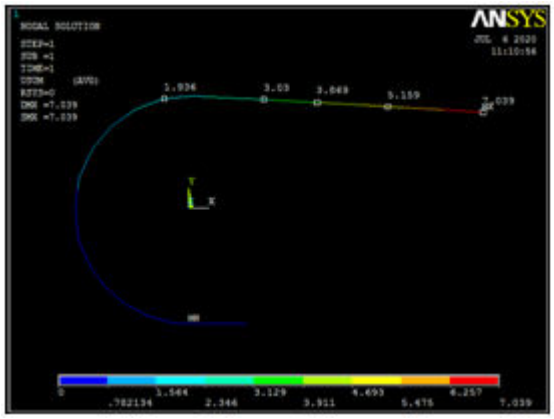


**Figure.5. Deformation values at various locations**

The deformation values from analytical and finite element method are tabulated as in table 1

**Table.1.Deformation values from analytical and finite element methods**

| Slno | Description of method | Deformation in mm |
|---|---|---|
| 1 | Analytical method | 6.82 |
| 2 | Finite element method | 7.03 |

## V. CONCLUSIONS

In the present work an attempt has been made to show the importance of using finite element method as a technique for finding out the deformation and stresses in a component with complex geometry. Solving for stresses and deformations using analytical techniques is time consuming. The curved beam is chosen for analysis. As deformation of the curved beam is essential for this application, only the deformation is calculated analytically. The deformation at the point of application of load is also found out by finite element method. The variation between analytical method and finite element method is found to be 3.1% which is quite a good approximation. From the analysis it can be concluded that the mechanical components with complex geometries such as those of curved beams can be effectively carried out using finite element technique.

## VI. REFERENCES

[1]. Souvik Das et.al,Goutam Mukhopadhyay, Sandip Bhat tacharyya Failure analysis of a40 ton crane hook at a Hot Strip Mill, MATEC Web of Conferences 165, 10006 (2018) https:// doi.org/10.1051/matecconf/201816510006 FATIGUE 2018

[2]. Kijun Kang & Jiwon Han, Analysis of a curved beam using classical and shear deformable beam theories, KSME Interna tional Journal volume 12, pages244–256(1998)

[3]. Amitkumar Premdas Chavan, Hong Zhou, Department of Mechanical Engineering, Texas A&M University-Kingsville, Kingsville, Texas, USA, Analysis and Simulation of Slender Curved Beams, International Journal of Engineering Research & Technology (IJERT), http://www.ijert.org ISSN: 2278-0181, IJERTV5IS110180, Vol. 5 Issue 11, November-2016

[4]. Yeong-Bin Yang, 1 A. M. ASCE, and Shyh-Rong K«oJ, Effect Of Curvature on Stability of Curved Beams, Article in Journal of Structural Engineering • January 1986, DOI: 10. 10 61/(ASCE)0733-9445(1987)113:6(1185)

[5]. G. Mathiyazhagan, N. Vasiraja, Finite Element Analysis on Curved Beams of Various Sections, Conference Paper • April 2013, DOI: 10.1109/ICEETS.2013.6533377

**JOURNAL OF CRITICAL REVIEWS**

ISSN- 2394-5125 VOL 7, ISSUE 17, 2020

# Mechanical Behavior of Heat Treated Al6061-Tungsten Carbide and Graphite Reinforced Hybrid Composites

**H. K. Govindaraju[1], Kiran M D[1], ARK Swamy[2], Deepak S[3] and Bhaskar Raju S A[4]**

[1]Department of Mechanical Engineering, BMS Institute of Technology and Management, Bangalore

[2] Department of Mechanical Engineering, Acharya Institute of Technology, Bangalore

[3]Department of Mechanical Engineering, MSRIT, Bangalore

[4]Department of Mechanical Engineering, DBIT, Bangalore

Received: 10 April 2020 Revised and Accepted: 26 June 2020

**ABSTRACT:** In the present investigation the mechanical behavior of 1 - 4 wt% tungsten carbide reinforced aluminum metal matrix composites and 4 wt% graphite reinforced hybrid metal matrix composites were studied. The composites were developed by liquid metallurgy technique. All the investigating composites were heat treated with T6 treatment for 1,3,5 aging period. It was found that, due to the thermal mismatch of base metal and reinforcement the mechanical properties were varied further results revealed that the tensile strength, compressive strength and hardness of MMCs and MMHCs were increased. The micrographs of the fractured surfaces confirmed the brittle fracture of the composite

**Keywords:** Tungsten carbide, Graphite, Liquid metallurgy technique, Hybrid Composites, Heat treatment

## I. INTRODUCTION

It is a well-known fact that the design of alloy composition and heat treatments of aluminum alloys and composites used in aerospace and automobiles etc., aims at a compromise between strength and damage tolerance [1]. Steels are widely used in structures and machine components. Different grades of steels are available from high strength steels to medium strength steels [3]. Now a days composite is replacing the aluminum alloys and steels wherever possible, because it is comparatively lighter in weight and resistant to corrosion[5]. The present day trend is to go in for light weight constructions for easy handling, reduced space with aesthetic appearance and high resistance to weathering attack. These factors have propelled the modern designers to develop newer composite materials up to the stage of large scale production with exacting requirements [2].

## II. MATERIALS AND METHODS

Among several series of Aluminum alloys, the AL6061 is an aluminum-magnesium-silicon alloy [4]. The chemical composition of the matrix material used in the present investigation is shown in table 1.

**Table 1 Chemical composition of base alloy (Al6061)**

| Elements | Si | Fe | Cu | Mn | Mg | Cr | Zn | Ti | Al |
|---|---|---|---|---|---|---|---|---|---|
| wt% | 0.62 | 0.23 | 0.22 | 0.03 | 0.84 | 0.22 | 0.10 | 0.1 | Bal |

Primary reinforcement material is Tungsten carbide (WC). It is commonly known as carbide. It is an inorganic compound having tungsten and carbon atoms in identical extent. In its most simple form it is a fine gray power. In the present examination WC of 5 microns size is used as primary reinforcement in preparing the composites. The wt% of WC was varied from 1 to 4 wt% in steps of 1 wt%. 4 wt% of Graphite (Gr) is used as a secondary reinforcement material in the production of hybrid composites (MMHCs).

ISSN- 2394-5125 VOL 7, ISSUE 17, 2020

The fabrication of composites was carried out by liquid metallurgy route via stir casting technique. The major components of the casting process consist of electrical resistance furnace, ceramic coated chromium steel impeller. The casted base alloy, MMCs and MMHCs were subjected to T6 heat treatment. In T6 heat treatment the casting were solutionised at a temperature of 530°C for 10 h and quenched in hot water at a temperature of 100°C, followed by natural ageing at room temperature for 12 h. Artificially aged at a temperature of 175°C for 1, 3 and 5 h respectively.

**Hardness Test**

The specimens were prepared from the as-cast and heat-treated castings according to ASTM E-10 standard. The tests were conducted on Brinell hardness testing machine with a ball indenter of diameter 10 mm with an applied load of 500 kg. The hardness was determined at four different points and the average values were recorded.

The hardness of as-cast base alloy was 55, in MMCs and MMHCs were 89 and 76 respectively for 3 wt% of WC reinforcement. This showed a significant increase in hardness of 62 % in MMCs and 39 % in MMHCs when compared with as cast base alloy. In T6 heat treated, 5 h aged base alloy, MMCs and MMHCs the observed hardness was 113, 166, and 142 respectively for 3 wt% of WC reinforcement in MMCs and MMHCs. It resulted in increase of 47 % of hardness in MMCs and 26% of hardness in MMHCs when compared with heat treated base alloy. The highest hardness was noticed in composites for 5 h aged with 3 wt% of WC reinforcement. There is a gain in hardness of 87 % due to heat treatment in both MMCs and MMHCs when compared with as-cast composites. In T6 heat treated Al6061-3wt%WC MMCs and Al6061-3wt%WC-4wt%Gr MMHCs the highest hardness was observed in 5 h aging time. It shows an improvement of 96% and 90% respectively when compared with T6 heat treated base alloy.

Fig 2(a) and 2(b) shows the effect of hardness with the tungsten carbide reinforcement on the of as-cast and T6 heat treated Al6061 base alloy, Al6061-WC MMCs and Al6061-WC-Gr MMHCs. It was observed that the hardness of composites increased significantly with increase in percentage of WC reinforcement upto 3 wt%. At 4 wt% and above led to the rejection of particulates from the melt during preparation through liquid metallurgy technique. The presence of denser particulates in the melt caused the settling of particulates at the bottom of the furnace, which resulted in decrease of hardness.

In the present study 3 wt% WC reinforced and 5 h aged MMCs and MMHCs have showed highest hardness. Highest hardness was observed in MMCs when compared with MMHCs. The improvement in the hardness of the composites with increased content of reinforcement mainly attributed to the higher hardness of the WC reinforcement. Increase in content of reinforcement in the matrix alloy leads to increase in hardness.

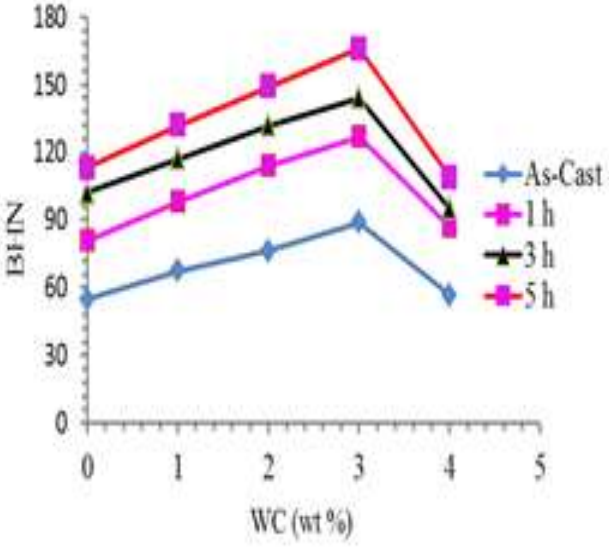


**Fig2(a) Hardness variation with WC reinforcement in base alloy Al6061, Al6061-WC MMCs**

ISSN- 2394-5125 VOL 7, ISSUE 17, 2020

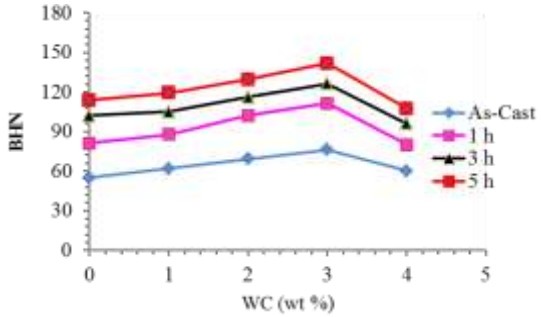


**Fig2(b) Hardness variation with WC reinforcement in base alloy Al6061, Al6061-WC-Gr MMHCs**

**Tensile Test**

The tests were conducted on computerized universal testing machine according to ASTM-E8 standard testing procedure. In order to ensure the consistency of the material properties multiple tests were conducted the average values were reported. The tests were conducted on computerized universal testing machine according to ASTM-E8 standard testing procedure. In order to ensure the consistency of the material properties multiple tests were conducted the average values were reported in fig 3(a) and Fig 3(b).

From the tensile test it was found that the tensile strength of base alloy was 96 MPa. The tensile strength of as-cast MMCs were 123, 143, 165 and 97 MPa respectively for 1, 2, 3 and 4 wt% of WC reinforcement. In as-cast MMHCs the tensile strengths reported were 125, 144, 167 and 102 MPa respectively for 1, 2, 3 and 4 wt% WC. In as-cast MMCs and MMHCs the tensile strength was increased with increase in percentage of WC reinforcement. At 3 wt% WC of reinforcement the strength was enhanced upto 72 % and 74% in MMCs and MMHCs respectively when compared with base alloy. At 4 wt% of WC reinforcement the strength was decreased in both the composites. The particulates rejected from the melt, due to the denser particulates of WC reinforcement. The increase in tensile strength was attributed to the presence of hard WC particulates that impart strength to the matrix alloy. Highest ultimate tensile strength was observed at 3 wt% of WC reinforcement in MMCs and MMHCs.

The tensile strength increased significantly in T6 heat treated MMCs and MMHCs. In MMCs the tensile strength is of the order of 257, 297 and 329 MPa for 1, 3, and 5 h aging time respectively at 3 wt% WC reinforcement. Whereas in case of MMHCs the tensile strength was 266, 302 and 336 MPa, for 1, 3 and 5 h aging time respectively for 3 wt% of WC. The increase in strength was marginal in MMHCs when compared to MMCs**.** The effect of reinforcement on the tensile strength of Al6061 alloy, MMCs and MMHCs for as-cast and heat treated conditions. It was observed that the tensile strength increased with increase in WC reinforcement (0 to 3 wt %) and ageing time (1 to 5 h). When the percentage of WC was increased beyond 3 wt%, the tensile strength decreased. From the results of the analysis it was found that 3 wt% WC with 5 h aged MMCs and MMHCs have shown best tensile strength.

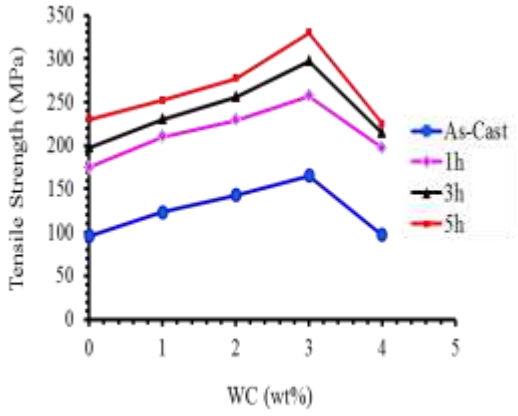


**Fig.3(a) Variation of ultimate tensile strength with WC reinforcement in base alloy Al6061, Al6061-WC MMCs**

ISSN- 2394-5125 VOL 7, ISSUE 17, 2020

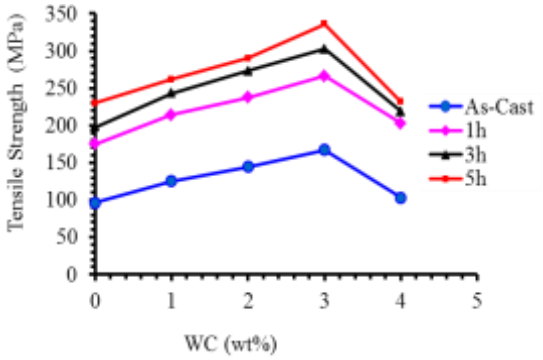


**Fig.3 (b) Variation of ultimate tensile strength with WC reinforcement in base alloy Al6061, Al6061-WC-Gr MMHCs**

From the result analysis it was found that the yield strength of the as-cast base alloy was 69 MPa and in as-cast MMCs at 1, 2, 3 and 4 wt% of WC reinforcement the yield strength was 94, 107, 118 and 77 MPa respectively. This shows the highest yield strength in MMCs at 3 wt% WC reinforcement. It showed an improvement 71 % in yield strength as compared with as-cast base alloy in 3 wt% WC. The yield strength of as-cast MMHCs was 97, 118, 131 and 101 MPa respectively for 1, 2, 3 and 4 wt% WC shown in Table 2.

]

**Table 2 Yield strength of heat treated MMCs and MMHCs**

| Materials | Composition | $\sigma_y$ (MPa) | | | |
|---|---|---|---|---|---|
| | | As-cast | 1h | 3h | 5h |
| Base alloy | Al6061 | 69±2 | 138±6 | 150±5 | 175±5 |
| MMCs | Al6061-1wt%WC | 94± 4 | 178±5 | 194±6 | 218±4 |
| | Al6061-2wt%WC | 107±4 | 186±4 | 207±4 | 237±6 |
| | **Al6061-3wt%WC** | **118±2** | **206±3** | **228±4** | **272±4** |
| | Al6061-4wt%WC | 77± 2 | 154±4 | 168±3 | 181±3 |
| MMHCs | Al6061-1wt%WC-4wt%Gr | 97± 3 | 192±5 | 213±3 | 242±4 |
| | Al6061-2wt%WC-4wt%Gr | 118±3 | 216±3 | 239±4 | 266±5 |
| | **Al6061-3wt%WC-4wt%Gr** | **131±2** | **239±4** | **263±5** | **309±4** |
| | Al6061-4wt%WC-4wt%Gr | 101±3 | 182±5 | 205±4 | 219±4 |

Yield strength was increased upto 90% with increase in WC reinforcement upto 3 wt%. The effect of reinforcement on yield strength of Al6061 alloy, Al6061-WC, and Al6061-WC-Gr hybrid composites for as-cast and T6 heat treated condition. Linear increase in strength was observed with the increase in WC reinforcement (0 to 3 wt %) and ageing time (1, 3 & 5 h). The highest strength was observed in MMCs and MMHCs for 3 wt% of WC reinforcement at 5 h ageing time. At 4 wt% of WC reinforcement the yield strength was decreased. Percentage of elongation for the as-cast base alloy, MMCs and MMHCs. The percentage of elongation was reduced marginally in as-cast MMCs and MMHCs when compared with as-cast base alloy. The values of percentage of elongation of T6 heat treated MMCs and MMHCs for different ageing time were shown in Table 3**.**

In T6 heat treated MMCs the ductility increased significantly with the aging time when compared with as-cast base alloy. It was observed that for the 3 wt% WC reinforcement MMCs the ductility was decreased by 23, 20 and 16 % for 1, 3 and 5h aging respectively when compared heat treated base alloy. Similarly in MMHCs the ductility decreased by 11, 11 and 8 % for 1, 3 and 5 h aging time respectively with respect to heat treated base alloy. The addition of graphite in MMHCs showed an improvement in ductility of the MMHCs when compared

ISSN- 2394-5125 VOL 7, ISSUE 17, 2020

with MMCs. Also, it was observed that ductility increased by 26 % and 29 % in MMCs and MMHCs due to heat treatment, which leads to the conclusion that ductility increases due to the heat treatment and addition of graphite.

The effect of reinforcement content and T6 heat treatment on the ductility of the investigating composites in terms of percentage of elongation. In as-cast MMCs, as the reinforcement content increases, the ductility decreased by 24 % with the increase of WC content from 0 to 3 wt%, and in as-cast MMHCs as the reinforcement content increases the ductility of the composite material decreases marginally. With the increase of WC reinforcement from 0 to 3 wt% the ductility was found to decrease by 12 %. When compared with the MMCs the ductility was improved in MMHCs due to addition of Graphite.

**Table 3 Percentage of elongation of heat treated MMCs and MMHCs**

| Composite materials | Composition | Elongation (%) | | | |
|---|---|---|---|---|---|
| | | As-cast | 1h | 3h | 5h |
| Base alloy | Al6061 | 5.0±0.5 | 5.3±0.5 | 5.5±0.4 | 5.7±0.6 |
| MMCs | Al6061-1wt%WC | 4.7±0.7 | 4.9±0.6 | 5.2±0.5 | 5.5±0.6 |
| | Al6061-2wt%WC | 4.4±0.6 | 4.7±0.4 | 4.9±0.5 | 5.3±0.5 |
| | **Al6061-3wt%WC** | 3.8±0.8 | 4.1±0.6 | 4.4±0.4 | 4.8±0.4 |
| | Al6061-4wt%WC | 3.3±0.5 | 3.3±0.6 | 3.7±0.6 | 3.9±0.4 |
| MMHCs | Al6061-1wt%WC-4wt%Gr | 4.7±0.4 | 5.2±0.6 | 5.4±0.6 | 5.6±0.4 |
| | Al6061-2wt%WC-4wt%Gr | 4.5±0.4 | 4.9±0.6 | 5.1±0.5 | 5.4±0.6 |
| | **Al6061-3wt%WC-4wt%Gr** | 3.8±0.5 | 4.7±0.4 | 4.9±0.5 | 5.3±0.5 |
| | Al6061-4wt%WC-4wt%Gr | 3.1±0.4 | 3.6±0.5 | 4.1±0.6 | 4.2±0.4 |

The addition of graphite as secondary reinforcement eases the movement of grains along the slip planes which explains the improvement in ductility in MMHCs compared to MMCs. The results obtained were in close agreement with the results of other researchers having observed that the ductility of the composites decreases with the increase in hard reinforcement content.

The decrease in ductility in comparison with the base alloy is a most commonly encountered disadvantage in discontinuously reinforced MMCs [8].

## III. COMPRESSION TEST

The specimens were prepared from the castings of as-cast and T6 heat treated base alloy, MMCs and MMHCs. The compression tests were conducted on computerized universal testing machine according to ASTM-E9 standard testing procedures. In order to ensure the consistency of the material property the multiple tests were conducted and the average values are shown in Table 4.

From the result analysis it was found that the compressive strength was 570 MPa. The compressive strength of as-cast MMCs at 1, 2, 3 and 4 wt% WC reinforcement were 696, 823, 846 and 743 MPa respectively. It shows upto 3 wt% of WC reinforcement the compressive strength was increased progressively. At 3 wt% of WC reinforcement 48% of higher compressive strength was observed when compared with base alloy.

The compressive strength of as-cast MMHCs are 756, 864, 918 and 821 MPa respectively for 1, 2, 3 and 4 wt% of WC reinforcement. Similar trend was observed in the compressive behavior of MMHCs at all wt% of WC reinforcement. The compressive strength of MMHCs was higher than MMCs in as-cast condition. It shows an improvement of 60% in compression strength when compared with base alloy. Also shows the marginal increase in compressive strength when compared with MMCs.

ISSN- 2394-5125 VOL 7, ISSUE 17, 2020

**Table 4 Compressive strength of investigating composites**

| Composite materials | Composition | Compressive strength (MPa) | | | |
|---|---|---|---|---|---|
| | | As-cast | 1h | 3h | 5h |
| Base alloy | Al6061 | 570±8 | 726±7 | 816±6 | 898±8 |
| MMCs | Al6061-1wt%WC | 696±9 | 958±8 | 1063±9 | 1170±7 |
| | Al6061-2wt%WC | 823±7 | 1071±7 | 1186±8 | 1279±9 |
| | **Al6061-3wt%WC** | **846±7** | **1139±9** | **1229±8** | **1314±8** |
| | Al6061-4wt%WC | 743±6 | 950±6 | 1047±7 | 1135±8 |
| MMHCs | Al6061-1wt%WC-4wt%Gr | 756±8 | 1032±9 | 1123±8 | 1227±7 |
| | Al6061-2wt%WC-4wt%Gr | 864±6 | 1125±6 | 1234±6 | 1362±6 |
| | **Al6061-3wt%WC-4wt%Gr** | **918±9** | **1183±8** | **1332±7** | **1457±7** |
| | Al6061-4wt%WC-4wt%Gr | 821±6 | 1064±7 | 1154±7 | 1291±8 |

The test results of T6 heat treated base alloy and composites for 1, 3 and 5h aging time were reported in Table6, 3 wt% of WC reinforced and 5 h aged MMCs and MMHCs have shown the highest compressive strength. The compressive strength of base alloy was 898 MPa and that of MMCs and MMHCs were 1314 MPa and 1457 MPa respectively. It shows an improvement of 46% and 62% respectively for MMCs and MMHCs. when compared with MMCs, the marginal improvement in compressive strength was observed in MMHCs. The compressive strength was reduced at 4 wt% of WC reinforcement in both the composites due to the rejection of particulates from the melt at higher density of WC.

In T6 heat treated 3 wt% of WC reinforced MMCs the compressive strength was increased for 1, 3 and 5 h aging in the order of 34.7, 45.36 and 55.37 % respectively when compared with heat treated base alloy. Similar improvement in compressive strength was observed for Metal Matrix Hybrid Composites (MMHCs) and there was a significant improvement in T6 heat treated MMHCs, the compressive strength was increased in the order of 28, 45 and 59 % for 1, 3 and 5 h aging time when compared with base alloy.

It was observed that the compressive strength was increased by 55% and 59% due to heat treatment in MMCs and MMHCs when compared with as-cast composites, which leads to the conclusion that the compressive strength of MMCs and MMHCs increased significantly with heat treatment. Heat treatment played an important role in making the strong bonding between reinforcement particles and aluminium matrix [13]. Hence the load sharing from matrix to reinforcements was increased and hence the load bearing capacity of the composites increased.

## IV. DENSITY

Density was determined experimentally and compared with the theoretical values, which have been evaluated by the rule of mixtures [12]. The density of the MMCs and MMHCs were linearly increased with the increase in percentage of wt% of WC reinforcement. The experimental and the theoretical density values were in line with each other, which conclude the uniform distribution of reinforcements in composites. Very small variation was observed between the experimental and theoretical density values.

All the calculated and experimentally measured density values are shown in Table 5. The density of Al6061 base alloy is 2.71 g/cc. The density of MMCs and MMHCs were increased when compared with the base alloy. At 4 wt% WC reinforcement the density of MMCs and MMHCs were 3.06 and 3.10 g/cc. It shows 14% and 15% increase in density of MMCs and MMHCs. The increase in density of the composites was attributed to the fact that the reinforcement material tungsten carbide (WC) possesses higher density than Al6061 base alloy. Highest density was observed in MMHCs when compared with MMCs, this may be due to the presence of graphite reinforcement. The increase in density of the composite in comparison with that of matrix material was mainly due to the higher density of reinforcement material.

ISSN- 2394-5125 VOL 7, ISSUE 17, 2020

**Table 5 Density of the investigating composites**

| Composite materials | Composition | Density (g/cc) | |
|---|---|---|---|
| | | Theoretical | Experimental |
| Base alloy | Al6061 | 2.71 | 2.68 |
| MMCs | Al6061-1wt%WC | 2.79 | 2.77 |
| | Al6061-2wt%WC | 2.90 | 2.87 |
| | **Al6061-3wt%WC** | **3.02** | **2.98** |
| | Al6061-4wt%WC | 3.13 | 3.06 |
| MMHCs | Al6061-1wt%WC-4wt%Gr | 2.81 | 2.8 |
| | Al6061-2wt%WC-4wt%Gr | 2.92 | 2.91 |
| | **Al6061-3wt%WC-4wt%Gr** | **3.03** | **3.02** |
| | Al6061-4wt%WC-4wt%Gr | 3.15 | 3.10 |

## FRACTOGRAPHIC EXAMINATION

The tensile fractured specimen surfaces were closely examined using SEM analysis. The tensile fractured surface of the as-cast Al6061alloy, MMCs and MMHCs. In Al6061 alloy dendritic arm spacing is very large when compared with MMCs and MMHCs. The fractured surface shows brittle failure, in which deep dimples were present in all the experimental composites. This is evident from the that shallow dimples were observed in MMCs and MMHCs which promote the brittle fracture.

The fractograph of heat treated base alloy, MMCs and MMHCs. The fracture surface shows suitable bonding between reinforcements and matrix alloy. The failure surfaces composed of pulled regions and a few cracked particles. The heat treated composites shows more dimples and plastic deformation was observed in MMCs and MMHCs as compared to as-cast composites. The fracture in both as-cast and heat treated composite was promoted by delamination at the particulate surface.

The fractured surfaces consist of more number of particles. Some particles were broken and pulled out. It was also found that the plastic dimples in the fractured surfaces of the MMCHs increased, resulting an increase in the strength of the composites.

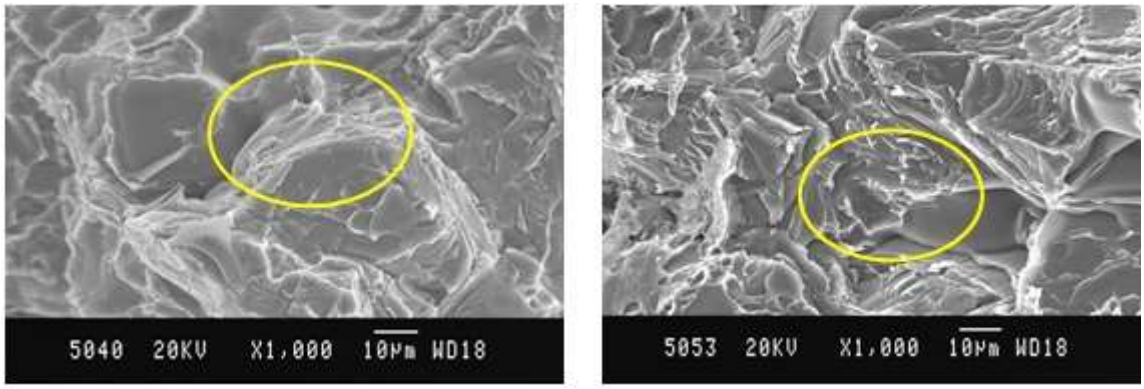


**SEM of tensile fractured surfaces of as-cast investigating composites Fig4(a) Al6061-3wt%WC, Fig4(b)Al6061-3wt%WC+4%Gr**

ISSN- 2394-5125 VOL 7, ISSUE 17, 2020

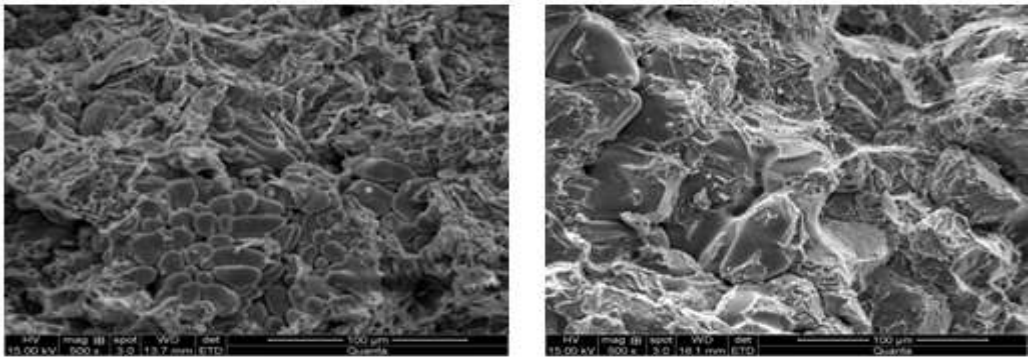

**SEM of heat treated tensile fractured surfaces of investigating composites Fig4(a) Al6061-3wt%WC, Fig4(b)Al6061-3wt%WC+4%Gr**

## V. CONCLUSIONS

From the results and analysis of the investigation the following conclusions were drawn on the mechanical and wear behavior of as-cast and T6 heat treated (1, 3, 5h aging time) base alloy, MMCs (Al6061-WC) and MMHCs (Al6061-WC-Gr).

- From the liquid metallurgy techniques Al6061base alloy, Al6061-WC MMCs and Al6061-WC –Gr MMHCs composites were prepared successfully.
- In T6 heat treated Al6061-3wt%WC MMCs and Al6061-3wt%WC-4wt%Gr MMHCs the highest hardness was observed in 5 h aging time. It shows an improvement of 96% and 90% respectively when compared with T6 heat treated base alloy.
- In T6 heat treated, 5 h aged base alloy, Al6061-3wt%WC MMCs and Al6061-3wt%WC-4wt%Gr MMHCs had shown the ultimate tensile strength of 230, 329 and 336 MPa. This shows an improvement of 109% and 113% respectively when compared with heat treated base alloy. Al6061-3wt%WC-4wt%Gr MMHCs have shown highest tensile strength.
- The compressive strength of heat treated 5 h aged base alloy, Al6061-3wt%WC MMCs and MMHCs are 898, 1314 and 1457 MPa respectively. This shown an improvement of 46% and 62% when compared with the heat treated base alloy.
- From the investigation it was concluded that, composites containing 3 wt% tungsten carbide and 4 wt% graphite reinforcements with 5 h ageing time exhibited superior mechanical properties.

## VI. REFERENCES

[1]. D. Dumont, A. Deschamps, Y. Brechet, (2003), "On the relationship between microstructure, strength and toughness in AA7050 aluminum alloy", Material Science and Engineering Vol. 356, pp. 326 – 336.

[2]. Zhihui Li, X. Baiqing, Z. Yongan , Z. Baohong, W. Feng, L. Hongwei, (2009), "Investigation on strength, toughness and microstructure of an Al–Zn–Mg–Cu alloy pre-stretched thick plates in various ageing tempers", Journal of Materials Processing Technology Vol. 209, pp. 2021–2027.

[3]. J. Gilbert Kaufman, (2002), "Properties of Aluminum Alloys; Tensile, Creep, and Fatigue Data at High and Low Temperatures", ASM International.

[4]. Farid Akhtar, (2009), "Synthesis, Microstructure and Mechanical Properties of Al203 Reinforced Ni3Al matrix composites," Material Science and Engineering, A, Vol.499, pp.415-420.

[5]. C.S. Ramesh, R. Keshavamurthy, B.H. Channabasappa, S. Pramod, (2009), "Influence of heat treatment on slurry erosive wear resistance of Al6061 alloy, Materials and Design" Vol. 30, pp 3713–3722.

[6]. N. Wang, Z. Wang, G.C. Weatherly, (1992), "Formation of Magnesium Aluminate (spinel) in Cast SiC Particulate-Reinforced Al(A356) Metal Matrix Composites", Metallurgical and Materials Transactions A, Vol. 23, pp. 1423-1430.

ISSN- 2394-5125 VOL 7, ISSUE 17, 2020

[7]. H. Ribes, M. Surely, G.L' Esperance, J.G. Legoux, (1990), "Microscopic examination of the interface region in 6061-Al/SiC composites reinforced with as-received and oxidized SiC particles", Metallurgical and Materials Transaction A, Vol. 21, pp. 2489-2496.

[8]. K. Komai, K. Minoshima, H. Ryoson, (1993), "Tensile and fatigue fracture behavior and water-environment effects in a SiC-whisker/7075-aluminum composite", Composites Science and Technology, Vol. 46, pp. 59-66.

[9]. Rupa Dasgupta, Humaira Meenai, (2005), "SiC particulate dispersed composites of an Al–Zn–Mg–Cu alloy: Property comparison with parent alloy", Materials Characterization, Vol. 54, pp. 438-445.

[10]. B. Torres, M. Campo, J. Rams, (2009), "Properties and microstructure of Al-11Si/SiCp composite coatings fabricated by thermal spray surfaces and coatings technology", Vol. 203, pp. 1947-1955.

[11]. Rong Chen, Akira Iwabuchi, Tomoharu Shimizu, (2000), "The effect of a T6 heat treatment on the fretting wear of SiC particle-reinforced A356 aluminium alloy matrix composite", Wear Vol 238, 110-119.

[12]. Prem Shankar Sahu, R. Banchhor(2016), "Fabrication methods used to prepare Al metal matrix composites- A review", International Research Journal of Engineering and Technology (IRJET), Volume: 03 Issue: 10 | Oct -2016.

[13]. A. K. Jha, G. S. Upadhyaya, (1983), "Properties of sintered 2014 aluminium alloy composite containing WC", Journal of materials science, Vol. 2, pp. 801-804.

[14]. H. R. Lashgari, Sh. Zangeneh, H. Shahmir, M. Saghafi, M. Emamy, (2010), "Heat treatment effect on the microstructure, tensile properties and dry sliding wear behavior of A356–10%B4C cast composites", Materials and Design, Vol. 31, pp. 4414–4422.

JOURNAL OF CRITICAL REVIEWS

ISSN- 2394-5125 VOL 7, ISSUE 15, 2020

# Dry sliding wear behaviour of short Carbon fibre reinforced aluminium matrix composites

**Nithin Kumar[1], Ezhil Vannan.S[2], Kiran M D.[3], Vincent Linish Dsouza[4], Madeva Nagaral [5]**

[1] Assistant Professor, Department of Mechanical Engineering, NMAMIT, Nitte, 574110, India
[2] Professor, Department of Mechanical Engineering, Malnad college of Engineering, Hassan-573202, India
[3]Assistant Professor, Department of Mechanical Engineering, BMS Institute of Technology and Management, India
[4]Assistant Professor, Department of Mechanical Engineering, NMAMIT, Nitte, 574110, India
[5]Deputy Manager, Aircraft research and design center, HAL, Bengaluru, 560037, India

Received: 17 March 2020 Revised and Accepted: 20 June 2020

**ABSTRACT:** In the present research work, the dry sliding wear behavior of nickel coated short carbon fibers (NCSCFs) reinforced aluminummatrix compositewere studied. The composites were fabricated by liquid metallurgy technique by varying with 2, 4, 6 & 8 wt% ofNCSCFs.The wear rateswere evaluated using a pin-on-disc wear-testing machine by varying the loads. The effects of percentageof fiber content, normal load, sliding speed, and wearmechanism were investigated. The results indicated that Al/NCSCFs composite had lower rates than that of Al alloy. The wear rates of the composites decreased with the increase of NCSCFs content.However, wear rates increased with the increase in normal load and rotating speed in both composites and Al alloy. NCSCF develops direct bridge gap between the matrix and counterpart thus, results in improving the better wear resistance in Al/NCSCFs composite.Theworn and fractured surfaces ofboth Al/NCSCFs compositeand Al alloy werecharacterized using SEM

**KEYWORDS:** Al alloy, NCSCF, sliding wear, wear resistance.

## I. INTRODUCTION

Over the decades,metal matrix composites (MMC) has drawn the attention of many investigators to carry the research onaluminiumbased MMC's due to its excellent combination of properties such as higher mechanical strength,young's modulus and good wear resistance [1]. AluminiumMMC's are widely used in automotive industry because of its good strength at high temperature, high weight ratio, high thermal conductivity [2], good dimensional stability and high structural rigidity[3]. AluminiumMMC's are particularly used in automobile like cylinder liners, brake rotors, connecting rods, drive shafts, pistons and reciprocating part, components of brake-system, engine blocks andaerospace industries and defence equipment's [2-3].Although aluminum and its alloy are known for excellent mechanical properties as well as corrosion resistance but in term of wear properties, they are poor. Hence, a strong drives to develop newer material to achieve the better tribological properties [4-5]. Hence, requirements for enhancements in wear resistance and service loads of materials in all these applications has forced researchers to develop and synthesise aluminium based composites.There are many fibres used as reinforcement for aluminium alloy, among that carbon fibre has been used as appealing reinforcements, which enhacethe wear resistance of the part and also reduces the coefficient of friction while maintaining its remarkable properties such as light weight, high specific strength, high thermal and electrical conductivity, high stiffness, specific modulus,low coefficient of thermal expansion and good self-lubricating abilities [6–7].

In spite of many advantages, the applications of carbon reinforced aluminum composite are limited by the industries due to its manufacturing problem [8]. Many researchers have carried out the investigations of fiber reinforced aluminum composites focusing on casting process and uniform distribution of reinforcement, but very limited study is reported about wear and coefficient of friction. Liu Leiet al. [9] studied the friction and wear properties of carbon reinforced aluminum matrix composites the results show that with short carbon fiber content the wear resistance was improved andwear rate was reduced. Daoud et al. [10] investigated CF/2014 Alalloy composites for their wear performance, his finding showed the wear resistance was improved significantly with incorporation of carbon fiber and improvement in seizure resistance.EzhilVannan.Set al. [11] studied the effect of basalt fiber on dry sliding wear behavior of basalt fiber reinforced alumiunium metal matrix composites reported that the wear rate decreased with increase in weight percentage of copper coated fiber basalt fiber. B.Venkataraman et al. [12] investigated the dry sliding wear condition of wear behavior of SiC particulate reinforced aluminiummatrix composites (Al-SiC) suggested that a strong correlation exist between friction and wear transition behavior. Kong et al. [13]studiedcarbon

fiber/Al felt composites for their tribological behavior and concluded that wear resistance can be improved with the presence of carbon film. In the case of Al6061 reinforced with $TiO_2$, it was observed that composites exhibit lower wear coefficient, exhibits better hardness as compared with the matrix alloy [14]. The volumetric wear loss is high because of increased loads and sliding distances, but the coefficient of wear is low in both matrix alloy and its composites. The high strength aluminium alloys Al7010, Al7009 and Al2024 reinforced with SiC particles exhibits significantly better sliding wear characteristics than that of alloys due to the addition of SiC particles [15]. Aluminium matrix composites reinforced with short steel fibres shows decrease in wear rate by increasing the reinforcement fibres decreased the rate of wear and coefficient of friction at different loading conditions [16]. Metal matrix composite of aluminium-7075 with nickel coated carbon fibers in the form of short fibers shows increasing in fatigue strength with increase in reinforcement loading [17]. Surface coating on carbon fibers increase the wettability and it increases the interfacial reaction between matrix and carbon. And it overcomes the arduous of obtaining better interface bonding between fibers matrix. Coating of nickel on surface of carbon fiber exhibits better interface bonding among matrix and fibers and also increases the oxidization resistance, strength of the composites with both metal and polymer matrix [18-19].

In present investigation, Al7075 alloy composite reinforced by NCSCFs were prepared by Liquid metallurgy process. The tribological behavior of Al7075 alloy and NCSCFs/Al7075 were methodically studied using Pin-on-Disc method.The surface, subsurface and the fragments are studied using scanning electron microscopy to analyse the wear mechanisms.

## II. Experimental

2.1. Sample preparation

In this study, Al7075 alloy is used as base matrix. The chemical composition of Al7075 is as shown in the table 1. Nickel coated short carbon fiber were used as reinforcement, long polyacrylonitrile (PAN)based carbon fibers were cut into short fiber to length about 1.0-1.5 mm after being dispersed.The properties of polyacrylonitrile(PAN) based fiber are: density is 1.76g/cm$^3$, average diameter of fiber is 7μm. The short fibers were coated with nickel deposition using electroless coatingtechnique; the reason was due to poor wettability between the matrix and reinforcement. The Composites were prepared by reinforcing Al7075 alloy with varying weight percentage of 0, 2, 4, 6 and 8 of carbon fibres coated with nickel using stir casting process.The matrix Al7075 was heated above its melting temperatureupto700$^0$C; at this temperature around 1% of magnesium metal powder is mixed with the molten metal.

**Table 1. The chemical composition of Aluminium alloy (wt. %)**

| Alloying Element | Si | Fe | Cu | Mn | Mg | Cr | Zn | Ti | Al |
|---|---|---|---|---|---|---|---|---|---|
| Weight % | 0.4 | 0.5 | 1.6 | 0.3 | 2.5 | 0.15 | 5.5 | 0.2 | Bal |

2.2. Wear tests

For wear testing, the specimens had been prepared with the size of Pin-on-Disc specimen measuring 8mm in dia. and 20mm height consistent with the ASTM G99 standard. All the specimens followed a single-track 115mm in diameter, with the tangential force during sliding is monitored by a force transducer continuously which is attached to the specimen holder. The coefficient of friction (μ) is obtained as the ratio of the tangential force to the normal force. The test is performed with a load range of 20N to 50 N at a sliding velocity of 7.35m/s to 31.5m/s and with a sliding distance of 2km. The specific gravity measurements were performed consistent with ASTM C127-88 Standard. For every load, volume losses from the surface of specimens had been determined as a feature of sliding distance, sliding velocity, and applied load. [20].

**Fig. 1Pin-on-Disc Test rig**

## III. Results and discussion

### 3.1 Wear Behaviour

The effects of reinforcement on wear rate were studied and found that Al/NCSCFs composite has superiortribologicalcharacteristics than Aluminium alloy. It was also observed that the wear resistance of the composite improved significantly with the increase in NCSCFs content. An investigation was carried out to study the effects of reinforcement on both applied load and sliding speed. Fig. 2(a) to 2(d) shows the graphs of sliding velocity vs wear rates of the Al/NCSCFs composites and Al alloy specimens at an applied load of 20, 30 and 40 N, respectively. From the graph, it is evident that the composite with 8 wt. % NCSCFs has the least wear rate for normal loads ranging from 10-40 N with increasing sliding distance at 300 RPM and also similar trends were observed for the same normal loads at 400 RPM and 500 RPM. However, for the initial sliding distance, the wear rate increased, after some duration, it decreased and then remained almost constant for the entire duration of the test.

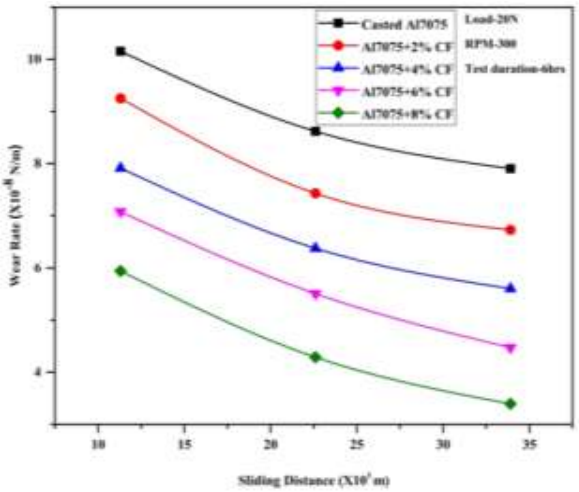


**Fig. 2(b) Wear rate at 20N load**

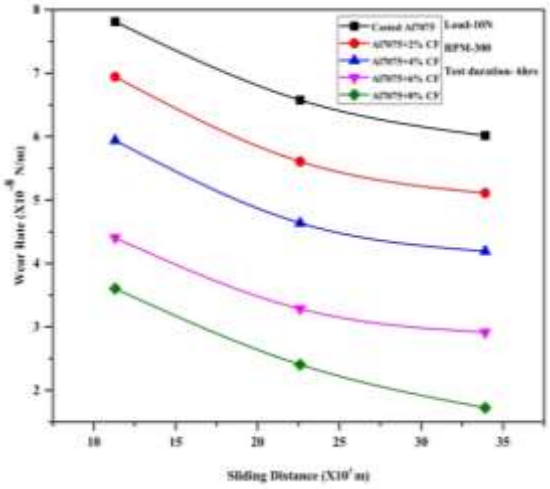


**Fig. 2(a)Wear rate at 10N load**

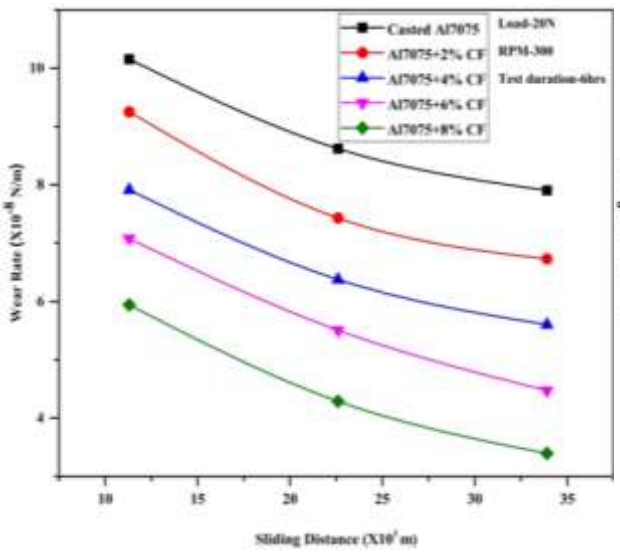


**Fig. 2(c)Wear rate at 30N load**

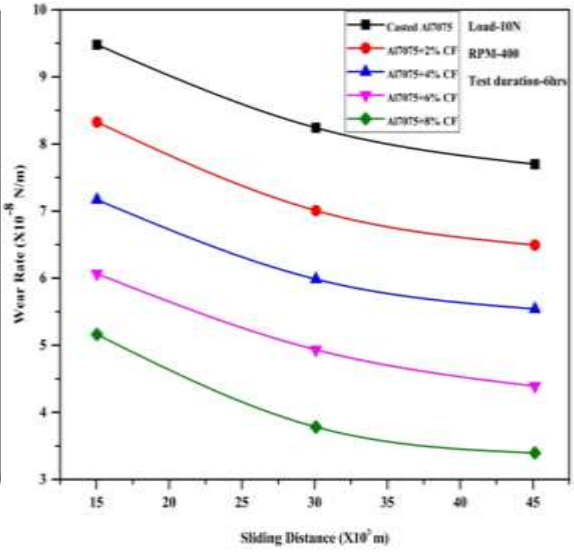


**Fig. 2(d) Wear rate at 40N load**

Fig. 3shows the result of normal load and rotational speed at 300 rpm on volumetric wear rateofAl/NCSCFs composites. The results indicate that the volumetric wear rate of both Al/NCSCFs compositesand Al alloy increased with the increase in normal load and showed almost linear trend.Owing to the fact that, for significantly greater amounts of normal load, the frictional thrust was observed to have increased and resulted in increased de-bonding and fracture that caused more volumetric wear loss. From the graph it is evident that the composite with 8 wt.% NCSCFshas least volumetric wear ratewhen compared to Al alloy.An additional increase in the load triggered the commencement of delamination which resulted in a higher volumetric wear rate for both, the Al alloy and its composites as observed by several researchers [23-25]. Similar trendswere observed at 400 and 500 rpm.

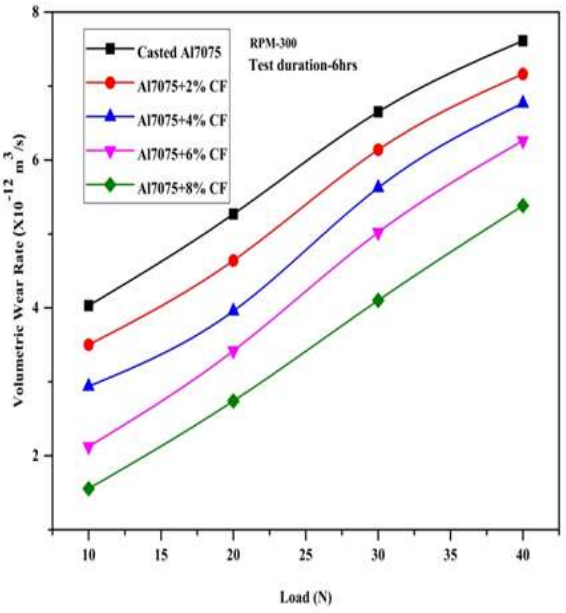


**Fig. 3Volumetric Wear rate at normal load and 300rpm**

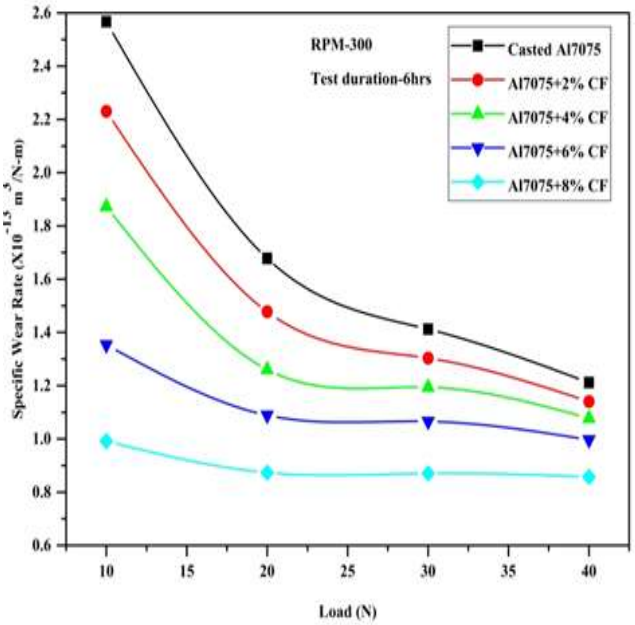


**Fig. 4 Specific Wear rate at normal load and 300rpm**

ISSN- 2394-5125VOL 7, ISSUE 15, 2020

Fig. 4shows the result of normal load and rotation speed at 300 rpm on specific wear rate ofAl/NCSCFs composites. The results indicate that the specificwear rate of both Al/NCSCFs compositesand Al alloy decreased with the increase in normal load with speed at 300 rpm. From the graph it is evident that the specific wear rate for Al/NCSCFs composites with 8 wt% NCSCFsshowed a nearly horizontal trend and was found to be much lesser in comparison with Al alloy. The reason being for lower speeds and loads, the difference between the specific wear rate for each specimen was found to be large which decreased with the increase in speed and load. However, for higher speeds of 400RPM and 500 RPM, the rate of specific wear decreases with the increase in normal load values including the 8 wt.% reinforced composite specimen.

3.2 Effect of reinforcement on the wear resistance

The effect of reinforcement on wear resistance is study at different load and speed. It has been observed from the graph that at both 30N and 40 N, the Al alloy seizes as sliding distance is increased, whilethe Al/NCSCFs compositeshad better wear resistance. At highload of 40N, only the 8% carbon fiber reinforced Al composite has better wear resistance, where as the pure Al alloy, 2, 4 and 6 % carbon fiber reinforced composites has high wear rate, which indicates that as reinforcement content is increased than the wear rate of the material is reduced indicating thepositive effect of the reinforcing.

3.3 Wear mechanism

In order to comprehend the wear mechanism of Al alloy and its composite, SEM micrographs observation of the wear surfaces was carried out.A typical worn surface ofthe Al alloy and Al/NCSCFs composites with 4% and 8% carbon fiber is shown in Fig.5.In order to comprehend the wear mechanism of Al alloy and its composite, SEM micrographs observation of the wear

surfaces was carried out. A typical worn surface ofthe Al alloy and Al/NCSCFs composites with 4% and 8% carbon fiber is shown in Fig.5. It is observed that Al alloy shows composition of deep grooves and small debris, indicating the presence of damages occurred due to plastic deformation. Further, some flake shape pieces began to peel off from fracture surface of Al alloy as worn surface becomes soft due increase in surface temperature. The worn surface of Al/NCSCFs composites with 4% and 8% carbon fibershow rough surfaces due to removal of material and also formation of white layers at the top most worn out surface, indicate that the temperature at the surfaces is very high.Moreover, presence of NCSCFs deforms the Al alloy, results a decrease of mass loss. It is observed that as the load increases, the fine scratches on the surface changes into distinct grooves and results in wear loss, which increases with the rise in the sliding speed. From the Fig. 6 it can be clearly seen from the fact that the grooves on the worn surfaces for 500 rpm were more than that of 300 rpm. From the images, it can be seen that extent of grooves in 8 wt% of carbon fibre reinforced composite is much less than 4 wt% carbon fibre reinforced composite and as cast Al7075 alloy in both the cases. Hence it is clear from the figures that adding carbon fibre increases the wear resistance of the composite. At low loads mixed abrasion-plastic deformation mechanism is observed where as in case of high loads it was observed the surface was severely damaged and many facture spots were visible. Resulting in high wear rates and moreover, the protective layer of carbon fibre remains unstable due to ploughing action.

ISSN- 2394-5125VOL 7, ISSUE 15, 2020


Casted Al7075

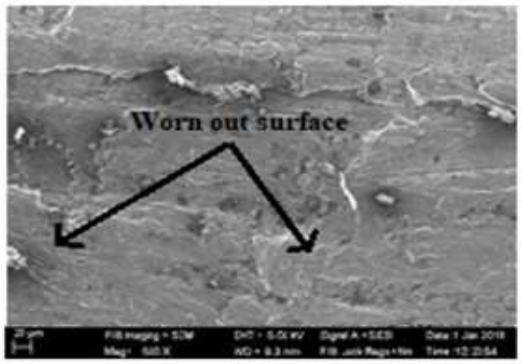


Al7075+4% CF

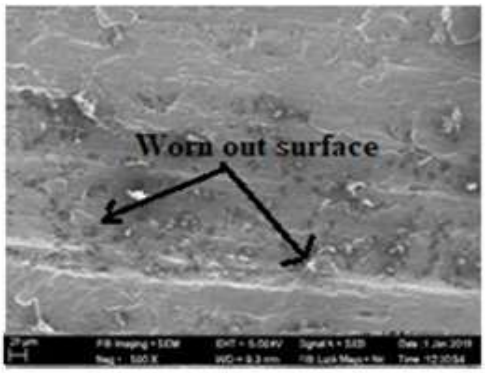


Al7075+8% CF


Casted Al7075

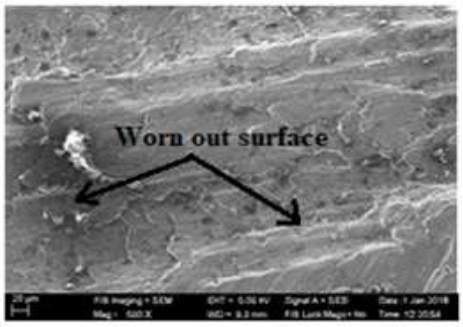


Al7075+4% CF

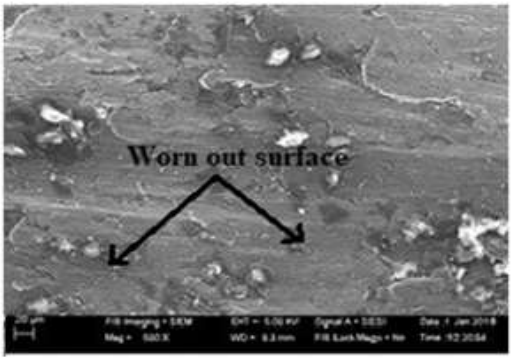


Al7075+8% CF

**Fig. 5 SEM morphology 500rpm**

ISSN- 2394-5125VOL 7, ISSUE 15, 2020

## IV. Conclusions

From the investigations of wear behavior the following conclusions are arrived.

1. Addition of NCSCFsin Aluminium alloy showed that wear resistance was improved significantly. With increase inwt% of short carbon fiber content,the wear rate is found to be decreased. The Al alloy and the Al/NCSCFs composites showed that wear rate was increased with increase in applied load.
2. With addition of NCSCFs with matrix,the direct contact between the counterpart and matrix was minimized, results great improvement in wear resistance.
3. At low loads abrasion wear was exhibited by the Al/NCSCFscomposite whereas in case of high loads delamination was observed and found to be superior,who was much evident from SEM micrographs.
4. For different conditions like change in the sliding distance, change in the sliding velocity and change in the applied normal load and at 8 wt% of the short carbon fiber as reinforcement the wear rate was found to be least.

## V. References


1. T.W. Clyne, P.J. Withers, An Introduction to Metal Matrix Composites, Cambridge University Press, 1993.
2. N. Chawla, K.K. Chawla, Metal Matrix Composites, Springer, 2006.
3. S.V. Prasad, R. Asthana, Aluminum metal-matrix composites for automotiveapplications: tribological considerations, Tribol. Lett. 17 (2004) 445–453.
4. P. J. Blau, "Friction and wear of aluminium-silicon alloys", ASM Handbook, friction, lubrication, and wear technology, vol. 18, pp. 785-794, 2013.
5. M.G Vassilaros, D.A.Davis, G.L.Stecker, J.P.Gudas, in "Proceedings of the Tri- Service Conference on Corrosion" US Air Force Academy, Colorado, November 1980, Vol II
6. A.I.Onen, B.T.Nwufo, E.E.Ebenso, R.M.Hlophe. Int.J.Electrochem.Sci., 5 (2010) 1563.
7. N.A.P.Rao, S.Biswas, P.K.Rohatgi, A. Santhanam, K.Narayanaswamy, Tribo, Int., 1(1980)
8. M.Saxena, B.K.Prasad, T.K.Dan, J.Mater.Sci., 27 (1992) 4805-4812
9. Liu Lei, LiWeiwei, Tang Yiping, Shen Bin, HuWenbin; "Friction and wear properties of short carbon fiber reinforced aluminum matrix composites", Journal of wear, vol.266, pp.733-738, 2009.
    A. Daoud,Wear performance of 2014 Al alloy reinforced with continuous carbon fibers manufactured by gas pressure infiltration, Materials Letters 58 (2004)3206–3213.
10. Ezhil Vannan. S, Paul vizhian. S Dry Sliding Wear Behaviour of Basalt Short Fiber Reinforced Aluminium Metal Matrix Composites; Journal of applied mechanics and materials, vol.592, pp.1285-1290, 2014.
11. B. Venkataraman , G. Sundararajan "Correlation between the characteristics of the mechanically mixed layer and wear behaviour of aluminium, Al-7075 alloy and Al-MMCs", Journal of wear, vol.245, pp.22-38, 2000.
12. X.-L. Kong, Y.-B. Lu, Y. Lu, B. Yang, Investigation of friction andwear behaviour of carbon fiber felt reinforced aluminium–matrix composites, Tribology 21 (2001)448–451 (Chinese).
13. Biswas S. K. and Pramila Bai. B. N., "Dry wear of aluminum graphite particle composites", vol. 68, pp. 347-358, 1981.
14. C. S. Ramesh, A. R. Anwar Khan, N. Ravikumar and P. Savanprabhu, "Prediction of wear coefficient of Al6061–TiO2 composites", Journal of wear, vol. 259, pp. 602-608, 2005.
15. R. N. Rao and S. Das, "Effect of matrix alloy and influence of SiC particle on the sliding wear characteristics of aluminium alloy composites", Materials and design, vol. 31, pp. 1200–1207, 2010.
16. D. Mandal and B. K. Dutta, "Wear and friction behavior of stir cast aluminium base short steel fiber reinforced composites", Wear, vol. 257, pp. 654–664, 2004.
17. Nithin Kumar, H. C. Chittappa, Albert Allen D. Mello, and M. D. Kiran "Fatigue Behaviour of Carbon Fiber Reinforced Aluminum Metal Matrix Composites" Advanced Science, Engineering and Medicine. 10(3), 1–4, 2018.
18. Zhongsheng Hua, Yihan Liu, Guangchun Yao, Lei Wang, Jia Ma, and Lisi Liang, "Preparation and Characterization of Nickel Coated Carbon Fibers by Electroplating", Journal of Materials Engineering and Performance, (2012) 21:324–330.
19. Nithin Kumar, H. C. Chittappa, S. Ezhil Vannan "Development of Aluminium-Nickel Coated Short Carbon Fiber Metal Matrix Composites", Materials today proceeding, vol.5, pp. 11336-11345 2018.

ISSN- 2394-5125VOL 7, ISSUE 15, 2020


20. S.C. Sharma, K.H.W. Seah, B.M. Girish, R. Kamath, B.M. Satish, Hardness of aged ZA-27/short glass fiber-reinforced composites,Mater. Design 18 (3) (1997) 155–159.
21. G. Ranganath, S.C. Sharma, M. Krishna "Dry sliding wear of garnet reinforced zinc/aluminium
22. metal matrix composites, Journal of wear, vol.251, pp.1408-1413, 2001.
23. Kiran M D, H K Govindaraju, T Jayaraju, "Evaluation of fracture toughness of epoxy-nickel coated carbon fiber composites with Al2O3 nano filler", *Advances in Polymer Composites: Mechanics, Characterization and Application,* AIP Conf. Proc. 2057, 020002-1–020002-5; https://doi.org/10.1063/1.5085573.
24. S. Arivukkarasan, V. Dhanalakshmi, A. Suresh Babu and M. Aruna, "Performance study on fatigue behavior in aluminium alloy and alumina silicate particulate composites", Journal of applied science and engineering, vol. 16, pp. 127-134, 2013.
25. C. S. Ramesh and Mir Safiulla, "Wear behavior of hot extruded Al6061 based composites", Journal of wear, vol. 263, pp. 629–635, 2007.

# Development of vertical axis wind turbine by Maglev suspension – An innovative approach

# Development of vertical axis wind turbine by Maglev suspension – An innovative approach

**T G Sriganesh[*1], G J Naveen[2], Vishnu P[3]**

[1]Department of Mechanical Engineering, BMS Institute of Technology and Management, Bengaluru, Karnataka, India
[2]Department of Mechanical Engineering, Sambhram Institute of Technology, Bengaluru, Karnataka, India.
[3]Department of Mechanical Engineering, BNM Institute of Technology, Bengaluru, Karnataka, India.

Email: gn2105@gmail.com

**Abstract**. Renewable energy sources like wind turbines are gaining more importance in recent years as apprehension of environment pollution has increased. Many developments have taken place to utilize solar and wind energy. Wind is present everywhere at all time but wind turbines are present in few places to generate power. An attempt has been made to make use of wind even from small regions by developing prototype of vertical axis wind turbine using maglev suspension to harness power. PVC pipes were used as wind turbine blades; simple and economic materials were also used in making this wind turbine. A new approach of having placed the magnets (double ended arrangement) has been experimented in this work. The voltage generated in double ended arrangement for different wind speeds was twice the voltage as that of single ended arrangement. The aim is to use simple low density material as wind turbine blade and generate power by magnetically levitated system. A new way of placing the neodymium permanent magnet and coils were deployed on the wind turbine plates and experimented in this work. On rotation of the wind turbine the magnetic arrangement would create axial flux while passing over copper coil arrangement.

## 1. Introduction

In favourable sites wind turbines are preferred over fossil fuels [1].Along with growth of power generated through solar energy, power generated through wind energy is growing rapidly worldwide [2]. Wind energy can be utilized effectively to generate power predominantly and also for other purposes. It is a reliable source of renewable energy as it's available at all altitude and at all seasons. Horizontal wind turbine is installed as gigantic structures to generate high power. However horizontal wind turbines are not preferred for medium to compact area as they occupy more space. On the other hand vertical axis wind turbines are chosen as they occupy less space and generate reasonable power. Vertical axis wind turbine (VAWT) accepts wind from any direction without any yawing mechanism as they are omnidirectional [3]. Shienbein et al presented their findings on mechanical and control systems of turbine for 50KW and 500KW darrieus wind turbine models [4].
Complex geometry of blades being used in VAWTs lead to manufacturing difficulty and associated cost has led to production limitation as mentioned by Eriksson S et al [5]. Savonius rotor has 20% less flow energy utilization than darrieus rotor [6]. Savonius rotors have the ability to self-

start when compared to other "lift type" Vertical axis wind turbines [7]. Efficiency can be improved by adding discs at both ends of the turbine as suggested by Muller et al [8]. Magnetic vertical axis wind turbine used by James A Rowan et al [9] in which foils were placed vertically and mounted are magnetically levitated above the turbines base; thereby reducing friction within the system. Cost is significantly low with smaller size generator in Maglev VAWT. Aravind C V et al [10] proposed the novelty of levitation concept which shows vertical axis wind turbine can be designed to work under low speed to produce power at 1 m/s.

## 2. Materials and Methods

Two O-ring neodymium magnets are arranged in the dimensions 40 mm, 20mm and 10mm of outer diameter, inner diameter with thickness respectively on the shaft which levitates non-rotating plate (stator) and rotating plate (rotor) due to the repulsive forces of the magnet. Ten disc type magnets of diameter 30mm and 4mm thickness were placed on the periphery of the rotor. Ten copper coils of 42 gauge having wire diameter of 0.102mm and 2000 turns in each coil of stator and magnets present on rotor are arranged on to the exterior in line with periphery. Arrangement of coils was in circumferential pattern to a radius of 10 cm and was connected serially in order to obtain maximum output voltage. For double ended; same set of arrangement is made on the other end of turbine blade. The repulsive force from the O-ring magnet give rise to the gap between the stator and rotor discs. Due to this magnetic levitation; rotor is free to rotate without much frictional forces and give rise to rotation of the wind turbine even at low wind speed. Magnetic levitation between the stator and rotor with the arrangement of magnets and coils are illustrated in the Fig 1.below as shown.

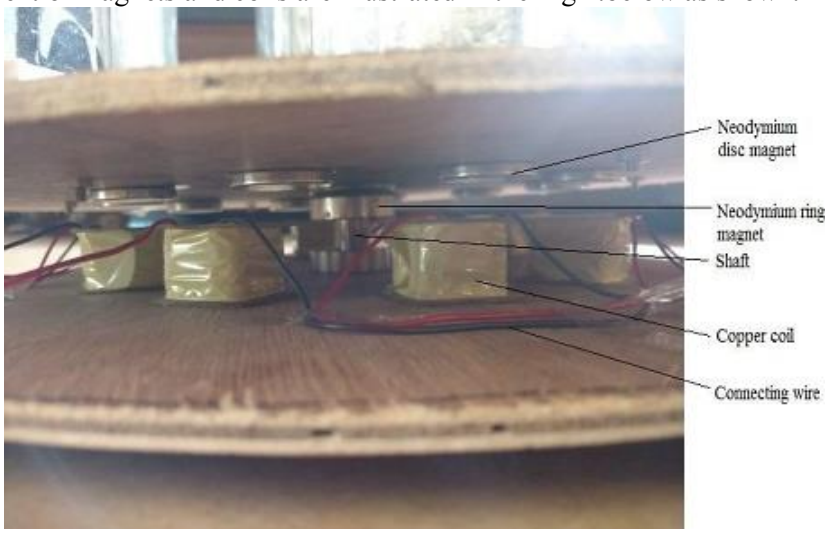


**Figure 1.** Levitation between Stator and Rotor

PVC pipes were used as wind turbine blades which were cut into two half forming a semicircular blade profile having a radius of 4.5cm and height 60cm. Fig.2 represents the wind turbine structure pictorially. The profile blades are attached to the rotor by using simple L clamp. This type of arrangement helps in fixing blades to the stator easily and also various blade profiles can be fixed to this setup in turn carrying experiments without changing the other components.

### *2.1. Single ended arrangement*

In single ended arrangement type of experiment; ten copper coils were mounted on the base plate (stator) and ten neodymium magnets were mounted on the bottom end of the lower disc (rotor) of the wind turbine wherein the rotor and stator are separated by the magnetic levitation generated by the O-ring magnet placed on the shaft.

**Figure 2.** Levitation between Stator and Rotor

*2.2. Double ended arrangement*

In order to generate more voltage a similar set of magnet and copper coils were arranged on the top end of the wind turbine blades. The coils present at both ends of the blade were connected in series and voltage generated was recorded using a multimeter during the rotation of wind turbine at various speeds.

## 3. Results and Discussion

VAWT was fabricated as described in material and methods. Testing was carried by placing the setup on house roof top which is about 60 feet above ground level. Anemometer was used to measure wind speed and output voltage caused due the rotation of wind turbine blades for both single and double ended arrangement was measured using multimeter. The experimental results are as shown in Table 1. It is observed from graph 1 that higher voltage is developed for double ended setup which almost 50% greater than the voltage developed in single ended setup at all wind speeds. This is due to the increase number of coils and magnet in double ended setup which cut more flux generating higher voltage.

On comparing with the speed of VAWT for single ended and double ended setup, rotation speed of double ended setup is lesser than that of the single ended setup. This may be due to the resistance to rotation caused by magnetic force created as the magnet passes over the coils. Table 1(b) and graph 2 indicates the speed of VAWT for single ended and double ended setup with respect to wind speed.

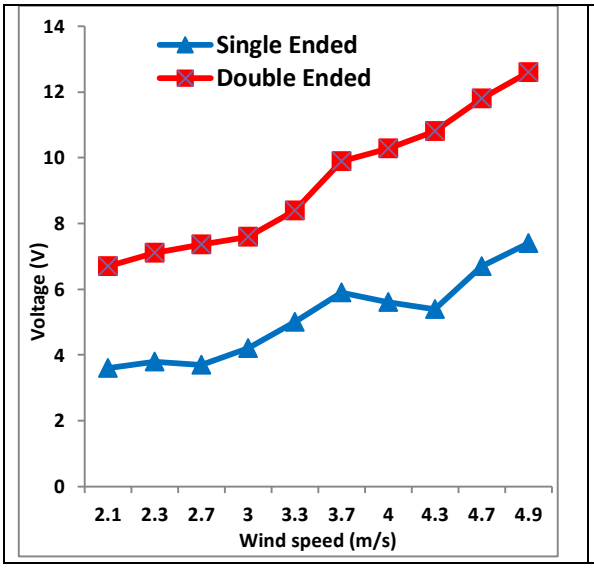


**Graph 1: Voltage v/s Wind speed**

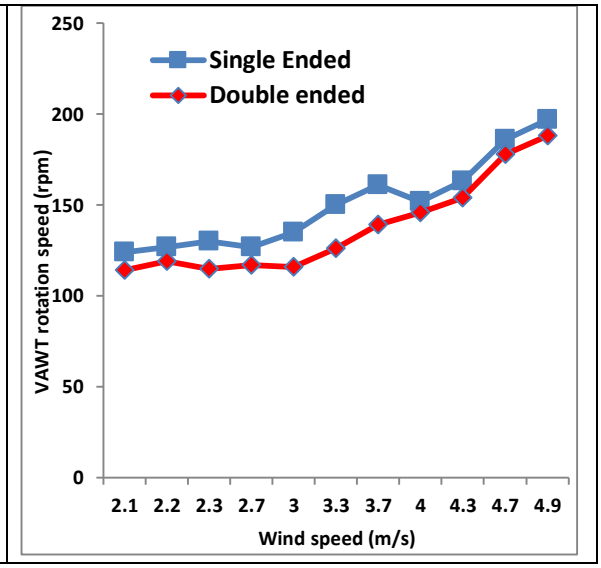


**Graph 2: Rotation speed v/s Wind speed**

**Table 1. Experimental Data**

| Sl. No | Wind Speed (m/s) | VAWT Speed (rpm) | Voltage (V) | |
|---|---|---|---|---|
| | | | Single Ended | Double Ended |
| 1 | 2.1 | 124 | 3.6 | 6.7 |
| 2 | 2.3 | 130 | 3.8 | 7.1 |
| 3 | 2.7 | 127 | 3.7 | 7.4 |
| 4 | 3 | 135 | 4.2 | 7.6 |
| 5 | 3.3 | 150 | 5 | 8.4 |
| 6 | 3.7 | 161 | 5.9 | 9.9 |
| 7 | 4 | 152 | 5.6 | 10.3 |
| 8 | 4.3 | 153 | 5.4 | 10.8 |
| 9 | 4.7 | 186 | 6.7 | 11.8 |
| 10 | 4.9 | 197 | 7.4 | 12.6 |

**(a)**

| Sl. No | Wind Speed (m/s) | VAWT Speed (rpm) | |
|---|---|---|---|
| | | Single Ended | Double Ended |
| 1 | 2.1 | 124 | 114 |
| 2 | 2.3 | 130 | 115 |
| 3 | 2.7 | 127 | 117 |
| 4 | 3 | 135 | 116 |
| 5 | 3.3 | 150 | 126 |
| 6 | 3.7 | 161 | 139 |
| 7 | 4 | 152 | 146 |
| 8 | 4.3 | 163 | 154 |
| 9 | 4.7 | 186 | 177 |
| 10 | 4.9 | 197 | 187 |

**(b)**

## 4. Conclusion

VAWT rotated at low wind speed even with simple blade geometry and as the density of blade material (PVC) is less. In double ended setup VAWT rotation speed is lesser than single ended setup which might be due to the resistance caused by the pulling magnetic force as the magnet is about to leave the coil surface. Voltage produced in double ended setup is twice that of single ended arrangement, even though rotation speed is less in double ended arrangement compared to single ended arrangement for same wind speeds due to the high magnetic flux density.

## Acknowledgement

We would like to sincerely acknowledge HOD's, Principal and Management in Department of Mechanical Engineering, at BMS Institute of Technology, Bengaluru; Sambhram Institute of Technology, Bengaluru and appreciate the support given to present and publish the research findings.

## References

[1] Baker J R., Features to aid or enable self-starting of fixed pitch low solidity vertical axis wind turbines,(2003)Journal of Wind Engineering and Industrial Aerodynamics; 15:369–80.
[2] Ponta F L, Seminara J J, Otero A D., On the aerodynamics of Variable-geometry oval-trajectory Darrieus wind turbines. Renewable Energy; 32(2007) 35–56.
[3] Chaichana T, Chaitep S., Wind power potential and characteristic analysis of Chiang Mai, Thailand, Mechanical Science and Technology; 24(2010) 1475–9.
[4] Shienbein L A, Malcolm D J. Design performance and economics of 50-kW and 500-kW vertical axis wind turbines. Journal of Solar Energy Engineering; 105(1983) 418–25.
[5] Eriksson S, Bernhoff H, Leijon M., Evaluation of different turbine concepts for wind power, Renewable and Sustainable Energy Reviews; 12(2008) 1419–34.
[6] Gorelov D N, Krivospitsky V P. Prospects for development of wind turbines with orthogonal rotor, Thermophysics and Aeromechanics; 15(2008) 153–7.
[7] Mohamed M H, Janiga G, Pap E, Thevenin D. Optimal blade shape of a modified Savonius turbine using an obstacle shielding the returning blade. Energy Conversion and Management; 52(2011)236–42.
[8] Muller G, Mark F, Jentsch M F, Stoddart E. Vertical axis resistance type wind turbines for use in buildings. Renewable Energy; 34(2009)1407–12.
[9] James A. Rowan, Thomas J. Priest-Brown, Magnetic Vertical Axis Wind Turbine, publication number-US7303369 B2, USA published on Dec 4, 2007.
[10] Aravind C V, Raj Parthipan B, Rajaprasad R, Wong Y V, "A Novel Magnetic Levitation Assisted, Vertical Axis Wind Turbine – Design Procedure and Analysis (2012) issued by IEEE.

.

JOURNAL OF CRITICAL REVIEWS

ISSN- 2394-5125 VOL 7, ISSUE 17, 2020

# Impact of Nanoadditives on Performance and Emission Characteristics of C.I. Engine Operated Using Blended Simarouba Oil Methyl Ester

**Keerthi Kumar N[1], T. K Chandrashekar[2], Jatadhara G S[3]**

[1]Assistant Professor, Department of Mechanical Engineering, BMS Institute of Technology and Management, Bangalore, Karnataka, India

[2]Professor, Department of Mechanical Engineering, RNS Institute of Technology, Bangalore, Karnataka, India

[3]Assistant Professor, Department of Mechanical Engineering, Siddaganga Institute of Technology, Tumkur, Karnataka, India

Received: 10 April 2020 Revised and Accepted: 26 June 2020

**ABSTRACT:** The present research targeted to study the influence and effect of injection pressure, synthesized aluminum and titanium oxide nanoparticles in Simarouba biodiesel (SuOME20) on engine performance and emission. To avoid the agglomerating of nanoparticles in SuOME20, test fuel samples were prepared using probe sonication process by mixing nano particles with 20mg/ltr dosage; sodium dodecyl sulfate is used for retaining the stability of nano particles in fuel. The test fuel used in the study is diesel at 180 bar, B20SuOME, B20SuOMEAL and B20SuOMETI at 200 bar. The aluminum nano fuel blend showed an enhancement in brake thermal efficiency and reduction in specific fuel consumption at full load than other test fuels due to enhanced micro explosion tendency of aluminum oxide. The heat release rate, peak pressure increased while unburnt hydrocarbon, carbon monoxide and smoke emissions were lesser. Marginal increment in emissions of oxides of nitrogen for blended and nonfuel blends compared with diesel mode of operation is observed.

**Keywords:** Simarouba oil methyl ester, Aluminum and Titanium oxide nanoparticles, performance, Emissions.

## I. INTRODUCTION

Rise in the population and rate of development of any country is one of the ways to measures of consumption of petroleum products. Many sectors namely, transportations, military, agricultural and power generation are majorly depends on engine run by conventional diesel fuel [1]. Due to rapid rise in population and increased modernization, there is huge demand for the petroleum products. To meet the demand of fossil fuels, an uncontrolled extraction of fossil fuels is leading to rapid depletion of petroleum products. Use of fossil fuels also leads to pollute the environment and rise in global warming. This fast growing energy requirements and environmental hazards has motivated many researchers to search a suitable alternative fuel for fossil fuels viz, diesel. Many researchers are worked on various plant seed oils and concluded as the oil produced from plant seed oil can be treated as suitable substitute for diesel [2-7]. Among all the different non edible seed oils, biodiesel produced from simarouba seed oil is considered as best alternative fuel for diesel fuel due to its nontoxic nature, and other properties like heating value, conversion rate etc., [2, 7]. But use of plan seed oil to run the engine is not feasible due to their higher viscosity. To overcome these problems, many researchers came with better solutions for the use of simarouba seed oil in engine. Transesterification of plant seed oil, use of fuel additives, which acts as catalysts and able to mitigate the combustion, pre heating, blending with diesel are popular among them [6]. Use of seed oils also tents to reduce the BTE and increase BSFC due to their properties. Methyl ester produced from plant seeds was most popular method adopted by many researchers to reduce the emissions. Use of nano additives is popular to enhance the engine performance. A significant reduction in all the emissions were recorded with the use of cerium oxide of 0.25g/lt in simarouba oil biodiesel, also increment in BTE are also recorded [12]. Small reduction in BTE and rise in NOx emissions with other emissions reduction is recorded by adding magnesium oxide nano particle in Calophyllum inophyllum based biodiesel [14]. Use of 200ppm aluminum oxide nano particles in neem biodiesel showed reduction in NOx, HC,

ISSN- 2394-5125 VOL 7, ISSUE 17, 2020

CO and smoke emissions compared to other dosage levels of nano particles [15]. Use of aluminum oxide nano particles up to 40ppm in jatropha biodiesel also showed similar trends with respect to emissions including smoke emission with 12% higher BTE [16]. BTE was increased with small rise in BSFC was observed when 50ppm aluminum oxide nano particles mixed with diesel ethanol blends of 15 to 35% compared to neat diesel mode of operation. N-butanol was used to prevent the phase separation [17]. Increased performance and combustion is observed when physiochemical properties of biodiesel are increased by addition of carbon coated aluminum nanoparticles in biodiesel [19]. 1.32% rise in BTE for B20 with 250ppm with reduction in CO and HC emissions were recorded compared to 500ppm of $T_iO_2$ nano particles in biodiesel [20], Table 1 shows the aluminum and titanium nano additives combined with diesel and blended biodiesels on CI engine performance and emission characteristics.

**Table 1. Effect of aluminum and titanium oxide nano additives in biodiesel on performance, combustion and emission characteristics of CI engine.**

| Biofuel Blends | Biodiesle, type of nano particles and there size | Dosage of NPs | Type of engine | Output | Ref |
|---|---|---|---|---|---|
| D, B10 and B20 aluminum nano additives | Madhuca indica and ANPs of 80nm. | ANPs of 0.1gm to 0.4 gm | 4-S , SC, DI, CI engine, 1500 rpm, 17.5:1 CR. | • Increase in BTE, PP, and HRR.<br>• Reduction in HC, CO, smoke and NOx for B20A0.4. | [27] |
| D, EM, EME20, Aluminum nano additives | Eucalyptus green fuel blend and ANP of 33 to 49 nm | ANPs of 50 and 100 ppm | 4-S, CRDI, IT of 23° (before TDC) with 250 -500kgf/cm$^2$ | • Increase in CV of nano fuel blends, with reduced flash point, reduction in BTE and HC and CO to around 25.86% and 47% with slight increment in NOx compared to EM, EME20. | [28] |
| D, B20, aluminum and cerium oxide nano additives | Waste cooking oil biodiesel and $Al_2O_3$ and $C_eCO_2$ of 50 nm | $Al_2O_3$ and $C_eCO_2$ of 250, 500 and 750 ppm | 4-S, 3.7kW, 17.5:1 CR, 200 bar IOP | • Highr BTE and reduced BSFC.<br>• Reduction in CO HC and NOx in B20A500C500, compared to all test samples | [29] |
| D, HOME(B20), aluminum nano additives | Honge oil methyl ester amd $Al_2O_3$ of 15-25 nm (±0.5 nm) | $Al_2O_3$ of 20, 40 and 60 | Kirloskar (TV1), 2400rpm, 205 bar IOP, 5.5kW and 17.5:1 CR | • Reduction in CO, HC and smoke 47.43%, 37.72% and 27.84%, respectively, compared to HOME(B20) fuel.<br>• Increment in BTE and NOx with enhanced combustion phenomenon. | [30] |
| D, JMEB20, ethanol BDE(10%), aluminum nano additives | Jatropha oil methyl ester and $Al_2O_3$ of 28-30nm. | $Al_2O_3$ of 25ppm | Kirloskar make, AC, CI engine with IT of 23°, 27°, and 19° | • Reduction in CO at 19°bTDC, HC increases by advancing while reducecd by retarding.<br>• But by ORD IT PM reduces with reduction in BSFC for for both ADV and | [31] |

ISSN- 2394-5125 VOL 7, ISSUE 17, 2020

| | | | | | |
|---|---|---|---|---|---|
| | | | | ORG IT.<br>• No change in BTE was noticed. | |
| D, BD100, B30, titanium oxide nano additives | Jatropha and $T_iO_2$ of 224.53nm | $T_iO_2$, 25 ppm, 50 ppm, 75 ppm, 100 ppm | Micro bosch in line pump, 12V engine, studied on only emissions | • Addition of nanoparticles showed a encouraging output on the variation of emission over all the test fuels. | [32] |
| D, D100+GO, titanium oxide nano additives | GO and $T_iO_2$ of 21 nm | GO, $T_iO_2$ and GO-$T_iO_2$- 50 mg/l . | HATZ-1B30-2, 21:5 CR, 5.4 kW, 1000rpm. | • Increase in peak pressure, HRR.<br>• Higher power output for same BSFC.<br>• More soot formation in GO-$T_iO_2$ fuel than neat diesel. | [33] |
| CB30, titanium oxide nano additives | Castor Methyl-Ester and $T_iN_2$ of >25 nm | $TiO_2$ of 40, 80 and 120 mg/l | HATZ-1B30-2, 21:5 CR, 5.4 kW, 2000rpm. | • Mixing of nano additives increases PP, combustion, reduction in NOx, significant improvement in BTE is observed in 80 mg/l of nano additives compared to other test fuel. | [34] |
| D100, B10, titanium oxide nano additives | Waste cooking oil and, $T_iO_2$-20-30nm, $Al_2O_3$20-30nm, B10$S_iO_2$-15-35nm. | All the nano particles of 100ppm, | Naturally aspirated engine of 7.5kW, 207 IOP, 2400 rpm. | • Addition of nanoparticles reduces CO.<br>• But $Al_2O_3$ recorded very less CO emission than other fuel.<br>• Highest NOx in D100. BSFC is also lower for aluminum oxide. | [35] |
| D, B20, titanium oxide nano additives | Mimusops elengi oil and $T_iO_2$ of 10 and 20 nm | $T_iO_2$ of 25, 50, 75, and 100ppm | Kirloskar TAF1, 4.4kW, 1500rpm, 200 bar IOP | • Better results at 100% load, higher HRR at 25ppm, HC and NOx reduced marginally with increment in BP. | [36] |

A detailed review of the previous research work indicates that several researchers have worked on adding various nanoparticles to improve the performance characteristics of biodiesel. However, very few attempts have been made on addition of aluminum or titanium nanoparticles to improve the performance characteristics especially simarouba biodiesel. This gap has been bridged through the present study. Hence, the present work is taken to study the effect of aluminum and titanium nanoparticles along with SuOME on the performance, combustion and emission products of B20 SuOME with dosage of 20mg/ltr of both aluminum and titanium nanoparticle.

## II. MATERIALS AND METHODS

The tests were performed on 4 stroke, single cylinder CI engine. In the first phase of the work, engine was run using diesel and blended fuel. In the next stage, nano additives were added to the blended fuel and test were carried to evaluate the combustion, performance and emission characteristics. All the materials used and methods adopted during the tests were discussed in the following section in detail.

ISSN- 2394-5125 VOL 7, ISSUE 17, 2020

### 2.1 Preparation of Test Fuel

Substitute test fuel for conventional neat diesel fuel is prepared by mixing SuOME and nanoparticles of aluminum and titanium oxide to diesel. In the first phase, raw simarouba seed oil is purchased from University of agricultural science campus, Bangalore and is processed by means of 2 stage transesterification to reduce its viscosity. Test fuel of B20SuOME is obtained by mixing 20% of SuOME and 80% of neat diesel on volume basis, and magnetic stirrer is used for around 25 minutes to ensure proper mixing. In the second phase of test fuel preparation, B20SuOMEAL and B20SuOMETI were prepared by dispersing 20mg/ltr of both alumina and titanium oxide nanoparticles respectively to B20SuOME. Average size of $T_iO_2$ was 21-50nm and 20-50nm foe $AL_2O_3$. Tables 2 and 3 show the properties of nanoparticles and properties of tested fuels respectively as per ASTME standards. Ultrasonicator with a frequency of 24kHz was employed to disperse both the nanoparticles to B20SuOME. Hence, in this study diesel is considered as standard fuel and B20SuOME, B20SuOMEAL and B20SuOMETI are considered as test fuels.

**Table 2 Specifications of nanoparticles**

| Parameters | Titanium Oxide ($T_iO_2$) Nanoparticles | Aluminum Oxide ($Al_2O_3$) Nanoparticles |
|---|---|---|
| **Average particle size** | 21-50 nm | 20-50 nm |
| **Appearance** | White | White |
| **Melting point** | 1843°C | 2072°C |
| **Boiling point** | 2972°C | 2977°C |
| **Density** | 4.23g/cm$^3$ | 3.95g/cm$^3$ |

**Table 3 Properties of tested fuels**

| Test Fuel used | Density at 15 $^0$C (g/cm$^3$) | Calorific Value (kJ/kg) | Kinematic Viscosity at 40 °C (cSt) | Flash Point (°C) | Fire Point (°C) | Cetane Index |
|---|---|---|---|---|---|---|
| Diesel | 830 | 42,856 | 3 | 54 | 64 | 51.24 |
| B20SuOME | 835 | 41,889 | 2.8 | 65 | 70 | 58.28 |
| B20SuOMEAL | 843 | 42,380 | 2.9 | 58 | 62 | 59.41 |
| B20SuOMETI | 844 | 41,998 | 3 | 59 | 64 | 59.23 |

### 2.2 Experimental Setup

The experiments were conducted on single cylinder, four stroke, water cooled, Direct Injection (DI) diesel engine. Eddy current type dynamometer is used to apply the load on the engine. Operating speed of the engine is 1500 rpm and 5.2 kW loading capacity. The technical specification of engine used for experimentation is tabulated in Table 4. Piezo electric transducer was used to measure in-cylinder pressure. HARTRIDGE smoke meter was used to measure smoke from tail pipe. The emission characteristics of exhaust gases were measured by using DELTA 1600 S, a non-dispersive infrared technology analyzer to find the quantitative emission levels. Mechanical Fuel Injection System (MFIS) was adopted for fuel spray having a capacity to inject fuel with a pressure range of 205 to 260bar. The line diagram of engine used for present study is shown in Figure 1. Results are tabulated for different load conditions operated at injection pressure of 200bar. The percentage of coefficient of variance and uncertainty of various measured values was calculated by sequential perturbation technique and is shown in Table 5 and Table 6 respectively.

ISSN- 2394-5125 VOL 7, ISSUE 17, 2020

**Table 4 Technical Specification of Engine Test Rig**

| Sl No | Parameters | Specification |
|---|---|---|
| **1** | Make and type of engine | Kirloskar make, Single cylinder 4-stroke, DI water cooled diesel engine. |
| **2** | Nozzle operating pressure | upto 260 bar |
| **3** | Rated power | 5.2kW @1500rpm |
| **4** | Cylinder (Bore and stroke) | 87.5mm x 110mm |
| **5** | Compression ratio | 17.5:1 |
| **6** | Dynamometer | Eddy current type |

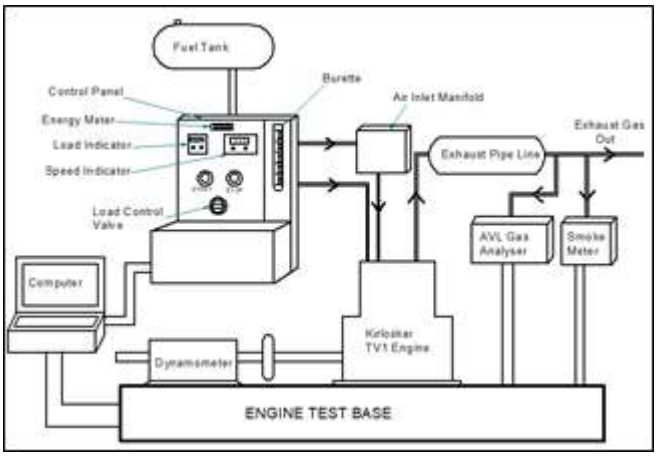


**Figure 1 Schematic diagram of experimental setup**

**Table 5 Maximum values of CoV (Co-efficient of Variance) of study parameters**

| Parameters | BTE | BSFC | Peak Cylinder Pressure | Ignition Delay | CO Emission | HC Emission | $NO_x$ Emission |
|---|---|---|---|---|---|---|---|
| Maximum COV | 3% | 4% | 5% | 4% | 2% | 2% | 6% |

**Table 6 Uncertainty analysis**

| Parameters | Air Flow Rate | Cylinder Pressure | Gas Flow Rate | Engine Load | Engine Speed | Temperature |
|---|---|---|---|---|---|---|
| Average uncertainties | 1.2% | 0.8% | 2.1% | 0.2% | 1.3% | 1.0% |

## III. RESULTS AND DISCUSSION

Experimental investigation was carried out on performance, combustion and emission characteristics of 4 stroke DI diesel engine done using neat diesel, B20SuOME, B20SuOMEAl and B20SuOMETi fuel samples and following results were obtained. All the experiments were carried out at constant engine speed of 1500rpm, operating at 200bar injection pressure for test fuels except diesel. Average of three trials of experiments has been reported.

ISSN- 2394-5125 VOL 7, ISSUE 17, 2020

### 3.1 Performance Analysis

#### *3.1.1 Brake Thermal Efficiency*

Variations in the brake thermal efficiency with various loads on the engine for diesel, B20SuOME, B20SuOMEAL and B20SuOMETI fuel samples operating at 200 bar injection pressure is presented in Figure 2. BTE of all tested fuels increased with an increase in the load on the engine. It is observed that BTE of B20SuOME fuel is lesser by 7.82% compared to diesel fuel. This may be endorsed to lower calorific value and higher viscosity of SuOME [14]. The fuel with lower heating value and higher viscosity decreases the possibility of air-fuel mixing which leads to incomplete combustion [13]. With the addition of 20 mg/ltr alumina & titanium oxide nanoparticles to B20SuOME, the BTE increased compared to B20SuOME and diesel fuel. Nanoparticles act as oxygen boosters and initiate the combustion quickly. This reduces the delay period. BTE at full load operation for diesel, B20SuOME, B20SuOMEAL and B20SuOMETI fuel samples was found to be 28.75%, 26.5%, 34% and 32.5% respectively. Addition of nanoparticles increased the thermal diffusivity of B20SuOME and improved the rate of heat transfer during the combustion and also provided high surface area to volume ratio which collectively contributes in enhanced BTE.

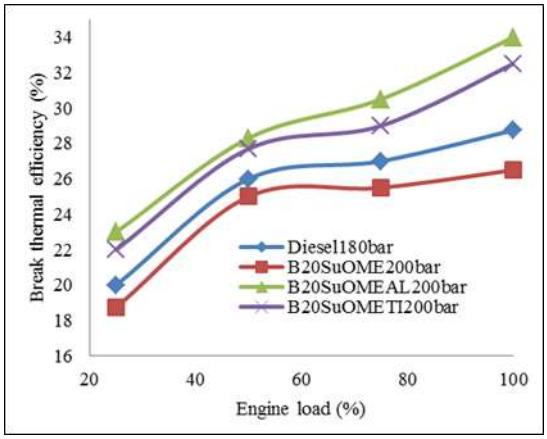


**Figure 2 Variations of brake thermal efficiency with engine load**

#### 3.1.2 Brake Specific Fuel Consumption

Figure 3 shows variations of brake specific fuel consumption (BSFC) of diesel and other test fuel samples with respect to brake power. BSFC of all tested fuel samples reduced with an increase in brake power of the engine at all loads. BSFC for B20SuOME is 1.85% higher than diesel at full load operation. Lower calorific value of SuOME leads to higher fuel consumption rate under all operating conditions. Fuel air mixing ability is reduced due to higher viscosity of SuOME and undergoes fractional and incomplete combustion which tend to consume more fuel [15, 16]. Addition of 20mg/ltr alumina & titanium oxide nanoparticles to B20SuOME shows significant reduction of 5.01% and 3.69% respectively in BSFC compared to diesel. This could be due to improved catalytic reaction and higher oxygen content of nanoparticles. Addition of alumina oxide nanoparticles showed enhanced combustion process than titanium oxide due to higher area to volume ratio hence, resulting in reduced BSFC [15]. BSFC at full load conduction are 0.379, 0.386, 0.36 and 0.365kg/kW-hr respectively for diesel, B20SuOME, B20SuOMEAL and B20SuOMETI respectively.

ISSN- 2394-5125 VOL 7, ISSUE 17, 2020

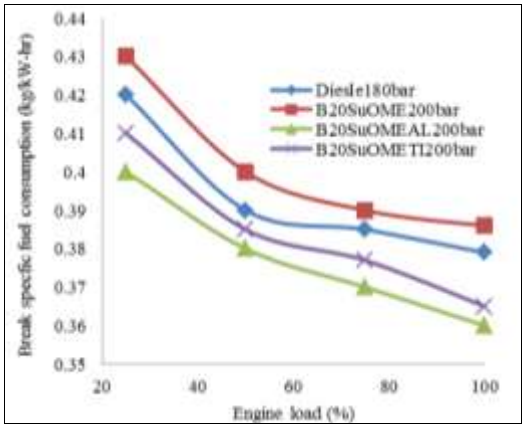


**Figure 3 Variations of brake thermal efficiency with engine load**

### 3.2 Combustion analysis

#### 3.2.1 Heat Release Rate

The rate of variation of heat release with the crank angle for diesel and test fuel samples is shown in Figure 4. The rate of heat release for B20SuOME fuel is considerably lower than neat diesel fuel. Adding Al and $TiO_2$ nanoparticles to B20SuOME fuel blends increases the HRR by 13.5% and 8.1% respectively. It enhances the combustibility and hence, higher in-cylinder pressure. Among the nanoparticles added, higher HRR was observed with Al oxide nanoparticle. This may be due to the lower volume to surface area ratio and higher thermal conductivity of Al nanoparticles, which results in reduced delay period and improved combustibility. [17-19]. Similar trend were observed by many researchers working with different biodiesel blends and nanoparticles addition [20, 21].

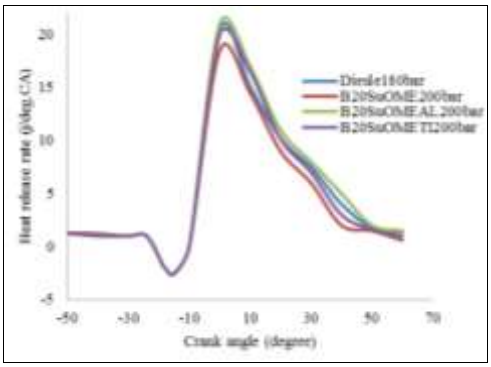


**Figure 4 Variations of heat release rate with crank angle**

#### 3.2.2 In- Cylinder Pressure

Figure 5 shows the variation of in-cylinder pressure of tested fuels with crank angle. A similar trend was observed for all the test fuels and neat diesel. The in-cylinder pressure for B20SuOME was lower than neat diesel fuel. This may be due to the lower volatility and increased viscosity of blended test fuel. The peak pressures inside the engine for diesel and B20SuOME fuels were observed to be 78 bar and 75 bar respectively. Addition of 20mg/ltr of nanoparticles to B20SuOME showed a significant rise in peak in-cylinder pressure compared to B20SuOME. A similar trend was noticed by other researchers. The higher thermal conductivity of nanoparticles results in reduced delay period. Due to this the combustion starts ahead of the intended period, thus causing higher peak pressure [21]. The peak pressure for B20SuOMEAL and B20SuOMETI fuels samples was 77 bar and 75.5 bar, which is lesser than that of diesel. Due to the higher volatility of diesel compared to other test fuel samples, the ignition delay period was shorter and resulted in uniform combustion and higher peak pressure [17,18]. Higher calorific value of diesel resulted in less quantity of fuel during combustion [22]. From the Figure 5. it is seen that maximum peak pressure for all the test fuel samples occurred at a crank angle of $7^{\circ}$ to $10^{\circ}$ after TDC.

ISSN- 2394-5125 VOL 7, ISSUE 17, 2020

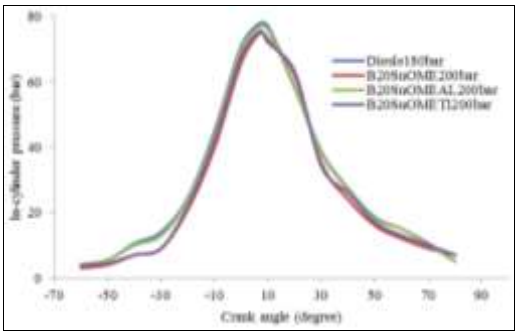


**Figure 5 Variations of in-cylinder pressure with crank angle**

### 3.3 Emission analysis

#### 3.3.1 Unburnt Hydrocarbon (UBHC)

Figure 6 presents the results of unburned hydrocarbon emissions for all test fuel at different loading conditions and constant engine speed. As the load increases UBHC emission increases for all the test fuels [23]. This trend is due to increased fuel input, which leads to rich mixture and hence partial and incomplete combustion at higher loads [24]. HC emission from test fuels is lesser than conventional diesel at all loads and this may be attributed to rich oxygen content and higher cetane number of the biodiesel. Addition of nanoparticles to the blend decreases the carbon activation temperature and enhances the combustibility. Further, HC emission for B20SuOMEAL fuel is lesser than B20SuOMETI, B20SuOME and diesel. The higher thermal conductivity of the alumina nanoparticles enhances the combustion process and leads to complete combustion and hence decreases HC emissions [9]. The HC emission at maximum loading conditions for diesel, B20SuOME, B20SuOMEAL, and B20SuOMETI are 69, 57.5, 36 and 45ppm respectively.

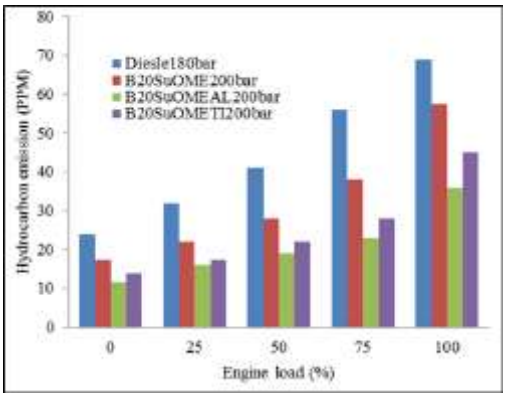


**Figure 6. Variations of hydrocarbon emission with engine load**

#### 3.3.2 Carbon Monoxide (CO)

The variation of CO emissions with the different loads for diesel, and other fuel test samples are shown in Figure 7**.** Decreasing trend of CO emissions was observed with increasing load. However, at full load CO emission was at its peak. This trend was seen for all test fuel samples. This may be attributed to the increase in load on the engine. The fuel consumption also increased. A CO emission from B20SuOME fuel is lesser than that of diesel fuel by 26% at maximum load and this is due to the rich oxygen content in SuOME. Addition of nanoparticles to blends further reduces CO emissions by 28.23% using alumina and 17.94% using titanium nanoparticles compared to B20SuOME. This may be due to the reduced ignition delay period and higher combustibility of nanoparticles than B20SuOME. Alumina nanoparticles are rich in oxygen content than titanium oxide. This results in higher CO formation in B20SuOMETI than B20SuOMEAl.

ISSN- 2394-5125 VOL 7, ISSUE 17, 2020

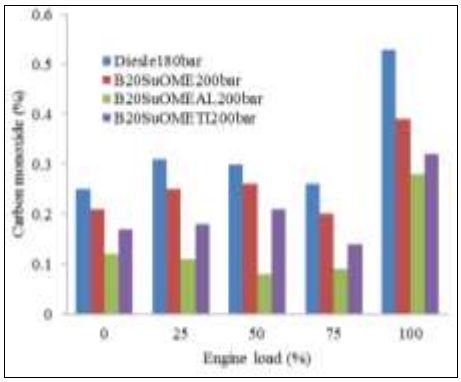


**Figure 7 Variations of carbon monoxide emission with engine load**

### 3.3.3 Oxides of Nitrogen ($NO_x$)

Figure 8 exhibits the $NO_x$ emissions for all test fuel samples. $NO_x$ emission increases with an increase in the load of engine. $NO_x$ emission of test fuel samples is higher than conventional diesel fuel due to the presence of oxygen in SuOME. Presence of oxygen mitigates the oxidation of nitrogen into its corresponding oxide during combustion process [25]. This is due to the higher cylinder temperature during combustion [20]. By the addition of nanoparticles to B20SuOME $NO_x$ emission is reduced and it is closer to $NO_x$ emission obtained from diesel. This may be owing to the improved catalytic action and rapid combustion process by using nanoparticles. Emission of $NO_x$ for diesel, other test fuel samples at maximum load is 1110, 1305, 1150 and 1203ppm respectively.

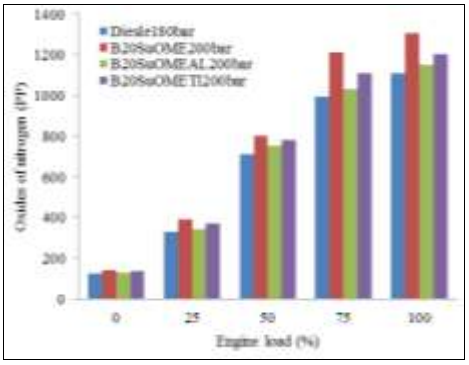


**Figure 8 Variations of oxides of nitrogen with engine load**

### 3.3.4 Smoke Opacity

The deviation of smoke opacity for all test fuel samples operated under different loading conditions is shown in Figure 9. For all the test fuels, smoke opacity increased as load due to higher fuel being consumed. A higher cetane number and rich oxygen content of SuOME helps in enhanced combustion compared to diesel resulting in decreased smoke opacity [26]. Addition of nanoparticles to SuOME biodiesel blend decreases the concentration of smoke opacity further due to enhanced rate of evaporation and higher chance of air fuel mixture resulting in shorter delay period, higher surface to volume ratio and improved oxidation rate. Percentage of smoke opacity for diesel, B20SuOME, B20SuOMEAL and B20SuOMETI are 64, 59, 52 and 54 respectively.

ISSN- 2394-5125 VOL 7, ISSUE 17, 2020

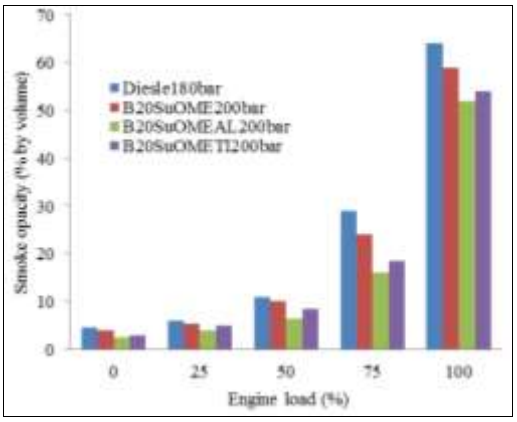


**Figure 9 Variations of smoke capacity with engine load**

## IV. CONCLUSIONS

In the first phase of the work, two stage methanol and acid esterification method was adopted to convert raw simarouba oil into its ester (biodiesel) by transforming free fatty acids. Transesterification process reduces the viscosity of raw simarouba oil which makes the oil suitable for use in engine. In the second phase, a test fuel samples were prepared using alumina and titanium oxide nanoparticles in the proportion of 20mg/ltr followed by experimentally evaluating the performance, emission and combustion behavior of the engine using test fuel samples. Following conclusions may be drawn from the results, similar kind of trends were observed by other researchers [8-25]

- Brake thermal efficiency was found to be highest in B20SuOMEAL followed by B20SuOMETI, diesel and B20SuOME respectively.
- BSFC at full load conduction was found to be least for B20SuOMEAL followed by B20SuOMETI, diesel and B20SuOME respectively. However, the Heat release rate was found to be higher for B20SuOMEAL followed by diesel, B20SuOMETI and B20SuOME respectively.
- The peak pressure was found to be maximum for diesel followed by B20SuOMEAL, B20SuOMETI and B20SuOME respectively.
- The HC, CO, and smoke emissions are generally low with simarouba oil biodiesel compared to neat diesel except $NO_x$ emission. An inclusion of 20mg/ltr of alumina and titanium nanoparticles in B20SuOME further reduced all emissions due to their inherent properties.
- The inclusion of alumina and titanium nanoparticles to simarouba oil biodiesel might be a feasible and renewable substitute for diesel fuel to run in engine without any major modifications.

## V. REFERENCE

[1]. S.Ch. Rao, M. Srinivasa Rao and Srikakulam, “Performance Analysis of DI Diesel Engine Fuelled with Diesel along with Nano Additives”. International Journal of Engineering Trends and Technology (IJETT), 2015, Volume 24, PP-107, ISSN: 2231-5381.

[2]. Sanjid A. Masjuki H.H, Kalam M.A, Rahman S.M.A, Abedin M.J and Shahir A, “An experimental investigation of biodiesel production, characterization, engine performance, emission and noise of Brassica juncea methyl ester and its blends”, Journal of Cleaner Production, 2014, 79:74–81.

[3]. Deka D.C and Saniay Basumatary S, “High quality biodiesel from yellow oleander (Thevetia peruviana) seed oil”, Biomass and Bioenergy, 2011, 35, 1797-1803.

[4]. N. Keerthi Kumar, T. K. Chandrashekar, N. R. Banapurmath and V. S. Yaliwal, “Effect of combustion geometry on combustion, performance and emission characteristics of CI engine using simarouba oil methyl ester”, IOP Conf. Series: Materials Science and Engineering, 2018.

[5]. Amani M.A, Davoudi M.S, Tahvildari K, Nabavi S.M and Davoudi M.S, “Biodiesel production from Phoenix dactylifera as a new feedstock”. Industrial Crops and Products 2013, Volume 43, PP 40-43.

[6]. Pullen James and Saeed Khizer, "Factors affecting biodiesel engine performance and exhaust emissions—part I: review", Energy, 2014, Volume 72, PP 1-16.

[7]. Mahmudula H.M, Hagosa F.Y, Mamata R, Adama A.A, Ishak W.F.W and Alenezi R, "Production, characterization and performance of biodiesel as an alternative fuel in diesel engines—a review". Renewable and Sustainable Energy Reviews, 2017, 72:497–509.

[8]. Basha, J. S and R B Anand, "Performance, emission and combustion characteristics of a diesel engine using carbon nanotubes blended jatropa methyl ester emulsions", Alexandria engineering journal, 2014, 53:259-73.

[9]. Debbarma S and Misra R.D, "Effects of iron nanoparticle fuel additive on the performance and exhaust emissions of a compression ignition engine fueled with diesel and biodiesel", Journal of Thermal Science and engineering applications, 2018, volume 10, issue 4.

[10]. Abdel RazakS M and Gad M. S, "Effect of aluminum oxide nano-particle in jatropha biodiesel on performance, emissions and combustion characteristics of DI diesel engine", International journal for research in applied science & engineering technology, 2017, Volume 5, No-IV, PP-358-372.

[11]. Annepu Shobha D., Ajaad D., Karteek P. and Lakshumu Naidu A, "Experimental investigation on the performance and emission characteristics of DI-diesel engine using diesel-ethanol blends and aluminium oxide nanoparticles", International journal of mechanical and production engineering research and development, 2017, Volume 7, No 5, PP 301-310.

[12]. Shankar Nag and Keerrthi Kumar N, "Esterification and Characteristics Study of Simarouba Glauca oil", International Journal of Emerging Research in Management and Technology, 2017, Volume 6, Issue 5, PP 1134-1139.

[13]. Banapurmath N R, Chavan A S , Bansode S B , Sankalp Patil , Naveen G , Sanketh Tonannavar , Keerthi Kumar N and Tandale M S, "Effect of Combustion Chamber Shapes on the Performance of Mahua and Neem Biodiesel Operated Diesel Engines", Journal of petroleum and environmental biotechnology, 2015, Volume 6, issue 4, ISSN: 2157-7463.

[14]. Rahman S.M.A, Masjuki H.H, Kalam M.A, Abedin M.J and Sanjid A, "Production of palm and Calophyllum inophyllum based biodiesel and investigation of blend performance and exhaust emission in an unmodified diesel engine at high idling conditions". Energy Conversion Management, 2013, 76:362–367.

[15]. Devarajan Y and Madhavan V.R, "Emission analysis on the influence of ferro fluid on rice bran biodiesel", Journal of the Chilean Chemical Society, 2017, Volume 62 (4), ISSN 0717-9707.

[16]. Radhakrishnan S, "Emissions analysis on diesel engine fueled with palm oil biodiesel and pentanol blends". Journal of Oil Palm Research, 2017, 380–386.

[17]. Venu H and Madhavan V, "Influence of diethyl ether (DEE) addition in ethanol-biodiesel- diesel (EBD) and methanol-biodiesel-diesel (MBD) blends in a diesel engine". Fuel, 2017, 189:377–90.

[18]. Devarajan Y, Nagappan B.K and Munuswamy D.B, "Performance and emissions analysis on diesel engine fuelled with cashew nut shell biodiesel and pentanol blends", Korean Journal of Chemical engineering, 2017, Volume 34, issue 4, PP 1021-1026.

[19]. Wu Q, Xie X, Wang Y and Roskilly T, "Experimental investigations on diesel engine performance and emissions using biodiesel adding with carbon coated aluminum nanoparticles", Energy Procedia 2017, Volume 142, PP 3603–3608.

[20]. Joy N, Devarajan Y, Nagappan B and Anderson A, "Exhaust emission study on neat biodiesel and alcohol blends fueled diesel engine", Journal of Energy Sources, Part A: Recover, Utilization, and environmental effects, 2018, Volume 40, issue 1, PP115-119.

[21]. Shaafi T and Velraj R, "Influence of alumina nanoparticles, ethanol and isopropanol blend as additive with diesel–soybean biodiesel blend fuel: combustion, engine performance and emissions", Renewable Energy, 2015, 80: 655–63.

[22]. Yuvarajan devarajan, Dinesh B M and Mahalingam A, "Performance, combustion and emission analysis on the effect of ferro fluid on neat biodiesel", Process Safety and environmental protection, 2017, 111, 283−291.

[23]. Caliskan H and Mori K, "Thermodynamic, environmental and economic effects of diesel and biodiesel fuels on exhaust emissions and nanoparticles of a diesel engine", Transportation research board, 2017. Volume 56, PP 203–221.

[24]. Devarajan Y, Mahalingam A, Munuswamy D.B and Nagappan B, "Emission and combustion profile study of unmodified research engine propelled with neat biofuels", Environment Science and Pollution Research, 2018, 25(20):19643-19656.

[25]. Maiboom A, Tauzia X and Hetet J.F, "Experimental study of various effects of exhaust gas recirculation (EGR) on combustion and emissions of an automotive direct injection diesel engine", Energy, 2008, 33:22–34.

[26]. Palash S.M, Masjuki H.H, Kalam M.A, Masum B.M, Sanjid A and Abedin M.J, "State of the art of NOx mitigation technologies and their effect on the performance and emission characteristics of biodiesel-fueled compression ignition engines". Energy Conversion Management, 2013, 76:400–420.

[27]. Rastogi P. M, Kumar N, Sharma A, Vyas D and Gajbhiye A, "Sustainability of Aluminium Oxide Nanoparticles Blended Mahua Biodiesel to the Direct Injection Diesel Engine Performance and Emission Analysis", Pollution, 2020, Volume-6, Issue-1, PP-25-33, ISSN:2383-4501.

[28]. N.S. Senthur, R. Karthikeyen, S. BalaMurugan, S. Divakara and M. Esakkiraja, "Experimental investigation of nano metal oxide blended Eucalyptus bio fuel on common rail direct injected diesel engine", Materials Today: Proceedings, https://doi.org/10.1016/j.matpr.2019.12.426.

[29]. A. Murugesan, A. Avinash, E. James Gunasekaran and A. Murugaganesan, "Multivariate analysis of nano additives on biodiesel fuelled engine characteristics", Fuel 2020, 275, 117922.

[30]. Manzoore Elahi M. Soudagar, Nik-Nazri Nik-Ghazali, M.A. Kalam, Irfan Anjum Badruddin, N.R. Banapurmath, Mohamad Azlin Bin Ali, Sarfaraz Kamangar, Haeng Muk Cho and Naveed Akram, "An investigation on the influence of aluminium oxide nano-additive and honge oil methyl ester on engine performance, combustion and emission characteristics", Renewable energy, 2020, Volume 146, PP 2291-2307.

[31]. H. Venu and V. Madhavan, "Effect of Al2O3 nanoparticles in biodiesel-diesel ethanol blends at various injection strategies: performance, combustion and emission characteristics", Fuel 186, 2016, PP 176-189

[32]. P. Karthikeyan and G. Viswanath, "Effect of titanium oxide nanoparticles in tamanu biodiesel operated in a two cylinder diesel engine", Materials Today: Proceedings, https://doi.org/10.1016/j.matpr.2019.10.138.

[33]. Yusuf H. Bello, Shinichi A. Ookawara, Mahmoud A. Ahmed , Mohamed A. El-Khoulye, Ibrahim M. Elmehasseb , Nagi M. El-Shafai and Ahmed E. Elwardany, "Investigating the engine performance, emissions and soot characteristics of CI engine fueled with diesel fuel loaded with graphene oxide-titanium dioxide nanocomposites", Fuel, 269, 117436, 2020.

[34]. E. A. Elsharkawy, M. M. Abou Al Sood, M. K. El Fakharany, M. Ahmed, "Enhancing the Impact of Biodiesel Blend on Combustion, Emissions, and Performance of DI Diesel Engine", Arabian Journal for Science and Engineering, 2020, 45:1109–1123.

[35]. Ümit Ağbuluta, Mustafa Karagöz, Suat Sarıdemir and Ahmet Öztürk, "Impact of various metal-oxide based nanoparticles and biodiesel blends on the combustion, performance, emission, vibration and noise characteristics of a CI engine", Fuel, 270, 2020, 117521,.

[36]. Dhinesh Balasubramanian and Krupakaran Radhakrishnan Lawrence, "Influence on the effect of titanium dioxide nanoparticles as an additive with Mimusops elengi methyl ester in a CI engine", Environmental Science and Pollution Research, https://doi.org/10.1007/s11356-019-04826-7.

International Journal of Mechanical and Production Engineering Research and Development (IJMPERD)
ISSN (P): 2249–6890; ISSN (E): 2249–8001
Vol. 10, Issue 3, Jun 2020, 2085-2094




# EXPERIMENTAL STUDY ON CHARACTERISTICS OF DIRECT INJECTION COMPRESSED IGNITION ENGINE USING WASTE PLASTIC OIL AND BIODIESEL BLENDS

**JATADHARA. G. S[1], DR. T.K. CHANDRASHEKAR[2], KEERTHI KUMAR. N[3]**

[1]*Assistant Professor, Department of Mechanical Engineering, Siddaganga Institute of Technology, Tumkur, Karnataka, India*

[2]*Associate Professor, Department of Mechanical Engineering, RNS Institute of Technology, Bangalore, Karnataka, India.*

[3]*Assistant Professor, Department of Mechanical Engineering, BMS Institute of Technology and Management, Bangalore, Karnataka, India.*

***ABSTRACT***

***Natural concern and quick exhausting of oil powers have caused interest for substitute fuel for mankind. Plastics are non-biodegradable polymer for the most part containing carbon, hydrogen and other different components in small proportions. The use of substitute fuels are intended to decrease ozone depleting substances, which includes water vapors, carbon dioxide, methane, nitrous oxide and ozone. In this regard the plastic oil obtained from waste plastic could be possible alternate fuels for internal combustion engines. This will not only provide solution to the fuel supply demand problem, but also we know that the plastic disposal is a greater challenge and is huge environmental concern. The processing of waste plastic in to plastic oil will lead to solution for plastic disposal. The plastic oil is derived from the waste plastics through the chemical pyrolysis process. The plastic oil obtained from the waste plastic have characteristics similar to conventional fuel and has calorific valve near to diesel. The blended of the plastic along with biodiesel B20 has been tested on engine and found to have better emission characteristics.***

***KEYWORDS: Plastic Oil, Biodiesel & Chemical Pyrolysis***

**Received:** Jun 04, 2020; **Accepted:** Jun 24, 2020; **Published:** Jul 03, 2020; **Paper Id.:** IJMPERDJUN2020196

Original Article

## 1. INTRODUCTION

Diesel engines are most preferred prime movers in view of their higher thermal efficiency and extraordinary drive limit. The neat WPO can be used as fuel for an engine without any modification. It is also made sense of that oxides of nitrogen, carbon dioxide were more for plastic oil diverged from diesel fuel [1].

It is seen that when diverged from standard injection timing of $23^0$ BTDC the decreased timing of $14^0$ reduces emission and has higher efficiency[2]. It was demonstrated that use of emission reduction techniques along with plastic oil diminishes $No_x$ emission. The emission characteristics will be compared with waste plastic oil and its blends. The exhaust characteristics will be study with respect $No_x$, hydrocarbons, carbon monoxide and level of smoke. The present work of using waste plastic oil with biodiesel may improve the emission characteristics of the engine. [3]

A conversion process in presence of catalyst of High Density Polyethylene (HDPE) polymer was done in a fixed-bed reactor at $400^0$C utilizing two sulphate adjusted Zirconium impetuses with point of getting important and recyclable fluid items The quality of waste plastic oil acquired from plastic is having properties like that of diesel[5]. It is the measure of output delivered to energy consumed. The brake thermal efficiency of diesel and

biodiesel are near one another [6].

The foundations for $No_x$ arrangement are increase temperature of exhaust and fuel mechanism. It has been seen that there is increment in $No_x$ because of longer start delay, however LDPE900 delivers low $No_x$. It has been noticed that carbon monoxide diminishes for input energy as load is increased and it is sign of stable ignition [7].

The brake thermal efficiency reduces for all loads up with increase in load. More plastic oil is consumed than diesel for a comparable output. The performance of the compressed ignition engine with the waste plastic oil and diesel blends of B10, B20, B30 will be compared with the present work of experimental investigation of the engine with plastic oil with the blending of proper biodiesel, which will improve the properties of the plastic oil and its influence on the performance parameters of the engine will be studied [8].

Ioannis Kalargaris, etal [9] It very well may be seen that the $NO_X$ releases of the PPO900 are a lot higher than those of diesel and PPO700. PPO900 makes twofold the UHC emanations appeared differently in relation to diesel, while PPO700 has half higher UHC releases. The expansion of diesel basically diminishes the UHC discharges, which could be explained by the expanded ignition execution related with the lower aromatic substance of diesel. The high UHC outflows of the oils can be credited to their extended aromatic substance and longer start delay, which realizes shorter burning span.Ioannis Kalargaris, etal [10,11]. The foundations for Nox development are increase heat release, mechanism of fuel combustion. It has been seen that there is increment in Nox because of longer start delay, however LDPE900 delivers low Nox . Fuel properties of waste polyethylene mixes are practically identical with those of diesel fuel aside from the Cetane number and pour point estimations of WPE100 and CPE100.Power output with blends increased most extreme by 1.63% with WPE5 mix contrasted and diesel fuel. Torque yield of mixes diminished by 2.73% with WPE5 contrasted with diesel fuel particularly at higher speed. While CO discharge is diminished by 20.63% with WPE5 mix and CO2 emanation is expanded by 3.34% with WPE5 mix. NOx emanation is expanded by 9.17% with WPE5 contrasted with diesel fuel [11, 12]. The diesel-WPO fuel mixes at different loads are found to have consequences on CO, NOx, HC, and smoke. The NOx emanation is seen as lower by mixing diesel with WPO. The diminished NOx emanation is because of the lessening of the in-chamber temperature as the impact of non-homogeneity of WPO. The convergence of HC of WPO-diesel mixes is higher than that of diesel. The higher HC discharge in WPO-diesel mixes contrasted with diesel might be credited with the explanation that the fuel shower doesn't engender further into the copying chamber. The expanded CO emanation is because of deficient burning as the impact of diminished in-chamber temperature, poor blend planning, and neighbourhood rich area. At long last, the smoke is practically comparative at lower loads. In any case, the smoke for WPO-diesel mixes is higher at a higher load. A higher smoke delivered in WPO-diesel mixes might be because of the poor atomization of WPO. The bigger size of fuel particles contained in WPO is considered to bring about poor atomization [13, 14].

## 2. RESULTS AND DISCUSSIONS

**Figure 2.1: Waste Plastic Bottles Used**

**Figure 2.2: Crushed Plastic Bottles**

**Figure 2.3: Plastic Oil Extraction Unit**

**Figure 2.4: Engine setup**

**Table 2.1: Specification of the Engine**

| Engine Parameter | Specification |
|---|---|
| Model | Kriloskar Tv1 |
| Engine | Single cylinder four stroke water cooled diesel engine |
| Bore in mm | 87.5 |
| Stroke in mm | 110 |
| Rated power in Kw | 5.2 |
| Speed in rpm | 1500 |
| Compression ratio | 17.5:1 |

The waste plastic oil is extracted from plastic glucose bottles, which is waste disposal from hospitals. First the bottles are crushed on to small pieces. The crushed plastic is mixed thoroughly with fly ash which acts as catalyst and the mixture is put in to the reactor and start heating the mixture. After some time sufficient temperature has been reached, the distillation of oil takes place which is collected in the measuring flask.

The amount of plastic put in to the reactor is 5kg to which 250 g of fly ash is mixed and heated. When the temperature reached to $200^0$C there is no distillation of oil, only gaseous product comes out. When the reaches around $270^0$C the distillation of plastic oil stats and continues up to the temperature of $350^0$C. After $350^0$C oil distillation decreases and finally stops distillation of oil above $400^0$C.

The amount of plastic oil collected is around 2.5 litres for 5 kg of plastic for a time period of 5 hours. The distillation unit consists of reactor completely sealed to which condenser is collected for the condensing vapours to liquid and provision for heating and for measuring temperature.

The engine is run at rated speed for different loads as 20%, 40%, 60%, 80% and 100%. The different fuel used for testing are base diesel fuel, 100% waste plastic oil (WPO), 25%WPO, 50%WOP and 50%WOP mixed with Biodiesel 20%.

For the above said blends performance, combustion and emission characteristics are determined.

**Table 2.2: Properties of Fuel and its Blends**

| Properties/Fuel | Diesel | 100WPO | 25WPO | 50WPO | 50WPO+B20 |
|---|---|---|---|---|---|
| Specific gravity | 0.840 | 0.8 | 0.8 | 0.80 | 0.80 |
| Flash point 0C | 50 | Below 25 | Below 25 | 65 | 45 |
| Fire point 0C | 56 | Below 25 | Below 25 | 72 | 55 |
| Kinematic viscosity cst | 2.0 | 1.62 | 1.3 | 1.94 | 1.69 |

| | | | | | |
|---|---|---|---|---|---|
| Gross Calorific oil MJ/kg | 46.5 | 45.54 | 44.680 | 43.923 | 40.435 |
| Cetane number | 55 | 51 | - | - | - |
| Cloud point 0C | - | -2 | 15 | -4 | 10 |
| Pour point 0C | - | -10 | 5 | -8 | 0 |
| Sulphur Content %w/w | - | - | - | 0.72 | 0.14 |
| Carbon residue% w/w | 0.045 | - | - | 0.02 | - |

### 2.1 Combustion Characteristics

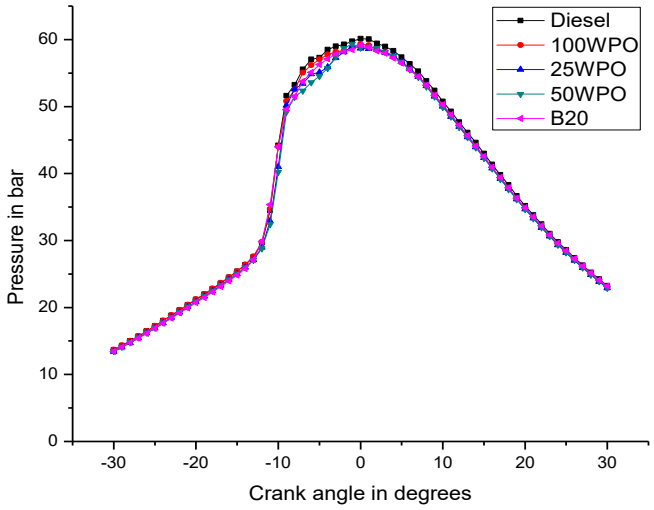


**Figure 2.1.1: Pressure Crank Angle Diagram**

The engine that was used to test the WPO and its mixes with diesel and biodiesel is a water-cooled diesel motor. The particulars of the motor are appeared in Table 6.1; the sensors are introduced so as to screen the motor's presentation. The test were performed at an evaluated speed of 1500 rpm and five different conditions as 20%, 40%, 60%, 80% and 100% of load. As per the test technique, at first the engine was running on diesel for 30 min to heat up and achieve consistent coolant — oil temperatures before it was changed to the chose oil mix. The assessment of the information was beginning 5 min after the engine was changed to the fuel blends. The connection between engine pressure crank angles is as appeared in figure for the different blends contrasted with base diesel fuel. The greatest pressure is recorded for diesel is 60.152 bar and for various of plastic oil the pressure is around 58 bar. At full load WPO100 delineates comparable profile to diesel with possibly lower profile, while WPO25 and WPO50 present somewhat longer ignition delay period and lower top chamber pressure. The B20 has comparative pattern with different mixes of WPO.

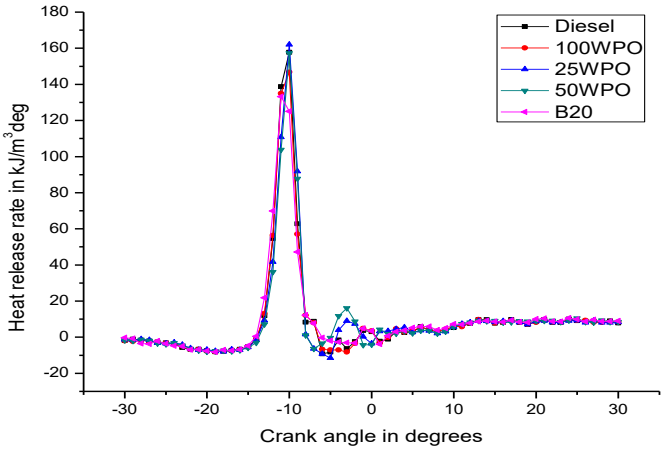


**Figure 2.1.2: Heat Release Diagram**

The heat release rate (HRR) for diesel, WPO, WPO25, WPO50, B20 is shown in Fig. 6.6. It can be observed that the there is an increase release rate for WOP25 compared with diesel at 100% loading. The heat release rate for the 50WPO is found similar to the diesel fuel. For B20 at lower loads its has better heat release rate with increasing loading the heat release rate decreases.

**2.2 Performance Characteristics**

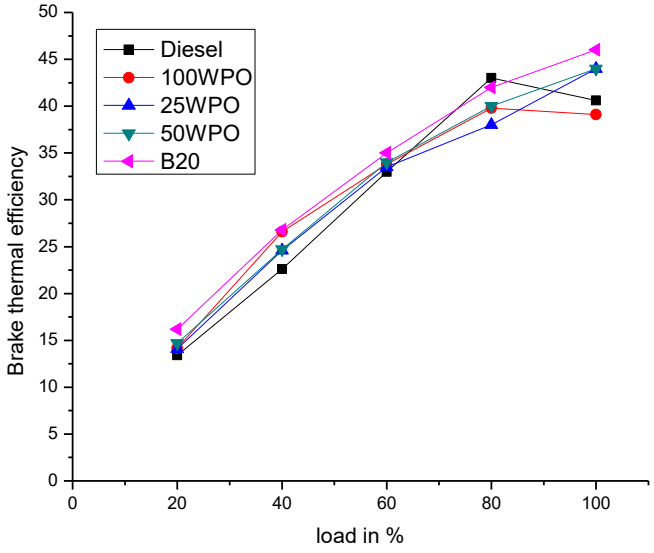


**Figure 2.2.1: Variation of Brake Thermal Efficiency Versus Load**

The variation of brake thermal efficiency (BTE) for diesel and fuel blends with brake power is presented in Fig 6.7. At lower loads brake thermal efficiency has better compared to diesel. But with increasing loading diesel has better efficiency than oil blends. The blended B20 has better thermal efficiency compared to other blends.

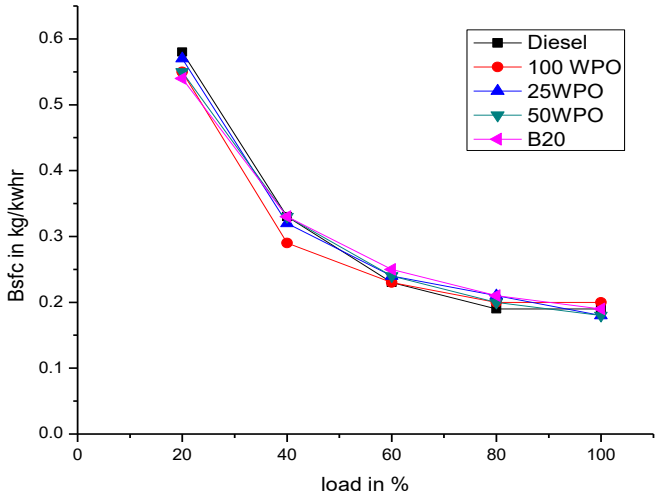


**Figure 2.2.2: Variation of Brake Specific Fuel Consumption Versus Load**

The variation of brake specific fuel consumption (Bsfc) for diesel and fuel blends with brake power is presented in Fig 6.8. At lower loads diesel has higher fuel consumption compared to other blends at higher loads 100WPO and 25 WPO have less fuel consumption compared to diesel.

### 2.3 Emission Characteristics

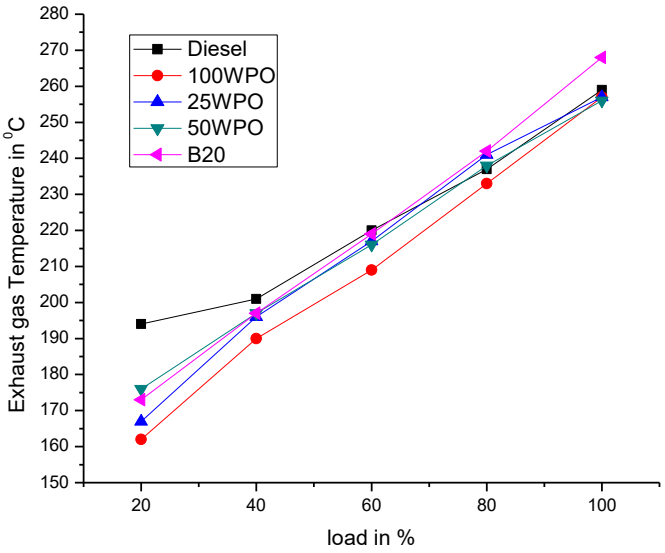


**Figure 2.3.1: Variation of Exhaust Gas Temperature Consumption versus load**

All the blends at lower loads have low exhaust gas temperature compared to diesel. Other blends of WOP expect B20 have low exhaust temperature compared to diesel fuel.

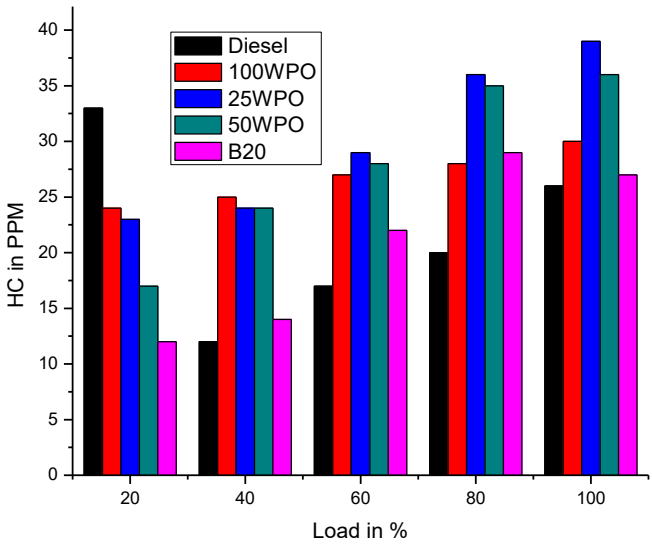


**Figure 2.3.2: Variation of Hydrocarbon versus load**

It is seen that there is in increase in unconsumed hydrocarbons for with increase in level of blends ratio. Regardless, for same blending extent, unconsumed hydrocarbon diminishes with increment in load. The clarification behind addition in unconsumed hydrocarbon is because of plastic oil properties which need to be addressed.

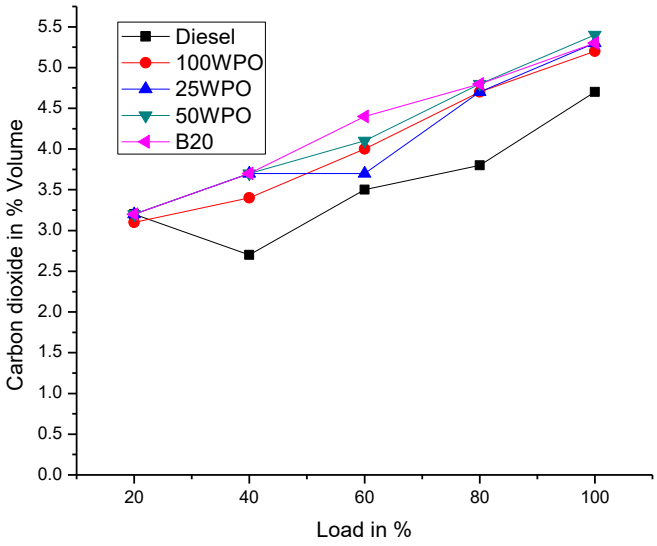


**Figure 2.3.3: Variation of Carbon dioxide versus load**

For all the blends carbon dioxide has been increased for the all the blends of WPO. In order to reduce the Carbondioxide fuel properties are modified with proper biodiesel and enhance the quality of blend fuel.

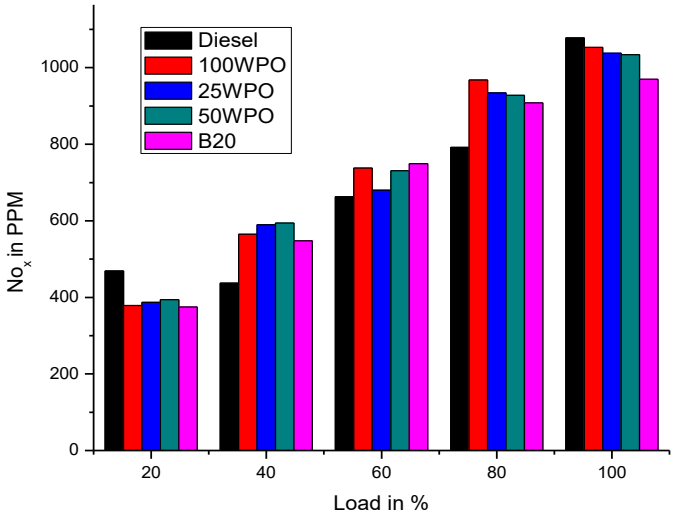


**Figure 2.3.4: Variation of Oxides of Nitrogen versus Load**

At lower loads $No_x$ are less for WPO blends compared to diesel but for increase loading Nox also increase. At 100% loading blends have reduce $No_x$ emissions.

## 3. CONCLUSIONS

- *Plastic oil and its blends have properties like diesel and have better burning qualities.*
- *2.100% WPO and its blends have increment in exhaust gas temperature and increment in Nox at higher loads.*
- *WPO mixed with biodiesel has upgraded the properties of fuel and emission for found to be less for B20 running at 100% load.*

***REFERENCES***

1. *M Mani, G Nagarajan, S. Sampath "Characterisation and effect of using waste plastic oil and diesel fuel blends in compression ignition engine" Energy 36(2011) 212-219.*
2. *M Mani, G Nagarajan " Influence of injection timing on performance, emission and combustion characteristics of a DI diesel engine running on waste plastic oil". Energy 34(2009) 1617-1623.*
3. *M Mani, G Nagarajan, S. Sampath "An experimental investigation on a DI diesel engine using waste plastic oil with exhaust gas recirculation". Fuel 89(2010) 1826-1832.*
4. *Mochamad Syamsiro, Harwin Saptoadi, Tinton norsujoanto, putrid Noviasri, Shuo Cheng, Zainal Alimuddin, kunio yashikawa " Fuel oil Production from municipal plastic wastes in sequential pyrolysis and catalytic reforming reactors". Energy Procedia 47(2014)180-188.*
5. *Naik, R. T., and C. Nilesh. "Emission characteristic of a high speed diesel engine." International Journal of Mechanical Engineering, 5, 29 36 (2016).*
6. *Jerzy Walendziewski " Engine fuel derived from waste plastic by thermal treatment". Fuel 81(2002) 473-481.*
7. *S M Ashrafur Rahman, H H Masjuki, M A Kalam, A Sanjid, M J Abedin " Assessment of emission and performance of compressed ignition engine with varying injection timing". Renewable and sustainable energy reviews 35 (2014) 221-230.*

8. *Krishna, MVS Murali, and K. Vamsi Krishna. "Studies on Exhaust Emissions of Di Diesel Engine with Low Grade LHR Combustion Chamber Fuelled with Linseed Biodiesel." International Journal of Mechanical Engineering (IJME) 3.6 (2013): 63-72.*
9. *Abhishek Sharma, S Murugan " Investigation on the behavior of a DI diesel engine fueled with Jatropha Methyl Ester and Tyre pyrolysis oil blends". Fuel 108(2013) 699-708.*
10. *Pawar H.R. and Lawankar S.M." Experimental Investigation on Compression Ignition Engine with Waste Plastic Oil and its blends with Ethanol". Research Journal of Engineering Sciences Vol. 2(5), 1-5, May (2013).*
11. *Srikanth, D., et al. "Performance exhaust emissions, and combustion characteristics of cotton seed oil based biodiesel in ceramic coated diesel engine." International Journal of Mechanical Engineering 2.5 (2013): 67-82.*
12. *Ioannis Kalargaris, Guohong Tian, Sai Gu The utilisation of oils produced from plastic waste at different pyrolysis temperatures in a DI diesel engine Energy 131 (2017) 179e185.*
13. *Ioannis Kalargaris, Guohong Tian, Sai Gu The utilisation of oils produced from plastic waste at different pyrolysis temperatures in a DI diesel engine Energy 131 (2017).*
14. *Ioannis Kalargaris, Guohong Tian, Sai Gu* Combustion, performance and emission analysis of a DI diesel engine using plastic pyrolysis oil, Fuel Processing Technology 157 (2017) 108–115.*
15. *Ayoola, A. A., et al. "Comparison Of The Properties Of Palm Oil And Palm Kerneloil Biodiesel In Relation To The Degree Of Unsaturation Of Their Oil Feedstocks." International Journal of Applied And Natural Sciences 5.3 (2016): 1-8.*
16. *Ceyla Güngöra, Hasan Serina, Mustafa Özcanlıa, Selahattin Serinb & Kadir Aydına '' Engine Performance and Emission Characteristics of Plastic Oil Produced from Waste Polyethylene and ItsBlends with Diesel Fuel'' Journal of Green Energy, 12:1, 98-105.*
17. *Mochamad Syamsiroa,*, Harwin Saptoadib, Muhammad Kismurtonoc, Zahrul Mufrodid, Kunio Yoshikawae ''Utilization of waste polyethylene pyrolysis oil as partial substitute for diesel fuel in a DI diesel engine'' International Journal of Smart Grid and Clean Energy December 4, 2018.*
18. *Jatadhara G S, T.K Chandrashekhar ''Assessment on performance and emission parameter of diesel engine using waste plastic oil used as a fuel'', IOP Conf. Series: Materials Science and Engineering* ***376*** *2018.*
19. *Kumar, N. Keerthi, T. K. Chandrashekar, and N. R. Banapurmath. "Effects of combustion chamber profile on direct injection diesel engine operated with SuOME." AIP Conference Proceedings. Vol. 2128. No. 1. AIP Publishing LLC, 2019.*
20. *N. Keerthi Kumar, T. K. Chandrashekar, and N. R. Banapurmath, "Effect of combustion geometry on combustion, performance and emission characteristics of CI engine using simarouba oil methyl ester", IOP Conf. Ser.: Mater. Sci. Eng. 376 012001, IOP Publishing, 2018/6/7.*

# Wear behavior of aluminum metal matrix composites: A Taguchi approach

Cite as: AIP Conference Proceedings **2247**, 040005 (2020); https://doi.org/10.1063/5.0003802
Published Online: 16 July 2020

H. K. Govindaraju, M. D. Kiran, and B. R. Lokesh Yadhav



# Wear Behavior of Aluminum Metal Matrix Composites: A Taguchi Approach

H K Govindaraju[1,a)], M D Kiran[1] and B R Lokesh Yadhav[2]

[1]*BMS Institute of Technology and Management, Bengaluru 560064, India*
[2]*R L Jalappa Institute of Technology, Doddabalapura 561203, India*

[a)]Corresponding author: anchithgraj@gmail.com

**Abstract.** In the present investigation wear resistance of Aluminium Matrix Composites (AMCs) were studied using Taguchi analysis. Al-Si-Ce alloys and Al-Si-Ce-Gr AMCs were casted using stir casting metallurgy techniques and the castings were T6 heat treated. Cerium was added from 0.15 wt% to 0.3 wt% and Graphite of 4 wt% was added as reinforcement in the manufacture of AMCs. The Taguchi analysis was conducted with two different speeds and loads ie 100 rpm to 500 rpm and 10 N to 50 N. From the analysis, it was found that at higher speed and lower load wear loss and coefficient of friction was minimum in all the investigating alloys and composites. Maximum wear loss was observed at lower speed (100 rpm) with highest (50 N) load.

**Keywords** – Cerium, Aluminium Alloys, Metal Matrix Composites, Wear Behavior.

## INTRODUCTION

Composite materials can be defined in many ways. Some improved or desired properties can be obtained in Composite materials. The Matrix is a dispersed phase(s), dispensed in continuous medium and should maintain its uniqueness even after processing, during service or reprocessing [1]. They have heterogeneous composition. Metal Matrix Composites of Aluminum have extensive use in automotive, aerospace and defense industries because of their light weight, high strength to wear ratio, stiffness, and good wear resistance and enhanced electrical and thermal properties [2-3] Graphite particles dispersed in Aluminum alloys are known as potential materials for tribiological applications [4-7]. Aluminum alloy matrix yields at low stresses and deforms. This improves the deformation and fragmentation of the surface and sub-surface graphite particles. It provides a continuous film of graphite, which prevents metal to metal contact and seizure. Rohit Sharma et al [8] analyzed dry sliding behavior of Aluminum alloy LM6 reinforced with dual hybrid titanium dioxide and graphite particles. With increase in reinforcement percentage, wear rate decreased linearly and with above 15% reinforcement levels, wear rate started increasing. Wear rate increased at higher loads with decrease in Coefficient of Friction (CoF). Also, presence of reinforcement improved the micro hardness. Ravindran et al [9] used technique to study the wear behavior of hybrid aluminum composites. The loss of material and CoF were influenced by the applied normal load and sliding distance. Wear resistance of 5% SiC + 5% graphite reinforced hybrid composite was more compared to 5% SiC reinforced composites. Soft graphite with hard carbides increased wear resistance. Anru et al [10] published that the strength of the alloy increases by adding Ce at room and high temperature. It also helps to refine Eutectic structure, harden by dispersion, decrease ductility, and influence the rate and precipitation of solid phases. The solubility of Ce in Aluminum increases with increasing temperature. Secondary intermetallic phases forms during solidification and heat treatment for decrease in solubility from high concentrations at high temperatures to relatively low solubility. Anasyida Abu Seman et al [11] studied the effect of cerium addition on the Microstructure and Microhardness of Al-12.5Si-4Mg alloy. With the addition of 0.5 to 3.0 Wt% of Cerium dispersed fine cells having a mixture of α-Al, Eutectic Si and intermetallic Al4Ce phase was formed in Al-matrix. With increase in Ce content Microhardness of as cast alloy increases due to precipitated phase. Diffusion of Si and Ce induced by ageing at 2000C lead to clustering of Si and Precipitation of fine Al4Ce phase resulted in increase of the microhardness of as cast alloy. VivekBabu et al [12] evaluated the hardness of LM6 (aluminum)/Gr (Graphite) particulate metal matrix composite. With the addition of Gr particle up to a particular limit, the hardness value of LM6/Gr composite increased and then suddenly decreased. For around 4% Gr composition Maximum value of hardness was found. Wear loss analysis of 18% silicon-based Aluminum alloy was studied by Anirudh Biswas et al [13]. wear rate reached maximum value at 15N and decreased as applied load increased to 20N. At higher loads work-hardening of matrix due to plastic deformation helped in reduction of wear. Temperature increases appreciably at higher loads, lowers the strength of

*Advances in Mechanical Design, Materials and Manufacture*
AIP Conf. Proc. 2247, 040005-1–040005-8; https://doi.org/10.1063/5.0003802
Published by AIP Publishing. 978-0-7354-2006-9/$30.00

materials in contact and results in increase in contact area and CoF. A.S.Anasyida et al [14] studied the wear behavior of as-cast Al-4Si-4Mg alloys with cerium addition. Cerium addition to Al-4Si-4Mg resulted in intermetallic phase formation of Al-Ce and Al-Si-Ce. Enhanced wear resistance and lowered friction coefficient of as-cast alloy was obtained with increase of cerium up to 5Wt%. Amro M. AI-Qutub et al [15] studied Al2O3/6061 Aluminum particulate composite for dry wear behavior. Higher concentration of Al2O3 and higher load lead to higher wear rates. Friction coefficient had negligible effect due to Al2O3. S. Srivastava et al [16] used Al-Sn-based alloy with different amount of Graphite for tribiological properties at different normal loads and sliding speeds. Mechanical properties and tribiological properties due to presence of graphite in the matrix Improved. Increase of Graphite content increased the ductility of composite materials. With increase in Graphite content the CoF decreases. Wang and Rack [17], recorded that higher wear resistance is exhibited by overaged composites compared to underaged. Straffelini et al [18] also concluded that higher wear resistance is exhibited in over aged composites than under aged one in extruded and also in forged condition. From the above literature survey, it was found that still scope exists to work on Aluminum Metal matrix composites. In this investigation Graphite is reinforced in Al-Si-Ce alloys and its wear behavior has been evaluated.

## MATERIALS

Metal matrix composites are casted in various processes. The properties of the alloy are derived based on alloying elements, melting process and heat treatment. Based on the necessity mechanical properties of the Metal Matrix composites and alloys, the method of casting process varies. The casting characteristics depend upon various factors such as trace elements and tight control of molten metal. The composition of the alloy used in casting is as shown in the Table 1. In the process of casting, permanent dies of size 300 mm x 200 mm x 18 mm were used. The composition of Material (in wt%): Cu-0.1, Mg-0.1, Si-10, Fe-0.6, Mn-0.5, Ni-0.1, Zn-0.1 Pb-0.1, Sn-0.05, Ti – 0.2, Al- Rem, Ce-0.15 and 0.3 Gr-4. Four different investigating materials are prepared, investigating alloy-1 and Alloy -2 are having o.15 and 0.3 percent of cerium and AMC-1 and AMC-2 are having 4 percent of graphite.

## TAGUCHI DESIGN OF EXPERIMENTS

Taguchi method is a statistical analyzing tool which analyzes the influence of control factors on the response. It reduces the number of experiments to optimize the process parameters. A performance parameter called signal-to-noise (S/N) ratio is used in Taguchi method. It is defined as the ratio of the mean (signal) to the variance (Noise). We have three kinds of (S/N) ratio: smaller-the-better; larger-the-better and nominal the best. In the present investigation wear volume loss is to be minimum and therefore S/N ratio for smaller-the better was evaluated. In the Taguchi Design of Experiments, composition, speed and load are considered as factors. Minimum and maximum of 100 rpm and 500 rpm also with a minimum load of 10 N and a maximum load of 50 N was used (Table 1).
Two level of factors are used to know the effect of Graphite on volumetric loss and Coefficient of Friction (CoF). The considered factors are two different loads, speeds with the addition of cerium and graphite are as shown in Table 1.

## Comparison between Alloy-1/T6 and AMC-1/T6

### Effect of Load and Speed on Wear loss of Graphite

In Set -1 of Taguchi analysis, volumetric loss of ($mm^3$) of Alloy-1/T6 and AMC-1/T6 was studied for load and speed as factors to understand the effect of Graphite (Gr) on wear behaviour of composites. The objective of the experimentation is smaller the better type represents the quality characteristics. Wear volume is taken as system response and wear rate has to be minimum. The average of each response characteristics of S/N ratios and Means are studied. The relative magnitude of effects of all the factors are compared by the ranks based on Delta statistics. Based on the delta values ranks will be assigned (Minitab – 15). Rank one indicates highest delta value, second and third highest will be awarded based on respective values. From the analysis it was found that load is ranked one, indicates grater effect on wear loss followed by speed and graphite. According to Taguchi design of experiments, maximum value of S/N ratio represents the minimum wear loss. In order to maximize the S/N ratio the means of 4.72 from Gr column, 4.67 from speed and 3.623 from load column are measured from response. At these levels the

wear was minimum. The experimental results have confirmed the minimum wear loss at minimum load of 10 N at speed of 500 rpm in AMC -1/T6 with a weight loss of 0.00622 gm and a volumetric loss of 2.27 $mm^3$.

**TABLE 1** Taguchi Design of Experiments

| Set | Run | Material | Speed (RPM) | Load (N) | Gr | Ce |
|---|---|---|---|---|---|---|
| I | 1 | Alloy-1/T6 | 100 | 10 | 0 | -- |
| | 2 | | 500 | 50 | 0 | -- |
| | 3 | AMC -1/T6 | 100 | 50 | 4 | -- |
| | 4 | | 500 | 10 | 4 | -- |
| II | 1 | Alloy -1/T6 | 100 | 10 | -- | 0.15 |
| | 2 | | 500 | 50 | -- | 0.15 |
| | 3 | Alloy -2/T6 | 100 | 50 | -- | 0.3 |
| | 4 | | 500 | 10 | -- | 0.3 |
| III | 1 | AMC -1/T6 | 100 | 10 | -- | 0.15 |
| | 2 | | 500 | 50 | -- | 0.15 |
| | 3 | AMC -2/T6 | 100 | 50 | -- | 0.3 |
| | 4 | | 500 | 10 | -- | 0.3 |
| IV | 1 | Alloy -2/T6 | 100 | 10 | 0 | -- |
| | 2 | | 500 | 50 | 0 | -- |
| | 3 | AMC -2/T6 | 100 | 50 | 4 | -- |
| | 4 | | 500 | 10 | 4 | -- |

The contour plot Fig 1 showed that minimum wear volume ($mm^3$) right end upper corner belong to high speed of 500 rpm and 4 wt% of graphite. Wear volume ($mm^3$) is maximum at a speed 500 rpm with zero wt% Graphite. With increase in Graphite from 0 to 4 wt% wear volume reduces as speed increases from 100 to 500 rpm. In Fig 2 the contour plot showed the wear volume (mm3) is minimum at right end lower corner where load is 10 N and Graphite 4 wt%. Wear volume is maximum at load of 50 N and at a 4 wt% of Graphite. Wear volume increases with increase in load from 10 to 50 N as Graphite increases from 0 to 4wt%.

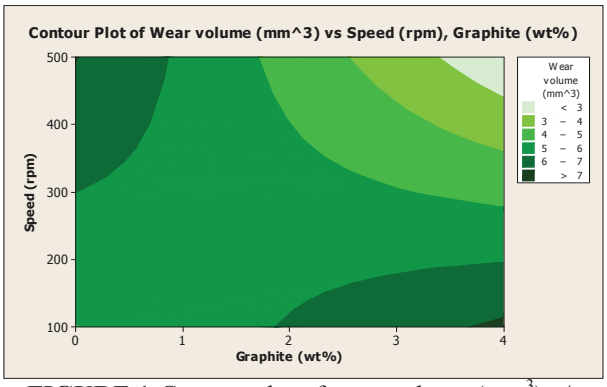


**FIGURE 1:**Contour plot of wear volume ($mm^3$) v/s speed (rpm), Graphite (wt %)

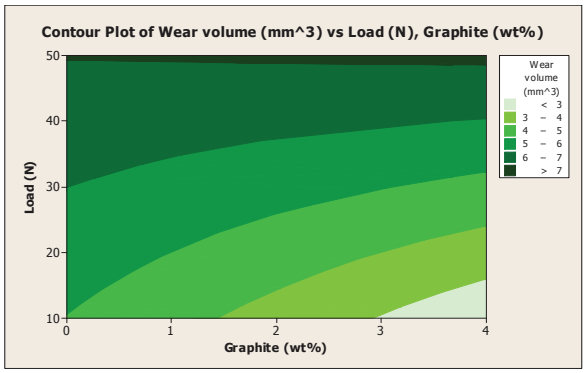


**FIGURE 2:**Contour plot of Wear Volume (mm3) v/s Load (N), Graphite (wt %)

**Effect of Co-efficient of friction with Graphite, Speed and Load:**

In order to evaluate the friction coefficient in Taguchi analysis coefficient of friction is considered as a system response load speed and graphite are ranked using delta value. From the analysis it was found that speed play an important role on the friction, graphite is the secondary factor on development of frictional force and the load takes the third place on the frictional behaviour of alloys and composites. Higher the speed with 4 wt of graphite and low load (10 N) leads to the development of low co-efficient of friction. In the analysis of Taguchi relative magnitude

effects of all the factors are considered and the average of each response. The relative magnitude effects are compared and based on delta statistics ranks are awarded for graphite, load and speed. It was found that speed is primary factor in the development of friction followed by graphite and load are the other parameters respectively contributes in the development friction.

According to Taguchi design of experimentation higher the signal to noise ration lesser will be the coefficient of friction. From response of means lowest values recorded are 0.2790 from Gr column, 0.272 from the speed column and 0.3110 from the load column are the optimal level parameters for minimizing the coefficient of friction for these levels mean response**.** The experimental results have showed lowest friction coefficient of 0.241 at high speed and low load in AMC- 1/T6 composites**.**

In **Fig 3** the plot shows the co-efficient of friction (CoF) minimum at right end upper corner where speed is 500 rpm

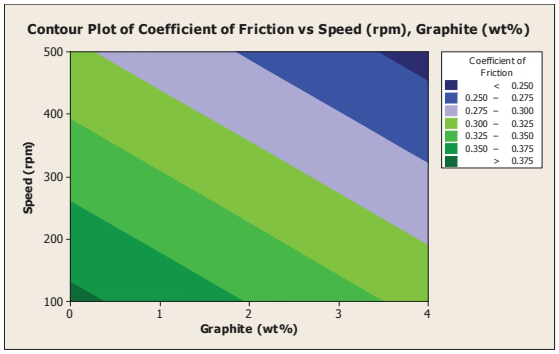


**FIGURE3:**Contour plot of coefficient of friction v/s speed (rpm), Graphite (Wt %)

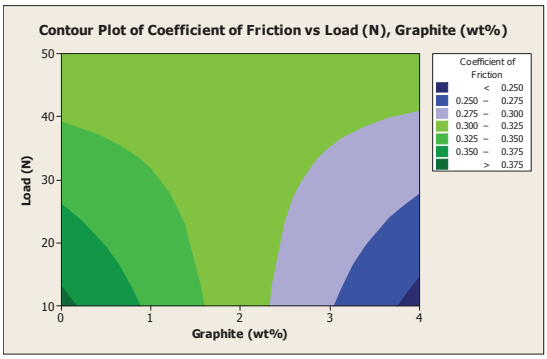


**FIGURE4:**Contour plot of co-efficient of friction V/S Load (N), Graphite (wt %)

and graphite 4 wt%. CoF is maximum at speed 100 rpm with Graphite 0 wt%. So with increase in graphite from 0 to 4 wt%, CoF reduces with increase in speed from 100 to 500 rpm. In **Fig 4** the plot shows the co-efficient of friction (CoF) is minimum at right end lower corner where load is 10N and Graphite 4 wt%. CoF is maximum where load is 10N and Graphite 0 wt%. CoF increases with decrease in Graphite wt% at load 10N and COF have higher valves with at load 50N with increase in Graphite wt%.

## Comparison between Alloy-1/T6 and Alloy-2/T6

Wear volume is taken as system response. The objective of Taguchi design of experimentation is for minimum wear rate. The analysis showed, rank one for load followed by cerium and speed are respectively responsible for wear

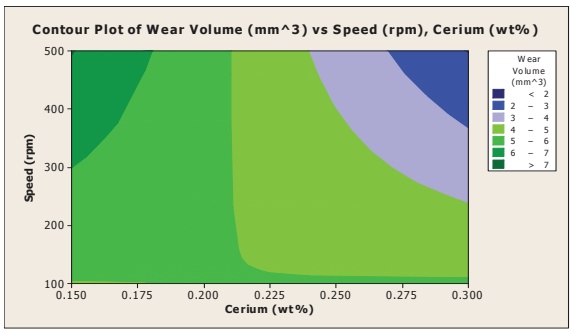


**FIGURE 5:**Contour plot of Speed v/s Cerium for the analysis of wear volume

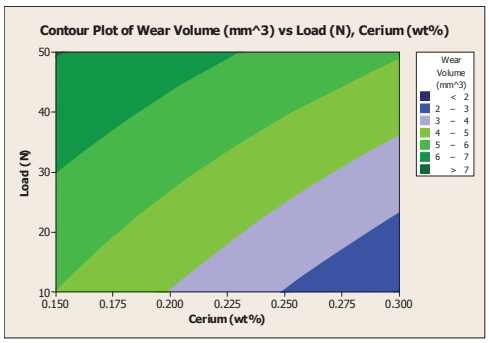


**FIGURE 6:**Contour plot of Load v/s Cerium for the analysis of wear volume

volume. In the analysis of Taguchi relative magnitude effects of all the factors are considered and the average of each response. The relative magnitude effects are compared and based on delta statistics ranks are awarded for graphite, load and speed. it was found that load is primary factor in the development of wear loss followed by

cerium and speed are the other parameters respectively contributes for wear loss. According to Taguchi design experiments and analysis maximum value of S/N ratio represents the minimum wear of alloys.

The values of 3.513 of cerium, 4.494 of speed and 3.460 of load column are considered as optimal parameters to maximize the S/N response. The experimental results have confirmed that the weight loss of 0.00530 gm and volume loss of 1.948 $mm^3$ at a maximum speed of 500 rpm and a minimum load of 10 N in Alloy- 2/T6 i.e. at 3 wt% of cerium.

The contour plot **Fig 5** showed the minimum wear volume ($mm^3$) at right end upper corner represents a highest speed of 500 rpm at 0.3 wt% of cerium. Wear volume is maximum at Cerium 0.15 wt% where speed is 500 rpm. Wear volume reduces with increase in cerium content from 0.15 to 0.3 wt% at speed 500 rpm. The contour plot **Fig 6** showed minimum wear volume ($mm^3$) at right end lower corner represents a minimum load of 10 N at 0.3 wt% of Cerium. Wear volume is maximum at 50N and Cerium 0.15 wt%. Wear volume increases with decrease in cerium wt% as load increases from 10 to 50N.

**Effect of Cerium on Co-efficient of friction in Alloy-1/T6 and Alloy-2/T6 on Load and Speed**

In the Taguchi design analysis represents smaller is better is the objective of experimentation. It is found that at level two 11.464 from cerium column, 12.293 from the speed column and 11.313 from load column responses are considered for the analysis. Coefficient of friction is taken as system response. The relative magnitude of effects of all the factors are compared by the ranks based on Delta statistics. The Delta statistic is the higher minus the lower average of S/N ratio and mean for each factor. Minitab 15 assigns ranks depend on Delta values; rank 1 indicates highest Delta value, rank 2 second highest and rank 3 third highest. From tables speed is ranked 1 which as greater effect on CoF. Cerium is ranked 2 and load ranked 3 which as lesser role. The values of 0.2810 of cerium, 0.2490 of speed and 0.2875 from load column are considered as optimal parameters to maximize the S/N response The results of experiments have shown the Co-efficient of friction of 0.194 at a high speed 500 rpm and a lower load of 10 N in Alloy-2/T6 (0.3 wt% Ce). **Fig 7** shows the plot of CoF v/s Speed, Cerium to understand the variation of CoF. The right end upper corner showed the minimum coefficient of friction represents a high speed of 500 rpm and at 0.3 wt% Ce. AlsoCoF is maximum for speed of 100 rpm and at 0.15 wt% Cerium. CoF increases with decreases in speed and Cerium wt%. In **Fig 8** the plot shows the CoF is minimum at right end lower corner where load is 10 N and cerium 0.3 wt%. Contour Plot shows CoF maximum at load of 10 N with cerium 0.15 wt% and at load 50 N with cerium 0.3% wt.

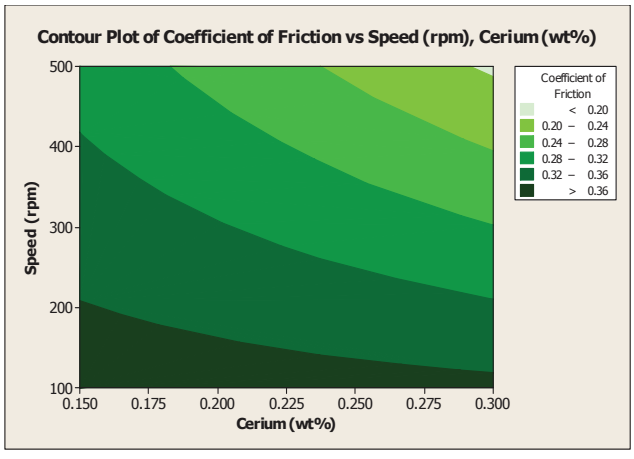


**FIGURE 7:**Contour plot of Co-efficient of friction v/s speed (rpm), Cerium (wt %)

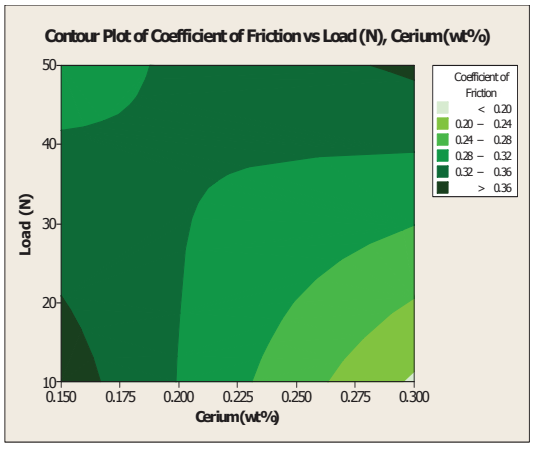


**FIGURE 8:**Contour plot of Co-efficient of friction v/s Load, Cerium

## Comparison between AMC-1/T6 and AMC-2/T6

### Effect of Cerium in AMC-1/T6 and AMC-2/T6 on wear loss with Speed and Load

Quality characteristics 'Smaller the better type' are the objective of experimentation as wear rate has to be minimum. Wear volume is taken as system response. In the analysis of Taguchi relative magnitude effects of all the factors are considered and the average of each response. The relative magnitude effects are compared and based on delta statistics ranks are awarded for cerium, speed and load. It was found that load is primary factor in the development of wear loss followed by cerium and speed are the other parameters respectively contributes to wear loss. Our goal of the experimentation is to minimize wear and therefore we want to maximize the S/N ratio in Taguchi experiments. InFig 9 the plot shows the wear volume ($mm^3$) is minimum at right end upper corner where speed is 500 rpm and cerium 0.3 wt%. Wear volume is maximum at speed of 500 rpm and cerium 0.15 wt%. Wear volume increases for decrease in cerium wt% with increase in speed. Better result would have come with cerium 0.3 wt%, speed 100 rpm and load 10 N or with the multiple tests.

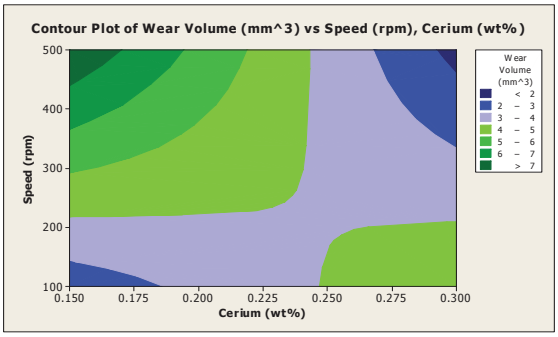


**FIGURE 9:**Contour plot of wear volume V/S speed, Cerium

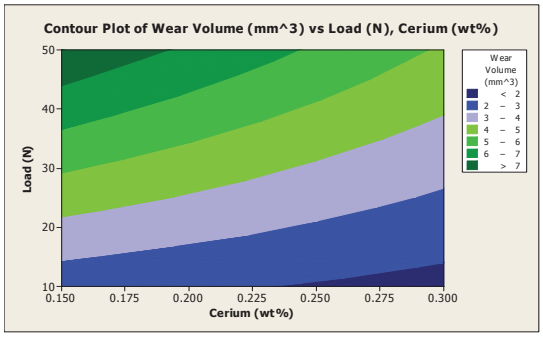


**FIGURE 10:**Contour plot of wear volume V/S load, cerium

In Fig 10 the plot shows the wear volume (mm3) is minimum at right end lower corner where load is 10N and cerium 0.3 wt%. Wear volume is maximum at load 50N and cerium 0.15 wt%. Wear volume increases with increase in load and decrease in cerium wt%.

### Taguchi Analysis for Co-efficient of Friction (CoF) with Cerium (wt %), Speed (rpm), Load (N) as factors

In the analysis of Taguchi relative magnitude effects of all the factors and the average of each response are considered. The relative magnitude effects are compared and based on delta statistics ranks are awarded for graphite, load and speed. It was found that speed is primary factor in the development of friction followed by cerium and load are the other parameters respectively contributes in the development friction

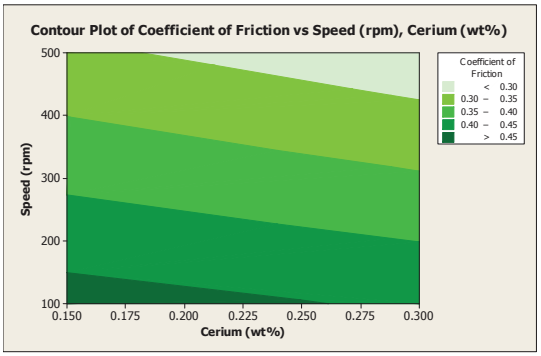


**FIGURE 11 Contour plot of Co-efficient of friction (CoF) V/S speed, Cerium**

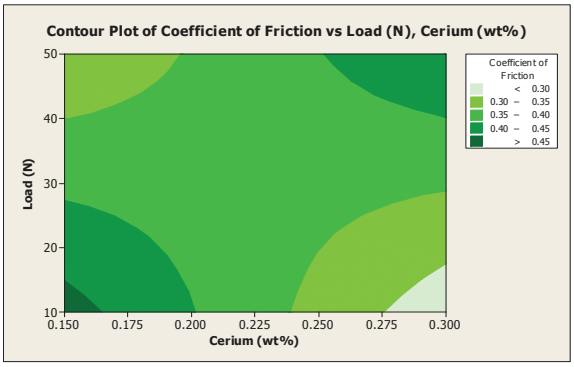


**FIGURE 12 Contour plot of Co-efficient of friction (CoF) V/S Load, Cerium**

Our goal of the experimentation is to minimize Coefficient of friction and therefore we want to maximize the S/N ratio in Taguchi experiments. The experimental results for 0.3% Ce have confirmed lowest coefficient of 0.267 at a highest speed of 500 rpm with a lowest load of 10 N levels of factors based on S/N ratio. The Co-efficient of friction (CoF) is minimum at right end upper corner where speed is 500 rpm and cerium 0.3 wt%. CoF is maximum at speed of 100 rpm and cerium 015 wt%. CoF increases with decrease in speed and cerium wt%.

In Fig 12 the plot shows the Co-efficient of friction (CoF) is minimum at right end lower corner where load is 10 N and cerium 0.3 wt%. Contour plot shows the COF is maximum for load 10N with cerium 0.15 wt% and load 50N with cerium 0.30 wt%.

## Comparison between Alloy-2/T6 and AMC-2/T6

In the fourth set of Taguchi experiments effect of Volume loss with Graphite v/s Speed, Load as factors in the analysis. Quality characteristics are smaller the better type is the objective of experimentation as wear rate has to be minimum. Wear volume is taken as system response. In the analysis of Taguchi relative magnitude effects of all the factors are considered and the average of each response. The relative magnitude effects are compared and based on delta statistics ranks are awarded for graphite, load and speed. It was found that load is primary factor in the development of friction followed by graphite and speed are the other parameters respectively contributes for the wear loss. In the Taguchi analysis, maximizing the S/N ratio minimizes the wear, in the present experimentation 3.275 from graphite column, 3.367 from speed column and 1.764 forms the load column are considered from response. In Fig 13 the plot shows the wear volume ($mm^3$) is minimum at right end upper corner where speed is 500 rpm and graphite 4 wt%. Wear volume is maximum at graphite 0 wt%. and speed 500 rpm. However better results would have for multiple experiments. In Fig 14 the plot shows the wear volume ($mm^3$) is minimum at right end lower corner where load is 10N and graphite 4 wt%. Wear volume is maximum at graphite 0 wt% and load 50N.wear volume increases with decrease in graphite wt% and increase in load.

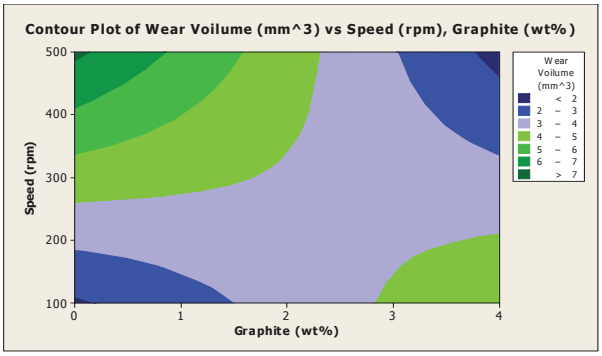


**FIGURE 13:**Contour plot of wear volume V/S speed, Graphite

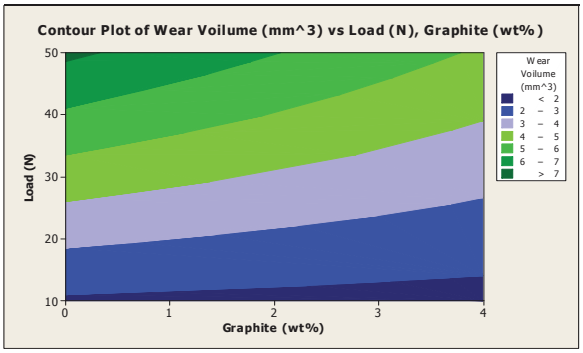


**FIGURE 14:**Contour plot of wear volume (mm3) V/S load (N), Graphite (wt %)

**Effect of Co-efficient of Friction (CoF) with Graphite, Speed and Load as factors are studied for Alloy-2/T6 and AMC-2/T6.**

In the analysis of Taguchi relative magnitude effects of all the factors are considered and the average of each response. The relative magnitude effects are compared and based on delta statistics ranks are awarded for graphite, load and speed. From the table 5.8 it was found that speed is primary factor in the development of friction followed by load and graphite are the other parameters respectively contributes in the development of friction. Our goal of the experimentation is to minimize Coefficient of friction and therefore we want to maximize the S/N ratio in Taguchi experiments. The bold marked S/N ratio in the response. The experimental results AMC-2/T6 had shown the lowest coefficient of friction at minimum load of 10 N and with a maximum speed of 500 rpm. In Fig 15 the plot shows the CoF is minimum at right end upper corner where speed is 500 rpm and graphite 4 wt%. CoF is maximum at speed 100 rpm and Graphite 4 wt%. CoF increases with increase in Graphite wt% at 100 rpm.

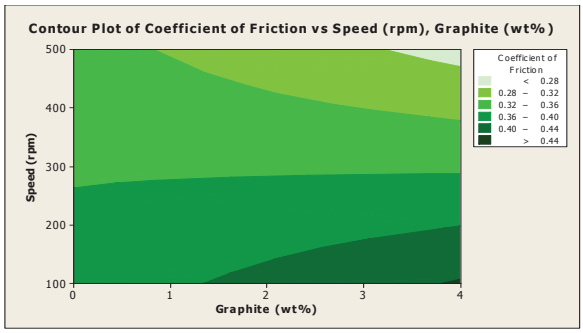


**FIGURE 15:**Contour plot of Co-efficient of Friction (CoF) V/S speed and Graphite for Alloy-2/T6 and AMC-2/T6

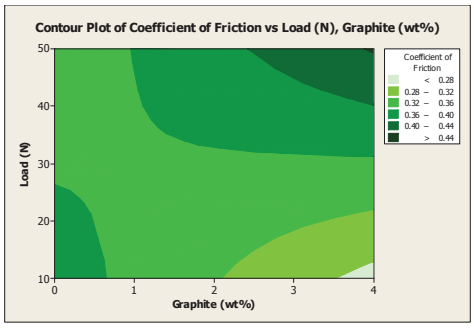


**FIGURE 16:**Contour plot of Co-efficient of Friction (CoF) V/S Load and Graphite for Alloy-2/T6 and AMC-2/T6

In **Fig 16** the plot shows the CoF is minimum at right end lower corner where load is 10 N and graphite 4 Wt% CoF is maximum at load 50N and Graphite 4 wt% also CoF has higher values at load 10N and Graphite 0 wt%.

## CONCLUSION

The Taguchi analysis the following conclusions were drawn on the wear behavior. Wear volume was progressively reduced and coefficient of friction was increased at low speed and low load in all the investigating alloys and composites. At high load and high-speed highest wear loss was observed when compared with all other loading conditions. At low speed and high load higher wear loss and higher coefficient was observed in alloys when compared with composites. At high speed to low load wear loss was minimum in all the investigating alloys and composites. Also, high coefficient of friction was observed in alloys when compared with composites.

## REFERENCES


1. M. Balasubramanian, Composite Materials and Processing, CRC Press, Taylor & Francis Group, 2014.
2. M.K Surappa, P.K Rohatgi, Preparation and properties of cast aluminum-ceramic particle composites, Journal of materials science, 16(1981), P983-993.
3. J.W.Kaczmar, K.Pietrzak, W. Wlosinski, The production and application of metal matrix composite materials, Journal of material processing technology, 106(2000), p106:58-67.
4. M.G Vassilaros, D.A.Davis, G.L.Stecker, J.P.Gudas, in "Proceedings of the Tri- Service Conference on Corrosion" US Air Force Academy, Colorado, November 1980, Vol II
5. A.I.Onen, B.T.Nwufo, E.E.Ebenso, R.M.Hlophe. Int.J.Electrochem.Sci., 5 (2010) 1563.
6. N.A.P.Rao, S.Biswas, P.K.Rohatgi, A. Santhanam, K.Narayanaswamy, Tribo, Int., 1(1980)
7. M.Saxena, B.K.Prasad, T.K.Dan, J.Mater.Sci., 27 (1992) 4805-4812
8. Rohit Sharma, Pushpinder Sharma, Gagandeep Singh, Dry sliding behavior of aluminium alloy reinforced with hybrid ceramic particles, International Journal of Multidisciplinary Research and Development, 2015, volume: 2, Issue:10, p485-491
9. Ravindran P, manisekar K, narayanasamy P, selvakumar N, Narayanasamy R, Application of factorial techniques to study the wear of Al hybrid composites with graphite addition. Mater Des 2012; 39:42-54.
10. WUAnru, XIA Changqing and WANG Shaowu, (2006) Rare Metals, 25, 371-376. [11] WUAnru, XIA Changqing and WANG Shaowu, (2006) Rare Metals, 25, 371-376.
11. Vivekbabu, Rajamohan, P.A. Abdul Samad, Hardness evaluation of LM6/Gr PMMC prepared by stir casting method, International Journal of emerging Technology and Advanced Engineering (2013), Vol:3, Issue7
12. AnirudhBiswas, NehaRastogi, AyushSoni and Rajendrasingh, Wear loss analysis of 18% silicon-based Aluminum alloy, International Journal of Emerging Technology and Advanced Engineering (2014), Vol:4, special Issue 1, p196-202.
13. A.S.Anasyida, A.R.Daud and M.J.Ghazali, Dry sliding wear behavior of Al-4Si-4Mg alloys by addition of cerium, International Journal of Mechanical and Materials Engineering Vol.4, No.2, 2009, p127-130.
14. Amro M. AI-Qutub, Ibrahim M. Allam M. A. Abdul Samad, Wear and friction of Al-Al2O3 composites at various sliding speeds, Journal of Material Science, 43, (2008), 5797-5803.
15. S.Srivastava, S. Mohan, YogeshSrivastava and Aman J. Shukla, Study of the wear and friction behavior of immiscible as-cast-AlSn/Graphite composite, International Journal of Modern Engineering Research (IJMER), Vol.2, Issue.2, (2012), 025-042.
16. Wang A, Rack HJ, Transition wear behavior of SiC-particulate and SiC-whisker-reinforce 7091 Al metal matrix composites, Mater SciEng 1991; A147:211-24
17. Straffelini G, Bonollo F, Molinari A, tiziani A, Influence of matrix hardness on the dry sliding behavior of 20 vol% Al2O3 particulate reinforced 6061 Al metal matrix composite. Wear 1997; 211: 192-7

# Fracture toughness of surface treated short fiber reinforced epoxy composites

Cite as: AIP Conference Proceedings **2247**, 020006 (2020); https://doi.org/10.1063/5.0003825
Published Online: 16 July 2020

M. D. Kiran, H. K. Govindaraju, and T. Jayaraju



# Fracture Toughness of Surface Treated Short Fiber Reinforced Epoxy Composites

M D Kiran[1,a)], H K Govindaraju[1] and T Jayaraju[2]

[1]*BMS Institute of Technology and Management, Bengaluru 560064, India.*
[2]*NIE Institute of Technology, Mysuru, India*

[a)]kiranmdg@gmail.com

**Abstract.**In the present investigation Epoxy composites reinforced with nickel coated and uncoated short carbon fibers were manufactured using open mould techniques. The short fibers were mixed in different percentages using stir casting technique. All the experiments were conducted as per the ASTM test standards. The fracture toughness of nickel coated short carbon fiber reinforced composites have showed better mechanical properties and fracture toughness when compared to uncoated short carbon fiber reinforced epoxy composites. The fractured surfaces have shown the cleavage fracture in microstructural analysis.

**Key words:** Carbon fibers; Nickel coated carbon fiber; Epoxy; Fracture toughness.

## INTRODUCTION

Conventional materials have been replaced by polymer composites in light weight structures, complex structures of automotive, aircrafts, household appliances, sports goods etc. [1]. This can be attributed to high specific strength and stiffness, ease of processing and productivity presented by polymer composites over other conventional materials. The properties of polymer composites are modified by means of different fibers to provide high strength and modulus based on applications [2-3]. Most of the polymer composites with epoxy matrices are reinforced by short fibers to enhance the mechanical and thermal properties, since short fiber reinforcement has easier processability and low manufacturing cost compared to composites with continuous fibers [4 - 7].

Load applied on composites transferred through matrix-fiber interference, adhesion strength between fiber and matrix plays a significant role on the mechanical properties of polymer composites reinforced with fibers [8]– [10]. The chemical inertness and smoothness of carbon fibers shows poor bonding behaviour with polymer matrix. Both oxidative and cryogenic surface treatments significantly increase the surface roughness of fibers and it shows improvement in interfacial adhesion bonding strength due to mechanical interlocking between fiber and matrix and it results in improvement of mechanical properties [11].

Generally, fibers are provided with the coatings of nickel, copper, magnesium, borax etc. Both electroless and electroplating processes are used to coat single or dual metal layers on the surface of carbon fibers. Coating of nickel on fibers using electroplating technique provides better strength and oxidation resistance at higher temperature [12],[13]. The epoxy matrix composites with the addition of short fibers reveals remarkably enhanced fracture toughness compared to neat epoxy resin. Composites reinforced with short carbon fibers have improved fracture toughness compared to composites reinforced with glass short fibers [14–17].

In the present work electroplating technique is used to coat the nickel on carbon fiber. Epoxy composites are fabricated with 1wt% and 2wt% uncoated and coated short carbon fibers using open moulding technique. The mechanical and fracture properties of both coated and uncoated carbon fibers reinforced epoxy composites are evaluated. Configurations and morphology of coated carbon fibers and the fractography of composites are studied by using scanning electron microscopy (SEM).

*Advances in Mechanical Design, Materials and Manufacture*
AIP Conf. Proc. 2247, 020006-1–020006-6; https://doi.org/10.1063/5.0003825
Published by AIP Publishing. 978-0-7354-2006-9/$30.00

## MATERIALS

Epoxy resin formed by Diglycidyl ether of bisphenol-A reaction (Lapox L-12 (ARL-12)) was used as matrix with 10:1 ratio of Hardener K6 TriethyleneTetro amine (TETA) of grade K6. Short carbon fiber with coating of nickel using electroplating technique supplied by Blu Dot Asia Pte Ltd, Singapore were used.

### Fabrication of Composites

The short carbon fibers of 1wt% and 2 wt% were mixed with epoxy resin by mixing with hardener. The mixture was stirred at low speed for 30 min and carried out sonication about 10 min using ultra-sonicator. After sonication the mixture with bubble free was poured to mold that had been coated with mold releasing agent and cured for 24 hours at room temperature. After removed from mould post curing of composite was carried out at $110^0$ C for 1hour and $140^0$ C for 2 hours in a conventional oven.

**Table 1.Composition of theComposites in wt%**

| Matrix | Reinforcement | Designation |
|---|---|---|
| Epoxy – 100 wt% | Nil | E |
| Epoxy – 99 wt% | Uncoated Carbon Fibers – 1 wt% | E/1UCF |
| Epoxy – 98 wt% | Uncoated Carbon Fibers – 2 wt% | E/2UCF |
| Epoxy – 99 wt% | Nickel Coated Carbon Fibers – 1 wt% | E/1NCF |
| Epoxy – 98 wt% | Nickel Coated Carbon Fibers – 2 wt% | E/2NCF |

## EXPERIMENT METHODS

The tensile characterization of composites was carried out using ASTM D-638 standard testing procedures using the specimen of size 165 mm x 19 mm x 4 mm. Izord impact strength test was carried out using ASTM D-256 standards with specimen of size 63.5mm x 12.7 mm x 3.2 mm and fracture toughness tests were conducted using single edge notched beam method as per the ASTM D5045-99. The water jet cutting method was used to cut out the specimens from composite plates. The morphology of composites has been carried out using SEM to study the distribution and orientation of fibers and bonding of fibers with matrix

## RESULTS AND DISCUSSION

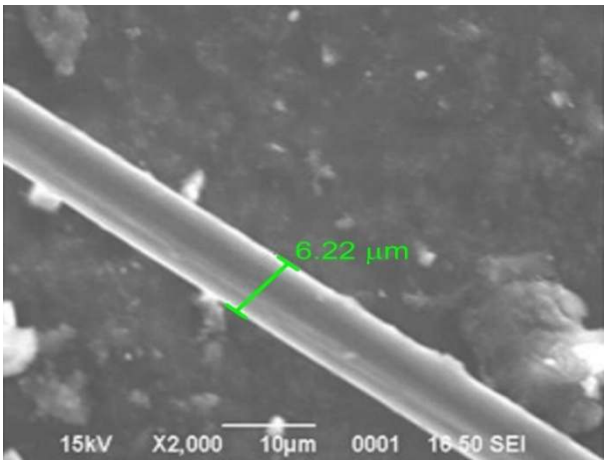


**FIGURE 1.** Uncoated carbon fiber

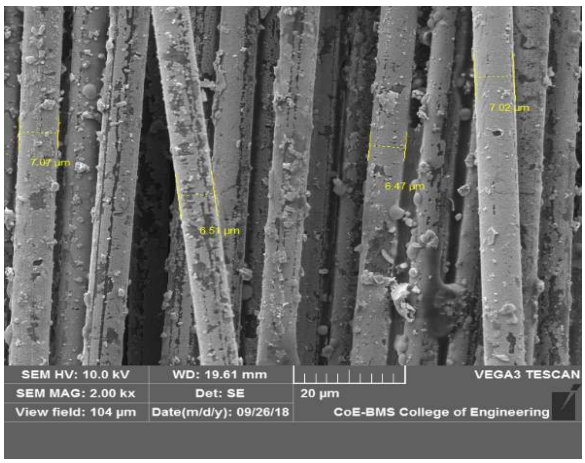


**FIGURE 2.** Coated carbon fiber

EDS scanning results show the composition of a material of fiber and it contains the nickel, carbon copper and gold. The large peaks in figure.3 shows carbon fiber surface predominantly contains the nickel. The EDS analysis confirmed the presence of nickel on surface of carbon fibers and it indicates the effective activation and metallization process during electroplating. Dispersion of fiber in melt mixing technique depends on various factors,

like, temperature, time, shearing action, pressure, rotor speed, amount of filler incorporation and nature of filler and polymer.

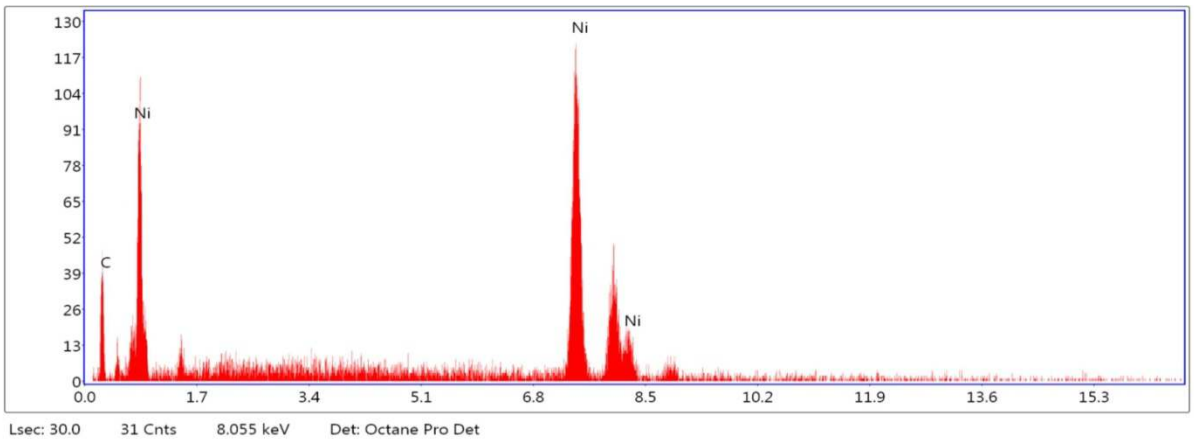


**FIGURE 3.** The elemental composition present at a particular point on the fiber.

Experimental data are evaluated as tensile strength, impact strength and fracture toughness values are tabulated in Table 2. The mechanical properties of the epoxy and epoxy/short carbon fiber composites was evaluated based on the tensile strength ($\sigma_y$), impact strength and fracture toughness measurements.

**TABLE 2.** Mechanical and Fracture properties of composites

| Specimen designation | Tensile Strength (MPa) | Impact Strength (kJ/m$^2$) | Fracture Toughness ($K_{IC}$) MPa $\sqrt{m}$ |
|---|---|---|---|
| E | 15.87 | 3 | 1.41 |
| E/1UCF | 17.16 | 4 | 1.82 |
| E/2UCF | 18.11 | 5 | 2.01 |
| E/1NCF | 22.31 | 7 | 2.31 |
| E/2NCF | 23.50 | 9 | 2.58 |

Figure 4 and 5 shows the increased tensile strength ($\sigma_y$) and impact strength values of the composites with increasing short carbon fiber content and it further increased with addition of nickel coated short carbon fiber. The tensile strength ($\sigma_y$) values of the composites with increasing short carbon fiber content and it further increased with addition of nickel coated short carbon fiber shown in Fig.4. The $\sigma_y$ values of the composites improved from an initial value of 15.87 MPa for neat epoxy to 17.16 MPa when the addition of 1 wt% of short carbon fiber in the composite and it further increased to 18.11 MPa when it was 2 wt% short carbon fiber. The tensile strength of composites further enhanced with addition of nickel coated fiber to 22.31 MPa for 1 wt% and 23.50 MPa for 2 wt% nickel coated short carbon fiber. This increased tensile strength of the nickel coated short carbon fiber composites is due to surface treatment of fibers and it attributed to strong interfacial adhesion between matrix- fiber interface [4].

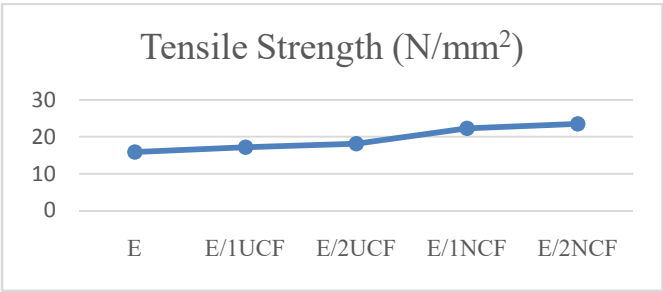


**FIGURE 4.** Tensile strength of epoxy/epoxy composites

The impact strength values of the composites improved from an initial value of 3kJ/m$^2$ for neat epoxy to 4 kJ/m$^2$ and 5 kJ/m$^2$ when the addition of 1 wt% and 2 wt% of short carbon fiber in the composite and it further enhanced with addition of nickel coated fiber to 7 kJ/m$^2$ for 1 wt% and 9 kJ/m$^2$ for 2 wt% nickel coated short carbon fiber shown in Fig.5.

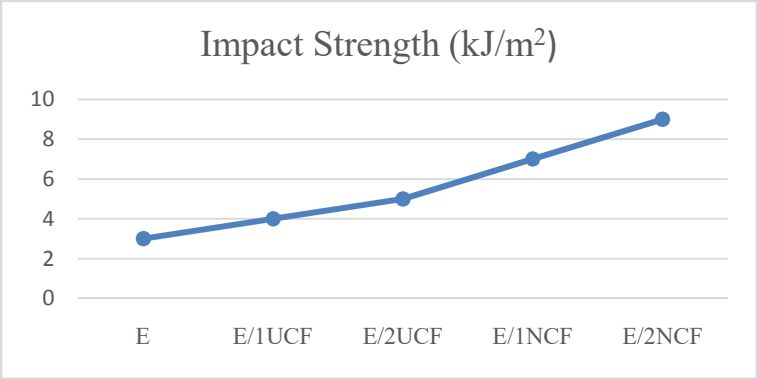


**FIGURE 5.** Impact strength of epoxy/epoxy composites

The fracture toughness of neat epoxy and epoxy composites was studied using critical stress intensity factor ($K_{IC}$) and shown in Fig.6. the fracture toughness of short fiber reinforced composites have been increased when compared with neat epoxy.

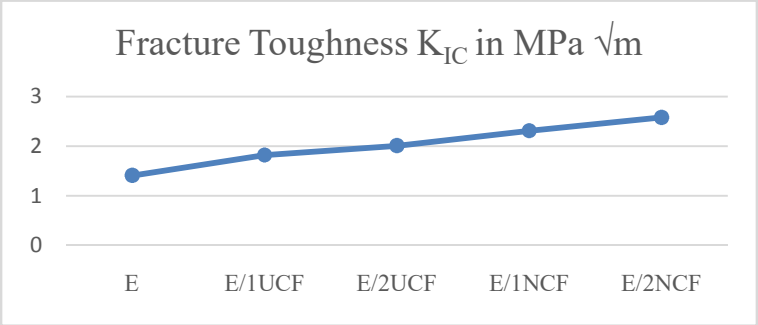


**FIGURE 6.** Fracture toughness of epoxy/epoxy composites

Fracture toughness was improved by 29% and 42% with the addition of 1 wt% and 2 wt% of uncoated short fibers respectively than neat epoxy. And it further improved with addition of 1 wt% and 2 wt% nickel coated short carbon fiber as 64% and 83% respectively compared to neat epoxy and it shows 17% improvement with 1 wt% nickel coated short carbon fiber compared to 1 wt% of uncoated short carbon fiber, and 28% improvement with 2 wt% nickel coated short carbon fiber than 2 wt% uncoated fiber.

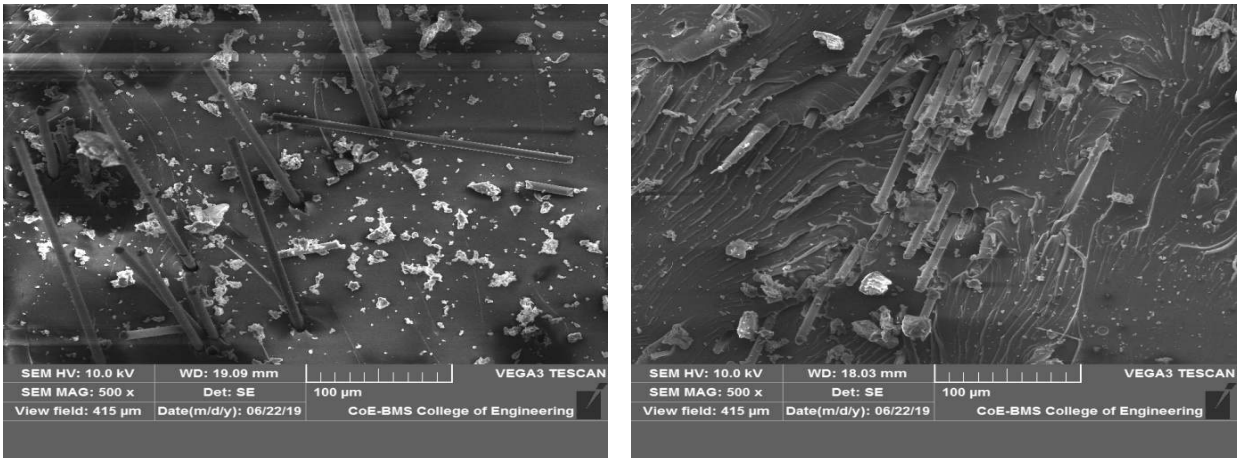


**FIGURE 7.** SEM of epoxy composites after $K_{IC}$ tests with: (a) 2 wt% short carbon fiber; (b) 2 wt% nickel coated short carbon fiber.

This is due to addition of short carbon fiber improves the fracture toughness of composites and also surface treatment of carbon fiber attributed to strong interfacial adhesion between matrix- fiber interface and it shows improved fracture toughness of the nickel coated short carbon fiber composites [12], [16].

The analysis of fractured surfaces of the epoxy composites with short carbon fiber and nickel coated short carbon fiber were carried out using SEM, as shown in Fig.7. The epoxy composites with short carbon fiber shows pull out of fiber from matrix shown in Fig. (a).

The composites with nickel coated short carbon fiber were characterized it shown comparatively rough surface which effectively increases the adhesion with matrix and also it resists the crack propagation and deformation of the composites, as shown in Fig. 7(b) [18].

## CONCLUSION

The tensile strength, impact strength and fracture toughness of the epoxy and epoxy composites were examined using ASTM standards. The tensile strength, impact strength and fracture toughness epoxy composites were significantly enhanced with addition of short carbon fiber as reinforcement to relative to neat epoxy and it further improved with addition of nickel coated short carbon fibers. Nickel coating on carbon fiber using electro electroplating technique enhanced the bonding strength and it results in improvement in mechanical properties and fracture toughness. This surface treatment of fibers increases the surface roughness of fibers and it leads to improvement in interfacial adhesion bonding strength due to mechanical interlocking between fiber and matrix and it resists the crack propagation and deformation of the composites.

## REFERENCES


1. G. M N and A. N. Hari Rao, “Gururaja M N and Hari Rao A. N, ‘A Review on Recent Applications and Future Prospectus of Hybrid Composites’, International Journal of Soft Computing and Engineering (IJSCE), Vol. 1, No. 6, pp. 352-355.
2. Vinay H. B., H K Govindaraju, PrashanthBanakar, “Processing and Characterization of Glass Fiber And Carbon Fiber Reinforced Vinyl Ester Based Composites,” *Int. J. Res. Eng. Technol.*, vol. 04, no. 05, pp. 401–406, May 2015.
3. A. Yasmin and I. M. Daniel, “Mechanical and thermal properties of graphite platelet/epoxy composites,” *Polymer*, vol. 45, no. 24, pp. 8211–8219, Jan. 2004.
4. H. Zhang, Z. Zhang, and C. Breidt, “Comparison of short carbon fiber surface treatments on epoxy composites: I. Enhancement of the mechanical properties,” *Compos. Sci. Technol.*, vol. 64, no. 13, pp. 2021–2029, Oct. 2004.
5. H. Zhang, Z. Zhang, and C. Breidt, “Comparison of short carbon fiber surface treatments on epoxy composites: I. Enhancement of the wear resistance,” *Compos. Sci. Technol.*, vol. 64, no. 13, pp. 2031–2038, Oct. 2004.
6. I. Brnardic, M. Ivankovic, H. Ivankovic, and H. J. Mencer, “Isothermal and nonisothermal cure kinetics of an epoxy/poly(oxypropylene)diamine/octadecylammonium modified montmorillonite system,” *J. Appl. Polym. Sci.*, vol. 100, no. 3, pp. 1765–1771, 2006.
7. F.-X. Perrin, T. M. H. Nguyen, and J.-L. Vernet, “Modeling the Cure of an Epoxy-Amine Resin with Bisphenol A as an External Catalyst,” *Macromol. Chem. Phys.*, vol. 208, no. 1, pp. 55–67, 2007.
8. X. Fu, W. Lu, and D. D. L. Chung, “Improving the bond strength between carbon fiber and cement by fiber surface treatment and polymer addition to cement mix,” *Cem. Concr. Res.*, vol. 26, no. 7, pp. 1007–1012, Jul. 1996.
9. D. M. Blackketter, D. Upadhyaya, T. R. King, and J. A. King, “Evaluation of fiber surfaces treatment and sizing on the shear and transverse tensile strengths of carbon fiber-reinforced thermoset and thermoplastic matrix composites,” *Polym. Compos.*, vol. 14, no. 5, pp. 430–436, 1993.
10. J. D. H. Hughes, “The carbon fiber/epoxy interface—A review,” *Compos. Sci. Technol.*, vol. 41, no. 1, pp. 13–45, Jan. 1991.
11. S.-J. Park and M.-H. Kim, “Effect of acidic anode treatment on carbon fibers for increasing fiber-matrix adhesion and its relationship to interlaminar shear strength of composites,” *J. Mater. Sci.*, vol. 35, no. 8, pp. 1901–1905, Apr. 2000.

12. Z. Hua, Y. Liu, G. Yao, L. Wang, J. Ma, and L. Liang, “Preparation and Characterization of Nickel-Coated Carbon Fibers by Electroplating,” *J. Mater. Eng. Perform.*, vol. 21, no. 3, pp. 324–330, Mar. 2012.
13. N. Kumar, H. C. Chittappa, A. Allen D. Mello, and K. M D, “Fatigue Behavior of Carbon Fiber Reinforced Aluminum Metal Matrix Composites,” *Adv. Sci. Eng. Med.*, vol. 10, pp. 463–466, Mar. 2018.
14. M. D. Kiran, H. K. Govindaraju, and T. Jayaraju, “Evaluation of fracture toughness of epoxy-nickel coated carbon fiber composites with Al2O3 nano filler,” *AIP Conf. Proc.*, vol. 2057, no. 1, p. 020002, Jan. 2019.
15. G. Agarwal, A. Patnaik, and R. K. Sharma, “Mechanical and Thermo–Mechanical Properties of Bi-directional and Short Carbon Fiber Reinforced Epoxy Composites,” vol. 9, p. 15, 2014.
16. W. Dong, H.-C. Liu, S.-J. Park, and F.-L. Jin, “Fracture toughness improvement of epoxy resins with short carbon fibers,” *J. Ind. Eng. Chem.*, vol. 20, no. 4, pp. 1220–1222, Jul. 2014.
17. J. M. L. Reis and A. J. M. Ferreira, “Assessment of fracture properties of epoxy polymer concrete reinforced with short carbon and glass fibers,” *Constr. Build. Mater.*, vol. 18, no. 7, pp. 523–528, Sep. 2004.
18. B. Y. Park, S. C. Kim, and B. Jung, “Interlaminar Fracture Toughness of Carbon Fiber/Epoxy Composites using Short Kevlar Fiber and/or Nylon-6 Powder Reinforcement,” *Polym. Adv. Technol.*, vol. 8, no. 6, pp. 371–377, 1997.